Noise in dual-frequency semiconductor and solid-state lasers

Syamsundar De

Université Paris-Sud
Ecole doctorale Ondes et Matière
Laboratoire Aimé Cotton

Discipline: Physics

Doctorate Thesis

Defended on 29/06/2015
by

Syamsundar De

Noise in dual-frequency semiconductor and solid-state lasers

Director of thesis	Mr. Fabien Bretenaker	Directeur de recherche	LAC
Co-director of thesis	Mrs. Rupamanjari Ghosh	Professor	JNU-SNU

Jury members:

Jury president	Mrs. Rosa Tualle-Brouri	Professor	IOGS-LCF
Reviewers	Mrs. Anne Tropper	Professor	Univ. of Southampton
	Mrs. Anne Amy-Klein	Professor	Univ. Paris 13
Examiners	Mr. Mehdi Alouini	Professor	Univ. de Rennes 1
	Mrs. Isabelle Robert-Philip	Chargée de recherche	LPN
	Mrs. Ghaya Baili	Ingénieur de recherche	TRT
Invited member	Mr. Fabien Bretenaker	Directeur de recherche	LAC

Contents

General Introduction

The invention of the laser, in 1960 [Maiman, 1960], is truly one of the towering achievements of the twentieth century. Soon after this first demonstration, numerous types of lasers have emerged, such as, solid-state, semiconductor, gas, dye lasers, etc. Because of their several fascinating properties, nowadays, lasers are used almost everywhere, starting from optical communication, information-storing in digital recordings, spectroscopy, imaging, micromachining, precision metrology, to biology, medical surgery, military applications, entertainment displays, and so on. Some of the key features which have made lasers an essential tool for such a wide range of applications are good spatial and temporal coherence, high optical power, excellent beam quality, etc. Among others, the semiconductor [Agrawal and Dutta, 1993; Chow and Koch, 1999; Kapon, 1999a] and the solid-state lasers [Koechner and Bass, 2003; Hooker and Webb, 2010] have come out as the preferred ones for applications like fiber-optic communication, high resolution spectroscopy, short pulse generation, etc, because of their compact construction, chemical and mechanical stability, durability, wide wavelength coverage, ability of high-speed modulation, and low-cost.

Recently, the development of a special type of semiconductor laser, namely vertical-external cavity surface-emitting laser (VECSEL) [Kuznetsov et al., 1997; Tropper et al., 2004; Keller and Tropper, 2006], has drawn considerable attention because of its unique qualities. These lasers include advantages of both the semiconductor and solid-state lasers. For example, on the one hand, semiconductor diode lasers are well known for coverage of wide range of wavelengths, small size, electrical excitation and modulation, good efficiency [Agrawal and Dutta, 1993; Kapon, 1999b]. However, achieving a good beam quality together with a multiwatt output power level is difficult with semiconductor lasers, even though such a combination is useful for several applications. On the other hand, solid-state lasers can provide very high optical power (hundreds of watts) with a

very good beam quality, but with a limited wavelength coverage due to the discrete values of the electronic transitions in ions [Koechner, 2006]. This leads to the development of VECSELs, which can cover a wide wavelength range as well as deliver several watts of output power with an excellent beam quality [Okhotnikov, 2010]. Nevertheless, the importance of solid-state lasers, in particular the ones pumped by laser diodes, cannot be put aside either for applications in science and technology or for fundamental research [Koechner and Bass, 2003; Hooker and Webb, 2010].

The advancement of laser technologies has revolutionized the modern communication systems, in particular, the fiber-optic communications [Agarwal, 2002] upon which internet, telephone, television, etc., are dependent. Moreover, the integration of lasers with microwave systems, commonly known as microwave photonics, constitutes one key building block of broadband wireless access networks, sensor networks, radar, satellite communications, instrumentation, and electronic warfare systems. The optical generation of a high spectral purity widely tunable microwave local oscillator is one of the major functions of any modern microwave photonics link [Seeds and Williams, 2006; Yao, 2009]. To optically generate a microwave signal one can heterodyne two optical signals with a frequency difference in the radio frequency (RF) range. Moreover, it is worth mentioning also that apart from microwave photonics applications, two optical waves with a high degree of correlation is also an interesting tool for applications like atomic clock [Knappe et al., 2007; Vanier, 2005], pump-probe experiment, metrology [Nerin et al., 1997; Du et al., 2005], among many others. However, in this thesis, we mainly focus on the microwave photonics applications. There exist several techniques to emit two optical frequencies such as using two different lasers or two longitudinal modes of a single laser [Scheller et al., 2010]. Unfortunately, the use of two different lasers due to their independent fluctuations leads to a relatively large linewidth of the generated microwave signal, whereas the microwave signal generated by optical mixing of two longitudinal modes of a single laser suffers from a poor tunability. It is therefore useful to develop a laser source that can emit two modes with, in one hand, a widely tunable frequency difference in the RF range and having, on the other hand, low noises with a high degree of correlation. This paves the way for dual-frequency lasers, which sustain simultaneous oscillation of two linear-orthogonal polarization modes with a frequency difference lying in the radio frequency (RF) range and tunable over a wide range. Moreover, since the two modes in a dual-frequency laser oscillate inside the same optical cavity and they are pumped by

the same source, one could expect their fluctuations to be strongly correlated. Such dual-frequency oscillation has been realized for both solid-state (mainly Nd^{3+}-, Er^{3+}-doped) [Brunel et al., 1997; Alouini et al., 1998; Czarny et al., 2004] and semiconductor active media (VECSEL) [Baili et al., 2009; De et al., 2013b; Dumont et al., 2014].

Ideally, one would want a laser source, which can deliver one or more optical signals, depending on the requirement, with a well defined amplitude, phase, and frequency. However, in reality, there hardly exits such a laser source. Generally, a laser exhibits fluctuations of amplitude, phase and frequency. The fluctuations of the amplitude lead to the fluctuations of the laser output power, whereas the phase or frequency noise is reflected in the spectral width of the laser light. Laser noises can arise from several sources such as spontaneous emission, mechanical or acoustic vibration, thermal fluctuations, pump sources (electrical or optical), etc. For many years, the noise in lasers has been a subject of strong interest among the scientific community not only for numerous laser applications but also because of very rich underlying physics. For example, laser noise can be a good probe for the illustration of the laser dynamics [McCumber, 1966]. Moreover, for metrology applications like extremely precise interferometric length measurements useful for gravitational wave detection, spectroscopic measurements, high performance atomic clocks, etc, the precise knowledge of the laser noise is of utmost importance. Therefore, a good understanding of the noise mechanisms in a laser is essential, on the one hand, to further implement this knowledge for other types of laser to understand their noise properties, and on the other hand, to upgrade the performance of several laser based applications. Analyzing the noise properties of a dual-frequency laser is even more fascinating as in such two mode lasers, there exists competition between the modes for the gain. The competition becomes strong or weak depending on whether the gain-saturation by one mode reduces the gain for the other mode by a large or a small amount. This mode competition dictates both steady-state and transient behaviors of a two-mode laser. For example, the degree of mode competition determines different stability regimes e.g., bistability or simultaneity, of the two-mode lasers [Sargent III et al., 1974]. Moreover, this mode competition establishes nonlinear coupling between the two modes. As a result, the laser dynamics becomes complex and noise analysis in such two-mode lasers therefore becomes extremely challenging.

In the context of the targeted microwave photonics applications, the spectral purity of the optically generated microwave signal is of particular interest [Alouini et al., 2001; Pillet

et al., 2008]. Any phase fluctuation of the microwave signal degrades its spectral purity. The spectral purity of the microwave signal, generated by optically mixing the two modes of a dual-frequency laser, depends on the phase noises of the laser modes. Specifically, the phase noise of the microwave beatnote is equal to the difference between the phase noises of the two laser modes. Moreover, in semiconductor lasers, the phase fluctuations are coupled with intensity fluctuations as in semiconductor active media carrier density fluctuations cause refractive index fluctuations. This phase-intensity coupling is usually described by the large linewidth enhancement factor or α-factor of the semiconductor laser media [Henry, 1982; Agrawal, 1989]. Consequently, the spectral purity of the microwave beatnote is governed not only by the phase noises, but also by the intensity noises of the two laser modes. Moreover, the intensity noises of the two laser modes dictate the beatnote amplitude noise, which deteriorates the beatnote signal to noise ratio. Additionally, since the correlated part of the noises are canceled out in the beatnote, the correlations between different noises of the two laser modes also play an important role to determine the spectral purity of the microwave beatnote.

The main objective of the work presented in this thesis is to thoroughly investigate the noise mechanisms in both semiconductor (VECSEL) and solid-state (Nd:YAG) dual-frequency lasers, and then to understand how these laser noises propagate to the microwave beatnote, generated by optically mixing the two laser modes. The focus of this thesis is mainly experimental. However, we have consistently proposed new analytical models or adopted the models already existing in the literature to verify and interpret the experimental results in order to gain a better understanding. The present manuscript is divided into two parts. In the first part, **Part I**, we deal with noise in dual-frequency VECSELs, and the second part, **Part II**, includes noise analysis in dual-frequency solid-state lasers, particularly, dual-frequency Nd:YAG lasers.

Part I is distributed in three chapters. In **Chapter 1**, we start by recalling the description of a dual-frequency VECSEL operating at $1\,\mu$m. Then following [Baili et al., 2009], we reproduce the spectral properties of the optically-carried microwave signal, generated by beating the two cross-polarized modes of the $1\,\mu$m dual-frequency VECSEL. In particular, we study the phase and amplitude noise spectra of the RF beatnote. Our focus will be mainly on how class-A dynamical behavior, achieved by making photon lifetime inside the cavity longer than the population inversion lifetime, leads to an improved noise performance of the RF beatnote of the DF-VECSEL. Furthermore, knowing that

the most suitable wavelength for the fiber-optic communication is the telecom wavelength, we demonstrate, for the first time, a low noise optically-pumped dual-frequency VECSEL operating at 1.55 μm. The detailed descriptions of the composition of the gain-structure, the cavity configuration are presented. Finally, we try to gauge the potentialities of the telecom wavelength dual-frequency VECSEL for the optical generation of the microwave signal by primarily looking at the beatnote phase noise spectrum.

In **Chapter 2**, we carry out a thorough analysis of the noise properties of a dual-frequency VECSEL operating at telecom wavelength. We investigate the spectral behaviors of the correlation between the intensity noises of the two modes of the VECSEL, the phase noise of the RF beatnote, and the correlation between the RF beatnote phase noise with the intensity noises of the two laser modes, which generate the beatnote via optical mixing. The influence of the mode competition on the spectral behaviors of the different noises and their correlations by controlling the degree of cross-gain saturation is also explored. We introduce a simple rate-equation based heuristic model for the illustration of how the intensity noise of the pump laser in the dual-frequency VECSEL propagates to the phase noise of the RF beatnote. Finally, we give a physical interpretation of the results in terms of the linear response of two-coupled over-damped oscillators.

In **Chapter 3**, we propose a developed theoretical model to describe different steady-state and transient behaviors of the dual-frequency VECSEL. The modeling of the dual-frequency VECSEL is done by taking into account the spin-dependent dynamics of the carriers in the quantum-well based active medium [San Miguel et al., 1995]. We illustrate how this developed model can successfully explain few important features of the dual-frequency VECSEL regarding nonlinear coupling strengths, stability of oscillation, etc, which the simple rate equation model are unable to do. Moreover, we show that one can recover the previous heuristic model from the present developed model by adopting approximations valid for our dual-frequency VECSEL. Finally, to further check the consistency of this developed model, the spectral properties of the intensity noises and their correlation are reproduced using the predictions of the present model.

In the second part, **Part II**, of this manuscript, our interest lies in exploring the noise properties of dual-frequency solid-state lasers, in particular, Nd:YAG lasers. In **Chapter 4**, we report the spectral behaviors of the intensity noises and their correlations for different nonlinear coupling strengths between the two laser modes of the dual-frequency Nd:YAG laser. We mainly look at the influence of the class-B dynamics of the Nd:YAG

laser coming from the shorter photon lifetime inside the cavity than the population inversion lifetime on its intensity noise properties. In particular, our focus is to realize how the presence of the relaxation oscillations in dual-frequency Nd:YAG lasers inherent to their class-B dynamics modifies the intensity noise correlation spectra. In the support of the experimental results, we introduce a theoretical model following the formalism of [Schwartz et al., 2009] assuming that the light emitting dipoles behave as if they were aligned along the crystallographic axes in the Nd:YAG active medium. Similar to the dual-frequency VECSEL, we interpret the results in the framework of the linear response of two-coupled weakly damped oscillators.

Finally, in the last chapter, **Chapter 5**, we describe an experimental technique for the minimization of the anti-phase relaxation oscillation peak in the intensity noise spectra of the two cross-polarized modes in a dual-frequency Nd:YAG laser. The anti-phase noise reduction technique relies on the proper design of the laser architecture paying special attention to the active medium cut and the polarization directions of the two laser modes.

Part I

Noise Properties of Dual-Frequency Vertical-External-Cavity Surface-Emitting Lasers (VECSELs): Experiment and Theory

Chapter 1

Dual-frequency VECSELs

Contents

1.1 Introduction

High-purity and widely tunable microwave or millimeter wave signals are interesting for many applications such as radars, wireless communications, remote sensing, modern instrumentation, metrology, etc. The generation of such microwave or millimeter wave signals in electrical form includes multi-stage electronic circuitry, which is complex and costly. Moreover, the high losses of electrical transmission lines, like coaxial cables, limit the use of microwave signals in electrical form for applications requiring distribution of microwave signals to remote places. On the other hand, the use of optical fibers permits to obtain large bandwidth, extremely low loss, immunity to external radiations, parallel signal processing, etc. This leads to the very concept of microwave-photonics link, which takes into account advantages of both microwave and optical technologies for the above mentioned applications. In any microwave photonics link, optical generation of microwave or millimeter-wave appears to be one of the main functions among others such as processing, amplification, control, and distribution of signals [Seeds and Williams, 2006; Yao, 2009]. Specifically, optical generation of microwave and millimeter-wave signals is emerging as a key building block for future optoelectronic communication systems such as broadband mobile systems [Ni et al., 1990], satellite networks [Gliese et al., 1991], short-range video transmission [O'Reilly and Lane, 1994], long-range transmission of high-purity radio frequency (RF) references [Alouini et al., 2001; Narbonneau et al., 2007], wide-band radar signal processing [Tonda-Goldstein et al., 2006; Rideout et al., 2007], and so on. These applications require the following properties for the optically carried microwave signal: good spectral purity, continuous tunability over a wide range, and 100% modulation depth. In addition to that, the optical system must be compact and easy to implement. There exists several techniques to generate optically-carried microwave signals, such as direct or external modulation of a single mode laser [O'Reilly and Lane, 1994], heterodyning of two independent lasers [Steele, 1983; Williams et al., 1989; Ni et al., 1990; Scott et al., 1992], optical mixing of two longitudinal modes of a single laser [Lima et al., 1995], mode locking of semiconductor lasers [Lau, 1988], and so on. However, all these techniques suffer from different drawbacks, such as poor modulation depth as well as requirement of bulky and expensive RF signal generator for external modulation of a laser source, large linewidth of the RF signal generated by heterodyning two independent lasers, poor tunability of the RF signal obtained from optical mixing of two longitudinal modes of single

laser, etc. This leads to the concept of dual-frequency laser, which has the capability to overcome all the shortcomings of the previously mentioned techniques, and can provide high spectral purity, wide tunability, and 100% modulation depth of the optically-carried microwave signal. In dual-frequency lasers (DFLs), the cavity sustains simultaneous oscillation of two linear orthogonal polarization modes with tunable frequency difference in the RF range (Fig. 1.1). Therefore, the RF signal can be generated by optical mixing of the two-cross polarized modes from a DFL using a polarizer at 45°. The photodector following the polarizer enables us to obtain the RF beatnote in electrical form (Fig. 1.1). Such dual-frequency oscillation has been realized in different optically-pumped solid-state

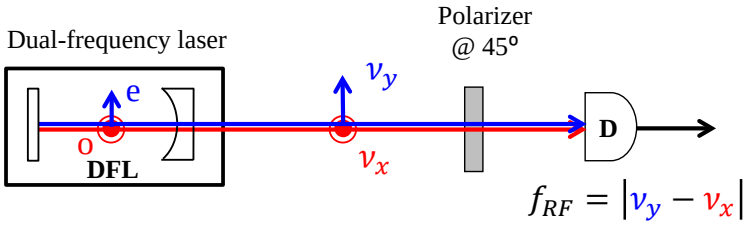

Figure 1.1: Optical generation of a radio frequency (RF) signal using a dual-frequency laser (DFL). D: photodiode.

lasers, e.g., in Nd:YAG [Brunel et al., 1997], Yb,Er:Glass [Alouini et al., 1998], Yb:KGW lasers [Czarny et al., 2004]. However, these solid-state lasers suffer from relaxation oscillations (ROs) inherent to their class-B dynamical behavior. This is due to the fact that the photon lifetime inside the cavity is shorter than or comparable to the population inversion lifetime inside these solid-state active media [Arecchi et al., 1984; Taccheo et al., 1996]. As a result, the spectral purity of the RF beatnote generated by such solid-state lasers is severely degraded due to the presence of the excess noise peaks at the RO frequencies [Alouini et al., 2001]. One of the ways to overcome these ROs is that the laser exhibits class-A dynamical behavior, which requires the photon lifetime inside the cavity to be much longer than the population inversion lifetime inside the active medium. The population inversion lifetime inside the above mentioned solid-state active media is of the order of few hundreds of microseconds. Therefore, to achieve class-A dynamical behavior in such solid-state lasers, the cavity should be km-long for a few percent of intra-cavity losses, which is quite difficult to design. On the other hand for lasers based on semiconductor active media, it is quite easy to achieve class-A dynamics as the pop-

ulation inversion lifetime inside such semiconductor hetero-structure is typically of the order of few nanoseconds, and hence cm-long cavities having sufficiently high finesses can provide intra-cavity photon lifetimes of the order of few tens of nanoseconds. Class-A dynamical behavior has been indeed achieved for a vertical external-cavity surface-emitting laser (VECSEL) having a cm-long high-finesse cavity [Baili et al., 2007, 2008]. Moreover, dual-frequency oscillation in class-A VECSELs operating at different wavelengths such as 1 μm [Baili et al., 2009; De et al., 2013b], 852 nm [Dumont et al., 2014], has also been demonstrated.

In this chapter, our aim is to investigate the potentialities of the VECSELs in terms of dual-frequency oscillation. The chapter is organized as follows: in Sec. 1.2, we reproduce the results of optically-pumped DF-VECSEL operating at 1 μm, which has first been demonstrated by G. Baili et. al., [Baili et al., 2009]. In particular, we describe the design of the gain structure, the architecture of the cavity, and finally the spectral behavior of the RF beatnote generated by optical mixing of the two cross-polarized modes of the DF-VECSEL. However, the DF-VECSEL operating at 1 μm is incompatible with most microwave photonics applications. As we know, the most suitable wavelength for microwave photonics applications is the telecom wavelength. It is important to mention here that we started with 1 μm-VECSEL as it was the only laser we had at the beginning. Then, high power and low noise single mode optically-pumped VECSEL operating at telecom wavelength was realized by G. Baili, et al., [Baili et al., 2014]. But as discussed previously, the targeted microwave photonics applications require not only VECSEL operating at telecom wavelength, but also simultaneous oscillation of two linear cross-polarized modes with different frequencies inside the laser cavity. We have demonstrated, for the first time, a class-A dual-frequency VECSEL operating at telecom wavelength [De et al., 2014a]. This DF-VECSEL is optically pumped with a diode laser at 980 nm. It is worth mentioning here that the ultimate goal is to have a DF-VECSEL with electrical pumping, since otherwise an additional pump laser with its pump optics and power supplies is required. However for VECSELs, which typically have large beam area, electrical pumping suffers from several issues such as non-uniform current injection, current crowding, Joule heating, free carrier absorption in the doped layers, etc, [Tropper et al., 2004]. Nevertheless, the electrically-pumped VECSEL is on its way somewhat overcoming the above mentioned hurdles [Hadley et al., 1993; Kurdi et al., 2004; Keeler et al., 2005; Frougier et al., 2013], but still not readily available. In Sec. 1.3, we describe in detail the composition of the gain

structure, the cavity configuration for the telecom DF-VECSEL. Additionally, we analyze the performance of the telecom DF-VECSEL for the targeted application of generating optically carried RF signal. Particularly, we give a first observation of the phase noise properties of the RF beat signal generated by optically mixing the two-cross polarized modes of the DF-VECSEL.

1.2 1-micron dual-frequency VECSEL

In this section, we discuss the results obtained from a DF-VECSEL operating at 1 micron wavelength. Specifically, we are interested in reproducing the results of [Baili et al., 2009], which has demonstrated the generation of high-purity optically carried microwave signal using DF-VECSEL at 1 μm. These results will serve as an introduction to (i) the demonstration of DF-VECSELs operating at 1.5 μm of Sec. 1.3 and (ii) the detailed noise analysis of Chapter 2.

1.2.1 Description of the 1/2-VCSEL structure

The DF-VCSEL operating at 1 micron wavelength is based on a semiconductor gain structure, called a 1/2-VCSEL [Baili, 2008]. The 1/2-VCSEL structure has been grown by Isabelle Sagnes and her collaborators at Laboratoire de Photonique et de Nanostrutures (LPN) using metal organic chemical vapor deposition (MOCVD) technique [Laurain et al., 2009]. The 1/2-VCSEL structure contains a Bragg mirror and an active region made of quantum wells (QWs) and barriers. The name, 1/2-VCSEL, suggests that the structure corresponds to the half of a standard VCSEL (vertical-cavity surface-emitting laser), which consists of an active region sandwiched between two Bragg mirrors forming the laser cavity. The detailed description of the 1/2-VCSEL structure is given in Fig. 1.2. The Bragg mirror consists of 27 pairs of GaAs/AlAs layers of thickness $\lambda/4n$ where n is the refractive index of the semiconductor and λ is the wavelength of the laser emission. The number of GaAs/AlAs pairs, knowing the contrast of their refractive indices, is chosen in such a way that the reflectivity of the mirror becomes higher than 99.9% at 1 μm wavelength. The active region includes GaAs barriers and 6 strained-QWs of InGaAs. Each strained InGaAs QW of thickness 8 nm is sandwiched between two GaAsP layers of thickness 28 nm for the compensation of the strain. The QWs are positioned inside the

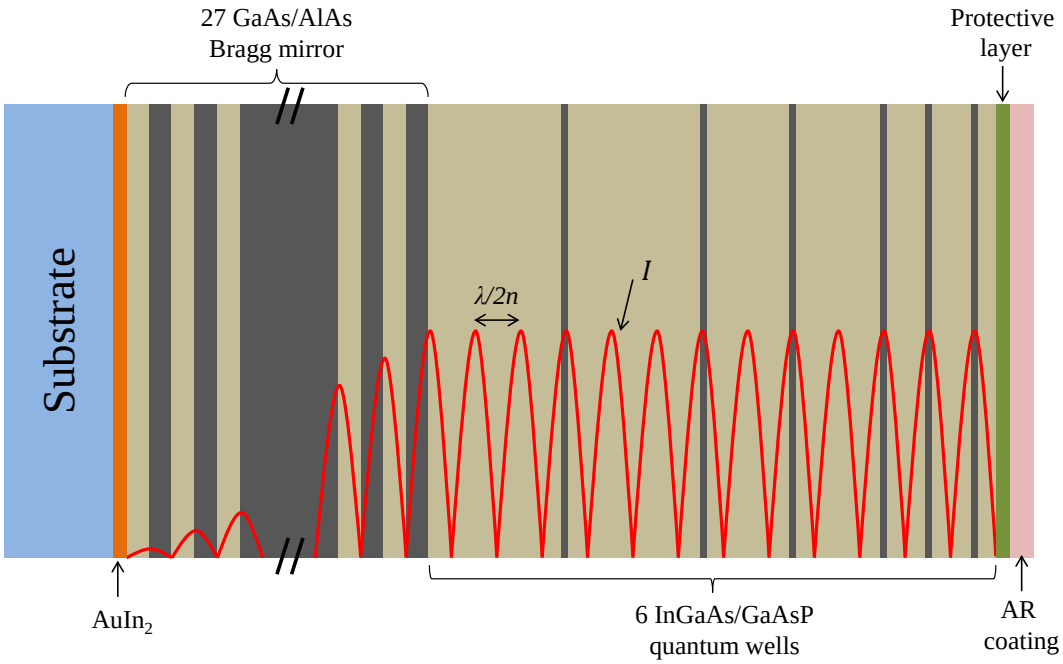

Figure 1.2: Description of the 1/2-VCSEL structure of a DF-VECSEL at wavelength $\lambda = 1\,\mu$m. n; local refractive index inside the semiconductor, I; intensity distribution inside the micro-cavity.

barriers having thicknesses equal to multiples of $\lambda/2n$. This positioning of the QWs at the intra-cavity standing wave antinodes inside the semiconductor structure, know as resonant periodic gain arrangement [Raja et al., 1989], permits to optimize the efficiency of the laser. By choosing the thickness of the last barrier as $\lambda/4n$ instead of $\lambda/2n$, the Fabry-Perot effect between the Bragg mirror and the air-semiconductor interface is reduced. One protective layer is added after the last GaAs barrier. This protective layer is made of a 30 nm thick AlAs, a 10 nm thick GaAs layer, and an InGaP cap layer of thickness 8 nm to prevent the oxidation of the aluminum layer. Finally, an anti-reflection (AR) coating of Si_3N_4 is deposited by means of plasma enhanced chemical vapor deposition (PECVD). This helps to reduce the residual etalon effect of the micro-cavity formed between the Bragg mirror and the air-semiconductor interface. The structure is grown in reverse order. The relatively poor thermal conductivity of GaAs (~ 45 W.m^{-1}.K^{-1}) limits the heat removal from the active region to the heat sink through the Bragg mirror. As a result the semiconductor structure is heated up excessively, resulting in low efficiency of

the laser. For better heat dissipation, the structure is bonded onto a 270 μm-thick SiC substrate, having high thermal conductivity (~ 490 W.m^{-1}.K^{-1}), by solid-liquid inter-diffusion (SLID) bonding with $AuIn_2$, on the Bragg mirror side.

1.2.2 Cavity configuration

The cavity architecture of the 1 μm DF-VECSEL, sustaining simultaneous oscillation of two linear orthogonal polarization modes with a frequency difference in the RF range, is schematized in Fig. 1.3. The 1/2-VCSEL structure as shown in Fig. 1.2 is glued on top of a Peltier thermoelectric cooler using thermal grease. The Peltier cooler is fixed on a copper heat sink and the temperature of the structure is maintained at 20°C. We recall that our aim is to design a laser cavity such that the laser exhibits class-A dynamical behavior. As we know, this can be achieved by making the photon lifetime (τ_{cav}) inside the cavity much longer than the population inversion lifetime (τ) inside the active medium. Previous studies with this kind of 1/2-VCSEL structure have shown that τ is around 3 ns [Baili, 2008; Baili et al., 2008]. Consequently, we need to make τ_{cav} at least of the order of 10 ns. Now, we know that τ_{cav} depends on the optical length of the cavity (L_{cav}), the intrinsic linear losses (α_i), and the reflectivities (R_1, R_2) of the end mirrors of the cavity in the following manner:

$$\tau_{\text{cav}} = \frac{L_{\text{cav}}}{c\left[ln\left(\frac{1}{R_1 R_2}\right) + \alpha_i L_{\text{cav}}\right]} \ , \tag{1.1}$$

where c is the velocity of the light inside the cavity. Moreover, the round-trip gain of the 1/2-VCSEL structure is typically around 2% [Baili, 2008; Baili et al., 2008]. Henceforth, the total losses inside the cavity per round-trip must be less than 2% for lasing. Thus, τ_{cav} of the order of 10 ns can be achieved by making a few centimeter long cavity and choosing the output coupler with a transmitivity around 1%. It is important to note that the intrinsic losses inside the mostly free-space cavity are normally quite small in this kind of external-cavity laser due to a small thickness (few microns) of the highly lossy semiconductor structure (typically $\alpha_i = 3\,\text{cm}^{-1}$). This is a huge advantage compared to the all semiconductor-cavity laser such as VCSELs. In our DF-VECSEL, the length of the laser cavity is nearly equal to 1.5 cm and it is closed with a concave mirror having radius of curvature of 2.5 cm and transmitivity equal to 0.5%. This leads to a τ_{cav} of about

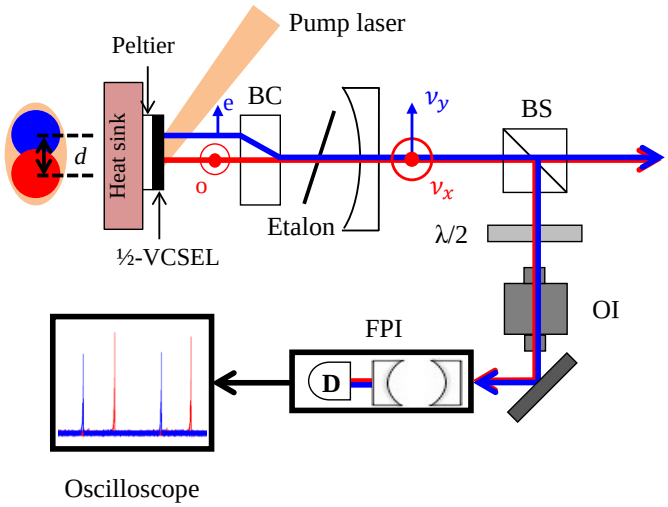

Figure 1.3: Schematic of the cavity-architecture for a DF-VECSEL. d: spatial separation between the ordinary (o) and extraordinary (e) polarizations inside the active medium, BC: birefringent crystal, BS: beam splitter, $\lambda/2$: half-wave plate, OI: optical isolator, FPI: Fabry-Perot interferometer.

20 ns, provided the transmission of the output coupler is the dominant source of losses. Thus τ_{cav} should be sufficiently longer than τ (3 ns). The DF-VECSEL based on the 1/2-VCSEL structure of Fig. 1.2 operates at 1 μm wavelength for pumping at 808 nm with a fiber-coupled diode laser. The fiber is multi-mode with a core diameter of 105 μm, and numerical aperture (NA) of 0.22. The pump laser can deliver up to 3 W of continuous wave power and the angle of incidence on the gain structure is around 40°. The pump diode is placed on a heat radiator and its temperature is maintained at 25°C to stabilize the pump laser emission. An YVO_4 birefringent crystal (BC) with AR coating at 1 μm is introduced inside the cavity to lift the polarization degeneracy. Since the semiconductor structure exhibits a linear gain dichroism as the QWs are strained, the maximum gain axis must be oriented along the bisector of the ordinary (o) and extra-ordinary (e) eigenpolarization directions of the BC to provide nearly identical gain for the two polarizations. The BC, cut at 45° of its optic axis, spatially separates the o- and e-polarized modes inside the gain structure by a distance d depending on its thickness. It is important to introduce a spatial separation between the two modes inside the gain medium as their robust simultaneous oscillation requires the nonlinear coupling constant C between them to be less than unity [Sargent III et al., 1974; Baili et al., 2009; Pal et al., 2010]. The present cavity configuration

leads to a waist radius of 62 μm for both laser modes inside the gain structure. We use, as a first try, a 1 mm-thick BC, leading to d of 100 μm, which is large enough to allow simultaneous oscillation of the two modes. The gain bandwidth of the 1/2-VCSEL structure is quite large (of the order of few nm). As a result, the laser cavity with a free spectral range (FSR) close to 3 GHz permits oscillation of several longitudinal modes for both polarizations. The introduction of a 150 μm-thick uncoated glass etalon forces each polarization to oscillate in a single longitudinal mode. The output of the DF-VECSEL is continuously analyzed with a Fabry-Perot interferometer (FPI) of FSR equal to 10 GHz, followed by an oscilloscope. This enables us to check that the two perpendicularly polarized modes oscillate simultaneously inside the laser cavity without any mode hopping during the duration of the data acquisition. The optical isolator (OI) in front of the FPI prevents any unwanted reflection from the FPI which could disturb the laser stability. Moreover, we also make sure oscillation of only the fundamental transverse mode for both polarizations by optimizing the overlap between the pump and the two laser beams. Additionally, this optimized overlapping between the pump and the laser beams provides maximum efficiency of our DF-VCSEL, and induces nearly identical powers in the two polarizations.

1.2.3 Generation and characterization of the RF beatnote in DF-VECSEL

As mentioned previously, the DF-VECSEL is an interesting source for microwave photonics applications [Seeds and Williams, 2006; Yao, 2009], in particular, for the generation of high spectral purity, widely tunable RF signal. The RF signal can be generated simply by optical heterodyning the two cross-polarized modes of the DF-VECSEL (Fig. 1.1). Let us assume that the electric fields of the two cross-polarized modes of the laser can be expressed as follows

$$E_x = E_{0x}\cos(2\pi\nu_x t + \phi_x)\ , \tag{1.2}$$

$$E_y = E_{0y}\cos(2\pi\nu_y t + \phi_y)\ . \tag{1.3}$$

Here, E_{0x}, E_{0y} are the amplitudes, ν_x, ν_y are the frequencies, and ϕ_x, ϕ_y are the phases of the x(o)- and y(e)- polarized modes of the DF-VECSEL, respectively. When the two

cross-polarized modes are mixed with a polarizer at 45° and the polarizer output is sent to a photodector (Fig. 1.1), the photodector output current is given by

$$\begin{aligned} I_D &= A_0\left(1 + p\cos\left[2\pi(\nu_y - \nu_x)t + (\phi_y - \phi_x)\right]\right) \\ &= A_0\left(1 + p\cos\left[2\pi f_{RF}t + \Delta\phi_{RF}\right]\right) \ , \end{aligned} \tag{1.4}$$

where $p = 1$, if $E_{0x} = E_{0y}$. Here, the current amplitude A_0 is determined by E_{0x}, E_{0y} and the responsivity of the detector. It is worth mentioning that the sum frequency is blocked by the detector due to its limited bandwidth. Therefore, for $p = 1$, the RF component of the detector output reads as

$$I_{RF} = A_0\cos\left[2\pi f_{RF}t + \Delta\phi_{RF}\right] \ , \tag{1.5}$$

Equation (1.5) shows that an electrical signal with a frequency (f_{RF}) equal to the difference of the optical frequencies (ν_y, ν_y) of the two cross-polarized modes of the DF-VECSEL is generated. As can be seen from Eq. (1.5), the RF beatnote electrical signal has a constant amplitude A_0 and a constant phase $\Delta\phi_{RF}$, provided the amplitudes (E_{0x}, E_{0y}) and the phases (ϕ_x, ϕ_x) of the two optical waves are constant. However, in reality this hardly occurs as the amplitudes and the phases of the laser modes always undergo fluctuations due to several noise sources (mechanical noise, acoustic noise, thermal noise, pump noise, etc.,). Then, the RF beatnote signal can be written as

$$I_{RF}(t) = A(t)\cos\left[2\pi f_{RF}t + \Delta\phi_{RF}(t)\right] \ , \tag{1.6}$$

where

$$A(t) = A_0 + \delta A(t) \ , \tag{1.7}$$

$$\Delta\phi_{RF}(t) = \Delta\phi_{RF} + \delta\phi_{RF}(t) \ . \tag{1.8}$$

Here, $\delta A(t)$ and $\delta\phi_{\mathrm{RF}}(t)$ respectively denote the amplitude and the phase fluctuations of the RF beat signal. For the sake of simplicity, we assume $\Delta\phi_{RF} = 0$. Considering small fluctuations i.e., $\delta\phi_{RF}(t) \ll 2\pi$ and $\delta A(t)/A_0 \ll 1$, and keeping only the first order

fluctuation terms, we can simplify Eq. (1.6) as

$$I_{RF}(t) \simeq A_0 \left[\cos(2\pi f_{RF}t) + \frac{\delta A(t)}{A_0}\cos(2\pi f_{RF}t) - \delta\phi_{RF}(t)\sin(2\pi f_{RF}t)\right] . \quad (1.9)$$

Equation (1.9) proves that the amplitude fluctuations are in-phase, whereas the phase fluctuations are in phase quadrature with the carrier signal (RF beatnote). However, both of these fluctuations degrade the spectral purity of the RF beat signal. The spectral properties of the RF beatnote generated by optical mixing of two cross-polarized modes of a DF-VECSEL at 1 μm have been first reported by G. Baili et al. [Baili et al., 2009]. In the same spirit, we have analyzed the spectral behavior of the RF beatnote in our DF-VECSEL operating at 1 μm. All the measurements have been performed for a pump power of 1.5 W, which provides total output power of 60 mW for the DF-VECSEL. The schematics of the measurement setup for the RF beatnote spectrum are given in Fig. 1.4. The x(o)- and y(e)- polarized modes of our DF-VECSEL are mixed with the combination of a half-wave plate ($\lambda/2$) placed in front of a polarization beam splitter (PBS). The RF beatnote is detected using a high-speed photodetector (D), then the detector output is amplified with a RF amplifier (RFA). Finally, the beatnote spectrum is recorded with an electrical spectral analyzer (ESA). The difference between the optical frequencies (ν_x, ν_y)

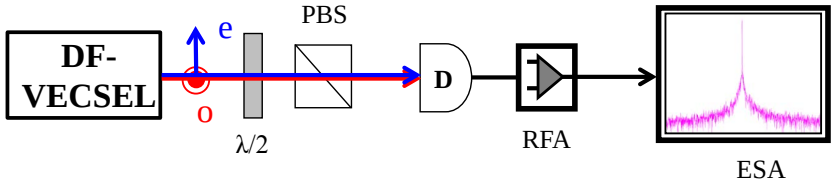

Figure 1.4: Schematic of the measurement setup of the RF beatnote. $\lambda/2$: half-wave plate, PBS: polarization beam splitter, D: photodetector, RFA: RF amplifier, ESA: electrical spectrum analyzer.

of the two modes is linked to their optical cavity length difference introduced by the BC. The frequency difference between the two modes can be expressed as follows,

$$f_{RF} \equiv (\nu_y - \nu_x) = \frac{c}{2}\left[\frac{m_y}{L_{\mathrm{cav,y}}} - \frac{m_x}{L_{\mathrm{cav,x}}}\right] , \quad (1.10)$$

where c is the vacuum speed of light, $L_{\mathrm{cav,x}}$, $L_{\mathrm{cav,y}}$ are the optical cavity lengths, and m_x, m_y are the mode numbers for $x-$ and $y-$polarized modes, respectively. To simplify Eq. (1.10), we consider following approximations,

$$\nu_y = \nu + \frac{f_{RF}}{2} \ , \quad \nu_x = \nu - \frac{f_{RF}}{2} \ . \tag{1.11}$$

In the same way, we define m, Δm, and L_{cav}, ΔL_{cav}. Moreover, we also consider that $\Delta m \ll m$, $f_{RF} \ll \nu$, and $\Delta L_{\mathrm{cav}} \ll L_{\mathrm{cav}}$. Then, Eq. (1.10) can be simplified in the first order approximation as

$$f_{RF} \ = \ \frac{c}{2L_{\mathrm{cav}}} \left[\Delta m - \frac{m \Delta L_{\mathrm{cav}}}{L_{\mathrm{cav}}} \right] \ , \tag{1.12}$$

Equation (1.12) shows that the beatnote frequency can be tuned using different parameters related to the cavity geometry. However, changing L_{cav} or m is not a practical choice for beatnote tuning, as this requires a modification of the macroscopic length of the cavity while maintaining simultaneous oscillation of the two modes. This is extremely difficult to implement. The most convenient way to tune the beatnote frequency is either by adjusting the intra-cavity birefringence (ΔL_{cav}) or the difference between the mode numbers (Δm) of the two polarizations. In our experiment, ΔL_{cav} is varied simply by rotating the BC, and Δm is adjusted by properly orientating the intra-cavity etalon. By doing so, in principle, the RF beatnote can be tuned over the entire gain spectrum (few nm). Figure 1.5 represents one such example of beatnote spectrum obtained from our DF-VECSEL operating at 1 μm wavelength. The beatnote spectrum is recorded with an ESA with resolution bandwidth (RBW) and video bandwidth (VBW) equal to 30 kHz. The beatnote is centered at about 4.082 GHz, which is higher than the FSR of our DF-VECSEL cavity (3 GHz). This shows that the two eigenpolarizations correspond to longitudinal modes of different orders ($m_x \neq m_y$). The linewidth of the beatnote is of few kilohertz in the free-running condition of our DF-VECSEL. This is comparable to free running dual-frequency solid-state lasers. Moreover, there are no side peaks around the RF beatnote, in particular, for offset frequencies within few kilohertz to few megahertz. This shows the absence of relaxation oscillations, contrary to dual-frequency solid-state lasers [Alouini et al., 2001; Pillet et al., 2008]. This corresponds to a great improvement of the noise performance of the DF-VECSEL for the generation of optically-carried RF

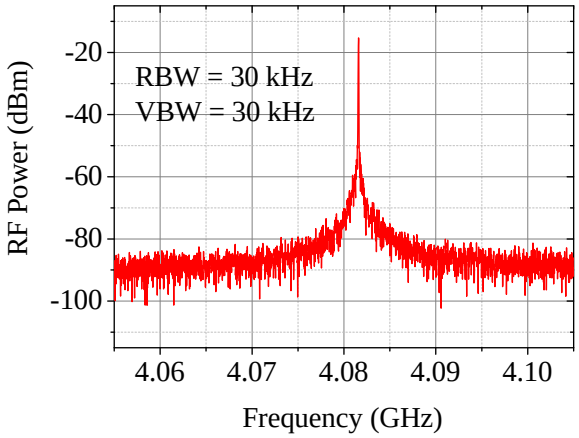

Figure 1.5: Spectrum of the RF beatnote measured with an ESA with resolution bandwidth (RBW) = 30 kHz and video bandwidth (VBW) = 30 kHz.

signals.

However, the beatnote signal is sitting over a pedestal of a few megahertz width, resulting from different noises as shown in Eq. (1.9). This degrades the spectral purity of the RF beat signal, and limits its use in stringent applications like high phase-purity optolectronics oscillators [Yao and Maleki, 1996, 1997]. Therefore, it is important to give a clear look at the different noise spectra of the RF beatnote. Measuring these noises is not at all straightforward, in particular if the phase and amplitude noises are comparable. This is linked with the fact that an electrical spectrum analyzer, which is only sensitive to the magnitude, cannot distinguish between these noises. Moreover, we have observed that the RF beatnote exhibits a frequency jitter of approximately 1 MHz for a millisecond time scale. This jitter limits the resolution at which the linewidth of the beat signal can be measured. Therefore, to further characterize the RF beatnote, we have followed the temporal measurement scheme as depicted in Fig. 1.6. One part of the RF beat signal is sent to the ESA to record its spectrum as described previously (Fig. 1.4). The other part of the RF beatnote is downshifted to intermediate frequency (IF) of few tens of megahertz by mixing it with a local oscillator (LO, Stanford-SG386). Suppose the local LO current can be written as

$$I_{LO} \quad = \quad A_{LO} \cos\left(2\pi f_{LO} t + \phi_{LO}\right) \ , \tag{1.13}$$

where f_{LO} is the LO signal frequency. Here, LO signal amplitude A_{LO} and phase ϕ_{LO} are

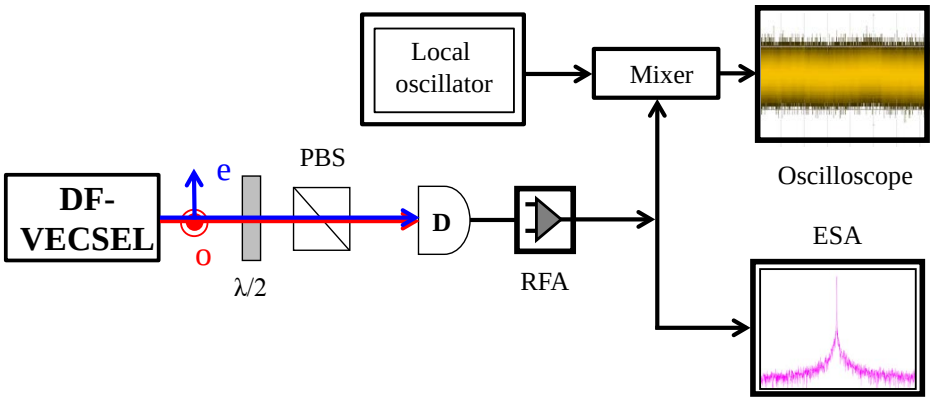

Figure 1.6: Schematic of the RF beatnote noise measurement setup. $\lambda/2$: half-wave plate, PBS: polarization beam splitter, D: photodetector, RFA: RF amplifier, ESA: electrical spectrum analyzer.

assumed to be constant. This assumption is reasonable as the amplitude and the phase noises of the LO, we used, were much lower than the respective noises of the RF beatnote. Again, for the sake of simplicity, we set $\phi_{LO} = 0$. Then, at the mixer output, we have

$$\begin{aligned} I_{IF}(t) &= A_{LO}\cos\left(2\pi f_{LO}t\right) \\ &\quad \times A_0\left[\left(1+\frac{\delta A(t)}{A_0}\right)\cos(2\pi f_{RF}t) - \delta\phi_{RF}(t)\sin(2\pi f_{RF}t)\right] . \end{aligned} \tag{1.14}$$

After a little algebra and low-pass filtering to remove sum frequency components, we obtain

$$\begin{aligned} I_{IF}(t) &= \frac{A_{LO}A_0}{2}\cos\left[2\pi(f_{RF}-f_{LO})t\right] \\ &\quad + \frac{A_{LO}A_0}{2}\left[\frac{\delta A(t)}{A_0}\cos\left[2\pi(f_{RF}-f_{LO})t\right] - \delta\phi_{RF}(t)\sin\left[2\pi(f_{RF}-f_{LO})t\right]\right] \end{aligned} \tag{1.15}$$

Then, the IF signal as shown in Eq. (1.15), is recorded in temporal domain using a deep memory digital oscilloscope. Finally, the oscilloscope data are processed to obtain phase and amplitude noise power spectral densities (PSDs) separately (Appendix A). We have found that the amplitude noise is very low compared to the phase noise [i.e., $\frac{\delta A(t)}{A_0} \ll \delta\phi_{RF}(t)$] in the considered frequency range (1 Hz to 50 MHz). The spectral behavior of

the phase noise of the RF beatnote of Fig. 1.5 is reproduced in Fig. 1.7. Figures 1.7(a),(b)

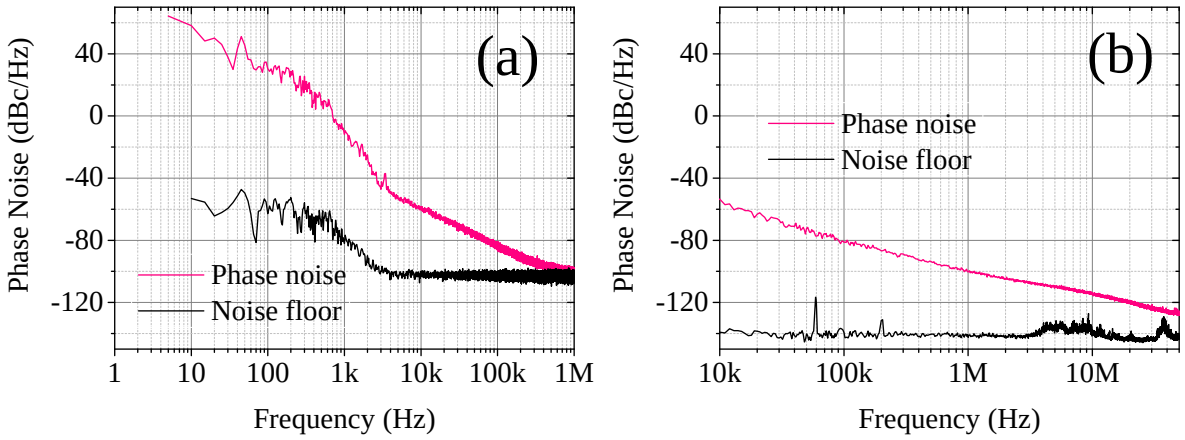

Figure 1.7: RF beatnote phase noise spectrum for (a) low, and (b) high offset frequencies.

show the phase noise of the RF beatnote for low (1 Hz to 1 MHz) and high (10 kHz to 50 MHz) offset frequencies, respectively. The phase noise spectra of Figs. 1.7(a),(b) are obtained for different frequency resolutions achieved by choosing different time windows in the oscilloscope. This permits us to obtain the phase noise spectrum over a wide offset frequency range, i.e., from 1 Hz to 50 MHz. Additionally, the fact that the measurements reproduced in Figs. 1.7(a),(b) lead to the same results from 10 kHz to 1 MHz confirms the validity of our measurement technique. In Figs. 1.7(a),(b), the pink curve represents the measured phase noise and the black curve is the measurement floor limited by the amplitude noise of the RF beatnote. It is important to note here that the noise PSD is expressed in the units of dBc/Hz. Here, dBc/Hz is preferred over the usual units of $\mathrm{dBrad}^2/\mathrm{Hz}$ for phase noise as then both amplitude and phase noise can be presented using the same scale and hence can be compared. It is worth mentioning that, here dBc/Hz simply means 3 dB less than $\mathrm{dBrad}^2/\mathrm{Hz}$ (Appendix A). One can notice that the slope of the phase noise spectrum is not uniform for all offset frequencies, which indicates different sources for the phase noise. The phase noise for offset frequencies lower than 5 kHz can be attributed to technical noises (mechanical vibrations, acoustic noise, etc.). For example, the peak at about 50 Hz can be identified as the electrical power supply noise. The change of slope at about 5 kHz offset frequency (Fig. 1.7(a)) shows that the phase noise for frequencies higher than 5 kHz originates from a different mechanism. Similarly, we

find that the slope changes again for frequencies higher than few hundreds of kilohertz, indicating another noise source for these frequencies (Fig. 1.7(b)). The important point to note here is that the phase noise spectrum does not exhibit the huge noise peak at the relaxation oscillation frequencies typically within few kilohertz to few megahertz as in dual-frequency solid-state lasers [Alouini et al., 2001; Pillet et al., 2008]. This again proves the interest of the DF-VECSEL for the targeted application of generating high spectral purity optically carried microwave signals.

1.3 Dual-frequency VECSEL at telecom wavelength

In the previous section, we have dealt with the DF-VECSEL operating at 1 μm wavelength. However, the most relevant source, in particular for fiber-optic applications, would be a DF-VECSEL operating at wavelength of 1.55 μm. In this section, we present the first demonstration of such a DF-VECSEL operating at 1.55 μm [De et al., 2014a]. One may wonder why it took so long to come into reality, while 1 μm DF-VECSELs were already there. The main reason behind this is the difficulty to fabricate a Bragg mirror with a high reflectivity as well as a good thermal conductivity. 1.5 μm-VECSEL is typically fabricated on InP substrates. One serious limitation of the InP-based structures is that the DBR must be thick because (i) the wavelength is long and (ii) the available refractive index contrast is low relative to that of GaAs/AlAs [Tropper et al., 2004; Tropper and Hoogland, 2006; Okhotnikov, 2010]. As a result the absorption and scattering losses become significant, and therefore the overall efficiency of the reflector is compromised. To counter this issue, several solutions have been realized recently such as (i) fusing GaAs/AlAs Bragg mirrors to the InP-based gain region, (ii) deposition of a gold layer to improve the reflectivity of InP/InGaAlAs mirrors, and so on [Kurdi et al., 2004; Bousseksou et al., 2006]. However, all these fabrication techniques are quite complex, explaining why it is more difficult to develop a VECSEL at 1.5 μm than at 1 μm.

1.3.1 Layer structure of the 1/2-VCSEL

The DF-VECSEL operating at 1.55 μm is based on a 1/2-VCSEL structure as depicted in Fig. 1.8. This structure has been grown by Sophie Bouchoule and her collaborators in LPN [Zhao et al., 2011]. It consists of an InP-based active region, including eight

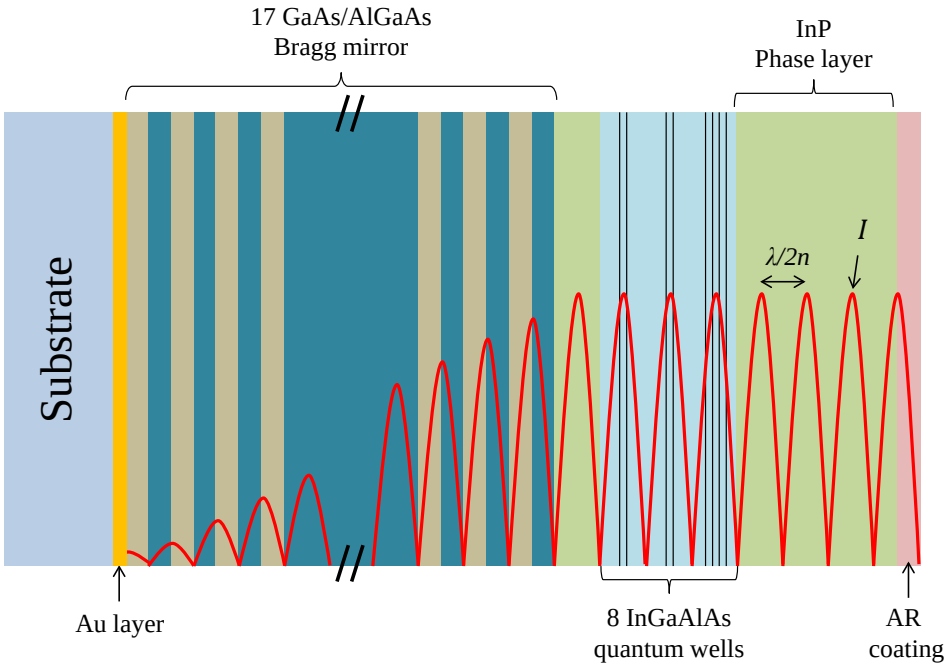

Figure 1.8: Description of the 1/2-VCSEL structure for DF-VECSEL operating at $\lambda = 1.55\,\mu$m. n; local refractive index inside the structure, I; intensity distribution inside the micro-cavity.

strained InGaAlAs quantum wells, which are distributed among three optical standing wave antinode positions with a 4-2-2 distribution. One serious limitation of the InP-based structures is the lack of availability of lattice-matched materials with high refractive index contrast for the fabrication of the Bragg mirror like in GaAs material system [Kuznetsov et al., 1999]. This leads to the requirement of thicker mirrors with more layers to achieve sufficient reflectivity for lasing [Lindberg et al., 2005], and consequently provides higher thermal impedance, thus limiting the laser efficiency. One standard way to avoid this problem is to grow the Bragg mirror with GaAs-based materials with high refractive index contrast in a separate wafer than the active region and then bonding it with the InP-based active region wafer. The bonding is done using wafer fusion technique, which thus does not require any lattice matching [Rautiainen et al., 2008]. In the 1/2-VCSEL structure we use, there is a metamorphic Bragg mirror containing 17 pairs of alternating GaAs/AlGaAs layers grown by molecular beam epitaxy (MBE). The reflectivity of the Bragg mirror is larger than 99.9% at 1.55 μm thanks to the deposition of a 150 nm−thick

gold (Au) layer. The overall gain structure is bonded on a chemical vapor deposition (CVD) polycrystaline diamond substrate thanks to an $AuIn_2$ eutectic bonding [Tourrenc et al., 2008]. The very high thermal conductivity (~ 2000 $Wm^{-1}K^{-1}$) of CVD-diamond substrate rapidly dissipates the pump induced heat leading to a good efficiency of our DF-VECSEL. A quarter-wavelength SiN_x AR-coating at the pump wavelength is finally deposited on the sample surface. Before that, the thickness of the top InP layer acting as phase layer is etched, so that the position of the resonant mode of the 1/2-VCSEL microcavity nearly coincides with the gain maximum after AR layer deposition, in a so called resonant periodic gain arrangement [Corzine et al., 1989].

1.3.2 Demonstration of dual-frequency oscillation in a 1.55-μm VECSEL

The basic configuration of the cavity for the DF-VECSEL operating at 1.55 μm can be again represented by Fig. 1.3. In this case, the pumping is done with a CW fiber-coupled diode laser at 980 nm delivering up to 4 W optical power with an incidence angle of 40°. The fiber is highly multimode with a core diameter of 105 μm, and NA equal to 0.22. The optical length of the cavity is equal to 4.76 cm leading to a FSR of 3.15 GHz. The output coupler of the cavity is a concave mirror with 99.4% reflectivity at 1.55 μm, and radius of curvature of 5 cm. Supposing that the cavity losses predominantly come from the output coupler, the photon lifetime is expected to be around 53 ns. This ensures the targeted relaxation oscillation free class-A dynamical behavior of the DF-VECSEL, as the photon lifetime becomes much longer than the population inversion lifetime (typically of the order of 1 ns) inside the 1/2-VECSEL structure. Moreover, this cavity configuration leads to a mode size of 72 μm for the two polarizations. The pump spot size on the gain structure is adjusted to obtain a maximum and nearly identical powers for the two laser modes. In this DF-VECSEL also, a 150 μm-thick uncoated glass etalon located between the BC and the output coupler inside the cavity ensures single longitudinal mode oscillation for the two eigenpolarizations. To have simultaneous and robust oscillation of the two perpendicularly polarized modes, their nonlinear coupling is reduced by spatially separating them inside the gain medium with an intra-cavity YVO_4 BC, cut at 45° with respect to its optic axis and AR coated at 1.55 μm.

Before going into the analysis of the performance of the DF-VECSEL for the generation

of optically-carried microwave signal, we check the robustness and the efficiency of the laser. We start by verifying that the laser is indeed sustaining two-mode oscillation. The optical spectrum of the laser, recorded with an optical spectrum analyzer with a resolution of 0.01 nm, is reproduced in Fig. 1.9(a). The two peaks in the spectrum prove the existence of two modes with different frequencies centered around 1.55662 μm. The output of the laser is also analyzed with an FPI with FSR of 10 GHz (Fig. 1.3). The temporal signal recorded with the oscilloscope is shown in Fig. 1.9(b). The yellow curve represents the FPI output and the blue curve stands for the ramp signal applied to the FPI for scanning. The two peaks in the output signal of the FPI within each period of the ramp signal again confirm the two-mode oscillation of the VECSEL. Moreover, this desired two-frequency oscillation is found to be stable without any mode hopping for several tens of minutes.

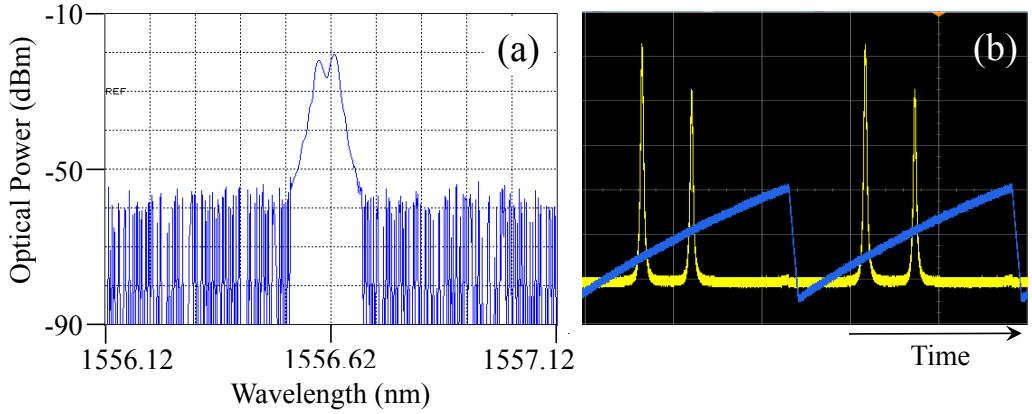

Figure 1.9: Observation of the dual-frequency oscillation at 1.55 μm: (a) optical spectrum recorded by an optical spectrum analyzer with resolution of 0.01 nm, and (b) the ramp signal and the output signal of the FPI, showing the two peaks corresponding to the simultaneous two-mode oscillation (time scale, 10 ms per division).

The other important property of the DF-VECSEL, after the robustness of two-mode oscillation, is the efficiency. We find that the spatial separation d between the two modes plays an important role to determine the efficiency of our DF-VECSEL. A smaller separation between the modes leads to a higher efficiency of the laser as the pump beam can be more tightly focused for nearly identical and optimal pumping of the two modes. On the contrary and as discussed previously, a large spatial separation is desirable for good robustness and stable simultaneous oscillation of the two modes because it decreases the nonlinear coupling between the modes much below unity. Therefore, it is important to

find an optimal value of d, which would be a good trade-off for both the robustness and the efficiency of our DF-VECSEL. Figure 1.10 shows the variation of the total output power of the DF-VECSEL with the variation of the pump power for nearly identical and optimal pumping of the two modes. The black squares represent the results for 0.5 mm thick BC, which corresponds to $d = 50\,\mu$m. The results for 1 mm thick BC corresponding to $d = 100\,\mu$m are shown by the red circles. As expected, the lasing threshold is lower and the efficiency is better for the smaller value of d. In both cases, the laser power starts to saturate for pump powers higher than 2 W as the pump-induced heating of the gain structure leads to an increasing spectral mismatch between the gain maximum and the micro-cavity resonance. In spite of the intra-cavity losses and the spatial separation of the two beams reducing the overlap with the pump, we can obtain more than 100 mW of optical power from our DF-VECSEL for a pump power around 2.5 W with a 0.5 mm thick BC inside the cavity. One might wonder, then, why not further reduce the spatial separation d between the modes. We try to further reduce it by using a 0.2 mm thick BC, corresponding to $d = 20\,\mu$m. However, this leads to a quite unstable dual-frequency oscillation. In particular, balancing the powers of the modes became extremely difficult. This proves that the coupling between the modes becomes too strong for robust simultaneous two-mode oscillation. Therefore, we may infer that a 0.5 mm thick BC is not far from being the optimal choice for our DF-VECSEL cavity.

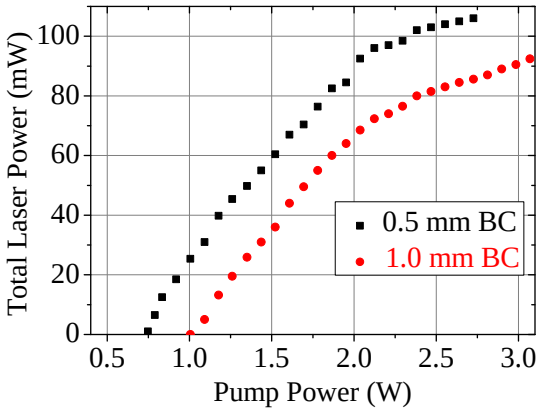

Figure 1.10: DF-VECSEL output optical power versus pump power for 1 and 0.5 mm thick BCs, respectively correspond to spatial separations d of 100 μm and 50 μm between the modes of waist size 72 μm inside the active medium.

1.3.3 Spectral analysis of the RF beatnote

After having discussed the effect of the spatial separation d between the modes on the robustness and the efficiency, it is important to analyze if there is any significant impact of d on the spectral purity of the RF beatnote generated by optical mixing of the two laser modes. The spectra of the RF beatnote and their phase noises have been investigated for two different BCs of thicknesses of 1 mm and 0.5 mm. The measurement scheme of the RF beatnote and its phase noise is identical to the one given in Fig. 1.5. The results for 1 mm thick BC, corresponding to spatial separation $d = 100\,\mu$m between the modes, are shown in Fig. 1.11. Figure 1.11(a) shows the beatnote spectrum measured with an

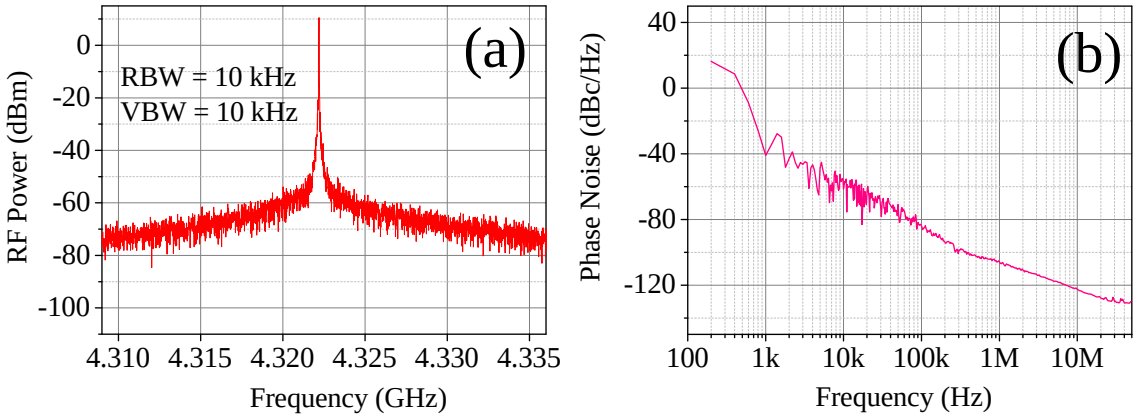

Figure 1.11: Phase noise spectrum for (a) low, and (b) high offset frequencies.

ESA with RBW and VBW equal to 10 kHz. The beatnote is centered around 4.322 GHz and has a linewidth of less than 10 kHz. The absence of side peaks in the vicinity of the beatnote proves the relaxation oscillation free class-A dynamical behavior of the DF-VECSEL. This greatly improves the spectral purity of the RF signal generated by the DF-VECSEL compared to dual-frequency erbium lasers operating at telecom wavelength [Pillet et al., 2008]. However, the beatnote signal having a width of few kilohertz is again associated with a few megahertz wide pedestal coming from the phase noise. The phase noise spectrum is shown in Fig. 1.11(b). As in the case of the $1\,\mu$m DF-VECSEL, the change of slope in the phase noise spectrum at different offset frequencies reflects the presence of different noise sources. The phase noise for frequencies lower than 1 kHz mainly originates from the technical noise, whereas for higher frequencies there must be other sources of noise, which will be explored in later chapters. Additionally, the change

of slope in the phase noise spectrum around few hundreds of kilohertz infers that there is more than one mechanism giving rise to the phase noise for high offset frequencies.

Previously, we have found that 0.5 mm thick BC corresponding to a spatial separation d of 50 μm is a good choice to have both the robust and efficient dual-frequency oscillation. Therefore, it is important now to compare the performance of the DF-VECSEL with 0.5 mm and 1 mm thick BC, in particular, regarding the spectral behaviors of the RF beatnote and its phase noise. The RF beatnote, measured with an ESA (RBW/VBW = 10kHz),

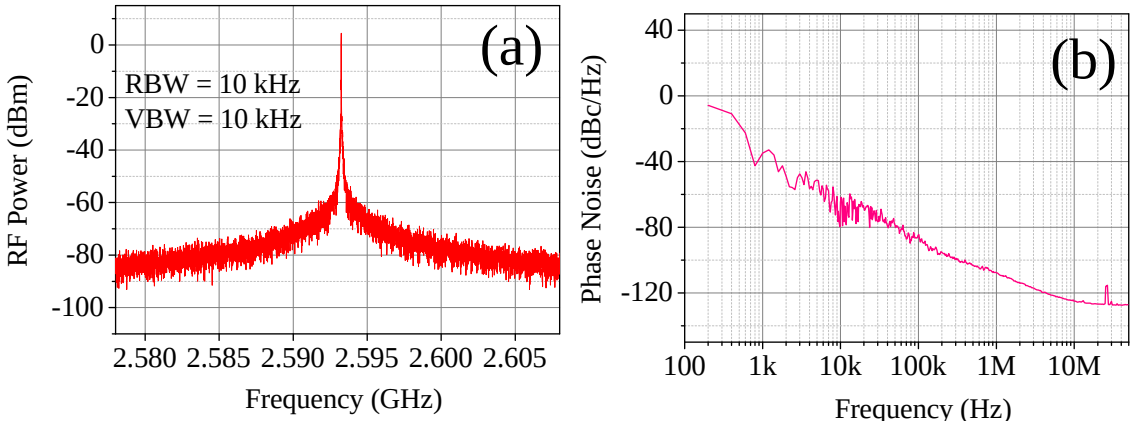

Figure 1.12: Phase noise spectrum for (a) low, and (b) high offset frequencies.

is now centered at about 2.593 GHz as reproduced in Fig. 1.12(a). Again, the beatnote spectrum is free from side peaks induced by the relaxation oscillation. However, the beatnote is found again to be resting on a pedestal of few megahertz width linked with the phase noise. Figure 1.12(b) shows the PSD of the phase noise. In this case also, the phase noise spectrum exhibits different slopes for different offset frequency ranges. For frequencies lower than 1 kHz, the technical fluctuations predominantly give rise to the beatnote phase noise. The phase noise for higher offset frequencies originates from other mechanisms. The change of slope of the phase noise spectrum around few hundreds of kilohertz proves the presence of more than one mechanism deteriorating the spectral-purity of the RF beatnote. Finally, if we compare the phase noise spectra of the RF beatnote for 1 mm and 0.5 mm thick BC, the noise levels are almost identical proving the fact that 0.5 mm thick BC is indeed a better choice for our DF-VECSEL.

1.4 Conclusions

In this chapter, we have reproduced the results of a DF-VECSEL operating at 1 μm as previously reported by G. Baili et al. [Baili et al., 2009]. Specifically, we have described the gain structure, the architecture of the cavity, and the spectral properties of the RF signal generated by beating the two linear cross-polarized modes of the DF-VECSEL. However, 1 μm wavelength is not so interesting for microwave photonics applications. The most relevant wavelength for the targeted microwave photonics applications is the telecom wavelength. We have demonstrated for the first time dual-frequency oscillation in a VECSEL operating at telecom wavelength. It has been found that a robust and highly efficient dual-frequency oscillation requires an optimized choice of the intra-cavity birefringent crystal, which spatially separates the two cross-polarized modes inside the active medium, and hence reduces their nonlinear coupling. We have shown that a 0.5 mm thick birefringent crystal corresponding to approximately 50% overlap between the modes is close to the ideal choice for optimum efficiency, robustness, and noise performance of the DF-VECSELs. The DF-VECSELs exhibit class-A dynamical behavior, and hence do not suffer from relaxation oscillation. As a result, the RF beatnote, generated by optical mixing of the two cross-polarized modes of the DF-VECSEL, does not posses any side peak originating from the relaxation oscillation. This shows why the DF-VECSELs are better than the dual-frequency solid-state lasers, which suffer from relaxation due to their inherent class-B dynamics. However, the RF beatnote obtained from a DF-VECSEL has been found to be associated with a few megahertz wide pedestal. We have evidenced that this pedestal mainly originates the phase noise of the beatnote. We have analyzed the spectral behavior of the RF beatnote phase noise for offset frequencies ranging from 100 Hz to 50 MHz. It has been found that the phase spectrum exhibits different slopes for different offset frequency ranges. This indicates the possible existence of different noise sources that deteriorate the spectral of the RF beatnote. In the following chapters of this first part of the thesis, we will elucidate those different noise mechanisms.

The following table summarizes the results presented in this chapter:

- Description of a DF-VECSEL operating at 1 μm as reported in [Baili et al., 2009].
- Demonstration of a DF-VECSEL at 1.55 μm for the first time.
- Optical generation of the RF signal by beating the two cross-polarized modes of the DF-VECSEL.
- High spectral purity of the RF beatnote due to relaxation oscillation free class-A dynamics of the DF-VECSEL.
- Existence of noise pedestal in the RF beatnote linked with its phase noise.
- Observation of different slopes in the RF phase noise spectrum indicating the presence of different noise sources.

Chapter 2

Study of noise in Dual-frequency VECSELs

Contents

2.1 Introduction

In the previous chapter, we have shown that the DF-VECSEL can indeed be an interesting choice for the generation of high-purity widely tunable optically-carried radio frequency (RF) signals, which are extremely essential for any modern microwave photonics link [Seeds and Williams, 2006; Yao, 2009]. It has been found that the class-A dynamics of our DF-VECSEL leads to a low phase noise of the RF beatnote, generated by optically mixing the two cross-polarized modes of the laser. In particular, the RF beatnote does not possess any side peak due to relaxation oscillation, unlike in dual-frequency solid-state lasers [Alouini et al., 2001; Pillet et al., 2008]. However, the experiments as described in the preceding chapter have shown that the RF beatnote with a few kilohertz width is sitting on a few megahertz wide pedestal. We have figured out that the pedestal of the RF beatnote mainly originates from its phase noise. One can wonder now from where this phase noise is coming. Of course, this is linked with the optical phase noises of the two laser modes, which generate the RF beatnote via optical mixing. Specifically, the phase noise of the RF beatnote is equal to the difference between the optical phase noises of the two laser modes. However, this is somewhat surprising, knowing that the two modes of the DF-VECSEL share the same optical cavity and are pumped by a single diode laser. Therefore, we expected the optical phase fluctuations of the two modes to be fully correlated, and hence they should have canceled out in the beatnote. Now, the presence of the pedestal is compatible with a total correlation of the modes if at least one of the two following conditions is fulfilled: i) the two noises have different amplitudes; or ii) the phase of the correlation is not zero. In addition to that, the phase and intensity fluctuations are expected to be strongly coupled in the DF-VECSEL due to the large $\alpha-$factor of the semiconductor active medium [Henry, 1982, 1986; Agrawal, 1989]. Therefore, the knowledge of the phase noise spectrum only, as described in the previous chapter, is not sufficient for complete understanding of the noise pedestal associated with the RF beatnote. It also requires exact knowledge about the correlation between different noises (intensity noise, phase noise) of the two laser modes. Moreover, the two cross-polarized modes of our DF-VECSEL are nonlinearly coupled due to their partial spatial overlap inside the gain structure. As a consequence, it is also important to investigate the effect of the nonlinear coupling between the two laser modes on the correlation between different noises. In this chapter, we explore the spectral behaviors of the intensity noises

of the modes and the phase noise of the RF beatnote, generated by optical mixing of the two modes of the DF-VECSEL [De et al., 2015]. Additionally, the correlation between the intensity noises of the two modes, and the correlation between the phase noise of the RF beatnote with the intensity noises of the two modes that generate the beatnote are studied. Moreover, the effect of the nonlinear coupling between the two cross-polarized modes of the DF-VECSEL on different noise correlation spectra is investigated. All the noises and their correlation spectra are analyzed in the frequency range of 10 kHz to 35 MHz. It is found that, in this frequency range, the intensity noise of the pump diode laser is the dominant source of noise for our DF-VECSEL. To put our understanding about the noise properties of the DF-VCSEL on more solid basis, we analyze the spectral behavior of the pump noise within the frequency range of our interest (10 kHz to 35 MHz). Additionally, we study how the two laser modes, which are spatially separated inside the active medium but pumped by the same pump laser, intercept the intensity fluctuations of the pump laser in different manners depending on their spatial separation. We evidence the fact that this dependence of pump noise properties on the spatial separation between the modes, defining the nonlinear coupling between them, plays an important role to determine the correlations between different noises of our DF-VECSEL. To better understand the influence of the pump noise on the noise properties of the DF-VECSEL, we introduce a simple theoretical model based on rate equations. The theoretical model shows good success to explain all the experimental results.

The chapter is organized as follows: we start by developing a theoretical model to describe the noise properties of our DF-VECSEL in Sec. 2.2. In Section 2.3, we present the spectral behavior of the pump noise, which is found to be the dominant source of noise in the targeted frequency range (10 kHz to 35 MHz). Section 2.4 provides a detailed description of the noise correlation measurement scheme. The spectral behaviors of the intensity noises and their correlation for different nonlinear coupling strengths between the two modes of the DF-VECSEL are illustrated in Sec. 2.5. Section 2.6 deals with spectral behaviors of the RF beatnote and its phase noise again for different nonlinear couplings between the two laser modes. The spectra of correlation between the phase noise of the RF beatnote with the intensity noises of the two laser modes, generating the beatnote via optical mixing for different nonlinear coupling between them, are reported in Sec. 2.7.

2.2 Theory: rate equation model of DF-VECSELs

In this section, our aim is to develop a theoretical model, which will be able to explain all the noise properties of our DF-VECSEL. Figure 2.1 shows a simplified cavity architecture of a DF-VECSEL, which we have described in detail in the previous chapter. In the DF-VECSEL, two linear orthogonal polarizations (x(o) and y(e)), having a frequency difference in the RF range, oscillate simultaneously inside the same laser cavity. The two cross-polarized modes are partially spatially separated inside the gain medium by an intra-cavity birefringent crystal (BC), and are pumped by a single pump laser. This spatial

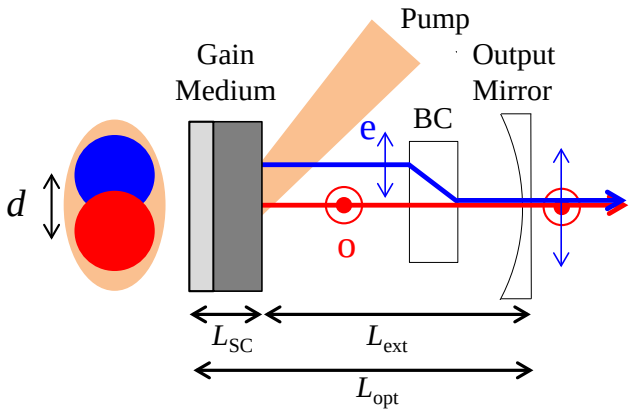

Figure 2.1: Schematic of the basic principle of the DF-VECSEL. The birefringent crystal (BC) spatially separates the two modes polarized along the ordinary (o) and extraordinary (e) directions by a distance d. The two polarizations partially overlap inside the semiconductor gain medium. The length of the semiconductor structure and the external cavity are L_{SC}, L_{ext}, respectively. L_{opt} denotes the total optical length of the cavity.

separation is required in order to make the simultaneous dual-mode operation robust by reducing their nonlinear coupling below unity [Baili et al., 2009; Pal et al., 2010]. Before going into the details of the theoretical modeling to obtain different noise spectra and their correlations, its important to define them first, which is done in the following.

2.2.1 Definition of noise spectra and correlations

The two cross-polarized modes of the DF-VECSEL can be characterized by their respective intensities, phases, and frequencies with the associated noises. Let us thus call $F_x(t)$ and $F_y(t)$ the (dimensionless) intra-cavity numbers of photons in the $x-$ and $y-$polarized modes, respectively. When theses two modes oscillate, their average steady-state intensities inside the cavity are denoted as F_{x0} and F_{y0}. Then the fluctuations in the numbers of photons are introduced as:

$$F_x(t) = F_{x0} + \delta F_x(t) \ , \tag{2.1}$$

$$F_y(t) = F_{y0} + \delta F_y(t) \ , \tag{2.2}$$

where $\delta F_x(t)$ and $\delta F_y(t)$ denote the fluctuations of photon numbers in $x-$ and $y-$polarized mode, respectively. The relative intensity noise (RIN) of the two polarizations are then defined by:

$$\mathrm{RIN}_x(f) = \frac{\left\langle |\widetilde{\delta F}_x(f)|^2 \right\rangle}{F_{x0}^2} \ , \tag{2.3}$$

$$\mathrm{RIN}_y(f) = \frac{\left\langle |\widetilde{\delta F}_y(f)|^2 \right\rangle}{F_{y0}^2} \ , \tag{2.4}$$

where f is the noise frequency and the tilde $\widetilde{\ }$ denotes Fourier-transformed quantities. Similarly, we introduce the optical phase noises $\delta\phi_x(t)$ and $\delta\phi_y(t)$ of the two modes, and thus the phase noise of the beatnote generated via optical mixing of the two polarizations can be written as:

$$\delta\phi_{Beat}(t) = \delta\phi_x(t) - \delta\phi_y(t) \ . \tag{2.5}$$

Therefore, the power spectral density (PSD) of the phase noise of the beatnote is expressed as following

$$S_{Beat}(f) = \left\langle |\widetilde{\delta\phi}_{Beat}(f)|^2 \right\rangle \ . \tag{2.6}$$

After defining the noises and their spectra, we aim at defining the spectra of correlations between different noises. The normalized correlation spectrum between the intensity

noises of the two laser modes is defined as

$$\Theta_{F_x-F_y}(f) = \frac{\left\langle \widetilde{\delta F}_x(f)\widetilde{\delta F}_y^*(f)\right\rangle}{\sqrt{\left\langle |\widetilde{\delta F}_x(f)|^2\right\rangle \left\langle |\widetilde{\delta F}_y(f)|^2\right\rangle}} . \tag{2.7}$$

Additionally, we are interested in the spectral behaviors of the correlations between the phase noise of the beatnote and the intensity noises of the $x-$ and $y-$polarized modes generating the beatnote via optical mixing. The normalized spectra of these correlation functions are defined as following:

$$\Theta_{Beat-F_x}(f) = \frac{\left\langle \widetilde{\delta\phi}_{Beat}(f)\widetilde{\delta F}_x^*(f)\right\rangle}{\sqrt{\left\langle |\widetilde{\delta F}_{Beat}(f)|^2\right\rangle \left\langle |\widetilde{\delta F}_x(f)|^2\right\rangle}} . \tag{2.8}$$

$$\Theta_{Beat-F_y}(f) = \frac{\left\langle \widetilde{\delta\phi}_{Beat}(f)\widetilde{\delta F}_y^*(f)\right\rangle}{\sqrt{\left\langle |\widetilde{\delta F}_{Beat}(f)|^2\right\rangle \left\langle |\widetilde{\delta F}_y(f)|^2\right\rangle}} . \tag{2.9}$$

The correlation spectra given by Eqs. (2.7-2.9) are complex quantities and thus have a modulus equal/smaller than 1, and an argument. The square of the modulus is called the correlation amplitude spectrum, whereas the argument is named as the correlation phase spectrum. A modulus equal to unity represents the situation of perfect correlation and the argument determines the phase of the correlation. The next parts of this section are devoted to the derivation of all these noise correlation spectra.

2.2.2 Simple rate equation model for a monomode laser

Before going into the complex scenario of our two-mode VECSEL, we start from the simple case of a single mode laser polarized along a fixed direction. To describe the dynamical properties of a laser, the convenient way is to write the rate equations for the laser variables. Considering the plane wave form of the intra-cavity field oscillating at an angular frequency ω, it can be written as

$$E(z,t) = \mathcal{A}(z,t)e^{-i(\omega t-kz)} + c.c. \tag{2.10}$$

Here, we assume that light is propagating along the z-direction inside the cavity. The fixed polarization direction of the field has allowed us to treat it as a scalar quantity. $\mathcal{A}(z,t)$ defines the slowly varying complex amplitude (dimensionless) of the field, meaning that its dependence on t and z is much slower than the plane wave term $e^{-i(\omega t-kz)}$. In the most general case, the laser dynamics is governed by three dynamical variables, namely the dipole polarization, the intra-cavity field, and the population inversion. However, in most semiconductor lasers, the polarization dynamics is so fast that it can be adibatically eliminated from the laser rate equations. This is valid for our VECSEL as well. Then, the laser dynamics can be described by the population inversion $N(t)$ and the intra-cavity field $\mathcal{A}(z,t)$. Moreover, in the limit of weak losses and gain, the z dependence of $\mathcal{A}$ can be ignored leading to the following rate equations for $\mathcal{A}(t)$ and $N(t)$ of a single mode semiconductor laser [Agrawal and Dutta, 1993]

$$\frac{d\mathcal{A}(t)}{dt} = -\frac{\gamma_{cav}}{2}\mathcal{A}(t) + \frac{\kappa}{2}(1+i\alpha)\,\mathcal{A}(t)N(t)\ , \tag{2.11}$$

$$\frac{dN(t)}{dt} = -\Gamma\left[N(t)-N_0(t)\right] - \kappa N(t)|\mathcal{A}(t)|^2\ . \tag{2.12}$$

Here, γ_{cav} and Γ respectively denote the inverse of the photon lifetime inside the cavity and the inverse of the carrier[1] lifetime. κ is the stimulated emission coefficient. N_0 is the unsaturated population inversion as ΓN_0 represents the rate of pumping. α stands for the so-called linewidth enhancement factor or Henry factor. It is defined as follows [Henry, 1982],

$$\alpha = \frac{\partial\chi_{\mathrm{Re}}(\mathrm{N})/\partial\mathrm{N}}{\partial\chi_{\mathrm{Im}}(\mathrm{N})/\partial N}\ , \tag{2.13}$$

where $\partial\chi_{\mathrm{Re}}(\mathrm{N})/\partial\mathrm{N}$ and $\partial\chi_{\mathrm{Im}}(\mathrm{N})/\partial\mathrm{N}$ respectively describe the change of the real and imaginary parts of the susceptibility ($\chi = \chi_{\mathrm{Re}} + i\chi_{\mathrm{Im}}$) with the population inversion N. The α-factor is responsible for the phase evolution of the field. Here, the presence of the $\alpha-$factor in the rate equation of $\mathcal{A}(t)$ is the signature of a semiconductor laser. The effect of the $\alpha-$factor will be more evident, if one writes separate rate equations for the modulus and argument of the complex field amplitude $\mathcal{A}(t)$. To this aim, we express $\mathcal{A}(t)$

[1] In a semiconductor laser the population inversion is the same thing as the carrier.

as

$$\mathcal{A}(t) = \sqrt{F(t)}e^{i\phi(t)} , \tag{2.14}$$

where $F(t)$ denotes the number of photons inside the laser cavity and $\phi(t)$ is the phase of the intra-cavity laser field. Substituting Eq. (2.14) in Eqs. (2.11-2.12), we obtain the following equations governing the laser dynamics

$$\frac{dF(t)}{dt} = -\gamma_{cav}F(t) + \kappa F(t)N(t) , \tag{2.15}$$

$$\frac{dN(t)}{dt} = -\Gamma\left[N(t) - N_0(t)\right] - \kappa N(t)F(t) , \tag{2.16}$$

$$\frac{d\phi(t)}{dt} = \frac{\alpha}{2}\kappa N(t) . \tag{2.17}$$

Equations (2.15-2.17) shows that the phase of the laser field is driven by the population inversion, which is again coupled with the laser intensity or the photon number through gain saturation. Thus the nonzero α-factor, alternatively known as saturable dispersion coefficient, establishes phase-intensity coupling in lasers. In case of most gas and solid-state lasers, the gain spectrum (χ_{Im}) is symmetric as it includes single atomic transition. Since the lasing takes place close to the gain maximum, both χ_{Re} and $\partial\chi_{\mathrm{Re}}(\mathrm{N})/\partial\mathrm{N}$ are zero at the transition frequency following from the Kramers-Kronig relation. On the contrary, for a semiconductor laser, the gain spectrum is not symmetric as the dipole transitions include energy bands and the occupation probability of these bands follows Fermi-Dirac distribution. Consequently, the gain maximum occurs at a frequency different from the transition linecenter. This leads to the non-zero values for χ_{Re} and $\partial\chi_{\mathrm{Re}}(\mathrm{N})/\partial\mathrm{N}$, and thus a non-zero α value for semiconductor active medium [Vahala et al., 1983; Yariv, 1975]. This accounts for the phase-sensitive dynamics of lasers based on semiconductor active media like our VECSEL. Our goal now is to extend this simple rate equation model of a single mode semiconductor laser to our two-mode VECSEL.

2.2.3 Modified rate equations for a DF-VECSEL

The main difficulty for modeling a two-mode laser such as the DF-VECSEL is to take into account competition between the modes for the gain and to analyze its consequences

on the laser dynamics . Generally, the problem of gain saturation in two-mode lasers is not at all straightforward to handle. However, we have chosen the simplest possible approach of introducing this mode competition heuristically, hoping to be able to explain different physical phenomena, in particular, the noise properties of the DF-VECSEL. The rate equations for a two-mode VECSEL can be written in their simplest form as follows,

$$\frac{dF_x}{dt} = -\gamma_x F_x + \kappa F_x N_x \ , \tag{2.18}$$

$$\frac{dF_y}{dt} = -\gamma_y F_y + \kappa F_y N_y \ , \tag{2.19}$$

$$\frac{dN_x}{dt} = -\Gamma(N_x - N_{0x}) - \kappa N_x(F_x + \xi_{xy} F_y) \ , \tag{2.20}$$

$$\frac{dN_y}{dt} = -\Gamma(N_y - N_{0y}) - \kappa N_y(F_y + \xi_{yx} F_x) \ , \tag{2.21}$$

$$\frac{d\phi_x}{dt} = \frac{\alpha}{2}\kappa N_x \ , \tag{2.22}$$

$$\frac{d\phi_y}{dt} = \frac{\alpha}{2}\kappa N_y \ . \tag{2.23}$$

Here κ, Γ, and α have the same meaning as in Eqs. (2.15-2.17). N_x and N_y denote the population inversions corresponding to $x-$ and $y-$polarized modes, respectively. γ_x, γ_y are the inverse of the photon lifetimes inside the cavity for the two modes. N_{0x} and N_{0y} stand for the unsaturated population inversions for the two modes as the pumping rates for them are given by ΓN_{0x} and ΓN_{0y}. The reason behind considering unequal intracavity photon lifetimes or pumping rates for the two modes is to take into account different losses/gains for them, which is the case in our experiments as discussed later. The coefficients ξ_{xy} and ξ_{yx} describe the ratios of the cross- to self-saturation coefficients, which take into account the effect of partial overlap between the modes inside the gain medium. Therefore,

$$C = \xi_{xy}\xi_{yx} \tag{2.24}$$

defines the nonlinear coupling constant [Sargent III et al., 1974]. This nonlinear coupling constant C determines different stability regimes for the steady-state solutions of a two-mode laser. We are interested in the situation of stable simultaneous oscillation of the two modes for which $C < 1$ must be satisfied [Sargent III et al., 1974]. It must be noted that

this definition of nonlinear coupling constant is a convenient way to phenomenologically take into account all the coupling/uncoupling mechanisms independently of their origin including mode polarization and geometrical overlap [Alouini et al., 2000]. This simple approach allows us to take into account different nonlinear coupling situations only by changing the values of ξ_{xy} and ξ_{yx}, which are linked to the degree of spatial overlap between the modes [Pal et al., 2010].

In the absence of noise, N_{0x} and N_{0y} can be replaced by their time averaged values $\overline{N}_{0x}$ and $\overline{N}_{0y}$, and the steady-state solution of Eqs. (2.18-2.21) corresponding to simultaneous oscillation of the two cross-polarized modes is

$$F_x \equiv F_{x0} = \frac{\Gamma/\kappa\left[(r_x-1)-\xi_{xy}(r_y-1)\right]}{(1-C)} , \tag{2.25}$$

$$F_y \equiv F_{y0} = \frac{\Gamma/\kappa\left[(r_y-1)-\xi_{yx}(r_x-1)\right]}{(1-C)} , \tag{2.26}$$

$$N_x \equiv N_{x\mathrm{th}} = \frac{\gamma_x}{\kappa} , \tag{2.27}$$

$$N_y \equiv N_{y\mathrm{th}} = \frac{\gamma_y}{\kappa} . \tag{2.28}$$

Here, $r_x = \overline{N}_{0x}/N_{x\mathrm{th}}$ and $r_y = \overline{N}_{0y}/N_{y\mathrm{th}}$ are the excitation ratios for the two modes. In reality, the laser never remains in perfectly stable situation. Different fluctuations (mechanical vibrations, thermal fluctuations, fluctuations of the pump, etc.) always drive the laser out of its steady-state leading to intensity, phase, and frequency noises of the laser. According to our experimental observations, which we will describe afterwards, the intensity fluctuations of the pump laser diode are the dominant source of noise in the targeted frequency range of 10 kHz to 35 MHz. In the following, we aim at introducing this pump noise in our model to be able to describe the different noise properties of our DF-VECSEL.

2.2.4 Pump noise properties

We choose to introduce the pump fluctuations for the two modes in the following manner,

$$N_{0x}(t) = \overline{N}_{0x} + \delta N_{0x}(t) , \tag{2.29}$$

$$N_{0y}(t) = \overline{N}_{0y} + \delta N_{0y}(t) , \tag{2.30}$$

where $\delta N_{0x}(t)$, $\delta N_{0y}(t)$ denote the fluctuations of the unsaturated population inversion numbers around the corresponding steady-state values $\overline{N}_{0x}$, $\overline{N}_{0y}$, respectively. Before proceeding further to describe the effect of pump noise on the noise properties of our DF-VECSEL, it is important to first characterize the pump noise itself. In the DF-VECSEL, two laser modes are pumped by the same laser. However, the two modes are facing different regions of the pump beam, as they are spatially separated. Keeping all this in mind, we introduce the following approximations

$$\left\langle |\widetilde{\delta N}_{0x}(f)|^2 \right\rangle \;=\; \left\langle |\widetilde{\delta N}_{0y}(f)|^2 \right\rangle = \left\langle |\widetilde{\delta N}_{0}|^2 \right\rangle \;, \tag{2.31}$$

$$\left\langle \widetilde{\delta N}_{0x}(f)\widetilde{\delta N}^{*}_{0y}(f) \right\rangle \;=\; \eta \left\langle |\widetilde{\delta N}_{0}|^2 \right\rangle e^{i\psi} \;, \tag{2.32}$$

where tilde ~ denotes Fourier transformed quantities. Equation (2.31) describes the fact that the pump noises entering into the two laser modes are white noises (independent of frequency) of identical amplitudes within the considered frequency range (10 kHz to 35 MHz). Our ultimate goal is to recover the correlation spectra of different noises in the DF-VECSEL. The noise correlation in the DF-VECSEL should depend on correlations between the noise sources, i.e. the pump noises. We assume the pump noise correlation spectrum as in Eq. (2.32). η denotes the correlation amplitude, and ψ stands for the correlation phase. We assume η and ψ to be constant in the frequency range of our interest (10 kHz to 35 MHz). It is important to mention here that all these approximations are verified by experiment as presented later. The RIN spectra of the pump noises for the two modes are defined as

$$\mathrm{RIN}_{Pump}(f) \;=\; \frac{\left\langle |\widetilde{\delta N}_{0x}(f)|^2 \right\rangle}{\overline{N}^2_{0x}} = \frac{\left\langle |\widetilde{\delta N}_{0y}(f)|^2 \right\rangle}{\overline{N}^2_{0y}} \;. \tag{2.33}$$

Of course, this way of linking the fluctuations of the unsaturated population inversions to the pump RINs would no longer be true at frequencies higher than the inverse of the electron relaxation time constants, i.e. higher than several hundreds of megahertz. However, within the frequency range of our interest (10 kHz to 35 MHz), this definition of pump RIN is perfectly valid. Next, we will utilize these pump noise spectral properties to recover the actual correlation spectra between different noises of the DF-VECSEL. In

the following, we start by analyzing the intensity noise properties of the DF-VECSEL.

2.2.5 Intensity noises

The pump fluctuations create fluctuations in the photon numbers defined in Eqs. (2.1-2.2), and also fluctuations in population inversion numbers around their steady-state values [Eqs. (2.27-2.28)], which we write as

$$N_x(t) = N_{x\mathrm{th}} + \delta N_x(t) \ , \tag{2.34}$$

$$N_y(t) = N_{y\mathrm{th}} + \delta N_y(t) \ . \tag{2.35}$$

Substituting Eqs. (2.1-2.2), Eqs. (2.29-2.30), and Eqs. (2.34-2.35) in Eqs. (2.18-2.21) and then performing standard linearization around the steady-state solutions [Eqs. (2.25-2.28)], we obtain

$$\frac{d}{dt}\delta F_x(t) = \kappa F_{x0}\delta N_x(t) \ , \tag{2.36}$$

$$\frac{d}{dt}\delta F_y(t) = \kappa F_{y0}\delta N_y(t) \ , \tag{2.37}$$

$$\frac{d}{dt}\delta N_x(t) = -\gamma_x\delta F_x(t) - \xi_{xy}\gamma_x\delta F_y(t) - r_x\Gamma\delta N_x(t) + \Gamma\delta N_{0x}(t) \ , \tag{2.38}$$

$$\frac{d}{dt}\delta N_y(t) = -\gamma_y\delta F_y(t) - \xi_{yx}\gamma_y\delta F_x(t) - r_y\Gamma\delta N_y(t) + \Gamma\delta N_{0y}(t) \ . \tag{2.39}$$

Thereafter, Fourier transforming Eqs. (2.36-2.39) and doing some simplification, we obtain the following expression relating the photon number fluctuations $[\widetilde{\delta F}_x(f), \widetilde{\delta F}_y(f)]$ of the two laser modes to the two pump fluctuations $[\widetilde{\delta N}_{0x}(f), \widetilde{\delta N}_{0y}(f)]$:

$$\begin{bmatrix} \widetilde{\delta F}_x(f) \\ \widetilde{\delta F}_y(f) \end{bmatrix} = \begin{bmatrix} M_{xx}(f) & M_{xy}(f) \\ M_{yx}(f) & M_{yy}(f) \end{bmatrix} \begin{bmatrix} \widetilde{\delta N}_{0x}(f) \\ \widetilde{\delta N}_{0y}(f) \end{bmatrix} \ , \tag{2.40}$$

where

$$M_{xx}(f) = \Gamma\frac{\left[\gamma_y - \frac{2i\pi f}{\kappa F_{y0}}(r_y\Gamma - 2i\pi f)\right]}{\Delta(f)} \ , \tag{2.41}$$

$$M_{xy}(f) = -\frac{\Gamma\gamma_x\xi_{xy}}{\Delta(f)} \ , \tag{2.42}$$

$$M_{yx}(f) \;=\; -\frac{\Gamma\gamma_y\xi_{yx}}{\Delta(f)}\;, \tag{2.43}$$

$$M_{yy}(f) \;=\; \Gamma\frac{\left[\gamma_x - \frac{2i\pi f}{\kappa F_{x0}}(r_x\Gamma - 2i\pi f)\right]}{\Delta(f)}\;, \tag{2.44}$$

with

$$\Delta(f) \;\;=\;\; \left[\gamma_x - \frac{2i\pi f}{\kappa F_{x0}}(r_x\Gamma - 2i\pi f)\right]\left[\gamma_y - \frac{2i\pi f}{\kappa F_{y0}}(r_y\Gamma - 2i\pi f)\right] - C\gamma_x\gamma_y\;. \tag{2.45}$$

Therefore, the RIN spectra of the two laser modes and their intensity noise correlation spectrum can be easily obtained from the definitions given by Eqs. (2.3),(2.4),(2.7) using Eqs. (2.40-2.45).

2.2.6 Phase noise of the RF beatnote

We have emphasized earlier that the targeted microwave photonics applications demand high spectral purity of the RF beat signal, generated by optically heterodyning the two cross-polarized modes of the DF-VECSEL. In the previous chapter, we have shown that the spectral purity of the RF beatnote is degraded mainly due to its phase noise. Here, our aim is to model this phase noise of the RF beatnote. The RF phase noise is nothing but the difference between the optical phase noises of the two modes of the DF-VECSEL as defined in Eq. (2.5). Now, using Eqs. (2.22-2.23), we obtain

$$\frac{d}{dt}\delta\phi^{\alpha}_{Beat}(t) \;\;=\;\; \frac{\alpha}{2}\kappa\left[\delta N_x(t) - \delta N_y(t)\right]\;. \tag{2.46}$$

The superscript 'α' indicates that the phase fluctuation $\delta\phi^{\alpha}_{Beat}(t)$ considers only the phase-intensity coupling effect due to the large α-factor of the semiconductor active medium. Therefore, the RF phase noise in the frequency domain can be calculated using Eqs. (2.36-2.37) in Eq. (2.46) and then performing Fourier transformation, leading to

$$\widetilde{\delta\phi}^{\alpha}_{Beat}(f) = \frac{\alpha}{2}\left[\frac{\widetilde{\delta F}_x(f)}{F_{x0}} - \frac{\widetilde{\delta F}_y(f)}{F_{y0}}\right]\;. \tag{2.47}$$

The PSD of the RF phase noise as defined in Eq. (2.6), then reads

$$S^{\alpha}_{Beat}(f) = \frac{\alpha^2}{4}\left[\frac{\left\langle|\widetilde{\delta F}_x(f)|^2\right\rangle}{F^2_{x0}} + \frac{\left\langle|\widetilde{\delta F}_y(f)|^2\right\rangle}{F^2_{y0}} - \frac{2\mathrm{Re}\left\langle\widetilde{\delta F}_x(f)\widetilde{\delta F}^*_y(f)\right\rangle}{F_{x0}F_{y0}}\right] . \quad (2.48)$$

One can notice in Eq. (2.48) that the phase-intensity coupling mechanism can indeed induce strong phase noise for the RF beatnote, when α is large. Moreover, the right hand side (RHS) of Eq. (2.48) indicates that the RF phase noise does not only depend on the intensity noises of the two modes (first two terms), but also on their correlation (last term). Additionally, Eq. (2.48) suggests that the RF phase noise can even be completely canceled out provided the sum of the first two terms inside the square brackets in the RHS is equal to the last term. This occurs when the intensities of the two modes are balanced and their noises are perfectly correlated. After developing the theoretical model, our goal is now to check the validity of this model by comparing with experimental results. In the model, the pump noise has been considered as the the dominant of source of noise in the considered frequency range from 10 kHz to 35 MHz. Moreover, we have assumed that the pump noises entering into the two laser modes are white noises of identical amplitudes [Eq. (2.31)]. However, they are partially correlated, $\eta < 1$, with a correlation phase ψ equal to zero [Eq. (2.32)]. In the following, we aim at testing these pump noise properties experimentally.

2.3 Pump noise measurement

In this chapter, we focus on the DF-VECSEL operating at 1.55 μm for which pumping is performed with a multimode fiber-coupled diode laser operating at 980 nm. As shown in Fig. 2.1, the two perpendicularly polarized modes of the DF-VECSEL are partially spatially separated inside the active medium, but pumped by the same pump laser source (Fig. 2.1). This spatial separation between the modes inside the gain medium forces them to face different regions of the spatially multimode pump beam (Fig. 2.1). Moreover, our ultimate goal is to analyze the noise properties of the DF-VECSEL for different nonlinear coupling strengths between the two laser modes, which will be achieved by changing the spatial separation between the two modes. In order to fully characterize the pump noises seen by the two modes, we mimic this situation by the setup schematized

in Fig. 2.2(a). Here, the pump beam is separated into two paths using a beam spliter (BS). In both paths, we introduce pinholes of identical radii (75 μm) mimicking the two laser modes (w $\simeq$ 75 μm). The two pinholes are placed on translation stages, which

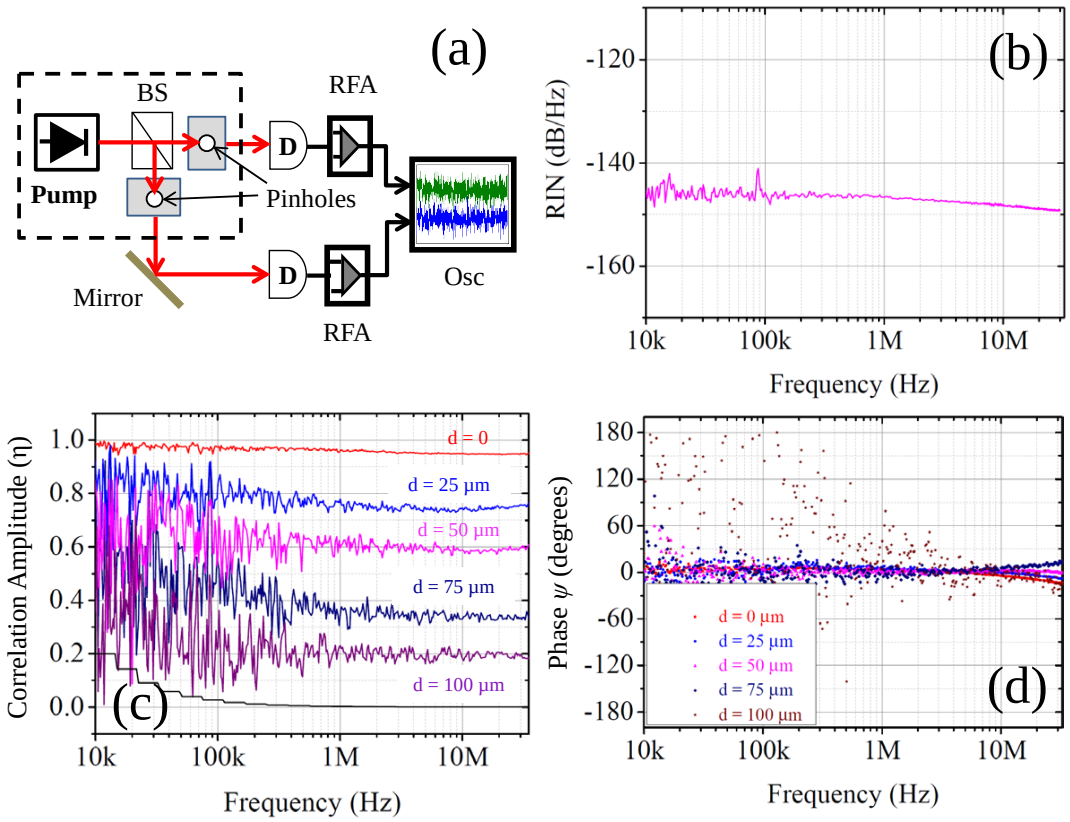

Figure 2.2: (a) Schematic of the pump noise correlation measurement setup. BS: beam spliter D: detectors, RFA: RF amplifiers. (b) Pump RIN spectrum. (c), (d) Noise correlation amplitude, and phase spectra respectively, for different values of d. The black staircase-line in (c) shows the measurement floor.

permit to obtain the situation when one pinhole acts as the exact image of the other. This situation reproduces the condition of perfect overlapping of the two laser modes inside the gain medium, i.e. $d = 0$. Therefore, by translating one of the pinholes in the horizontal direction we can reproduce the situations of different spatial separations d between the modes inside the gain structure of our DF-VECSEL. After passing through the pinholes, the pump beams are detected using photodiodes (D). The detected signals are then amplified with identical RFAs, and finally recorded with a digital oscilloscope. Then the oscilloscope data are processed using an algorithm designed by Grégoire Pillet

from Thales Research and Technology (TRT) to obtain the spectra of the pump noises and their correlation.

We investigate the pump noises for different values of d such as 0, 25 μm, 50 μm, 75 μm, and 100 μm. In all these cases, the RIN spectra of the two pump beams are nearly identical and given by Fig. 2.2(b). This confirms that the pump noises entering into the two spatially separated laser modes can be modeled identical white noises as assumed in Eqs. (2.31). Now, we check the validity of the approximations of Eq. (2.32), which describes the pump noise correlation spectrum. Figures 2.2(c),(d) respectively show the pump noise correlation amplitude (η) and phase (ψ) spectra for different values of d. Figure 2.2(c) proves that the pump noises entering the two spatially separated laser modes are partially correlated ($\eta < 1$), and the degree of correlation decreases with the increase of spatial separation d between the modes. Moreover, the correlated part of the pump intensity noises entering into the two laser modes are in phase ($\psi = 0$) for all values of d as presented in Fig. 2.2(d). Besides, these results confirm that η and ψ do not depend on the noise frequency f in the targeted frequency range from 10 kHz to 35 MHz (Figs. 2.2(c),(d)). However, one can wonder now why the pump noise correlation factor η depends on the spatial separation d. Actually, in our DF-VECSEL the pump beam is coming from a step-index multimode fiber-coupled diode laser. The maximum number of modes in a step-index multimode fiber can be calculated using the following simple expression,

$$N_{max} = \frac{V^2}{2}, \tag{2.49}$$

where $V = \frac{\pi D}{\lambda_p} \times \mathrm{NA}$. In our case, the multimode fiber [AFS105/125Y(0.22)] carrying the pump beam has a core diameter (D) of 105 μm, and a numerical aperture (NA) of 0.22. Therefore, at pump wavelength ($\lambda_p = 980$ nm) the maximum number of guided modes (N_{max}) in this fiber is equal to 2741. This large number of modes in the fiber carrying the pump beam interfere to form speckle pattern at the fiber output, leading to a nonuniform intensity distribution of the pump beam on the gain structure. This explains why the degree of correlation (η) of the pump noises entering into the two laser modes decreases with d.

In the following, these pump noise properties will be utilized to figure out different noise correlation spectra of the DF-VECSEL. We start by describing the noise correlation

measurement scheme.

2.4 Noise correlation measurement setup

The detailed description of the cavity architecture for the DF-VECSEL at 1.55 μm has already been provided in the previous chapter (Sec. III). The noise correlation measurements are performed keeping this DF-VECSEL configuration intact. Figure 2.3 shows

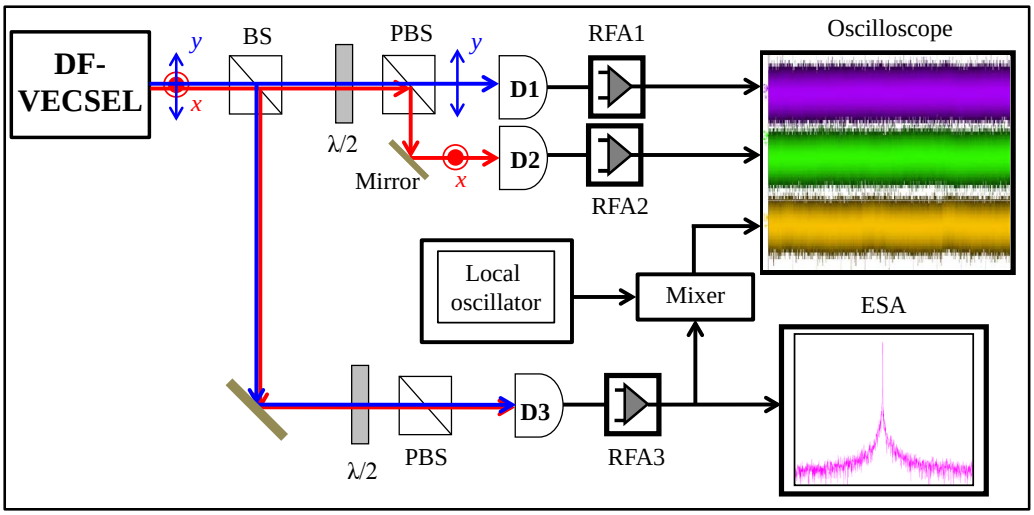

Figure 2.3: Schematic of noise correlation measurement setup. $\lambda/2$: half-wave plate, BS: beam spliter, PBS: polarization beam spliter, D1, D2, D3: detectors, RFA1, RFA2, RF3: RF amplifiers, ESA: electrical spectrum analyzer.

the schematic of the noise correlation measurement setup. As mentioned before, we are interested in analyzing the noise correlations for different nonlinear couplings between the modes. To this aim, we have used three different intra-cavity BCs of thicknesses 1 mm, 0.5 mm, and 0.2 mm, leading to d of 100 μm, 50 μm, and 20 μm, respectively. The coupling constant C, in addition to d, depends on the mode radii (w) of the two modes inside the gain structure as follows [Pal et al., 2010]:

$$C = C_0 \frac{\int I(x,y)I(x-d,y)dxdy}{\sqrt{\int I^2(x,y)dxdy \int I^2(x-d,y)dxdy}} = C_0 \exp\left(-\frac{d^2}{w^2}\right), \tag{2.50}$$

where $I(x, y)$ denotes the Gaussian intensity profiles of radii w of the laser modes. $C_0 = 0.8$ corresponds to the coupling constant when the two modes fully overlapped inside the gain structure [Pal et al., 2010]. We recall here that the planar-concave cavity of our DF-VECSEL as described in the previous chapter, leads to identical radii for the two modes, $w = 72\,\mu$m. However, thermal heating of the gain structure by the pump modifies the planar-concave cavity configuration of the VECSEL cavity. Actually, the intensity profile of the pump beam induces a temperature gradient and, consequently, a refractive index gradient inside the structure. For the InP-based gain structure of the 1.55 μm-VECSEL, the temperature dependence of the refractive index is positive ($\frac{dn}{dT} \sim 2\times10^{-4}\,\mathrm{K}^{-1}$), leading to a positive lens induced by the pump intensity distribution. Considering the Gaussian intensity profile of the pump beam with a radius w_{Pump} on the gain structure, the focal length (f_{lens}) of the pump induced thermal lens can be approximated as [Laurain, 2010]

$$f_{lens} \simeq \frac{w_{Pump}^2 R_T P_{Pump}}{2ln(2)L_{\mathrm{SC}}} \left(\frac{dn}{dT}\right) , \tag{2.51}$$

where L_{SC} , R_T respectively denote the length and the thermal impedance of the semiconductor structure, and P_{Pump} is the pump power. Using the parameter values corresponding to our experimental conditions ($L_{\mathrm{SC}} = 2\,\mu$m, $R_T = 8\,\mathrm{K.W}^{-1}$, $P_{Pump} = 1.7\,$W), we find that f_{lens} is around 30 cm. Taking into account this positive thermal lensing effect, the mode radii on the gain structure for the two modes become $w \simeq 75\,\mu$m. Considering this modified mode radii ($w \simeq 75\,\mu$m), we obtain the following coupling constant values from Eqs (2.50): $C \simeq 0.12$ for $d = 100\,\mu$m corresponding to 1 mm-thick BC, $C \simeq 0.5$ for $d = 50\,\mu$m corresponding to 0.5 mm-thick BC, and $C \simeq 0.75$ for $d = 100\,\mu$m corresponding to 0.2 mm-thick BC. We perform all the noise correlation measurements for a fixed pump power equal to 1.7 W, which leads to a total laser power of 25 mW, 40 mw and 60 mW for the 1 mm-, 0.5 mm-, and 0.2 mm-thick BCs, respectively. This difference in the output powers of our DF-VECSEL for different thicknesses of BC is linked with the fact that the pump beam could be more tightly focused for thinner BC, as then the spatial separation of the two laser modes is smaller. The key feature of the experimental scheme, as shown in Fig. 2.3, is the ability to measure all the relevant noises simultaneously, which is important to analyze their correlations. The output beam of our DF-VECSEL is divided into two parts using a beam spliter (BS), and then one part is used for intensity noise measurements, whereas the other one is utilized to generate the beatnote and measure its

phase noise. To measure the intensity noises of the two polarizations, we separate them using the combination of a half-wave plate ($\lambda/2$) followed by a polarization beam spliter (PBS). Thereafter, the two modes are detected using photodiodes (D1, D2). The signals are then amplified by two identical RF amplifiers (RFA1, RFA2), and finally sent to the two different channels of a deep-memory digital oscilloscope. To obtain the beatnote, the two polarizations are mixed using the combination of a $\lambda/2$-plate in front of a PBS. The RF beat signal is detected using a high-speed photodiode (D3). The detected signal is then amplified using a RF amplifier (RFA3). After that, one part of the signal is directly sent to an electrical spectrum analyzer (ESA) to record the spectrum of the RF beatnote. The other part is downshifted to an intermediate frequency (IF) by mixing it with a high purity local oscillator. Thereafter, the IF signal is sent to the third channel of the oscilloscope. This permits to measure the phase noise of the RF beatnote simultaneously with the intensity noises. Finally, all the channels of the oscilloscope are recorded simultaneously, and then these data are processed to obtain the noises and their correlation spectra.

2.5 Intensity noises and their correlations

The correlation between the intensity noises of the two modes in the DF-VECSEL is expected to play a pivotal role to determine the spectral purity of the RF beatnote, generated by optical mixing of the two modes. The reason behind this is twofold, (i) the phase fluctuations are coupled with the intensity fluctuations due to the large $\alpha-$factor of the semiconductor active medium of the DF-VECSEL, and (ii) the positively correlated part of the optical phase fluctuations of the two laser modes cancel out in the beatnote, generated by optical mixing of the modes. Now, it is well known that the dynamics of a multimode laser is strongly influenced by the nonlinear coupling between the modes [Otsuka et al., 1992]. Additionally, we have already evidenced that the correlation between the noise sources (pump noises) for the two laser modes of the DF-VECSEL depends on the spatial separation between the modes that defines their coupling strengths (Fig. 2.2). Therefore, the knowledge about intensity noise correlation and its dependence on nonlinear coupling strengths between the modes is of utmost importance for a better understanding of the spectral behavior of the RF beatnote and its phase noise in our DF-VECSEL. In this section, we present experimental and theoretical intensity noise correlation spectra for

different coupling strengths between the two cross-polarized modes of the DF-VECSEL.

2.5.1 Impact of nonlinear coupling

Intensity noise correlation spectra are studied for three coupling situations: weak ($C = 0.12$), intermediate ($C = 0.50$), and moderately strong ($C = 0.74$) coupling[2], which are obtained by using 1 mm-, 0.5 mm-, and 0.2 mm-thick BCs, respectively. In the following, we disclose how the noise correlation spectrum changes with the change of coupling strengths.

Weak coupling

The results for the weak coupling ($C = 0.12$) are shown in Fig. 2.4. Figures 2.4(a) represents the measured RIN spectra of the two modes in the DF-VECSEL, whereas the corresponding theoretical prediction is reproduced in Fig. 2.4(b). The red and the blue line correspond to the RIN spectra of $x-$ and $y-$polarized modes, respectively. The RIN spectra of both the laser modes are flat before they roll off starting from 1 MHz due to the limited bandwidth of the laser cavity. This first-order filter like behavior of the RIN spectra of the two laser modes confirms the relaxation oscillation free class-A dynamical behavior of our DF-VECSEL. It illustrates one more time how the intensity noise of the laser can be a good probe for the laser dynamics [McCumber, 1966]. The RINs of the two modes are slightly different as their losses and/or gains are not exactly identical. The experimental and theoretical correlation amplitude spectra are given in Figs. 2.4(c),(d), respectively. The degree of noise correlation is about - 7 dB for frequencies lower than 1 MHz, then it drops to a very low value (- 30 dB) around 5 MHz, and finally it increases slightly to become approximately -25 dB for all frequencies higher than 10 MHz. Figures 2.4(e),(f) respectively show the experimental and theoretical correlation phase spectra. These spectra describe that the correlation phase is π for frequencies lower than 1 MHz, then it starts to roll down and reaches zero at about 5 MHz and remains at zero for all higher frequencies. The staircase like black curve in Fig. 2.4(c) indicates the theoretical estimation of the minimum correlation that can be detected by our algorithm

[2]We do not use the phrase "strong coupling" because it would correspond to $C > 1$, a situation in which stable simultaneous oscillation of the two modes is impossible [Sargent III et al., 1974].

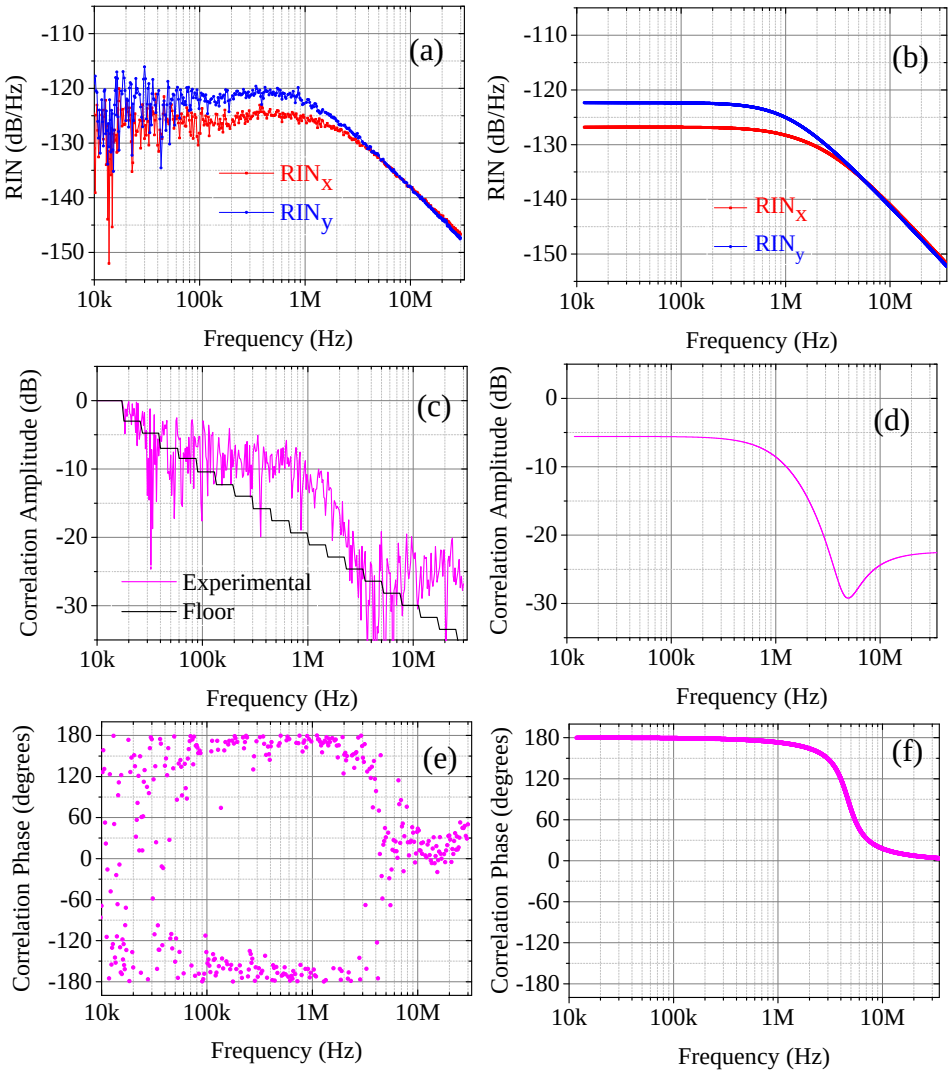

Figure 2.4: Results for the weak coupling ($C = 0.12$): The spectra of RINs: (a) experimental, (b) theoretical; correlation amplitude: (c) experimental, (d) theoretical; correlation phase: (e) experimental, (d) theoretical. The black line in (c) is the measurement floor. Parameter values used for simulation: $r_x = 1.2$, $r_y = 1.15$, $1/\gamma_x = 9.9$ ns, $1/\gamma_y = 10.4$ ns, $1/\Gamma = 1$ ns, $\eta = 0.2$, $\psi = 0$, $\mathrm{RIN}_{Pump} = -145$ dB/Hz.

used to compute the correlation spectrum. Indeed, this algorithm[3] averages the correlation amplitude over a number of samples which increases with the frequency. Thus, by supposing that the two signals are completely uncorrelated, the algorithm gives the level of correlation described by this black line. The theoretical predictions for RIN, correlation

[3]The algorithm is designed by Grégoire Pillet of Thales Research and Technology.

amplitude, and correlation phase spectra (Figs. 2.4(b),(d),(f), respectively) nicely agree with the corresponding experimental results (Figs. 2.4(a),(c),(e), respectively).

Intermediate coupling

The results for the intermediate coupling ($C = 0.50$) are presented in Fig. 2.5. Figure 2.5(a) shows the experimental RIN spectra, and Fig. 2.5(b) reproduces the theoretical prediction, confirming good agreement with the experiment. The RIN spectra of the two modes in this coupling case again prove the class-A dynamical of our DF-VECSEL. The RINs of the two modes are not exactly identical as their losses/gains are different. The experiment shows that, in this coupling case, the spectral behaviors of the correlation amplitude (Fig. 2.5(c)), and correlation phase (Fig. 2.5(e)) have changed quite significantly compared to the weak coupling situation. There is a dip in the spectrum of correlation amplitude at about 2 MHz, whereas it becomes - 3 dB, and - 5 dB respectively for frequencies lower and higher than 2 MHz. This spectral behavior of the correlation amplitude is also nicely reproduced by our theoretical model (Fig. 2.5(d)). The correlation phase spectrum ((Fig. 2.5(e)) exhibits a phase jump around 2 MHz. The phase is π for frequencies lower than 2 MHz and zero for higher frequencies. The model predicts the same spectral behavior for the correlation phase as shown in Figs. 2.5(f).

Moderately strong coupling

Figure 2.6 shows the results for the moderately strong coupling situation ($C = 0.75$). The RIN spectra, both experimental (Fig. 2.6(a)) and theoretical (Fig. 2.6(b)), again illustrate the class-A dynamical behavior of the laser. The inequality of the RINs for the two modes are coming from their different losses and/or gains. More importantly, one can notice a significant change of slope around 1 MHz in the RIN spectra, which was less prominent in the case of intermediate coupling (Fig. 2.5(a),(b)), and hardly visible for the weak coupling (Fig. 2.4(a),(b)). In this coupling case, the correlation amplitude (Figs. 2.6(c),(d)) also exhibits a significantly different spectral behavior compared to the weak or intermediate couplings. As obtained from the experiment (Fig. 2.6(c)), the correlation amplitude shows a dip at about 1 MHz, whereas it reaches almost 0 dB for frequencies lower than 1 MHz, and is close to -2 dB for frequencies higher than 1 MHz. The theoretical prediction, as shown in Fig. 2.6(d), nicely reproduces the experimental correlation amplitude

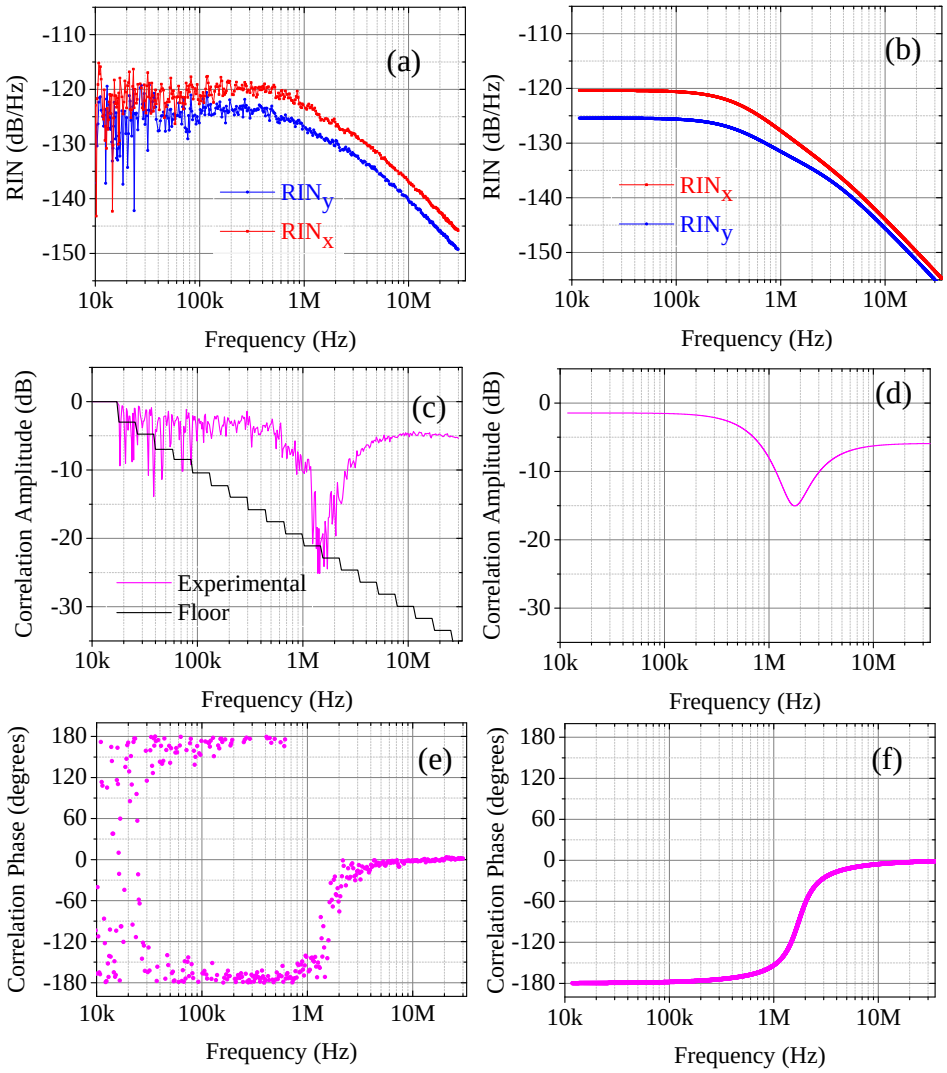

Figure 2.5: Results for the intermediate coupling ($C = 0.50$). The spectra of RINs: (a) experimental, (b) theoretical; correlation amplitude: (c) experimental, (d) theoretical; correlation phase: (e) experimental (d) theoretical. Parameter values used for simulation: $r_x = 1.32$, $r_y = 1.35$, $1/\gamma_x = 13.9$ ns, $1/\gamma_y = 16.7$ ns, $1/\Gamma = 1$ ns, $\eta = 0.6$, $\psi = 0$, $\mathrm{RIN}_{Pump} = -145$ dB/Hz.

spectrum (Fig. 2.6(c)). In the correlation phase spectrum, obtained from both experiment (Fig. 2.6(e)) and theory (Figs. 2.6(f)), there is a π-phase jump at about 1 MHz, whereas the phase is π for lower frequencies and zero for higher frequencies. The theory again shows very good matching with the experiment.

The parameter values used for simulations in all three coupling conditions are obtained

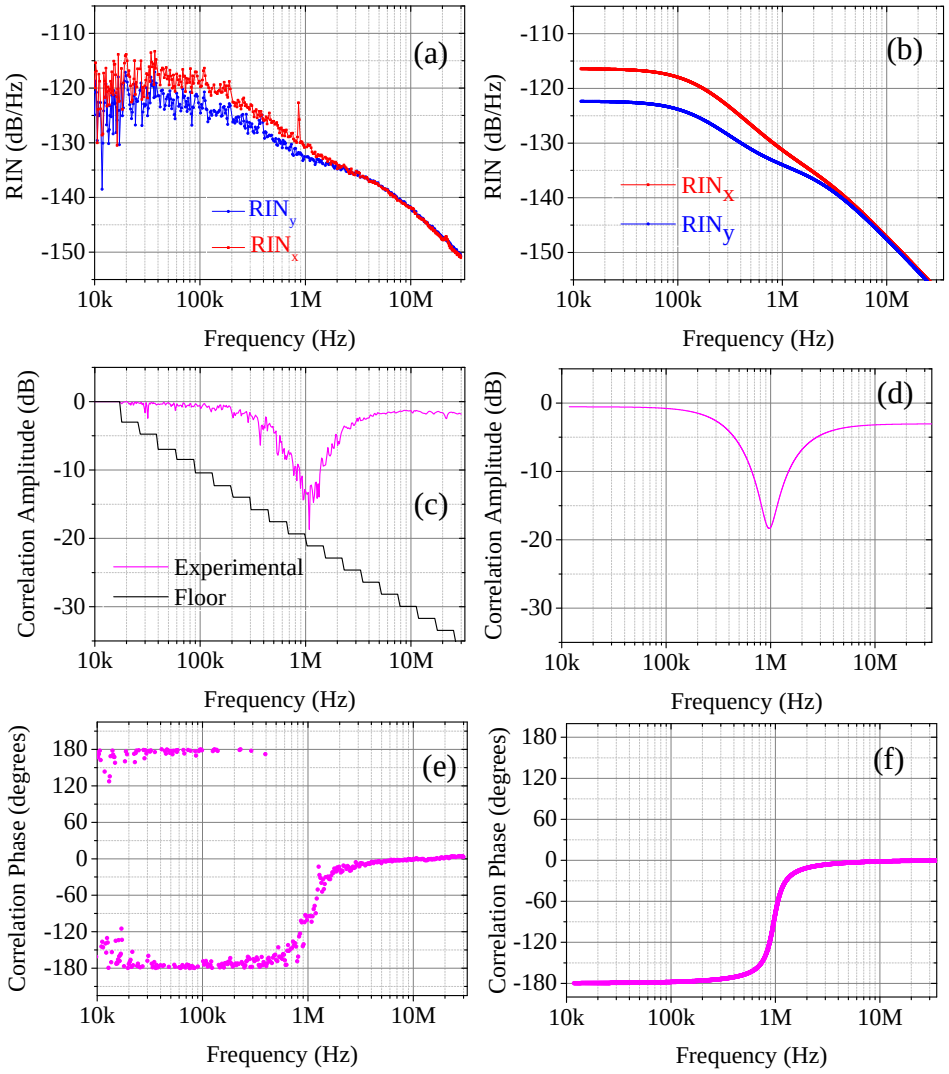

Figure 2.6: Results for the moderately strong coupling ($C = 0.75$). The spectra of RINs: (a) experimental, (b) theoretical; correlation amplitude: (c) experimental, (d) theoretical; correlation phase: (e) experimental (d) theoretical. Parameter values used for simulation: $r_x = 1.4$, $r_y = 1.42$, $1/\gamma_x = 20.2$ ns, $1/\gamma_y = 21.2$ ns, $1/\Gamma = 1$ ns, $\eta = 0.75$, $\psi = 0$, $\mathrm{RIN}_{Pump} = -145$ dB/Hz.

from the experimental conditions except for the value of τ (1 ns), which is taken from previous experiments performed using this structure [Zhao et al., 2011; Baili et al., 2014]. Here, the important points to note are the values of the pump RIN, the pump noise correlation amplitude η, and phase ψ used for different coupling situations. The pump RIN is equal to -145 dB/Hz for all coupling situations, whereas $\eta = 0.2$ for the weak

coupling ($d = 100$ μm), $\eta = 0.6$ for the intermediate coupling ($d = 50$ μm), and $\eta = 0.75$ for the moderately strong coupling ($d = 20$ μm) and ψ is zero in all the cases. These values are obtained from the pump noise measurements as shown in Figs. 2.2(c),(d). The good agreement between the experiment and the theoretical model in all the coupling situations proves the validity of our model. However, we are willing to fully understand why the spectral behaviors of the intensity noises and their correlations change significantly with the change of nonlinear coupling strengths. This leads to the physical interpretation of the noise correlation results contained in the following section.

2.5.2 Physical interpretation

We start by recalling the analogy between a single mode laser and a single mechanical oscillator (for example a mass attached to a spring). If this mechanical oscillator is driven out of its steady-state, it comes back to its steady-state either exponentially or in a damped-oscillatory manner depending on the level of damping. Similarly, the relaxation mechanism of a single mode laser around its steady-state is either exponential if the laser is class-A type or damped-oscillatory for the class-B laser. If one considers now the case of a two-coupled mechanical oscillator system, the relaxation mechanism of such a system can be analyzed by introducing the eigenrelaxation mechanisms of the global system such as the in-phase and the anti-phase relaxation mechanisms [Otsuka et al., 1992]. These two eigenrelaxation mechanisms exhibit different eigenfrequencies and/or damping rates. The dual-frequency laser, sustaining simultaneous oscillation of two coupled modes, is an exact analogue of a two-coupled mechanical oscillator system. Moreover, the class-A dynamics of the DF-VECSEL has some similarities with the over-damped behavior of a two-coupled mechanical oscillator system. Therefore, analogous to any coupled-oscillator system, the dynamical behavior of our DF-VECSEL must rather be analyzed by considering the in-phase and the anti-phase relaxation mechanism of the global system[4]. The transfer functions of the in-phase and anti-phase responses can be calculated by diagonalizing the 2×2 matrix of Eq. (2.40). The detailed derivation has been provided in Appendix C. The normalized spectra of the in-phase and the anti-phase noises [Eqs. (C.16-C.16) in Appendix C] for all three coupling situations are depicted in

[4]The in-phase and anti-phase relaxation modes are exact only when the two modes have the same gain and losses. In general, the relaxation modes are combinations of the two laser modes (Appendix C).

Fig. 2.7. It is important to note that the noise response of each laser mode is actually the superposition of the in-phase and the anti-phase response. With this simple physical analogy, we can well explain all the noise correlation spectra.

In the case of weak coupling, the anti-phase mechanism dominates over the in-phase one for frequencies lower than 5 MHz, whereas for higher frequencies the in-phase mechanism prevails, but by a very little margin, as shown by both experiment (Fig. 2.7(a)) and theory (Fig. 2.7(b)). This explains the π and the zero correlation phase respectively for frequencies lower and higher than 5 MHz in Figs. 2.4(e),(f). Additionally, the correlation amplitude is low (- 7 dB) for frequencies lower than 5 MHz and it becomes even lower (- 25 dB) for higher frequencies (Fig. 2.4(c),(d)). This low noise correlation is linked to the fact that the noise sources (pump noises) for the two laser modes are hardly correlated ($\eta = 0.2$). Moreover, the difference between the correlation amplitudes for frequencies higher and lower than 5 MHz is coming from the different degrees of dominance between the anti-phase and in-phase mechanisms (Fig. 2.7(a),(b)).

Figures 2.7(c),(d) represent the in-phase and anti-phase noise spectra for the intermediate coupling situation obtained from experiment and theory, respectively. These figures show that the anti-phase response is dominating over the in-phase one for frequencies lower than the anti-phase cut-off frequency of about 2 MHz, whereas above this cut-off frequency the in-phase mechanism becomes dominant. As a consequence, the correlation phase is π and zero respectively for frequencies lower and higher than 2 MHz (Figs. 2.5(e),(f)). Moreover, the $\pi-$phase jump around 2 MHz is associated with the fact that the transition from dominant anti-phase to dominant in-phase behavior occurs around this cut-off frequency. Additionally, the higher degree of correlation compared to the weak coupling case on both sides of the dip at 2 MHz in the correlation amplitude spectrum (Figs. 2.5(c),(d)) is linked with the facts that pump noises for the two modes are more correlated and the coupling is stronger than previously. The dip in the correlation amplitude spectrum around 2 MHz originates from the destructive interference between the nearly identical intensity noises of the two modes as the correlation phase exhibits a π-phase jump around this frequency (Figs. 2.5(e),(f)). Moreover, different degrees of dominance between the in-phase and anti-phase responses (Figs. 2.7(c),(d)) lead to the unequal values of correlation amplitude for frequencies lower and higher than 2 MHz. In this coupling case, the cut-off frequency of the anti-phase response (2 MHz) is lower than the weak coupling case (5 MHz) due to higher excitation ratios (r_x, r_y) of the two modes,

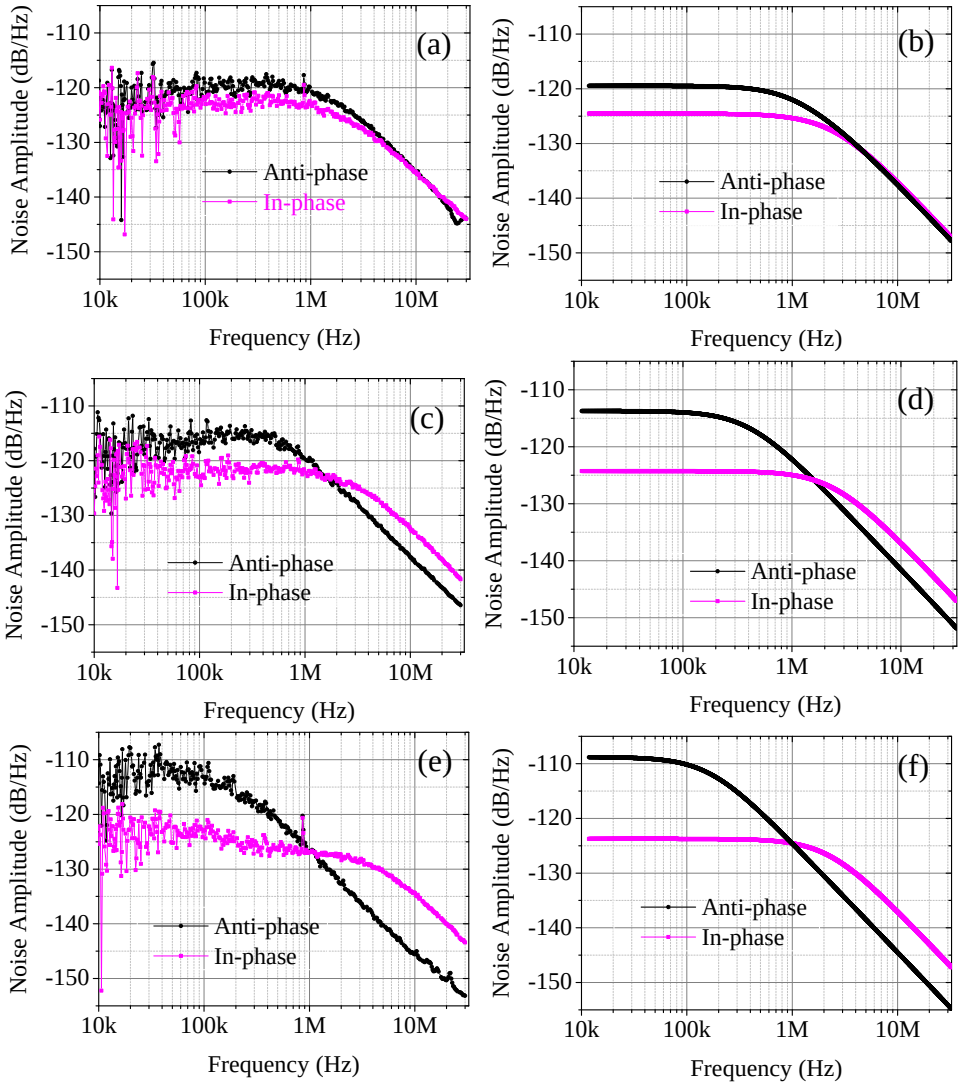

Figure 2.7: In-phase and anti-phase noise spectra. Weak coupling ($C = 0.12$): (a) experimental, (b) theoretical; intermediate coupling ($C = 0.50$): (c) experimental, (d) theoretical; moderately strong coupling ($C = 0.75$): (e) experimental, (f) theoretical. Parameter values used for simulation: (b) $r_x = r_y = r = 1.2$, $\tau_x = \tau_y = \tau = 10\,\text{ns}$, $\eta = 0.2$; (d) $r_x = r_y = r = 1.34$, $\tau_x = \tau_y = \tau = 15\,\text{ns}$, $\eta = 0.6$; (f) $r_x = r_y = r = 1.41$, $\tau_x = \tau_y = \tau = 20.5\,\text{ns}$, $\eta = 0.75$; $\psi = 0$, $RIN_{pump} = -145\,\text{dB/Hz}$ in all cases.

in addition to the stronger coupling.

For the moderately strong coupling, the in-phase and anti-phase noise spectra are reproduced in Fig. 2.7(e) (experimental) and Fig. 2.7(f) (theoretical). Figures 2.7(e),(f)

illustrate that the anti-phase response strongly dominates over the in-phase one for frequencies lower than 1 MHz, whereas for higher frequencies the in-phase response becomes stronger. Moreover, in this case the stronger coupling leads to a higher relative degree of dominance between the in-phase and anti-phase responses than the weak and the intermediate coupling situations. In addition to that, here the correlation between the pump noises for the two modes is also higher than the preceding coupling cases (Fig. 2.2). All these lead to a higher degree of correlation than the weak or the intermediate coupling case on both sides of the dip as depicted in Figs. 2.6(c),(d). Here also the dip in the correlation amplitude spectrum at 1 MHz originates from the destructive interference between the nearly identical intensity noises of the two laser modes as the correlation phase jumps by π at this frequency (Figs. 2.6(e),(f)). This $\pi-$phase jump at 1 MHz in the correlation phase spectrum is linked with the transition from dominant anti-phase to dominant in-phase behavior. Moreover, the correlation phases of π and zero for frequencies higher and lower than 1 MHz respectively come from dominant anti-phase and dominant in-phase responses as shown by Figs. 2.7(e),(f). Finally, the RIN spectra of the two laser modes, which can be obtained by superposing the in-phase and the anti-phase response, show a significant change of slope at about 1 MHz (Figs. 2.6(a),(b)). This is again linked with the fact that the anti-phase and in-phase noise spectra cross around 1 MHz. This crossing here occurs at a lower frequency than the weak or intermediate coupling, as the coupling between the two modes is stronger and their excitation ratios (r_x, r_y) are higher.

This simple physical picture does not only make our understanding better but also put our theoretical model on a more solid basis. To further prove the generality of the theoretical model, the intensity noise correlation measurements have been performed for a DF-VECSEL operating at 1 μm wavelength. For the 1 μm DF-VECSEL also, the theoretical model shows excellent agreement with the experimental results. The intensity noise correlation results for the 1 μm DF-VECSEL are reported in Appendix B.

2.6 RF beatnote and its phase noise

After describing the spectral behaviors of the intensity noises and their correlation, our goal now is to investigate the spectral behavior of the RF beatnote generated by optical mixing of the two modes and its phase noise. In the previous chapter, we have seen that the phase noise spectrum exhibits different slopes for different offset frequencies.

On the other hand, the intensity noise measurements, presented in the previous section, have revealed that the intensity noises of the two modes of our DF VECSEL are never perfectly correlated. Additionally, we have evidenced that the intensity noise correlation spectra strongly depend on the nonlinear coupling between the two laser modes. As predicted by our theoretical model [Eq. (2.48)], these intensity noise spectral properties can have a significant effect on the phase noise spectrum of the RF beatnote due to the large $\alpha-$factor of the semiconductor active medium of the DF-VECSEL. In the following, we aim at verifying all these facts by measuring the RF beatnote and its phase noise spectrum for different coupling situations, and comparing with the predictions of the theoretical model.

2.6.1 RF phase noise for different nonlinear couplings

We have measured the RF beatnote and its phase noise spectra in the targeted frequency range (10 kHz to 35 MHz) for three different coupling situations, similar to the intensity noise measurement such as the weak ($C = 0.12$), intermediate ($C = 0.50$), and moderately strong couplings ($C = 0.75$).

Weak coupling

Figure 2.8 presents the results for the weak coupling situation ($C = 0.12$). The PSD of the RF phase noise is presented in Fig. 2.8(a), whereas the corresponding RF beatnote spectrum is shown in Fig. 2.8(b). In Fig. 2.8(a), the filled-pink circles represent the experimental phase noise PSD, and the theoretical prediction from Eq. (2.48) is reproduced by the dash-dotted blue line. The black squares shows the measurement noise floor. Therefore, the model describes that for the weak coupling, the dominant contribution to the RF phase noise for offset frequencies higher than 500 kHz comes from the pump intensity noise via phase-intensity coupling due to the large $\alpha-$factor of the quantum-well based active medium of our DF-VECSEL. However, as can be seen from Fig. 2.8(a), for lower frequencies the measured phase noise level is much higher than the theoretical prediction. This will be clarified hereafter. The remaining small discrepancy between theory and experiment for frequencies higher than 5 MHz comes from the fact that the phase noise reaches the measurement floor. Therefore, it should not be taken into account for the discussion. In the beatnote spectrum as shown in Fig. 2.8(b), one can clearly see that

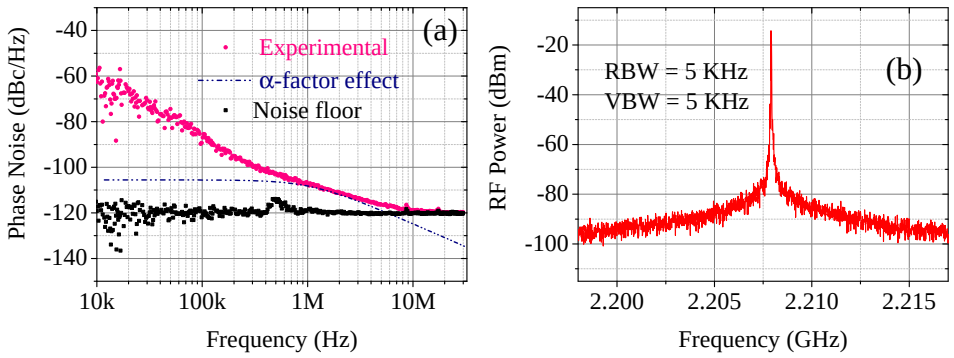

Figure 2.8: Results for the weak coupling ($C = 0.11$). (a) Power spectral density (PSD) of the phase noise of the RF beatnote. (b) Beatnote spectrum, measured by the ESA with resolution bandwidth (RBW) = 5 kHz and video bandwidth (VBW) = 5 kHz. Parameter values: $\alpha = 10$, the other parameter values are as in Fig. 2.4.

the beat signal centered at 2.208 GHz is sitting on a pedestal, originating from the phase noise as depicted in Fig. 2.8(a).

Intermediate coupling

The results for the intermediate coupling ($C = 0.50$) are given in Fig. 2.9. Figure 2.9(a) shows the experimental and theoretical results for the phase noise PSD, and Fig. 2.9(b) reveals the corresponding beatnote spectrum. Similar to the weak coupling case, here the beatnote centered at 4.1912 GHz is resting over a few megahertz wide pedestal linked with the phase noise of Fig. 2.9(a). One can see from Fig. 2.9(a) that the theory (dash-dotted blue line) reproduces the measured phase noise level (filled-pink circles) only for frequencies higher than 300 kHz, whereas for low frequencies the experiment exhibits a much higher phase noise level than what is expected from our theoretical model. This confirms that for frequencies higher than 300 kHz, the phase noise of the RF beat note comes from the pump intensity noise trough phase-intensity coupling linked with the large $\alpha-$factor of the semiconductor active medium of our laser. We again do not take into account the phase noise values for frequencies higher than 3 MHz as they are limited by the measurement floor (black squares).

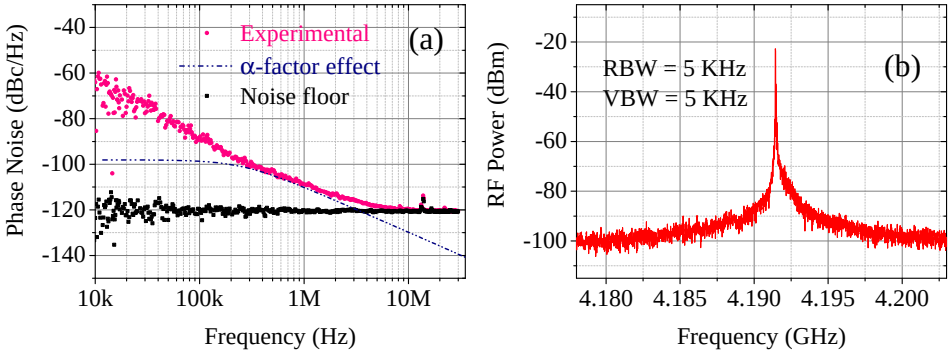

Figure 2.9: Results for the intermediate coupling ($C = 0.5$). (a) Power spectral density (PSD) of the phase noise of the RF beatnote. (b) Beatnote spectrum, measured by ESA with resolution bandwidth (RBW) = 5 kHz and video bandwidth (VBW) = 5 kHz. Parameter values: $\alpha = 10$, the other parameter values are as in Fig. 2.5.

Moderately strong coupling

The results corresponding to the moderately strong coupling situation are reproduced in Fig. 2.10. Here, the measured RF phase noise spectrum and the corresponding theoretical spectrum are respectively represented by the filled-pink circles and the dash-dotted blue line in Fig. 2.10(a). Similar to the preceding coupling cases, the theoretical spectrum

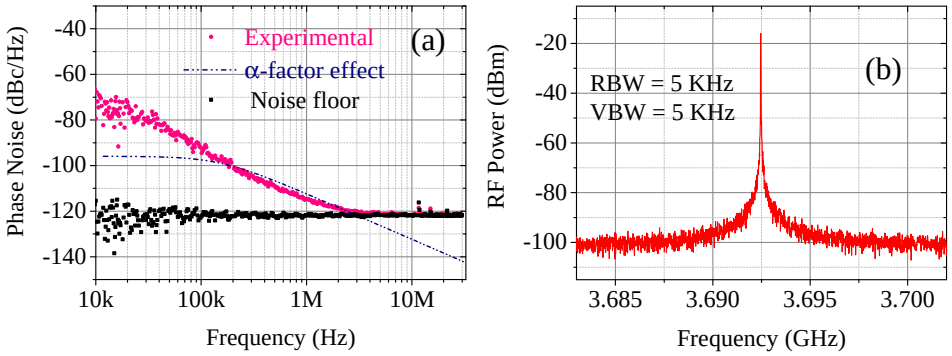

Figure 2.10: Results for the moderately strong couplning $C = 0.74$. (a) Power spectral density (PSD) of the phase noise of the RF beatnote. (b) Beatnote spectrum, measured by ESA with resolution bandwidth (RBW) = 5 kHz and video bandwidth (VBW) = 5 kHz. Parameter values: $\alpha = 10$, the other parameter values are as in Fig. 2.6.

is obtained from Eqs. (2.48), which takes into account only the phase-intensity coupling mechanism due to large $\alpha-$factor of the semiconductor gain medium of our laser. One can find in Fig. 2.10(a) that the theoretical prediction matches nicely the experiment only for

frequencies higher than 100 kHz, whereas for lower frequencies the experimental results show much higher phase noise level than what could be expected from the theory. For this moderately strong coupling situation, the beatnote centered at 3.692 GHz is again siting on a pedestal of a few megahertz width as shown in Fig. 2.10(b), and this pedestal originates from the phase noise of Fig. 2.10. Here also the mismatch between theory and experiments for frequencies higher than 2 MHz should not be considered as the phase noise reaches the measurement floor (black squares).

If now one carefully observes the theoretically expected phase noise spectra for different coupling situations, it can be found that the phase noise level increases for stronger coupling in the low frequency region of the spectra. Moreover, the matching between the experiment and theory is better for stronger coupling. In the following, we try to provide a physical explanation for this dependence of the RF phase noise on the nonlinear coupling strengths between the laser modes.

Explanation

To model the phase noise of the RF beatnote, we have only taken into the contributions from the intensity noises of the two modes via phase-intensity coupling mechanism, governed by the large $\alpha-$factor of the VECSEL. Therefore, since the intensity noises and their correlations are strongly dependent on the coupling strengths between the modes, so is it for the phase noise of the RF beatnote generated by mixing the two laser modes. To describe the intensity noise correlation spectra in the previous section, we have invoked the idea of the in-phase and anti-phase relaxation mechanisms. The same very idea can be utilized to explain the phase noise results as well. For low offset frequencies where the anti-phase mechanism is dominating (Fig. 2.7), the last term in the RHS of Eq. (2.48) becomes negative and effectively adds up to the first two terms, thus providing a high RF phase noise. On the contrary, for high offset frequencies the in-phase mechanism dominates (Fig. 2.7). Consequently, the last term of Eq. (2.48) remains positive and must be subtracted from the first two terms, leading to a low RF phase noise. Moreover, the relative dominance of the in-phase and anti-phase responses is dependent on the coupling strengths as shown in Fig. 2.7. Therefore, the stronger the nonlinear coupling, the stronger is the degree of dominance of the anti-phase response over the in-phase one for frequencies lower than the anti-phase cutoff frequency. This explains why the part of the phase noise

coming from phase-intensity coupling increases for low frequencies with the increase of the coupling strength (Figs. 2.8(a)-2.10(a)). Moreover, the in-phase response dominates for frequencies higher than the anti-phase cutoff frequency. Usually, in-phase response does not depend on the strength of coupling. However, if we compare the phase noise spectra of different coupling situations (Figs. 2.8(a)-2.10(a)), we can find that the phase noise level decreases with the increase of the coupling strength in the frequency range of dominating in-phase mechanism. This is due the fact the degree of correlation (η) between the noise sources (pump noises) for the two laser modes increases with the increase of nonlinear coupling. However, there is always some discrepancies between the measured phase noises and the corresponding theoretical predictions in all coupling situations for low frequencies as illustrated in Figs. 2.8(a)-2.10(a). This indicates that there must be some other mechanism apart from the phase-intensity coupling effect that degrades the spectral purity of the RF beatnote. In our DF-VECSEL, it is the thermal fluctuations, which predominantly contribute to the phase noise of the RF beatnote in these low offset frequencies. In the following, we further describe this thermal effect.

2.6.2 Thermal noise

Thermal fluctuations can deteriorate the noise performance of the laser by introducing fluctuations of the laser cavity length either by varying the effective refractive index inside the cavity or by varying the physical length of the cavity [Horak et al., 2006]. These cavity length fluctuations are translated into fluctuations of the optical phases of the laser modes. In the present section, we start by deriving the PSD of the optical phase noise for a single mode laser induced by such thermal fluctuations [Tropper and Hoogland, 2006; Laurain et al., 2009, 2010]. Then, we extend this to the case of our dual-frequency VECSEL.

Single mode laser

The instantaneous angular frequency of a laser, which is an integer multiple of the free spectral range of the cavity, is given by

$$\omega(t) \;=\; q\frac{\pi c}{L_{\mathrm{opt}}(t)}\;, \tag{2.52}$$

where q is an integer and c is the vacuum speed of the light. The time varying quantity $L_{\rm opt}(t)$ denotes the total optical length of the laser cavity, which can be expressed as

$$L_{\rm opt}(t) \;=\; L_{\rm ext} + n_{\rm SC} L_{\rm SC} \;, \tag{2.53}$$

where $L_{\rm ext}$ is the length of the external cavity, and where $n_{\rm SC}$ and $L_{\rm SC}$ are the effective refractive index and the thickness of the semiconductor structure (Fig. 2.1). Then the variation of the optical frequency due to a variation of the total cavity length can be given as

$$\delta\omega_T(t) \;=\; -\omega(t)\frac{\delta L_{\rm opt}(t)}{L_{\rm opt}(t)} \;. \tag{2.54}$$

We know that the optical length of the cavity can vary due to the variation of either the physical length of the cavity or the refractive index. Therefore, the variation of the total length of the cavity can be approximated as

$$\delta L_{\rm opt}(t) = \delta L_{\rm ext}(t) + \overline{\delta n}(t) L_{\rm SC} \;, \tag{2.55}$$

where $\overline{\delta n}(t)$ is the temporal fluctuations of the refractive index, thermally induced and averaged over the volume of the optical mode. Here, we have neglected the variation of the physical length of the semiconductor structure ($L_{\rm SC}$). Therefore the variation of the optical frequency can be given by

$$\delta\omega_T(t) \simeq -\frac{\omega_0}{L_{\rm ext}}\left[\delta L_{\rm ext}(t) + \overline{\delta n}(t) L_{\rm SC}\right] \;. \tag{2.56}$$

The dominant contribution in the thermal fluctuations of the optical length of the cavity comes from the fluctuations of the refractive index of the semiconductor structure [Laurain et al., 2009, 2010], leading to:

$$\delta\omega_T(t) \;\simeq\; -\frac{\omega_0}{L_{\rm ext}}\overline{\delta n}(t) L_{\rm SC} \;. \tag{2.57}$$

We can re-write it as

$$\delta\omega_T(t) \;\simeq\; -\omega_0 \Gamma_T \overline{\delta T}(t) \;, \tag{2.58}$$

where $\overline{\delta T}(t)$ denotes the fluctuation of the temperature, averaged over the optical mode volume and Γ_T is defined as

$$\Gamma_T = \frac{L_{\mathrm{SC}}}{L_{\mathrm{ext}}} \frac{d\overline{n}}{dT} . \tag{2.59}$$

In general, the temperature fluctuation $\overline{\delta T}(t)$ of the semiconductor structure averaged over the optical mode volume is the sum of two terms [Laurain, 2010]:

$$\overline{\delta T}(t) = \delta T_k(t) + \overline{R}_T \delta P_{Pump}(t) * h(t) , \tag{2.60}$$

where $\delta T_k(t)$ defines the fundamental thermodynamic fluctuations of the semiconductor, when it is maintained at a fixed temperature T and the last term of the right hand side describes the effect of temperature fluctuations induced by the pump power fluctuations. '$*$' represents the convolution product. $\overline{R}_T$ is the thermal impedance of the semiconductor structure, averaged over the volume of the optical mode. $\delta P_{Pump}(t)$ holds for the fluctuations of the pump power and $h(t)$ defines the impulse temperature response of the semiconductor structure to the pump power. As usually performed [Laurain et al., 2010], we model the thermal transfer function $H(f)$, which is the Fourier transform of $h(t)$, as a first-order low-pass filter, leading to:

$$|H(f)|^2 = \frac{1}{1 + (2\pi f \tau_T)^2} . \tag{2.61}$$

The order of magnitude of the response time (τ_T) of thermal diffusion is given as [Davis et al., 1998]

$$\tau_T \simeq \frac{w_{Pump}^2}{2\pi D_T} , \tag{2.62}$$

where w_{Pump} is the waist of the pump beam on the semiconductor medium and D_T is the thermal diffusion coefficient. To evaluate the order of magnitude of the first term in the right-hand side of Eq. (2.60), we write the variance of the intrinsic temperature fluctuations of the semiconductor due to the fundamental thermodynamic fluctuations

from [Chui et al., 1992; Gorodetsky and Grudinin, 2004; Lauer and Amann, 2005]:

$$\left\langle \delta T_k^2 \right\rangle = \frac{k_B T^2}{C_v V} . \tag{2.63}$$

Here k_B is Boltzman's constant ($k_B = 1.38 \times 10^{-23}\,\mathrm{J.K^{-1}}$), C_v is the specific heat capacity, and $V \simeq \pi w^2 L_{SC}$ represents the volume of the semiconductor, occupied by the optical mode (w, laser beam waist). Using parameter values relevant for our InP-based 1.55 μm-VECSEL ($T = 290\,\mathrm{K}$, $C_v = 1.2 \times 10^6\,\mathrm{J.K^{-1}.m^{-3}}$, $w = 75\,\mu\mathrm{m}$, $L_{SC} = 5\,\mu\mathrm{m}$), we obtain a temperature noise of $\sqrt{\langle \delta T_k^2 \rangle} \simeq 4\,\mu\mathrm{K}$. Considering a Gaussian distribution for δT_k leads to a full width at half maximum (FWHM) of about $10\,\mu\mathrm{K}$. This temperature noise induces refractive index fluctuations inside the gain medium due to its temperature dependence ($dn/dT \simeq 2 \times 10^{-4}\,\mathrm{K^{-1}}$, $d\lambda/dT \simeq 0.1\,\mathrm{nm.K^{-1}}$), leading to a FWHM linewidth of about 50 kHz. It is important to mention that this is a rough estimation of the effect. To be more rigorous, one needs to evaluate phase fluctuations due to this temperature fluctuations, and then Fourier transform it to obtain the spectrum. However, in our VECSEL the effect of this fundamental thermodynamic fluctuations is extremely small compared to the pump noise induced thermal effect as shown in the following.

The PSD of the thermal fluctuations induced by the fundamental thermodynamic fluctuations is given by [Laurain, 2010]

$$S_{\mathrm{Th}}(f) = \frac{4 k_B \tau_T T^2}{C_v V} . \tag{2.64}$$

Similarly, the thermal noise PSD induced by the pump power fluctuations can be expressed as

$$S_{\mathrm{P}}(f) = \overline{R}_T^2 |H(f)|^2 \mathrm{RIN}_{Pump}(f) P_{\mathrm{Pump}}^2 , \tag{2.65}$$

where $\mathrm{RIN}_{Pump}(f)$ is the pump RIN as defined in Eq. (2.33), and P_{Pump} is the incident pump power. For our laser, if we compare the PSD of the thermodynamic fluctuations ($S_{\mathrm{Th}}(f)$) with the PSD of the thermal fluctuations, induced by the pump power fluctuations ($S_P(f)$), we find that the effect of the fundamental thermodynamic fluctuations is very small ($\sim 10^5$ times smaller) compared to the effect of the pump power fluctuations. Therefore, in the following, we neglect the effect of fundamental thermodynamical

fluctuations, i.e., the first term in the right-hand side of Eq. (2.60). We can then Fourier transform Eq. (2.58) and obtain the optical phase noise PSD as

$$\begin{aligned} S^T(f) &= \frac{\omega_0^2 \Gamma_T^2 \overline{R}_T^2}{4\pi^2 f^2} |H(f)|^2 \mathrm{RIN}_{Pump}(f) P_{Pump}^2 \\ &= |\Lambda(f)|^2 |\widetilde{\delta N}_0(f)|^2 \ , \end{aligned} \tag{2.66}$$

where the transfer function $\Lambda(f)$ reads

$$|\Lambda(f)|^2 = \frac{\omega_0^2 \Gamma_T^2 \overline{R}_T^2 P_{\mathrm{Pump}}^2}{4\pi^2 f^2 N_0^2} |H(f)|^2 \ . \tag{2.67}$$

In the following, we will extend this thermal noise model of a single mode laser to our DF-VECSEL, sustaining simultaneous oscillation of the two cross-polarized modes.

Dual-frequency VECSEL

Our interest now is to evaluate the contribution from the thermal effect to the phase noise of the RF beatnote, generated by optical mixing of the two modes of the DF-VECSEL. We know that the phase noise of the RF beatnote is equal to the difference between the optical phase noises of the two laser modes [Eq. (2.5)]. Therefore, the phase fluctuations of the RF beatnote only due to the thermal fluctuations of the refractive index of the active medium induced by pump intensity noise can be expressed as

$$\begin{aligned} \widetilde{\delta\phi}_{Beat}^T(f) &= \widetilde{\delta\phi}_x^T(f) - \widetilde{\delta\phi}_y^T(f) \\ &= \Lambda_x(f)\widetilde{\delta N}_{0x}(f) - \Lambda_y(f)\widetilde{\delta N}_{0y}(f) \ , \end{aligned} \tag{2.68}$$

where $\widetilde{\delta\phi}_x^T(f)$, $\widetilde{\delta\phi}_y^T(f)$ are the fluctuations of the optical phases of the two laser modes due to the thermal noise and $\widetilde{\delta\phi}_{Beat}^T(f)$ is the corresponding RF phase fluctuation in the frequency domain (the superscript 'T' indicates that we consider only the thermal noise). Moreover, $\widetilde{\delta N}_{0x}(f)$ and $\widetilde{\delta N}_{0y}(f)$ are the pump fluctuations for the two cross-polarized laser modes as defined by Eqs. (2.29-2.30). Now, we have already evidenced that (Figs. 2.2), the pump noises entering into the two laser modes are white noises of identical amplitudes, and are partially correlated with a correlation amplitude $\eta < 1$, and a phase $\psi = 0$. Additionally, since the two cross-polarized modes with a frequency

difference in the RF range are oscillating inside the same cavity and pumped by the same laser, we can consider $|\Lambda_x(f)|^2 = |\Lambda_y(f)|^2 = |\Lambda(f)|^2$ [Eq. (2.67)]. Therefore, the RF phase noise PSD in our dual-frequency VECSEL due to the thermal fluctuations induced by pump intensity noise reads as

$$S^T_{Beat}(f) \;=\; 2(1-\eta\cos\psi)|\Lambda(f)|^2|\widetilde{\delta N}_0|^2 \;. \tag{2.69}$$

It is important to mention here that Eq. (2.69) is valid only when the other mechanism is neglected. Nevertheless, Eq. (2.69) infers that the phase noise of the RF beatnote due to the pump noise induced thermal fluctuations of the refractive index of the semiconductor medium does not only depend on the PSD of the pump noise, but also on the correlation (η, ψ) between the pump fluctuations entering into the two laser modes. More specifically, the pump noise induced thermal fluctuations provide a significant contribution to the RF phase noise as long as the pump fluctuations for the two laser modes are not perfectly correlated ($\eta < 1$). Once more time this proves the importance of the pump noises and their correlation to determine the noise properties of our DF-VECSEL.

2.6.3 Total phase noise of the beatnote

Now, one can wonder whether the two mechanisms, thermal effect and phase-intensity coupling effect, should be added coherently or incoherently to obtain the total phase noise of the RF beatnote. To clarify this doubt one should consider the driving forces behind these two mechanisms. In our DF-VECSEL, both the thermal and the phase-intensity coupling mechanisms are driven by the same source, which is the pump intensity noise. Therefore, the contributions from the thermal effect and the phase-intensity coupling effect must be added coherently to obtain the total phase noise, leading to

$$\widetilde{\delta\phi}_{Beat}(f) \;=\; \widetilde{\delta\phi}^{\alpha}_{Beat}(f) + \widetilde{\delta\phi}^{T}_{Beat}(f) \;. \tag{2.70}$$

This gives the following expression for the PSD of the total phase noise of the RF beatnote

$$S_{Beat}(f) \;=\; S^{\alpha}_{Beat}(f) + S^{T}_{Beat}(f) + 2\mathrm{Re}\left[\widetilde{\delta\phi}^{\alpha}_{Beat}(f)\widetilde{\delta\phi}^{T}_{Beat}(f)^*\right] \;. \tag{2.71}$$

It is important to note that the third term in the right hand side of Eq. (2.71) becomes zero if the two mechanisms, thermal effect and phase-intensity coupling effect, are incoherent.

In the following, we will compare the RF phase noise spectra as obtained from the experiment with the theoretical prediction of Eq. (2.71).

2.6.4 Complete description of the RF phase noise spectrum

We have already shown that the phase-intensity coupling mechanism due to the large $\alpha-$factor of our DF-VECSEL can only explain the high frequency part of the RF phase noise spectrum for all coupling cases (Figs. 2.8-2.10). Consequently, we have introduced the pump noise induced thermal effect in the model, hoping to be able to fully explain the phase noise spectrum of the RF beatnote. Moreover, the effect of spontaneous emission has also been investigated (see Appendix D). In Fig. 2.11, we have reproduced the theoretical predictions of the phase noise levels coming from different mechanisms such as thermal effect (dashed green line), phase-intensity coupling effect (dash-dotted blue line), spontaneous emission effect (dash-dotted red line) and compared with the measured phase noise spectra (filled-pink circles) in all three coupling cases. Figures 2.11(a),(b),(c) respectively represent the results for weak ($C = 0.12$), intermediate ($C = 0.50$), and moderately strong ($C = 0.75$) coupling situations. As one can observe in Fig. 2.11, in all three coupling situations, the RF phase noise for the low offset frequencies predominantly originates from the thermal noise, whereas the phase-intensity coupling effect dominates for the high frequencies. Moreover, the crossing between the contributions of the thermal (dashed green line) and phase-intensity coupling (dash-dotted blue line) mechanisms occurs at a lower offset frequency for a stronger coupling (Fig. 2.11). Additionally, the theoretical prediction of the phase noise coming from spontaneous emission (dash-dotted red line) shows that this effect hardly contributes in our laser.

Now, if we carefully look at the level of the phase noise coming from the thermal effect, we can notice that the noise level decreases with the increase of the nonlinear coupling strengths (Fig. 2.11). This is again linked with the fact that the pump noise correlation factor η is higher for smaller spatial separation (d), consequently stronger coupling (Fig. 2.2(c)), leading to lower RF phase noise as predicted in Eq. (2.69). This decrease of thermal noise also explains why the crossing between the dashed green and dash-dotted blue lines moves to a lower frequency for a stronger coupling. Therefore, we

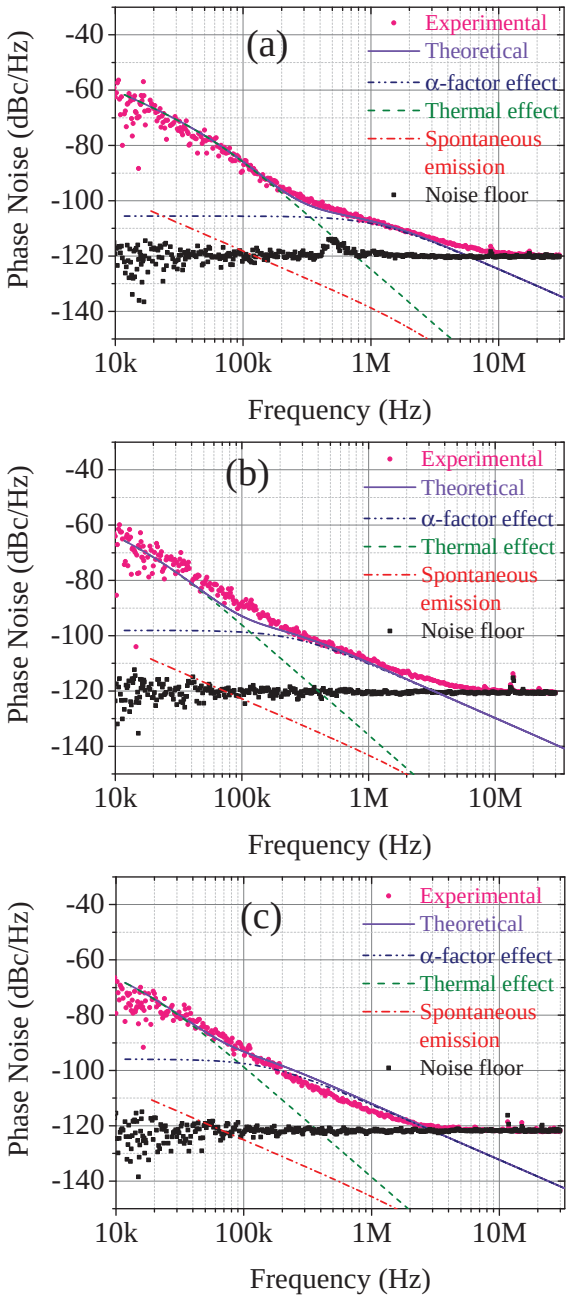

Figure 2.11: Comparison between the experiment and the complete theoretical model for the RF beatnote phase noise, (a) weak coupling, (b) intermediate coupling, and (c) moderately strong coupling. Parameter values: $D_T = 0.372\,\mathrm{cm^2S^{-1}}$, $d\overline{n}/dt = 2.0 \times 10^{-4}\,\mathrm{K^{-1}}$, $L_{\mathrm{SC}} = 5\,\mu\mathrm{m}$, $L_{\mathrm{ext}} = 4.76\,\mathrm{cm}$, $w_p = 50\,\mu\mathrm{m}$, $R_T = 12\,\mathrm{KW^{-1}}$, $P_{\mathrm{Pump}} = 1.7\,\mathrm{W}$. The other parameter values are identical as in Figs. 2.4,2.5,2.6 respectively for (a),(b),(c).

can conclude that our theoretical model is good enough to explain not only the intensity noise properties but also the phase noise spectra of the RF beatnote in our DF-VECSEL. The RF phase noise measurements are also performed with a DF-VECSEL operating at 1 μm. For this DF-VECSEL also, theory quite nicely reproduces all the experimental results. The phase noise spectra for the 1 μm DF-VECSEL for different coupling strengths between the two laser modes are presented in Appendix B. This again proves the generality of our simple theoretical model based on modified rate equations.

2.7 Correlation between RF phase noise and intensity noises

In the preceding sections, we have proved that the theoretical model can indeed fully explain the following noise properties of our DF-VECSEL, (i) the intensity noises and their correlations, and (ii) the phase noise of the RF beatnote for different coupling situations. However, in order to further test this model, in particular, the scenario that we have proposed for the propagation of the pump noise to the RF beatnote phase noise, we choose to measure the correlation between the phase noise of the RF beatnote and the intensity noises of the two laser modes generating the RF beatnote for all three previous coupling situations. Then, we compare these measured noise correlation spectra with the theoretically expected spectra.

Weak coupling

The experimental and theoretical results for the weak coupling ($C = 0.12$) are reproduced in Fig. 2.12. Figure 2.12(a) shows the measured correlation amplitude spectra. The red-squared-line and blue-circled-line represent the amplitude of the correlation between the RF phase noise with the intensity noises of x- and y-polarized modes, respectively. The correlation amplitudes for the two modes are not perfectly identical as their intensity noises are different (see Figs. 2.4(a),(b)) due to the difference between their losses and/or gains. The correlation amplitude is high (- 4 dB) for low frequencies and it starts to decrease for frequencies above 1 MHz. The theoretical model satisfactorily reproduces this behavior, as shown in Fig. 2.12(b). In Fig. 2.12(a), the decrease of the correlation amplitude for frequencies higher than 5 MHz is due to the fact that the RF phase noise reaches

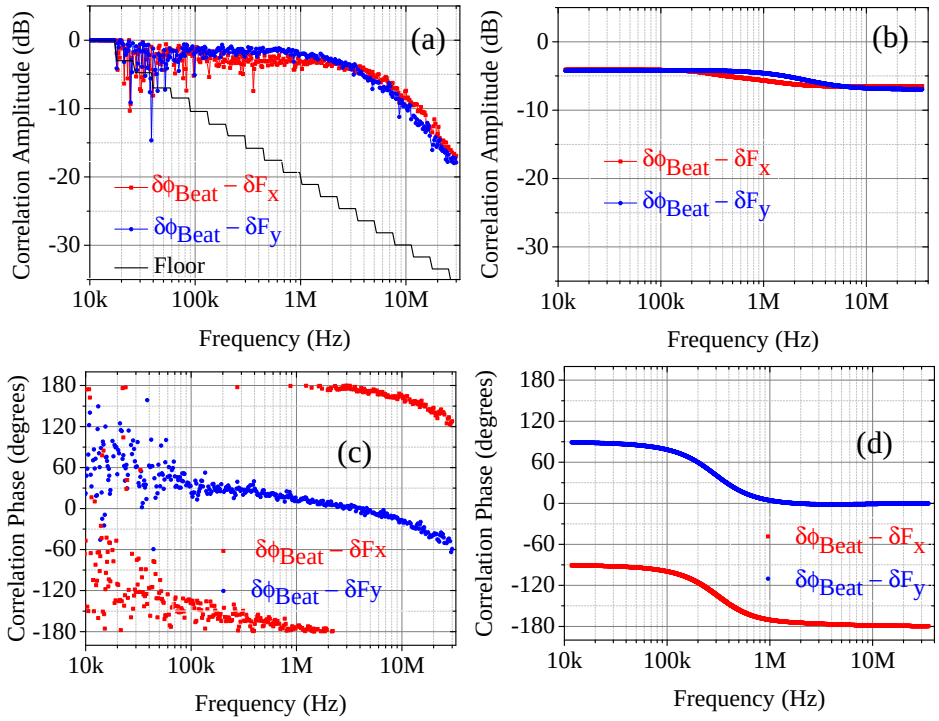

Figure 2.12: Correlation of the RF phase noise with the intensity noises for the weak coupling. Correlation amplitude: (a) experiment, (b) theory; correlation phase: (c) experiment, (d) theory.

the measurement floor level for these frequencies (Fig. 2.11(a)). This explains the discrepancy here with the theory (Fig. 2.12(b)). The experimental correlation phase spectra are reproduced in Fig. 2.12(c). The corresponding theoretical spectra (Fig. 2.12(d)) show good agreement with the experiment. The noise correlation phase associated with the $x-$polarized mode (red squares) always differs by π from the correlation phase associated with $y-$ polarized mode (blue circles). Moreover, the correlation phase is $+\pi/2(-\pi/2)$ for low frequencies, then it starts to roll-off around 100 kHz and reaches zero $(\pm\pi)$ at about 1 MHz, and remains at zero $(\pm\pi)$ for all higher frequencies for the y-polarized (x-polarized) mode. This phase shift is due to the transition between the frequency range where thermal phase noise dominates and the frequency range where the phase-intensity coupling mechanism dominates. We do not take into account the fall of the phase values for frequencies higher than 5 MHz in the experimental correlation phase spectra (Fig. 2.12(c)) as the RF phase noise approaches the measurement floor (Fig. 2.11(a)).

Intermediate coupling

Figure 2.13 reveals the correlation spectra between the intensity noises of the two-cross polarized modes with the RF phase noise for the intermediate coupling situation ($C = 0.5$). The measured correlation amplitude spectra are given in Fig. 2.13(a), whereas Fig. 2.13(b) shows the corresponding theoretical predictions. For the intermediate coupling also, the noise correlation amplitudes corresponding to the two modes (blue circled-line, red squared-line) differ due to their nonidentical intensity noises (see Figs. 2.5(a),(b)) linked with their unequal losses/gains. In this coupling case, the correlation amplitude becomes

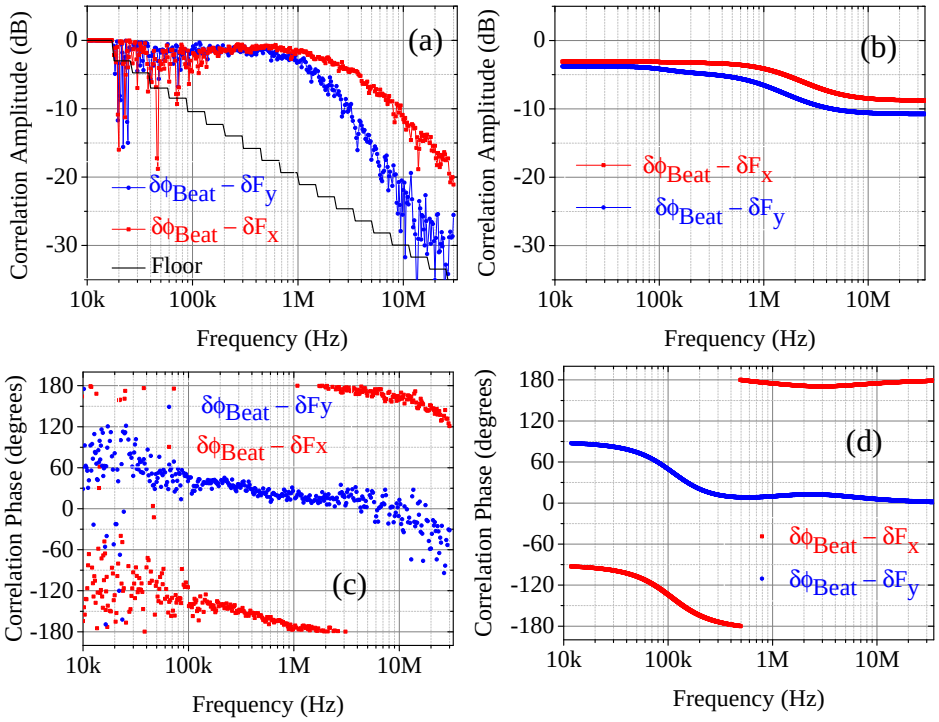

Figure 2.13: Correlation of the RF phase noise with the intensity noises for the intermediate coupling. Correlation amplitude: (a) experiment, (b) theory; correlation phase: (c) experiment, (d) theory.

slightly higher (- 3 dB) than the weak coupling one for frequencies lower than 500 kHz, and for higher frequencies it decreases as in the weak coupling case. Figures 2.13(c),(d) respectively represent the experimental and theoretical noise correlation phase spectra. Like in the weak coupling case, here also the correlation phases associated with $x-$ (red squares) and $y-$polarized mode (blue circles) always differ by π. In addition to that,

the correlation phase is $+\pi/2$ ($-\pi/2$) at the starting frequency of 10 kHz, then it starts rolling off and becomes zero ($\pm\pi$) around 500 kHz, and maintains this value for all higher frequencies for the $y-$polarized ($x-$polarized) mode. The theoretical predictions for both correlation amplitude (Fig. 2.13(b)) and phase spectra (Fig. 2.13(d)) are in good agreement with the corresponding experimental ones (Fig. 2.13(a),(c), respectively), except for frequencies higher than 3 MHz. This discrepancy is again linked with the fact that the phase noise of the RF beatnote is close to the measurement floor for these frequencies (Fig. 2.11(b)), and hence this should not be taken into account.

Moderately strong coupling

The results corresponding to the moderately strong coupling situation ($C = 0.75$) are reproduced in Fig. 2.14. In this case also, the difference between the correlation amplitudes for the two modes (blue circled-line, red squared-line) is coming from their different intensity noises (see Figs. 2.6(a),(b)) due to nonidentical losses and/or gains of them. For the moderately strong coupling as shown in Fig. 2.14(a), the correlation amplitude is higher (- 2 dB) compared to both the weak and intermediate couplings for low frequencies. However, the correlation amplitude starts to decrease for high frequencies starting from 300 kHz. Here again, we find a very good agreement between experiment (Fig. 2.14(a)) and theory (Fig. 2.14(b)). The decrease of experimental correlation amplitude for frequencies higher than 2 MHz is irrelevant as it is limited by the measurement floor for these frequencies (Fig. 2.11(c)). Additionally, as shown in Fig. 2.14(c), the noise correlation phases associated with the two modes (red squares, and blue circles) always differ by π, similarly to the two previous coupling situations. Moreover, starting from $+\pi/2$ ($-\pi/2$) at 10 kHz, the correlation phase rolls off to zero ($\pm\pi$) at about 300 kHz and remains at zero ($\pm\pi$) for all higher frequencies for the $y-$polarized ($x-$polarized) mode. The theoretical prediction (Fig. 2.14(d)) again shows nice agreement with the experiment (Fig. 2.14(c)). For the correlation phase also, the mismatch between the theory and experiment for frequencies higher than 2 MHz is linked with the identical levels for the measured phase noise and the measurement floor, and hence should be neglected.

In all three coupling situations, the reason behind the π phase difference between the correlation phases of $x-$ and $y-$polarized modes is the minus sign in Eq. (2.5). In addition to that, the change of correlation phases by $\pi/2$ centered around offset frequency of few

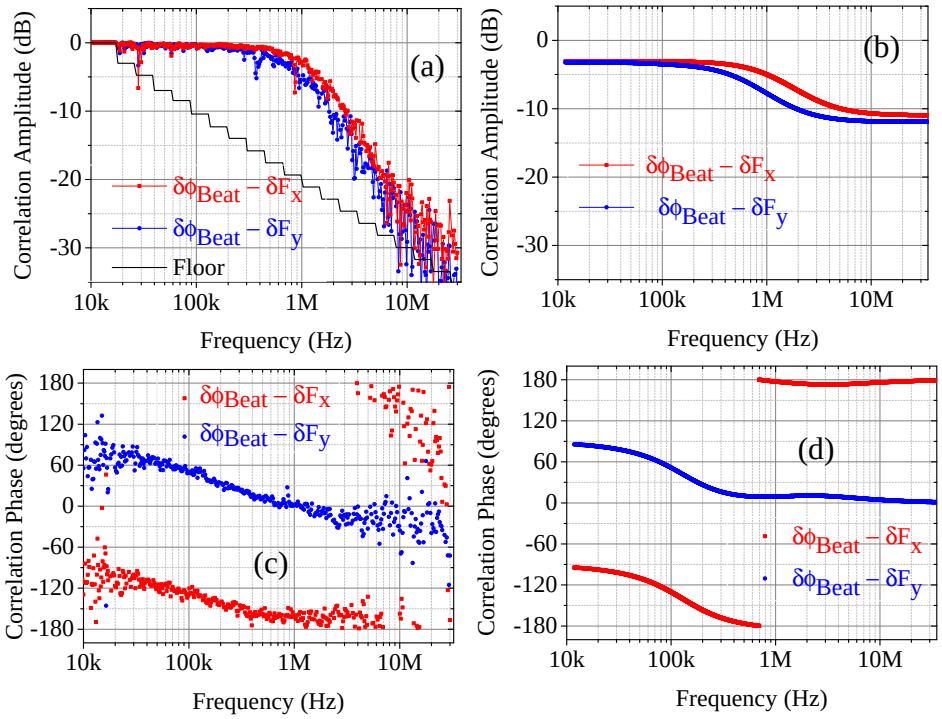

Figure 2.14: Correlation of the RF phase noise with the intensity noises for the moderately strong coupling. Correlation amplitude: (a) experiment, (b) theory; correlation phase: (c) experiment, (d) theory.

hundreds of kilohertz for both $x-$ and $y-$polarized modes, is related to the low pass filter like behavior of the thermal noise (Fig. 2.11). Indeed, a $\pi/2$-phase change is associated with this passage through the cut-off frequency, like in any first-order filter. Additionally, we observe that the correlation amplitude for low frequencies acquires higher value for stronger coupling between the two laser modes. This can be explained from the fact that the pump noise correlation factor η becomes higher for stronger coupling (Fig. 2.2(c)). Moreover, the thermal rolling-off of the correlation phase moves to a lower frequency with the increase of coupling strength as the cross-over between the thermal noise and the noise from the phase-intensity coupling effect occurs at a lower frequency for stronger coupling (Figs. 2.11).

2.8 Conclusion

In this chapter, we have explored, both experimentally and theoretically, the spectral behaviors of different noises in our DF-VECSEL, sustaining simultaneous oscillation of two linear cross-polarized modes with a frequency difference lying in the RF range. Specifically, we have analyzed the intensity noise spectra of the two modes and also the correlation between these intensity noises for three different coupling strengths between the modes. Moreover, we have presented the spectral behavior of the RF beatnote generated by optically mixing the two modes, and its phase noise spectra again for the three previous coupling situations. Additionally, we have demonstrated the correlation between the phase noise of the RF beatnote and the intensity noises of the two cross-polarized modes generating the beatnote via optical mixing for the three considered different coupling situations. We have evidenced the fact that the spectral behavior of the pump intensity noise, which happens to be the dominant source of noise in the targeted frequency range (10 kHz to 35 MHz), plays a significant role to determine the correlations between different noises of our DF-VECSEL. We have succeeded to measure the different pump noise properties using a dedicated experimental setup. The measurements show that the pump noises entering into the two spatially separated laser modes are white noises of identical amplitudes. Moreover, the pump noises for the two laser modes exhibit partial correlation with a degree of correlation (η) dependent on the amount of spatial separation (d) between the modes, that controls their coupling. Additionally, the correlated parts of the pump noises for the two modes are found to be always in phase. These pump noise properties are linked with the nonuniform intensity distribution of the pump beam on the gain structure due to the speckle pattern coming from the multimode fiber carrying the pump beam. The measurements of the pump noises, intercepted by the two spatially separated laser modes, have helped us to recover the following noise properties of the DF-VECSEL.

The intensity noises of the two laser modes never exhibit a perfect correlation as their noise sources (pump noises) are only partially correlated. Additionally, the intensity noise correlation spectra show strong dependence on the nonlinear coupling between the modes. To explain this, we have invoked the notion of the in-phase and anti-phase eigenrelaxation mechanisms of a two coupled-oscillator system. Indeed, we have succeeded in explaining the intensity noise correlation spectra by showing different degrees of dominance between the in-phase and anti-phase responses depending on the strength of coupling between the

two modes. In addition to that, the dependence of the pump noise correlation factor η on the spatial separation d between the two modes defining their coupling strength governs the intensity noise correlation spectra of our DF-VECSEL.

We have demonstrated the pump noise propagation scheme to the phase noise of the RF beatnote, that deteriorates its spectral purity. We have figured out two different mechanisms through which the pump noise degrades the spectral purity of the RF beatnote namely, (i) thermal fluctuation of the refractive index of the active medium, and (ii) coupling between the phase and the intensity fluctuations due to the large $\alpha-$factor of semiconductor active medium of the DF-VECSEL. Moreover, the nonlinear coupling between the laser modes also strongly impacts the RF phase noise spectrum. The reason for this is twofold: (i) the correlation between the noise sources (pump noises) for the two laser modes depend on the spatial separation between the modes, that determines their coupling, and (ii) the intensity noises of the two modes and their correlation, which contribute significantly to the phase noise of the RF beatnote via phase-intensity coupling mechanism due to large $\alpha-$ factor of the semiconductor active medium, exhibit strong dependence on the coupling between the modes.

We have further proved the pump noise propagation scheme to the phase noise of the RF beatnote by measuring the correlation spectra between the RF beatnote and the intensity noises of the two cross-polarized laser modes generating the beatnote via optical mixing. In particular, the different spectral behaviors of the correlation spectra depending on the offset frequencies further confirmed the presence of two dominant mechanisms, the thermal effect and the phase-intensity coupling effect, through which pump noise degrades the spectral purity of the RF beatnote.

Finally, we have introduced a simple theoretical model based on modified rate equations. The model has shown great success in explaining all the noises and their correlation spectra. Additionally, the generality of the model has been proved by analyzing the noise properties of DF-VECSELs operating at two different wavelengths ($1.55\,\mu$m, $1\,\mu$m). However, the success of the simple model is quite surprising, when one considers that the model has completely overlooked the spin-dependent carrier dynamics [San Miguel et al., 1995], which is usually introduced to explain different polarization dynamics of QW-based lasers such as VCSELs. The next chapter of this first part of the thesis deals with modeling our dual-frequency VECSEL by taking into account the spin dynamics of the carriers.

The following table summarizes the main results presented in this chapter:

- Exploration of the spectral behaviors of intensity noises and their correlation in DF-VECSELs operating at 1.55 μm and 1 μm wavelengths.
- Spectral analysis of the phase noise of the RF beatnote generated by optical mixing of the two cross-polarized of the DF-VECSELs.
- Demonstration of the correlation between the phase noise of the RF beatnote and the intensity noises of the two laser modes, which generate the RF beatnote via optical mixing.
- Investigation of the influence of the nonlinear coupling strengths between the two laser modes on the intensity and the phase noise correlations in DF-VECSEL.
- Measurement of the pump noises and their correlations, entering into the two spatially separated modes of the optically-pumped DF-VECSEL, which has enabled us to explain all the noise properties of the DF-VECSEL.
- Development of a simple theoretical model based on modified rate equations explaining the pump noise propagation scheme to the phase noise of the RF beatnote, that deteriorates its spectral purity.

Chapter 3

Spin-flip modeling of dual-frequency VECSELs

Contents

3.1 Introduction

In the preceding chapter, we have proved that different noise properties of a dual-frequency VECSEL can be well explained by a simple theoretical model based on modified rate equations. This simple heuristic model has been surprisingly successful, even though it has completely overlooked the spin-dependent dynamics of the carriers in the semiconductor active medium. On the other hand, the spin-flip model [San Miguel et al., 1995], abbreviated as SFM model, has achieved great success in explaining different polarization properties of quantum well (QW) based vertical-cavity surface-emitting lasers (VCSELs), such as selection of polarization state [Jewell et al., 1989], polarization dynamics [Chang-Hasnain et al., 1991b,a], switching of polarization state [George Pan et al., 1993]. This four-level model considers two different electronic transitions associated with different magnetic sublevels of the conduction and heavy-hole valence bands which provide gain for the two circularly polarized components of laser light of opposite helicities. Later, the SFM model has been extended to incorporate the effect of material birefringence (linear phase anisotropy), gain dichroism (gain anisotropy), saturable dispersion (linewidth enhancement factor or Henry factor), etc., which dictate different stability criteria of the linearly polarized modes of a VCSEL [Travagnin et al., 1996; Martín-Regalado et al., 1996, 1997; Travagnin et al., 1997; van Exter et al., 1998c,a; Martín-Regalado et al., 1999; Prati et al., 2002]. Moreover, many other properties such as the effect of nonlinear phase anisotropy [van Exter et al., 1998b], influence of polarization dynamics on the noise properties [Mulet et al., 2001; Kaiser et al., 2002], existence of elliptical or higher order transverse modes and possibilities of having chaotic behavior even in free running lasers [Virte et al., 2013b,a], have been quite successfully explained based on the fundamental ideas of spin dependent carrier dynamics as described in the SFM model. This leads to the subject of the present chapter as to analyze the properties of the two orthogonally polarized modes of a dual-frequency VECSEL from the perspective of the SFM model [De et al., 2014c]. We start by writing the rate equations for our laser based on the ideas of the SFM model and taking into account the partial spatial overlap between the modes. We also aim at adiabatically eliminating the carrier dynamics as our laser is of class-A type, hoping to be able then to derive the heuristic equations that we have used in Chapter 2.

The chapter is organized as follows: in Sec. 3.2, we recall the standard SFM model, developed for VCSELs. In Sec. 3.3, a developed rate equation model relevant for our dual-

frequency VECSEL is derived taking into account the ideas of the SFM model. Section 3.4 describes how these rate equations can be simplified thanks to the adiabatic elimination of the fast variables and averaging over rapidly varying phases. In Sec. 3.5, we use this model to define the nonlinear coupling between the two linear eigenpolarizations. The intensity noise properties are analyzed in Sec. 3.6. Finally, in Sec. 3.7, we summarize the main conclusions of this chapter.

3.2 Spin-flip model for VCSEL

In this section, we rederive the standard SFM Model [San Miguel et al., 1995], developed to describe the polarization dynamics of a VCSEL incorporating QW-based active medium. The polarization of the light from such laser, in addition to the anisotropies inside the laser cavity, depends on the angular momentum of the quantum states involved in the lasing transitions between the conduction and the valence bands. The band structure near the band gap can be schematized as shown in Fig. 3.1. The laser emission is assumed to be

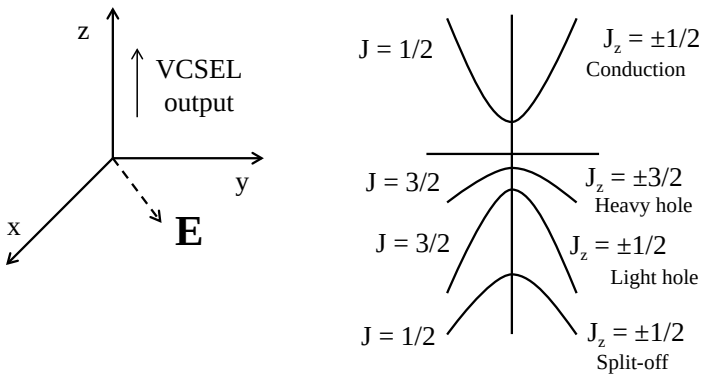

Figure 3.1: Schematic of the band structure of a quantum well (QW) based VCSEL. **E** denotes the laser field.

along z-direction, perpendicular to the surface of the QW based active medium slab, and the electric field is in the $x - y$ plane (Fig. 3.1). Considering the band structure near the band gap, the conduction band has zero orbital angular momentum, and thereby denoted by the quantum numbers $J = 1/2$, $J_z = \pm 1/2$. The valence bands having orbital angular momentum equal to 1 are commonly named as heavy hole (hh), light hole (lh), and split-off (so) bands, and respectively described by the quantum numbers $J = 3/2$, $J_z = \pm 3/2$;

$J = 3/2$, $J_z = \pm 1/2$; $J = 1/2$, $J_z = \pm 1/2$. In a VCSEL, the energy difference between the split-off and conduction bands is large enough to neglect any lasing transitions between them. Moreover, the quantum confinement along the z-direction inside the QWs lifts the degeneracy between the hh and lh bands, and splits them by such a large margin that the lasing transitions between the conduction and lh bands can be disregarded (Fig. 3.1). Thereby, the two remaining allowed dipole transitions, satisfying $\Delta J_z = \pm 1$, between the conduction and valence bands are as follows: the transition from $J_z = -1/2$ to $J_z = -3/2$ associated with right circularly polarized light (σ_+), and $J_z = 1/2$ to $J_z = 3/2$ associated with left circularly polarized light (σ_-). Therefore, the laser transitions can be simply described by a four-level scheme as depicted in Fig. 3.2. The vector electric field for a

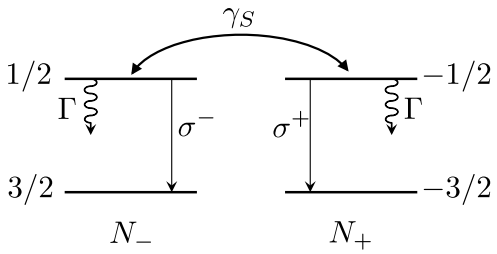

Figure 3.2: Level scheme involved in the SFM model [San Miguel et al., 1995]. N_+ and N_- are the population inversions for the σ^+ and σ^- transition, respectively. The decay rate of these population inversions is Γ. The spin-flip rate is γ_S.

single mode laser can be written as

$$\mathbf{E} \;=\; [E_x(x,y,t)\hat{\mathbf{x}} + E_y(x,y,t)\hat{\mathbf{y}}]e^{i(kz-\omega t)} + c.c.\ , \tag{3.1}$$

where E_x, and E_y denote the slowly varying field amplitudes along the x- and y-axis. However, since the lasing transitions in the scheme of Fig. 3.2 are associated with circularly polarized light, it is convenient to express the field amplitudes in terms of right and left circularly polarized components as

$$E_\pm \;=\; \frac{1}{\sqrt{2}}(E_x \pm iE_y)\ , \tag{3.2}$$

where $E_\pm$ corresponds to the transitions from $\mp 1/2$ to $\mp 3/2$.

3.2.1 Standard four-level model in circular polarization basis

In circular polarization basis, the laser dynamics can be described by the following Maxwell-Bloch equations [San Miguel et al., 1995]:

$$\frac{\partial E_\pm}{\partial t} = -\frac{\gamma_{cav}}{2}E_\pm - ig_0^* P_\pm \ , \tag{3.3}$$

$$\frac{\partial P_\pm}{\partial t} = -[\gamma_\perp + i(\omega_0 - \omega)]P_\pm + ig_0 E_\pm (N \pm n) \ , \tag{3.4}$$

$$\frac{\partial N}{\partial t} = -\Gamma(N - N_0) + [ig_0^*(E_+^* P_+ + E_-^* P_-) + c.c.] \ , \tag{3.5}$$

$$\frac{\partial n}{\partial t} = -\gamma_S n + [ig_0^*(E_+^* P_+ - E_-^* P_-) + c.c.] \ . \tag{3.6}$$

In the above equations, all the transverse spatial effects have been ignored. The slowly varying amplitudes of the dipole polarizations associated with the two lasing transitions are denoted with $P_\pm$. n and N respectively represent the spin population difference and the total population difference, which are defined as follows

$$N = \frac{1}{2}[(N_{\frac{1}{2}} + N_{-\frac{1}{2}}) - (N_{\frac{3}{2}} + N_{-\frac{3}{2}})] = \frac{1}{2}(N_+ + N_-) \ , \tag{3.7}$$

$$n = \frac{1}{2}[(N_{-\frac{1}{2}} - N_{-\frac{3}{2}}) - (N_{\frac{1}{2}} - N_{\frac{3}{2}})] = \frac{1}{2}(N_+ - N_-) \ , \tag{3.8}$$

where $N_{\pm\frac{i}{2}}$ denotes the population of the spin sublevel $\pm\frac{i}{2}$, and N_+, N_- define the population inversions associated with σ_+ and σ_- transitions, respectively (Fig. 3.2). The nonzero value of n introduces coupling between the σ_+ and σ_- transitions. Table 3.1 summarizes

Parameter	Description
ω	Cavity frequency.
ω_0	Resonant transition frequency for the active medium.
g_0	Atom-field coupling constant.
N_0	Incoherent pumping.
γ_{cav}	Inverse of photon lifetime inside the cavity.
$\gamma_\perp$	Relaxation rate of dipole polarizations.
Γ	Decay rate of the total population difference.
γ_S	Relaxation rate of spin-population difference.

Table 3.1: Parameters of the spin-flip model.

the parameters used in Maxwell-Bloch Eqs. (3.3-3.6) and describes the physical processes these parameters correspond to. It is important to mention that, in this model, the spin relaxation rate γ_S is introduced phenomenologically. It takes into account all the microscopic spin relaxation processes. In general, the relaxation rate of the dipole polarization ($\gamma_\perp$) is much faster than all the other time scales involved in the dynamics of the laser, hence the dipole polarization can be adiabatically eliminated by taking their steady-state values as

$$P_\pm = \chi_\pm E_\pm = \frac{g_0(-\Omega + i\gamma_\perp)}{\gamma_\perp^2 + \Omega^2}(N \pm n)E_\pm \ , \tag{3.9}$$

where $\Omega = \omega - \omega_0$ is the detuning. Then, the so-called constant $\alpha-$factor [Henry, 1982] of single-mode semiconductor laser can be associated with a large detuning Ω, and obtained simply by dividing the real and imaginary parts of the susceptibility ($\chi_\pm$) as

$$\alpha = \frac{\mathrm{Re}\chi_\pm}{\mathrm{Im}\chi_\pm} = -\frac{\Omega}{\gamma_\perp} \ . \tag{3.10}$$

Thereafter, substituting Eqs. (3.9-3.10) in Eqs. (3.3-3.6), we obtain the rate equations in much convenient form as

$$\frac{\partial E_\pm}{dt} = -\frac{\gamma_{cav}}{2}E_\pm + \frac{\kappa}{2}(1 + i\alpha)(N \pm n)E_\pm \ , \tag{3.11}$$

$$\frac{\partial N}{dt} = -\Gamma(N - N_0) - \kappa(|E_+|^2 + |E_-|^2)N - \kappa(|E_+|^2 - |E_-|^2)n \ , \tag{3.12}$$

$$\frac{\partial n}{dt} = -\gamma_S n - \kappa(|E_+|^2 - |E_-|^2)N - \kappa(|E_+|^2 + |E_-|^2)n \ , \tag{3.13}$$

where $\kappa = 2\frac{|g_0|^2}{\gamma_\perp^2 + \Omega^2}$ is the stimulated emission coefficient. Without any anisotropy inside the laser cavity, any linearly polarized field is a solution of Eqs. (3.11-3.13), but the orientation is arbitrary and dynamically diffuses because of noise. However, the presence of optical anisotropies inside the VCSEL forces laser emission along a fixed direction.

3.2.2 Four-level model in linear polarization basis

In general, VCSELs possess two types of linear anisotropies, amplitude anisotropy or dichroism and phase anisotropy or birefringence. Conventionally, these two anisotropies

can be modeled via two parameters, $\gamma_a/2$ and $\gamma_p/2$, respectively correspond to dichroism and birefringence. The introduction of these two anisotropies modifies the rate equations [Eq. (3.11)] of the fields as follows,

$$\frac{\partial E_\pm}{dt} = -\frac{\gamma_{cav}}{2}E_\pm + \frac{\kappa}{2}(1+i\alpha)(N \pm n)E_\pm - \frac{1}{2}(\gamma_a + i\gamma_p)E_\mp \ , \tag{3.14}$$

while the equations [Eqs. (3.12-3.13)] for the populations remain unchanged. To better understand the effects of the anisotropies, it is convenient to express the rate equations in linear polarization basis as

$$\frac{dE_x}{dt} = -\frac{\gamma_x}{2}E_x - i\frac{\gamma_p}{2}E_x + \frac{\kappa}{2}(1+i\alpha)(NE_x + inE_y) \ , \tag{3.15}$$

$$\frac{dE_y}{dt} = -\frac{\gamma_y}{2}E_y + i\frac{\gamma_p}{2}E_y + \frac{\kappa}{2}(1+i\alpha)(NE_y - inE_x) \ , \tag{3.16}$$

$$\frac{dN}{dt} = -\Gamma(N - N_0) - \kappa N(|E_x|^2 + |E_y|^2) - i\kappa n(E_x^* E_y - E_x E_y^*) \ , \tag{3.17}$$

$$\frac{dn}{dt} = -\gamma_S n - \kappa n(|E_x|^2 + |E_y|^2) - i\kappa N(E_x^* E_y - E_x E_y^*) \ , \tag{3.18}$$

where $\gamma_x = \gamma_{cav} + \gamma_a$, and $\gamma_y = \gamma_{cav} - \gamma_a$ respectively define the decay rates of $x-$, $y-$polarized photons inside the cavity. From the above equations (3.15-3.18), one can notice that the birefringence ($\gamma_p/2$) leads to a frequency difference of γ_p between the $x-$ and $y-$polarized modes, whereas dichroism ($\gamma_a/2$) provides different thresholds for the two linear eigenpolarizations. Here, we insist on the fact that n is created only when E_x and E_y are non-zero [Eq. 3.18]. The significance of this fact will be clarified later. In the following, we will extend this model to our DF-VECSEL.

3.3 Extension of SFM model to the DF-VECSEL

The aim of this section is to utilize the ideas of the standard SFM model for the modeling of a dual-frequency VECSEL, sustaining oscillation of two orthogonal linearly polarized modes, which are partially spatially separated by an intra-cavity birefringent crystal (BC) as schematized in Fig. 3.3. This dual-frequency VECSEL has two main differences compared to the standard VCSEL. The first difference is the cm-long external cavity, which ensures class-A dynamical behavior of the laser as then the intra-cavity photon lifetimes

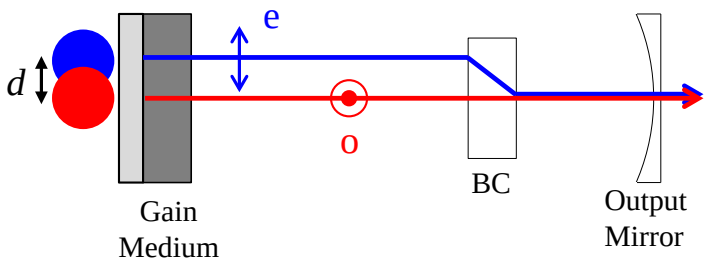

Figure 3.3: Schematic representation of the dual-frequency VECSEL. The intra-cavity birefringent crystal (BC) spatially separates (d) the ordinary (o) and extraordinary (e) polarized modes inside the gain medium.

($\sim$ 10 ns) for the two modes become longer than the population inversion lifetime ($\sim$ 1 ns) as evidenced in the preceding chapters. On the contrary, in standard VCSELs the photon lifetime ($\sim$ 1 ps) inside the cavity is usually much shorter than the population inversion lifetime ($\sim$ 1 ns) leading to a class-B dynamical behavior of the laser [Scott et al., 1994; Tauber et al., 1993]. The second difference originates from the intra-cavity BC, which spatially separates the two modes inside the gain structure. This ensures simultaneous oscillation of the two orthogonally polarized modes by reducing their nonlinear coupling below unity [Sargent III et al., 1974]. The nonlinear coupling is lowered as the partial overlap between the modes reduces the cross-saturation effect. Moreover, this permits to achieve different nonlinear coupling strengths between the two laser modes simply by varying the thickness of the BC as described in Chapter 2. Besides, the BC introduces a strong linear phase anisotropy inside the cavity, which enables to obtain a frequency difference in the RF range between the two modes polarized along the ordinary and extraordinary eigenpolarizations of the BC (Chapter 2).

Therefore, the main difficulty to model our dual-frequency VECSEL in the framework of the SFM model is to incorporate the effect of the partial spatial overlap between the two laser modes. This has been taken care of by introducing the dimensionless parameter Π ($0 \leq \Pi \leq 1$), which we define as:

$$\Pi = \frac{\int I(x,y)I(x-d,y)dxdy}{\sqrt{\int I^2(x,y)dxdy \int I^2(x-d,y)dxdy}} = \exp\left(-\frac{d^2}{w^2}\right), \tag{3.19}$$

where $I(x,y)$ denotes the Gaussian intensity profiles of radius w of the laser modes in

the active medium and d is the spatial separation between the axes of the ordinary and extraordinary modes inside the gain structure (see Fig. 3.4). In is important to mention

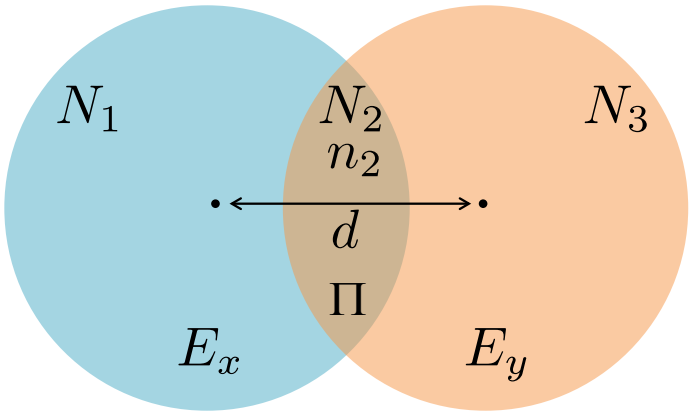

Figure 3.4: Schematic representation of the two modes in the gain medium of the dual-frequency VECSEL. We model the two beams as two top-hat cylindrical beams with circular sections. E_x (resp. E_y) is the complex amplitude of the x-polarized (resp. y-polarized) field. N_1 (resp. N_3) is the total population inversion in the region where only the x-polarized (resp. y-polarized) mode has a non-zero intensity. N_2 is the total population inversion and n_2 is the population inversion difference in the region where both modes are superimposed. The parameters d and Π respectively represent the spatial separation and the relative overlap between the two modes.

here that Π could also be used to model other effects which tend to increase the effective overlap between the two modes such as carrier diffusion. However, in case of our DF-VECSEL based on either GaAs (VECSEL at 1 μm) or InP (VECSEL at 1.5 μm) material system, the diffusion length of electrons (having higher mobility than holes) is typically of the order of few microns [Dargys and Kundrotas, 1994; Levinshtein et al., 1996], which is much less than the mode size ($\sim 60 - 70\,\mu$m) of our DF-VECSEL inside the active medium. Therefore, we can safely neglect the carrier diffusion effect in our DF-VECSEL. The basic hypotheses of our model are schematized in Fig. 3.4. For the sake of simplicity, we model the two modes as two top-hat cylindrical beams with circular sections, with an overlap Π. We then choose to consider three population reservoirs associated with the three different regions schematized in Fig. 3.4: Region 1 (resp. 3) is the region where only the x-polarized (resp. y-polarized) mode is present with a complex field amplitude E_x (resp. E_y) while region 2 is the place where both modes overlap. We can then model the

dual-frequency VECSEL using the following rate equations:

$$\frac{dE_x}{dt} = -\frac{\gamma_x}{2}E_x - i\frac{\gamma_p}{2}E_x + \frac{\kappa}{2}(1+i\alpha)\left[(N_1+N_2)E_x + in_2E_y\right] \ , \tag{3.20}$$

$$\frac{dE_y}{dt} = -\frac{\gamma_y}{2}E_y + i\frac{\gamma_p}{2}E_y + \frac{\kappa}{2}(1+i\alpha)\left[(N_2+N_3)E_y - in_2E_x\right] \ , \tag{3.21}$$

$$\frac{dN_1}{dt} = -\Gamma(N_1 - N_{01}) - \kappa N_1|E_x|^2 \ , \tag{3.22}$$

$$\frac{dN_2}{dt} = -\Gamma(N_2 - N_{02}) - \kappa N_2(|E_x|^2 + |E_y|^2) - i\kappa n_2(E_x^*E_y - E_xE_y^*) \ , \tag{3.23}$$

$$\frac{dN_3}{dt} = -\Gamma(N_3 - N_{03}) - \kappa N_3|E_y|^2 \ , \tag{3.24}$$

$$\frac{dn_2}{dt} = -\gamma_S n_2 - \kappa n_2(|E_x|^2 + |E_y|^2) - i\kappa N_2(E_x^*E_y - E_xE_y^*) \ , \tag{3.25}$$

where the notations E_x, E_y, γ_x, γ_y, Γ, γ_S, γ_p, κ, and α have the same meaning as in Eqs. (3.15-3.18). It is worth noticing that all the populations entering these equations, denoted as N_1, N_2, N_3, and n_2, and their pumping terms N_{01}, N_{02}, and N_{03}, are dimensionless number of atoms. Since the quantities N_1, N_2, and N_3 that we have used in Eqs. (3.20-3.25) are dimensionless number of atoms, they are already the results of the integration of the density of atoms over the transverse mode field distributions. Consequently, they have already taken into account the confinement factors of the two modes that appears explicitly when the equations are written in terms of atomic densities [Sargent III et al., 1974; Wieczorek and Chow, 2004, 2005]. Moreover, since only the x-polarized (resp. y-polarized) mode is present in region 1 (resp. 2) of Fig. 3.4, we need to introduce only a total population inversion N_1 (resp. N_3) in this region, and no population inversion difference n_1 (resp. n_3) is created in this region. On the contrary, in region 2 where the two modes overlap, we introduce both the total population inversion N_2 and the population inversion difference n_2. Indeed, the population inversion difference n can exist only when both E_x and E_y are non-zero [Eq. 3.18].

Here, the overlapping factor Π between the two modes has entered the model through the pumping rates N_{01}, N_{02}, and N_{03}. More precisely, the amount of overlap determines the strength of the pumping N_{02} that goes to the region of the active medium where the two modes overlap with respect to the pumping rates N_{01} and N_{03} in the regions where only one of the modes has a non vanishing intensity. Quantitatively, if we introduce the total pumping rates N_{0x} and N_{0y} for the x- and y-polarized modes, respectively, then N_{01},

N_{02}, and N_{03} can be defined by:

$$N_{01} = N_{0x} - \Pi\frac{N_{0x}+N_{0y}}{2} , \tag{3.26}$$

$$N_{02} = \Pi\frac{N_{0x}+N_{0y}}{2} , \tag{3.27}$$

$$N_{03} = N_{0y} - \Pi\frac{N_{0x}+N_{0y}}{2} . \tag{3.28}$$

One can notice from Eqs. (3.20-3.25) that, if we suppose that one of the modes vanishes (for example $E_y = 0$ or $N_{02} = N_{03} = 0$), we then retrieve the two usual rate equations for E_x and $N_x = N_1 + N_2$. Moreover, in the case where the modes totally overlap ($\Pi = 1$ and $N_{0x} = N_{0y}$, or similarly $N_{01} = N_{03} = 0$ and $N_{02} \neq 0$), Eqs. (3.20-3.25) reduce to Eqs. (3.15-3.18) with $N = N_2$, $n = n_2$, and $N_1 = N_3 = 0$. This proves the consistency of the present model for the DF-VECSEL with the standard SFM model.

3.4 Simplification of the rate equations

The aim of the present section is to simplify the general rate equations (3.20-3.25) by considering different approximations valid for our DF-VECSEL. We start by adiabatic elimination of the spin dynamics as this is much faster than all other time scales involved in the laser dynamics.

3.4.1 Adiabatic elimination of the spin dynamics

Actually, the spin-flip processes tend to balance the populations associated with the σ_+ and σ_- transitions inside the QW-based active medium as shown in Fig. 3.2. All the microscopic spin-flip relaxation processes have been incorporated in the model by the decay parameter γ_S. Measurements have shown that γ_S^{-1} is of the order of a few tens of picoseconds inside quantum wells [Damen et al., 1991; Bar-Ad and Bar-Joseph, 1992], whereas $\Gamma^{-1} \approx 1$ ns and $\gamma_x^{-1}, \gamma_y^{-1} \approx 10$ ns for our DF-VECSEL, as described in the previous chapters. Therefore, one can adiabatically eliminate the dynamics of n_2 from the laser rate equations by setting $dn_2/dt = 0$ in Eq. (3.25). This leads to

$$n_2 = \frac{-i\kappa N_2(E_x^* E_y - E_x E_y^*)}{\gamma_S + \kappa(|E_x|^2 + |E_y|^2)} . \tag{3.29}$$

To obtain Eq. (3.29), we have also assumed that the relative phase between the two fields evolves slower than the spin relaxation rate, namely, $\gamma_p \ll \gamma_S$. This is indeed true for our DF-VECSEL, which sustains oscillation of two cross-polarized modes with a frequency difference (γ_p) of few gigahertz as shown in the preceding chapters. We can now suppose that the field amplitudes E_x and E_y in Eqs. (3.20-3.25) are normalized in such a way that the squares of their moduli correspond to the numbers of photons F_x and F_y inside the cavity for the two polarization states, leading to:

$$E_x = \sqrt{F_x} e^{i\phi_x} \ , \ E_y = \sqrt{F_y} e^{i\phi_y} \ , \tag{3.30}$$

where we have introduced the phases ϕ_x and ϕ_y of the two modes. We define their difference as

$$\phi \ = \ \phi_x - \phi_y \ . \tag{3.31}$$

With these notations, Eq. (3.29) reads

$$n_2 \ = \ -2\varepsilon \frac{\kappa}{\Gamma} N_2 \sqrt{F_x F_y} \sin\phi \ , \tag{3.32}$$

where we have supposed that the large value of γ_S leads to $\dfrac{\kappa}{\gamma_S} F_{x,y} \ll 1$, and where we have introduced

$$\varepsilon \ = \ \Gamma/\gamma_S \ , \tag{3.33}$$

which is assumed to be much smaller than 1. Replacing n_2 in Eqs. (3.20-3.24) by its steady-state value [Eq. (3.32)], we obtain

$$\frac{dF_x}{dt} \ = \ -\gamma_x F_x + \kappa(N_1 + N_2)F_x - 2\kappa^2 \frac{\varepsilon}{\Gamma} N_2 F_x F_y \sin\phi(\sin\phi - \alpha\cos\phi) \ , \tag{3.34}$$

$$\frac{dF_y}{dt} \ = \ -\gamma_y F_y + \kappa(N_3 + N_2)F_y - 2\kappa^2 \frac{\varepsilon}{\Gamma} N_2 F_x F_y \sin\phi(\sin\phi + \alpha\cos\phi) \ , \tag{3.35}$$

$$\frac{dN_1}{dt} \ = \ -\Gamma(N_1 - N_{01}) - \kappa N_1 F_x \ , \tag{3.36}$$

$$\frac{dN_2}{dt} \ = \ -\Gamma(N_2 - N_{02}) - \kappa N_2(F_x + F_y) + 2\kappa^2 \frac{\varepsilon}{\Gamma} N_2 F_x F_y \ , \tag{3.37}$$

$$\frac{dN_3}{dt} = -\Gamma(N_3 - N_{03}) - \kappa N_3 F_y \ , \tag{3.38}$$

$$\frac{d\phi}{dt} = -\gamma_p + \frac{\kappa}{2}\alpha(N_1 - N_3) - \frac{\kappa^2\varepsilon}{2\Gamma}N_2[F_y(\sin 2\phi + 2\alpha \sin^2\phi) - F_x(\sin 2\phi - 2\alpha \sin^2\phi)] \ . \tag{3.39}$$

3.4.2 Averaging the relative phase

The frequency difference between the two cross-polarized modes of our DF-VECSEL is typically of the order of few gigahertz as shown in the preceding chapters. Moreover, this is also the interesting frequency range for the targeted microwave photonics applications. Now, The frequency difference of a few gigahertz between the two cross-polarized modes of the DF-VECSEL is ruled by the term γ_p [Eq. (3.39)], coming mainly from the intra-cavity BC. This leads to a much faster dynamics of the relative phase (ϕ) between the two laser fields than the population inversion decay rate ($\Gamma \approx 3 \times 10^8$ s^{-1}) in the gain medium, allowing us to further simplify the rate equations (3.34-3.38) by averaging over all values ϕ from 0 to 2π. Then, we obtain

$$\frac{dF_x}{dt} = -\gamma_x F_x + \kappa(N_1 + N_2)F_x - \kappa^2\frac{\varepsilon}{\Gamma}N_2 F_x F_y \ , \tag{3.40}$$

$$\frac{dF_y}{dt} = -\gamma_y F_y + \kappa(N_2 + N_3)F_y - \kappa^2\frac{\varepsilon}{\Gamma}N_2 F_x F_y \ , \tag{3.41}$$

$$\frac{dN_1}{dt} = -\Gamma(N_1 - N_{01}) - \kappa N_1 F_x \ , \tag{3.42}$$

$$\frac{dN_2}{dt} = -\Gamma(N_2 - N_{02}) - \kappa N_2(F_x + F_y) + 2\kappa^2\frac{\varepsilon}{\Gamma}N_2 F_x F_y \ , \tag{3.43}$$

$$\frac{dN_3}{dt} = -\Gamma(N_3 - N_{03}) - \kappa N_3 F_y \ . \tag{3.44}$$

3.4.3 Class-A approximation

In the previous chapters, we have demonstrated that our DF-VECSEL exhibits class-A dynamics as the intra-cavity photon lifetimes (γ_x^{-1}, $\gamma_y^{-1} \sim 10$ ns) of the two laser modes are higher than the lifetime of the population inversions ($\Gamma^{-1} \sim 1$ ns). Therefore, we can adiabatically eliminate N_1, N_2, and N_3 from Eqs. (3.40-3.44) by setting $dN_1/dt = 0$,

$dN_2/dt = 0$, and $dN_3/dt = 0$ in Eqs. (3.42-3.44). This leads to

$$N_1 = \frac{N_{01}}{1+\frac{\kappa}{\Gamma}F_x} , \tag{3.45}$$

$$N_2 = \frac{N_{02}}{1+\frac{\kappa}{\Gamma}(F_x+F_y)-2\frac{\kappa^2\varepsilon}{\Gamma^2}F_xF_y} , \tag{3.46}$$

$$N_3 = \frac{N_{03}}{1+\frac{\kappa}{\Gamma}F_y} . \tag{3.47}$$

By injecting Eqs. (3.45-3.47) into Eqs. (3.40-3.41), we obtain the two following equations

$$\frac{dF_x}{dt} = -\gamma_x F_x + \kappa\left[\frac{N_{01}}{1+\frac{\kappa}{\Gamma}F_x} + \frac{N_{02}}{1+\frac{\kappa}{\Gamma}(F_x+F_y)-2\frac{\kappa^2\varepsilon}{\Gamma^2}F_xF_y}\left(1-\frac{\kappa\varepsilon}{\Gamma}F_y\right)\right]F_x , \tag{3.48}$$

$$\frac{dF_y}{dt} = -\gamma_y F_y + \kappa\left[\frac{N_{03}}{1+\frac{\kappa}{\Gamma}F_y} + \frac{N_{02}}{1+\frac{\kappa}{\Gamma}(F_x+F_y)-2\frac{\kappa^2\varepsilon}{\Gamma^2}F_xF_y}\left(1-\frac{\kappa\varepsilon}{\Gamma}F_x\right)\right]F_y . \tag{3.49}$$

3.4.4 Weak saturation limit

Most often, it is convenient to express the laser rate equations in the so-called "third order of field" version. In the case where the laser is just above threshold and the saturation of the active medium is weak, i. e., $\kappa F_x/\Gamma, \kappa F_y/\Gamma \ll 1$, one can keep only terms up to first order in $\kappa F_x/\Gamma$ and $\kappa F_y/\Gamma$ in Eqs. (3.48-3.49), leading to the following "third order in field" version for Eqs. (3.48-3.49):

$$\frac{dF_x}{dt} = -\gamma_x F_x + \kappa\left[(N_{01}+N_{02})(1-\frac{\kappa}{\Gamma}F_x) - \frac{\kappa}{\Gamma}N_{02}(1+\varepsilon)F_y\right]F_x , \tag{3.50}$$

$$\frac{dF_y}{dt} = -\gamma_y F_y + \kappa\left[(N_{03}+N_{02})(1-\frac{\kappa}{\Gamma}F_y) - \frac{\kappa}{\Gamma}N_{02}(1+\varepsilon)F_x\right]F_y . \tag{3.51}$$

Equations (3.50-3.51) end up in the same form as the classical equations of Lamb's model [Sargent III et al., 1974]. In particular, the coefficients ξ_{xy}, ξ_{yx} which define the ratios between the cross- to self-saturation coefficients and which describe the nonlinear coupling of the two laser modes are given by

$$\xi_{xy} = \frac{N_{02}(1+\varepsilon)}{N_{01}+N_{02}} = \frac{\Pi}{2}(1+\varepsilon)\left(1+\frac{N_{0y}}{N_{0x}}\right) , \tag{3.52}$$

$$\xi_{yx} = \frac{N_{02}(1+\varepsilon)}{N_{03}+N_{02}} = \frac{\Pi}{2}(1+\varepsilon)\left(1+\frac{N_{0x}}{N_{0y}}\right) . \tag{3.53}$$

Equations (3.50-3.51) allow us to retrieve the heuristic model that was used in Chapter 2. However, in that simple model ξ_{xy} and ξ_{yx} were introduced heuristically. On the contrary, the present model provides analytical expressions for these coupling coefficients [Eqs. (3.52-3.53)], showing their dependence on the amount of spatial overlap (Π) between the modes and the value of the spin-relaxation decay rate (γ_S) relatively to the population inversion decay rate (Γ). It is indeed expected that the spin-flip process, mixing the populations associated with σ_+ and σ_- polarizations, must have some kind of influence on the gain cross-saturation, and hence on the coupling coefficients.

3.5 Transient and steady-state behaviors of DF-VECSEL

In this section, we aim at analyzing the transient and the steady-state behaviors of our DF-VECSEL to check the validity of the theoretical model derived in the previous section. We start by looking at the transient behavior during the laser switching on.

3.5.1 Laser switch-on

To analyze the dynamical behavior of a laser one standard way is to study how the laser switches on. We have used Eqs. (3.40-3.44) to simulate the switching on of our DF-VECSEL. The temporal evolution of the intra-cavity photon numbers (F_x, F_y) of the two modes and of the populations for different values of the spatial separation d are displayed in Fig. 3.5. These values of d correspond to those used in the experiments described in Chapter 2. Moreover, to perform the numerical integration of Eqs. (3.40-3.44), we have chosen values of the parameters w, κ, Γ, γ_x, γ_y representative of the experiments reported in Chapter 2. Only the value of ε has been estimated from the orders of magnitude of γ_S that one can find in the literature [Damen et al., 1991; Bar-Ad and Bar-Joseph, 1992]. We have supposed that the laser is 1.3 times above threshold, that the two cross-polarized modes are equally pumped, i. e., $N_{0x} = N_{0y}$, but that the x-polarized mode experiences slightly more losses than the y-polarized one. The results of Fig. 3.5 show that the two polarization eigenstates can oscillate simultaneously for all three values of d. However, when d decreases, the increase of the competition makes the final unbalance between their intensities more important. This is consistent with the picture expected

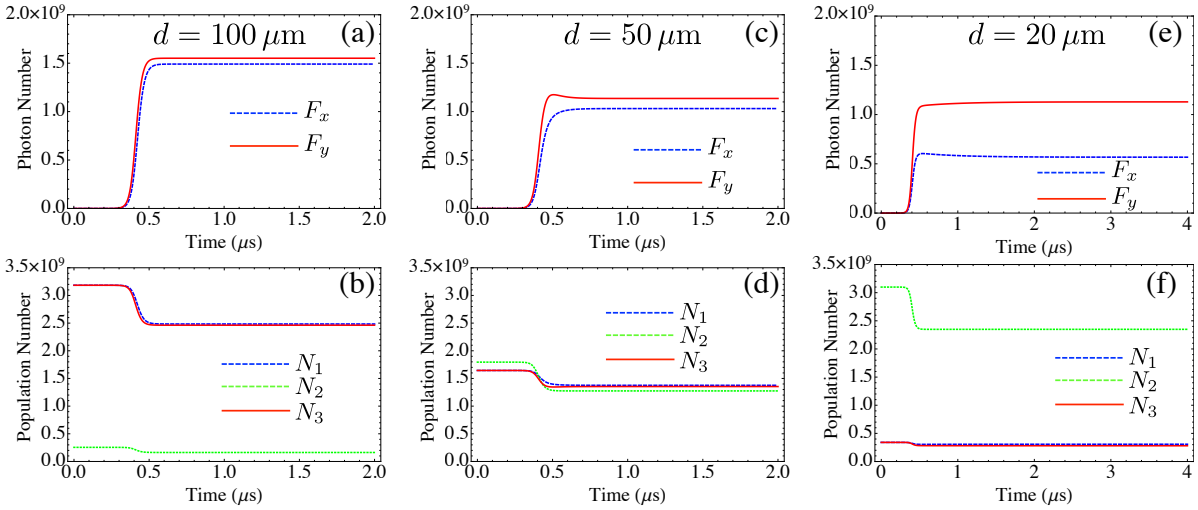

Figure 3.5: Time evolution of (a) the intra-cavity photon numbers F_x and F_y and (b) the population inversions N_1, N_2, and N_3 for $d = 100\,\mu$m, $w = 62\,\mu$m, $1/\gamma_x = 6$ ns, $1/\gamma_y = 6.05$ ns, $1/\Gamma = 3$ ns, $\varepsilon = 0.02$, $\kappa = 6.3 \times 10^{-2}\,\mathrm{s}^{-1}$, $N_{0x} = N_{0y} = 1.3 \times \gamma_x/\kappa$. In this case $\Pi = 0.074$. (c),(d): Same as (a),(b) for $d = 50\,\mu$m, corresponding to $\Pi = 0.52$. (e),(f): Same as (a),(b) for $d = 20\,\mu$m, corresponding to $\Pi = 0.90$.

from an increase of nonlinear coupling due to an increase of Π. The comparison of the evolution of the populations N_1, N_2, and N_3 in the three cases of Figs. 3.5(b), 3.5(d), and 3.5(f) is also interesting. One can notice that when d decreases, the increase of the overlap of the two modes leads to an increase of the relative weight of N_2 with respect to N_1 and N_3. Moreover, this decrease of d also leads to a decrease of the total number $N_1 + N_2 + N_3$ of atoms providing gain to the laser. This is consistent with an increase of the competition between the two modes. Before going further into the exploration of the behavior of steady-state solutions in our model, we check its consistency by verifying that it can also describe the well known damped relaxation behavior of a class-B laser. We have thus strongly increased the value of $1/\Gamma$ and simulated the switching on of the laser using Eqs. (3.40-3.44). The results are reproduced in Fig. 3.6. The laser clearly exhibits the in-phase and anti-phase relaxation oscillations, showing that our model consistently describes the behavior of class-B lasers also [Arecchi et al., 1984; Oka and Kubota, 1988].

To further check the generality of our model, we choose to simulate Eqs. (3.34-3.39) by considering a large value of $1/\Gamma$ as in Fig. 3.6, but for two different values of $1/\gamma_p$: one is of the same order as $1/\Gamma$, and the other one is much smaller than $1/\Gamma$. Figure 3.7

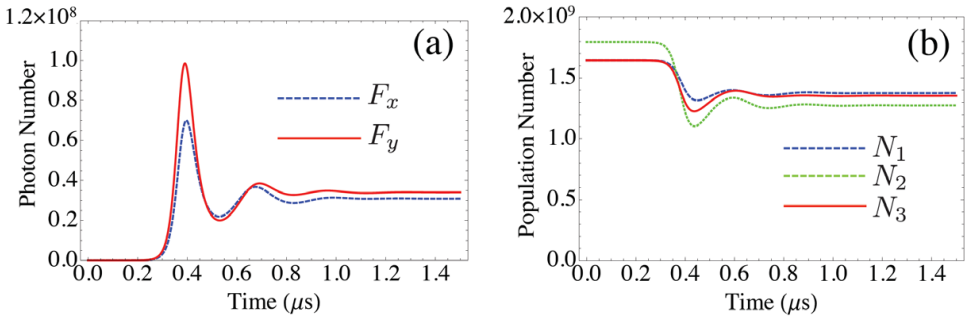

Figure 3.6: Same as Fig. 3.5(c,d) in the case of a class-B lasers. The values of the parameters are $d = 50\,\mu$m, $w = 62\,\mu$m, $1/\gamma_x = 6$ ns, $1/\gamma_y = 6.05$ ns, $1/\Gamma = 100$ ns, $\varepsilon = 0.02$, $\kappa = 6.3 \times 10^{-2}\,\mathrm{s}^{-1}$, $N_{0x} = N_{0y} = 1.3 \times \gamma_x/\kappa$.

reproduces the simulation results. The results illustrate that when the beatnote frequency

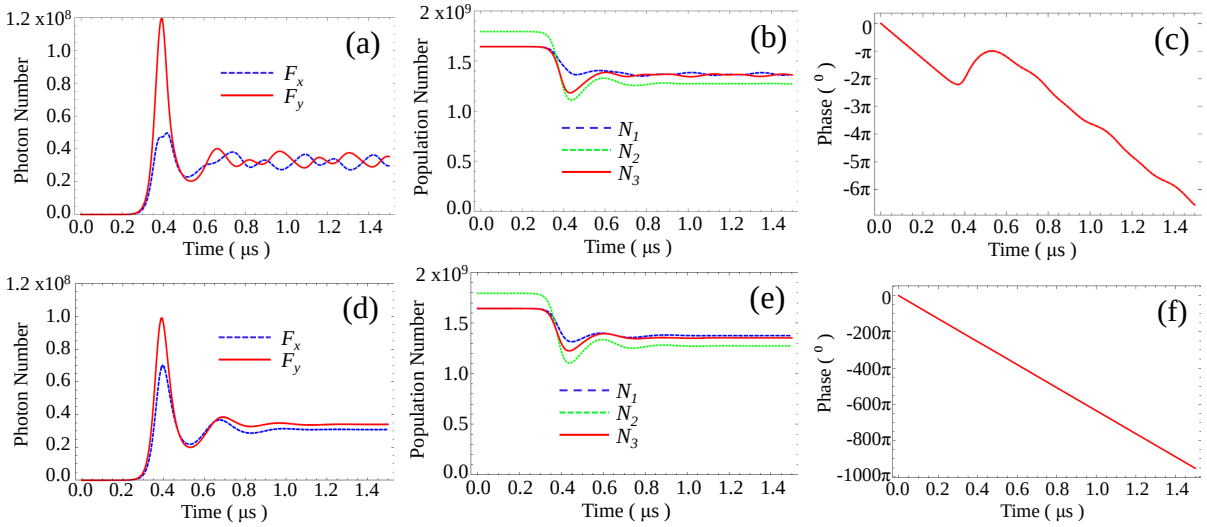

Figure 3.7: Time evolution of (a) the intra-cavity photon numbers F_x and F_y, (b) the population inversions N_1, N_2, and N_3, and (c) the beatnote phase ϕ for $d = 50\,\mu$m, $w = 62\,\mu$m, $1/\gamma_x = 6$ ns, $1/\gamma_y = 6.05$ ns, $\varepsilon = 0.02$, $\kappa = 6.3 \times 10^{-2}\,\mathrm{s}^{-1}$, $N_{0x} = N_{0y} = 1.3 \times \gamma_x/\kappa$, $1/\Gamma = 100$ ns. In this case $\gamma_p = 100$ ns. (d),(e),(f): Same as (a),(b),(c) for $\gamma_p = 1$ ns.

γ_p is of the same order as the carriers' decay rate Γ, the dynamics of the beatnote phase governs the dynamics of the photon numbers and population inversion numbers as reproduced in Figs. 3.7(a),(b),(c). In this case, one can again notice pulsations of the photon numbers and the population inversions ensuring class-B dynamical behavior of the laser

(Figs. 3.7(a),(b)). However, these pulsations are not at all straightforward to analyze as apart from the two usual dynamical variables (photon number and population inversion number) of a standard single mode class-B laser, the dynamics of DF-VECSEL includes the nonlinear coupling between the two laser modes and their relative phase (Figs. 3.7(c)). In principle, this might even give rise to chaotic behavior like in a standard single mode class-C laser as the laser dynamics involves more than two coupled dynamical variables [Bergé et al., 1987; Arecchi et al., 1986; Pieroux et al., 1994]. However, further investigations are required to confirm this point. Figures 3.7(d),(e),(f) show the simulation results, when the beatnote frequency γ_p is considered to be much larger than the carriers' decay rate Γ. One can observe that the temporal evolution of the photon numbers and population inversion numbers as represented by Figs. 3.7(d),(e) are exactly identical to those of Figs. 3.6(a),(b), respectively. This emphasizes the fact that the dynamics of relative phase between the two modes does not influence the dynamics of photon numbers and population inversions. Therefore, it can be eliminated from the laser rate equations (3.34-3.38) for γ_p much larger than Γ as done in Eqs. (3.40-3.44).

3.5.2 Steady-state solutions

After having analyzed the transient behavior, we now investigate the steady-state behavior of our DF-VECSEL as predicted by the present model. In particular, our focus is on the class-A case corresponding to our experimental situation. In this case, the steady-state solutions for the laser intensities can be obtained by finding the steady-state solutions of Eqs. (3.48-3.49). Specifically, we have plotted the intra-cavity photon numbers for the two modes versus pumping rates N_{0x} and N_{0y}, as shown in Fig. 3.8 keeping the other parameters as in Fig. 3.5. Here, we again choose three different values of d, just like in Fig. 3.5. The two modes are considered to have slightly different losses ($\gamma_x > \gamma_y$), but equal pumping rates ($N_{0x} = N_{0y}$). This fact is reflected by the different pumping thresholds for the two modes. Additionally, one can see that the unbalance in photon numbers increases with the decrease of d. This again proves the picture we considered for our DF-VECSEL that the mode competition becomes stronger for smaller separation (d) between the modes.

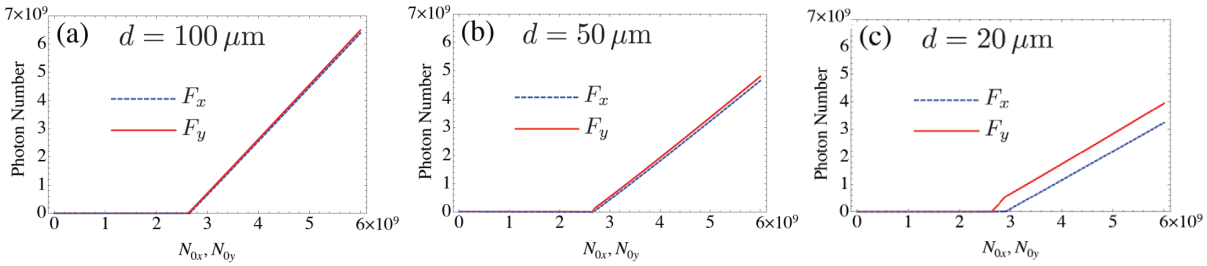

Figure 3.8: Evolution of the steady-state photon numbers F_x and F_y versus pumping rate $N_{0x} = N_{0y}$. The values of the parameters are $w = 62\,\mu$m, $1/\gamma_x = 6$ ns, $1/\gamma_y = 6.05$ ns, $1/\Gamma = 3$ ns, $\varepsilon = 0.02$, $\kappa = 6.3 \times 10^{-2}\,\mathrm{s}^{-1}$. (a) $d = 100\,\mu$m; (b) $d = 50\,\mu$m; (c) $d = 20\,\mu$m.

3.6 Nonlinear coupling constant

In the previous chapter, we have figured out how the nonlinear coupling between the two cross-polarized modes dictates the noise properties of the DF-VECSEL. Moreover, the nonlinear coupling is a key phenomenon when one considers the stability of the laser. Whether the coupling constant, $C = \xi_{xy}\xi_{yx}$, is higher or lower than 1 leads respectively to two distinct regimes such as bistability or simultaneity. In a DF-VECSEL, the nonlinear coupling constant C has already been measured [Pal et al., 2010]. However, in that study C has been estimated only by considering the amount of spatial overlap between the two modes. This is also what we have followed in the previous chapter. On the other hand, Eqs. (3.52-3.53) indicate that the spin-relaxation mechanism should have some kind of impact on the nonlinear coupling strength between the modes. This leads to the subject of the present section as to thoroughly analyze the nonlinear coupling constant in our DF-VECSEL from the view point of the present spin-flip model. To this aim, we consider the situation in which the laser exhibits class-A dynamics, as in Figs. 3.5 and 3.8, which corresponds to the experimental results of the previous chapter we wish to reproduce. In the case of weak saturation, Eqs. (3.52-3.53) have shown that the coupling does not only depend on the overlap Π, as expected and as shown by the simulations of Fig. 3.5,3.8. It also depends on the ratio ε between the spin and the population relaxation rates. Fig. 3.9 shows the results obtained when one simulates the laser switch-on for different values of ε when the two modes experience slightly different losses. This simulation is performed using Eqs. (3.40-3.44). It is clear from this figure that the larger ε, the stronger is the coupling between the two modes. By increasing ε from 0.01 to 0.1, one can see that a

small difference between the losses γ_x and γ_y experienced by the two modes (which have the same gain) can lead either to a small difference in intensities (Figs. 3.9(a),(b)) when ε is small or to the fact that the stronger mode forbids oscillation of the other one (Figs. 3.9(e),(f)) when ε is larger.

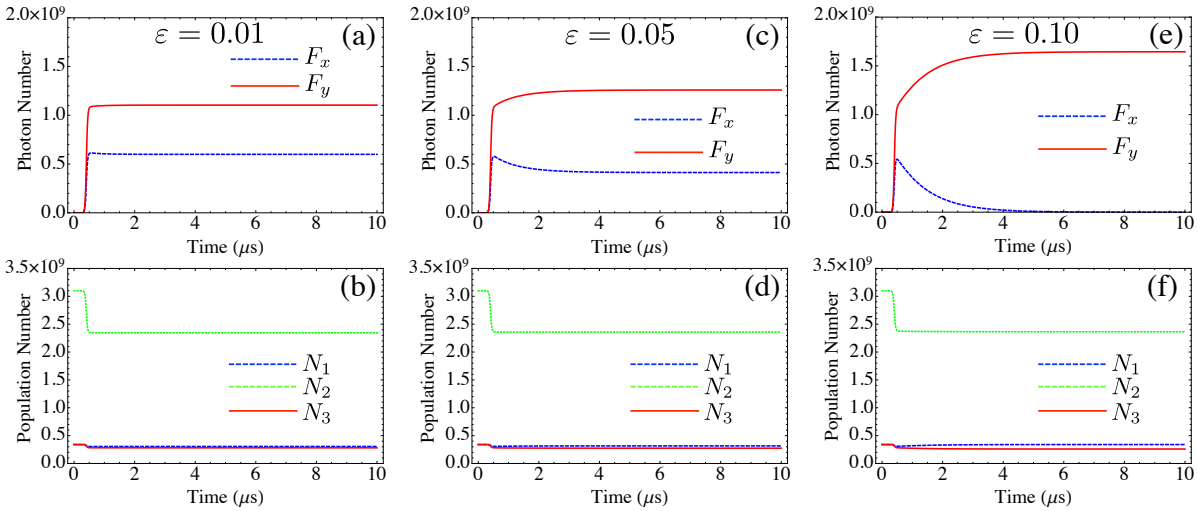

Figure 3.9: Time evolution of (a),(c),(e) the intra-cavity photon numbers F_x and F_y and (b),(d),(f) the population inversions N_1, N_2, and N_3 for $d = 20\,\mu$m, $w = 62\,\mu$m, $1/\gamma_x = 6\,$ns, $1/\gamma_y = 6.05\,$ns, $1/\Gamma = 3\,$ns, $\kappa = 6.3 \times 10^{-2}\,\mathrm{s}^{-1}$, $N_{0x} = N_{0y} = 1.3 \times \gamma_x/\kappa$. (a),(b) $\varepsilon = 0.01$; (c),(d) $\varepsilon = 0.05$; (e),(f) $\varepsilon = 0.1$.

Equations (3.52-3.53) also predict that if $N_{0x} \neq N_{0y}$, i.e., if the pumping or equivalently the gain to loss ratios for the two modes are not identical, then the two coupling coefficients ξ_{xy} and ξ_{yx} are not identical as soon as ε is different from 0. To check whether this prediction remains valid beyond the third order approximation, we generalize Eqs. (3.52-3.53) using the following definitions [Pal et al., 2010]:

$$\xi_{xy} = -\frac{\partial F_x/\partial \gamma_y}{\partial F_y/\partial \gamma_y}\,, \tag{3.54}$$

$$\xi_{yx} = -\frac{\partial F_y/\partial \gamma_x}{\partial F_x/\partial \gamma_x}\,. \tag{3.55}$$

Fig. 3.10 illustrates the evolution of ξ_{xy} and ξ_{yx} versus δN_0 when one varies the pumping

rates of the two modes in two opposite ways, namely:

$$N_{0x} = N_0(1+\delta N_0)\ , \tag{3.56}$$

$$N_{0y} = N_0(1-\delta N_0)\ . \tag{3.57}$$

Fig. 3.10 compares the results obtained from Eqs. (3.54-3.55) using the steady-state pho-

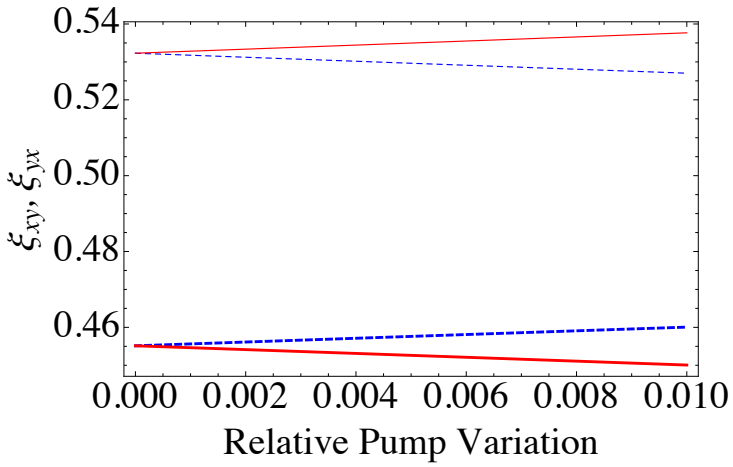

Figure 3.10: Evolution of ξ_{xy} (dashed blue line) and ξ_{yx} (full red line) versus δN_0 with $N_{0x} = N_0(1+\delta N_0)$ and $N_{0y} = N_0(1-\delta N_0)$. Thick lines: calculation from Eqs. (3.54-3.55) using the steady-state photon numbers F_x and F_y obtained from Eqs. (3.48-3.49). Thin lines: calculation from Eqs. (3.52-3.53). The values of the parameters are $d = 50\,\mu$m, $w = 62\,\mu$m, $1/\gamma_x = 6\,$ns, $1/\gamma_y = 6\,$ns, $1/\Gamma = 3\,$ns, $\varepsilon = 0.02$, $\kappa = 6.3\times10^{-2}\,\mathrm{s}^{-1}$, $N_0 = 1.3\gamma_x/\kappa$.

ton numbers F_x and F_y obtained from Eqs. (3.48-3.49) with the results obtained using the weak saturation approximation [Eqs. (3.52-3.53)]. One can see that both calculations indicate that the coefficients ξ_{xy} and ξ_{yx} become asymmetric when the pumping rates for the two modes become different ($N_{0x} \neq N_{0y}$). However, although the values of ξ_{xy} and ξ_{yx} given by the weak saturation approximation [Eqs. (3.52-3.53)] are close to the ones obtained from the complete model [Eqs. (3.54-3.55)], their evolution with the asymmetry of the pumping rates are opposite. Additionally, the difference between ξ_{xy} and ξ_{yx} leaves $C = \xi_{xy}\xi_{yx}$ unchanged, at least for small values of the pumping asymmetry δN_0. This can

also be seen in the weak saturation limit using Eqs. (3.52-3.53):

$$C = \xi_{xy}\xi_{yx} \simeq \frac{\Pi^2}{4}(1+2\varepsilon)\frac{(N_{0x}+N_{0y})^2}{N_{0x}N_{0y}} \ , \tag{3.58}$$

which, at first order, does not depend on δN_0 when N_{0x} and N_{0y} obey Eqs. (3.56-3.57), and reads as

$$C \simeq \Pi^2(1+2\varepsilon) \ . \tag{3.59}$$

Therefore, the observation of unequal values of the two coefficients ξ_{xy} and ξ_{yx} that was found by previous experiments [Pal et al., 2010] can be explained in our model. Notably, the simple model of Chapter 2 was not able to explain nonidentical values of ξ_{xy} and ξ_{yx}. Therefore, this is a significant achievement of the present model, which includes spin-dynamics of the carrier. Moreover, the present model explains why the variations of ξ_{xy} and ξ_{yx} leave C constant, as experimentally observed.

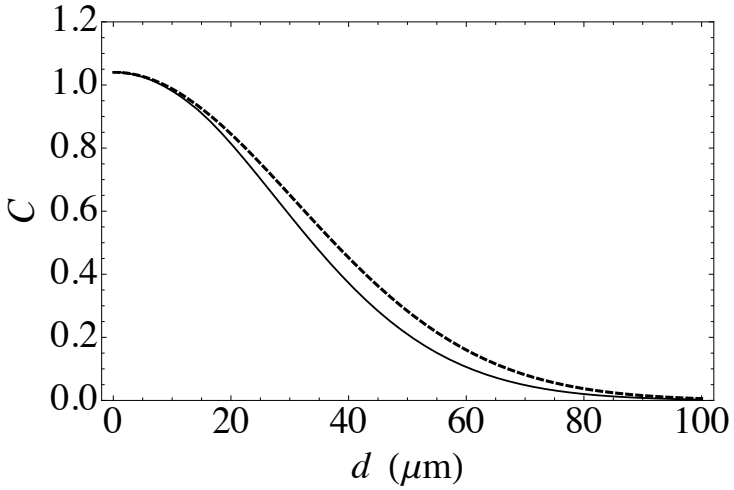

Figure 3.11: Evolution of $C = \xi_{xy}\xi_{yx}$ (full line) versus d obtained from Eqs. (3.54-3.55) using the steady-state photon numbers F_x and F_y obtained from Eqs. (3.48-3.49). Dashed line: calculation from Eq. (3.58). The values of the parameters are $w = 62\,\mu$m, $1/\gamma_x = 6\,$ns, $1/\gamma_y = 6\,$ns, $1/\Gamma = 3\,$ns, $\varepsilon = 0.02$, $\kappa = 6.3 \times 10^{-2}\,\mathrm{s}^{-1}$, $N_{0x} = N_{0y} = 1.3\gamma_x/\kappa$.

Fig. 3.11 reproduces the evolution of C with d. The results obtained either from the full calculation based on Eqs. (3.54-3.55) using the steady-state photon numbers F_x and F_y obtained from Eqs. (3.48-3.49), or from the simplified expressions of Eq. (3.58) lead to

almost the same result. This explains why the simplified heuristic model of the previous chapter has been so successful. The maximum value of C, obtained for $d = 0$, depends on ε. The fact that it is larger than unity explains why a partial spatial separation is necessary to obtain simultaneous oscillation of the two polarizations. Moreover, this predicts the existence of polarization bistability for d close to 0. This is also a new achievement of this spin-flip model of the DF-VECSEL compared to the previous simple model.

In the following, the present model will be utilized to reproduce the intensity noise properties of the DF-VECSEL as described in detail in the previous chapter.

3.7 Intensity noise properties

Till now, we have shown that the present model can successfully reproduce different transient and steady-state phenomena of our DF-VECSEL. Moreover, this developed model could explain few properties of the DF-VECSEL such as unequal values of the coupling coefficients, bistability, which were not possible to deduce from the simple model of Chapter 2. However, in the previous chapter we have realized that the simple model can well explain different noise properties of the DF-VECSEL, suitable for numerous microwave photonics applications. Specifically, the simple heuristic model has led to a very good agreement with the measurements of intensity noise spectra and of intensity noise correlations between the two modes. In the previous chapter, we have also figured out that the predominant source of intensity noise for the dual-frequency VECSEL is the pump intensity noise. This is an important issue for microwave photonics applications because this intensity noise is then transferred to the phase noise through the phase-intensity coupling mechanism as demonstrated in Chapter 2. The aim of the present section is thus to apply the present model, and more precisely Eqs. (3.40-3.44), to the description of the intensity noises of the two modes of the laser, including their correlations. The intensity fluctuations of the two cross-polarized modes are introduced through the photon number fluctuations as in Eqs. (2.1-2.2) of Chapter 2. Additionally, the pump intensity fluctuations are modeled as in Eqs. (2.29-2.30) of the previous chapter. Then by linearizing Eqs. (3.40-3.44) around their steady-state solutions with Mathematica, we succeed to extract linear relations between the fluctuations of the photon numbers, of the population inversions, and of the pumping rates. After taking the Fourier transforms of these equations, we can eliminate the fluctuations of the population inversions and end up with

numerical expressions relating the fluctuations of the photon numbers $\widetilde{\delta F}_x(f)$, $\widetilde{\delta F}_y(f)$ in the frequency domain to the pump fluctuations $\widetilde{\delta N}_{0x}(f)$ and $\widetilde{\delta N}_{0y}(f)$. Finally, we calculate the RINs of the two modes using the definition of Eqs. (2.3-2.4) and the normalized spectrum of the correlation between the intensity noises of the two modes from Eq. (2.7) of Chapter 2.

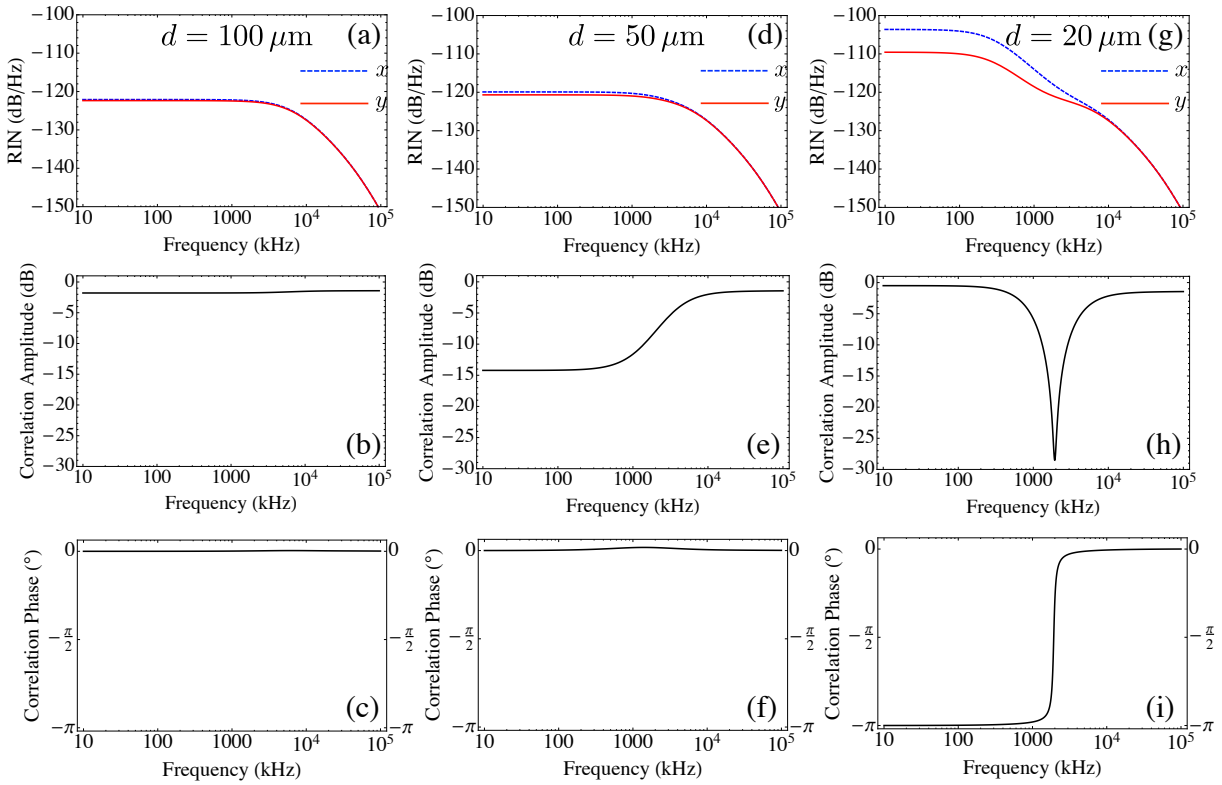

Figure 3.12: (a) Relative intensity noise (RIN), (b) correlation amplitude, and (c) correlation phase spectra calculated from the present model. The values of the parameters are $w = 62\,\mu$m, $1/\gamma_x = 6$ ns, $1/\gamma_y = 6.05$ ns, $1/\Gamma = 3$ ns, $\varepsilon = 0.02$, $\kappa = 6.3 \times 10^{-2}\,\mathrm{s}^{-1}$, $\overline{N}_{0x} = \overline{N}_{0y} = 1.3 \times \gamma_x/\kappa$, $\mathrm{RIN}_p = -135$ dB/Hz, and $d = 100\,\mu$m, corresponding to an overlap $\Pi = 0.074$. (d),(e),(f): Same as (a)-(c) for $d = 50\,\mu$m, corresponding to $\Pi = 0.52$. (g),(h),(i): Same as (a)-(c) for $d = 20\,\mu$m, corresponding to $\Pi = 0.90$.

Figure 3.12 reproduces the results obtained for three values of the spatial separation d, namely 100, 50, and 20 μm as in the experiments described in Chapter 2. These results are in good agreement with the corresponding experiments and with the spectra obtained from the simple heuristic model that we have developed in the previous chapter. In par-

ticular, these results reproduce the fact that for the weak coupling ($C \simeq 0$, Fig. 3.11) corresponding to $d = 100\,\mu$m (Figs. 3.12(a)-(c)), the relative intensity noise (RIN) spectra look like the transfer function of first order filters and hence illustrate the class-A dynamical behavior of our laser (Fig. 3.12(a)). The RIN spectra for the two modes are not identical as we have taken slightly different losses for the two modes. The intensity noises for the two modes are partially correlated (Fig. 3.12(b)) and their correlated parts are in phase (Fig. 3.12(c)) all over the considered frequency range (10 kHz - 100 MHz). These results show excellent agreement with the experiments as well as the predictions of the simple theoretical model (Fig. B.2 of Appendix B).

The simulation results for a spatial separation $d = 50\,\mu$m between the modes are shown in Figs. 3.12(d)-(f). In this intermediate situation, the coupling constant C is nearly equal to 0.3 as shown in Fig. 3.11. The RIN spectra again look like the transfer function of first order filters (Fig. 3.12(d)). As shown by Figs. 3.12(e),(f), the correlation amplitude is very low for frequencies lower than $\sim$1 MHz, whereas the correlation amplitude is strong and the correlation phase is 0 for higher frequencies. The results are again in good accordance with the experiment and the spectra obtained from the simple theoretical model as shown in Fig. B.3 of Appendix B.

Finally, Figs. 3.12(g)-(i) reproduce the simulation results for a spatial separation $d = 20\,\mu$m between the modes, which corresponds to a moderately strong nonlinear coupling ($C \simeq 0.8$) as shown in Fig. 3.11. The RIN spectra as presented in Fig. 3.12(g) now exhibit a change of slope at about 1 MHz. The correlation amplitude is strong except for a dip around 1 MHz, as reproduced in Fig. 3.12(h). The correlation phase jumps from π at frequencies lower than 1 MHz to 0 for higher frequencies, as reported in Fig. 3.12(i). These predictions are in good agreement with the experiments and the predictions of the simple model (Fig. B.4 of Appendix B).

As described in the previous chapter, these spectral behaviors of the intensity noises and their correlations for different nonlinear coupling strengths between the modes can again be physically interpreted in the framework of the in-phase and anti-phase eigenrelaxation mechanisms for the out-of-equilibrium fluctuations of any two-coupled oscillator system [Otsuka et al., 1992]. To this aim, we calculate the in-phase and anti-phase noise spectra from the present model and the simulation results are shown in Fig. 3.13. To calculate the in-phase and anti-phase noise spectra we use the definitions of Eqs. (C.10-C.11). From the in-phase and anti-phase noise spectra of Fig. 3.13 we can perfectly explain all

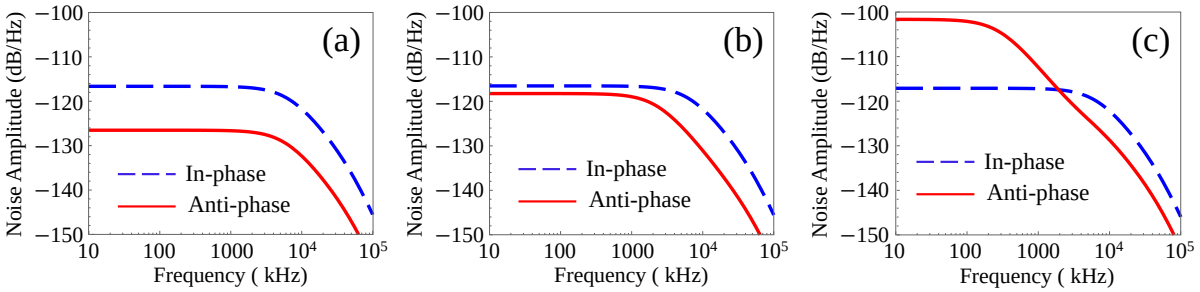

Figure 3.13: In-phase (dashed-blue line) and anti-phase (solid-red line) noise spectra for (a) $d = 100\,\mu$m (RIN), (b) $d = 50\,\mu$m, and (c) $d = 20\,\mu$m calculated from the present model. The values of the parameters are same as in Fig. 3.12.

the spectral behaviors of the intensity noises and their correlations. One can observe in Fig. 3.13 that the in-phase response is independent of the coupling, whereas the anti-phase response strongly depends on the coupling and has a cut-off frequency (∼1 MHz for our VECSEL) much lower lower than the in-phase one. For $d = 100\,\mu$m, the two laser modes are almost uncoupled ($C \simeq 0$). As a result, the in-phase response dominates over the anti-phase response for all frequencies within 10 kHz to 100 MHz (Fig. 3.13(a)). This leads to partially correlated (Fig. 3.12(b)) and in phase (Fig. 3.12(c)) intensity noises induced by partially correlated ($\eta < 1$), in phase ($\psi = 0$) pump fluctuations. For $C \simeq 0.3$, corresponding to $d = 50\,\mu$m, the amplitude of anti-phase response becomes comparable to the amplitude of the in-phase response for frequencies lower than the cut-off frequency of the anti-phase response (∼1 MHz), whereas for higher frequencies the in-phase response dominates (Fig. 3.13(b)). This explains the low values of the correlation amplitude for frequencies lower than 1 MHz, and the high values of the correlation amplitude and 0 correlation phase for frequencies higher than 1 MHz (Figs. 3.12(e,f)). For $d = 20\,\mu$m, which corresponds to a stronger coupling situation ($C = 0.8$), the anti-phase response strongly dominates over the in-phase response for frequencies lower than anti-phase cut-off frequency (1 MHz), but the in-phase response always dominates for higher frequencies (Fig. 3.13(c)). Consequently, the correlation phase is π for frequencies lower than 1 MHz but 0 for higher frequencies (Fig. 3.12(i)). Moreover, the phase jump at about 1 MHz (Fig. 3.12(i)) due to the transition of the laser dynamics from dominant anti-phase to in-phase behavior gives rise to the dip in the correlation amplitude (Fig. 3.12(h)) as the fluctuations of nearly identical amplitudes of the two modes interfere destructively. These spectral behaviors of the intensity noises and their correlations are exactly identical to

the spectra obtained from experiments and the simple theoretical model as described in Chapter 2 (1.55 μm DF-VECSEL) and in Appendix B.

3.8 Conclusion

In this chapter, we have developed a rate equation model taking the spin dynamics of the carriers into account in order to predict the different properties of a dual-frequency VECSELs sustaining simultaneous oscillation of two linear orthogonal polarization modes. Specifically, we have shown how the relative value of the spin relaxation rate of the carriers with respect to the carrier decay rate inside the QW-based gain medium determines the dynamics of the dual-frequency VECSEL. Moreover, this model has achieved great success in describing the steady-state and transient behaviors of the laser for both class-A and class-B dynamics. Another important achievement of this model has been to derive an analytical expression for the nonlinear coupling between the two modes showing how the coupling depends on the degree of spatial overlap between the modes and the spin-relaxation of the carriers for our DF-VECSEL. In addition to that, the properties of the intensity noises and their correlations have also been successfully reproduced by this model. Furthermore, this theoretical approach to the dual-frequency VECSEL, based on the ideas of SFM model, generalizes the previous simple heuristic model, described in Chapter 2. In addition to that, the present model has predicted a few properties of dual-frequency VECSELs such as the possible existence of bistability of the two modes and unequal values of the ratios of cross- to self-saturation coefficients, which could not be explained by the simple model. Moreover, it has opened interesting perspectives concerning the laser dynamics when the frequency difference between the two modes becomes too slow to be averaged out, leading to possible self-pulsing [Brunel et al., 1999a,b] and other dynamical phenomena such as chaos [Virte et al., 2013b,a].

The main results of this chapter are summarized in the following table:

- Development of an improved rate equation model for DF-VECSELs taking into account the spin dynamics of the carriers.
- Analyzing the importance of the relative value of the spin-relaxation rate of the carriers with respect to carriers' decay rate inside the QW-based active medium to determine the laser dynamics.
- Successful description of the steady-state and transient behaviors of the laser for both class-A and class-B dynamics by the present model.
- Explanation regarding the unequal values of the ratios of cross- to self-saturation coefficients, which was not possible by the simple model.
- Finding analytical expressions for the ratios of the cross- to self-saturation coefficients, and hence the nonlinear coupling constant between the two modes.
- Reproduction of the properties of the intensity noises and their correlations with great success by this developed model.
- Generalization of the previous simple heuristic model, described in Chapter 2.
- Predictions concerning possible existence of bistability, chaos in DF-VECSELs.

Part II

Experimental and Theoretical Analysis of Noise in Dual-Frequency Nd:YAG Lasers

Chapter 4

Intensity noise correlations in dual-frequency Nd:YAG lasers

Contents

4.1 Introduction

In the first part of this thesis, we have explored different noise properties of dual-frequency VECSELs, which are emerging as a key building block for numerous microwave photonics applications. The DF-VECSELs, sustaining simultaneous oscillation of two linear-orthogonal polarizations with a frequency difference lying in the RF range, are based on quantum-well based active medium. In Chapter 2, we have analyzed the spectral behaviors of the following phenomena in a DF-VECSEL: (i) intensity noises of the two laser modes and the correlation between these noises, (ii) the RF beatnote generated by optical mixing of the two laser modes and the phase noise of the RF beatnote, and (iii) the correlation between the phase noise of the RF beatnote with the intensity noises of the two laser modes, which generate the RF beatnote via optical mixing. It has been found that the spectral behaviors of all these noises and their correlations strongly depend on several factors such as the nonlinear coupling between the two laser modes, the spectral behaviors of the pump noises and their correlations, and finally the class-A dynamical behavior of the DF-VECSEL. On the other hand, dual-frequency oscillation has also been realized in several solid-state lasers [Brunel et al., 1997; Alouini et al., 1998; Czarny et al., 2004]. Obviously, there are some differences between the gain mechanisms in the solid-state lasers and the semiconductor lasers such as VECSELs. More importantly, solid-state lasers exhibits class-B dynamics, whereas VECSELs obey class-A dynamical behavior as shown previously. The class-B dynamical behavior of the solid-state lasers is linked with the fact that the population inversion lifetime (few hundreds of microseconds) in solid-state active medium is typically much longer than the photon lifetime (few nanoseconds) inside the few centimeter-long cavity. Because of this class-B dynamics, the noise properties of solid-state lasers largely differ from the class-A VECSELs. The most significant difference is the presence of a resonant peak in the intensity noise spectrum of the solid-state lasers at low frequencies i.e., from a few kilohertz to a few megahertz, due to relaxation oscillations [Taccheo et al., 1996; Alouini et al., 2001]. This is a huge drawback compared to the class-A laser like VECSEL, in which the intensity noise spectrum is analogous to a first-order function as demonstrated previously. Moreover, for a dual-frequency solid-state laser, which sustains simultaneous oscillation of two perpendicularly polarized modes inside the cavity, the situation is even worse. Then, each laser mode exhibits two peaks in its intensity noise spectrum. The first one is linked with the well known in-phase (stan-

dard) relaxation oscillation, for which the intensities of the two mode relax in phase. The second one, which is inherent to all coupled oscillator systems, corresponds to the anti-phase relaxation regime of the intensities of the two eigenstates [Otsuka et al., 1992]. This causes severe degradation of the intensity noise properties of dual-frequency solid-state laser, and limits its use for microwave photonics applications [Alouini et al., 2001; Pillet et al., 2008]. Additionally, these relaxation mechanisms deteriorate the spectral purity of the RF beatnote, generated by optically mixing the two laser modes of the dual-frequency solid-state lasers. This is also a notable disadvantage of a dual-frequency solid-state laser compared to its class-A counterpart like a dual-frequency VECSEL.

However, in a dual-frequency VECSEL, because of its semiconductor active medium, the phase noises of the two oscillating modes are coupled with the intensity noises of these modes via the $\alpha-$factor [Henry, 1982]. This is why it was important to understand and control the correlations between the intensity noises of the two modes in such a dual-frequency VECSEL as described in Chapter 2. On the contrary, the value of the $\alpha-$factor is usually very small in solid-state lasers, leading to a negligible phase/intensity coupling. In spite of that, a complete understanding of the noise characteristics of such dual-frequency solid-state lasers is highly desirable. In all cases, as far as the addressed application requires the use of the two laser modes (atomic clock [Knappe et al., 2007; Vanier, 2005], pump-probe experiments, metrology [Nerin et al., 1997; Du et al., 2005], etc...), the degree of intensity noise correlation between the two modes must be known precisely. This explains why it is also important to explore the correlations between the intensity noises of the two modes of a dual-frequency solid-state laser.

The aim of this chapter is therefore to investigate the intensity noise correlation behavior for a dual-frequency solid-state laser, specifically a dual-frequency Nd:YAG laser [De et al., 2013a]. In particular, the main interest here is to analyze how the presence of the relaxation oscillation peaks in the intensity noise spectra of a class-B dual-frequency Nd:YAG laser modifies the spectral behavior of the noise correlation compared to the class-A DF-VECSEL. In the present chapter, we thus investigate, both experimentally and theoretically, the relative intensity noise (RIN) spectra and also the correlation between the intensity noises of the two lasing modes for different coupling situations in the same spirit as demonstrated for dual-frequency VECSEL in Chapter 2. The present chapter is organized as follows: in section 4.2, we remind the spectroscopic properties of Nd:YAG active medium and the cavity configuration of the dual-frequency laser based

on Nd:YAG gain medium. In Sec. 4.3, we develop a theoretical model, based on the assumption that the emitting dipoles behave as if they are aligned along the crystallographic axes of the gain medium [Schwartz et al., 2009]. Moreover, in the model we consider that the intensity noise of the pump laser is the dominant source of noise in the frequency range of 0-120 kHz, where the laser intensity noise is well above shot noise. This is subsequently verified by experiment. In Sec. 4.4, we give a detailed description of the experimental setup aiming at measuring the intensity noise correlation between the two orthogonally polarized modes of the dual-frequency Nd:YAG laser. Thereafter, we provide a comparative analysis between the intensity noise correlation spectra as obtained from the experiment and predicted by the theoretical model. Then, we try to give a physical insight for further comprehension.

4.2 Description of dual-frequency Nd:YAG laser

Before going into analyzing the noise properties of a dual-frequency Nd:YAG laser, in this section we provide a brief description of the key elements inside the laser. We start by reminding the spectroscopic properties of the Nd:YAG active medium.

4.2.1 Nd:YAG gain-medium

Neodymium-doped yttrium aluminum garnet, abbreviated as Nd:YAG, is one of the preferred active medium for building a laser. In Nd:YAG, the Nd^{3+} ion replaces the Y^{3+} ion of the host YAG ($Y_3Al_5O_{12}$). The size of the Nd^{+3} (98 pm) is greater than the size of the Y^{+3} (90 pm), limiting the doping of Nd^{+3} to less than 1.5% without undue straining of the crystal. It is worth mentioning that a 1% concentration of Nd^{+3} corresponds to a density of $1.386 \times 10^{20}\,cm^{-3}$. The electronic configuration of the trivalent neodymium ion reads as $Nd^{3+} : [Xe]4f^3 5s^2 5p^6$, where [Xe] represents the ground state configuration of xenon. The fluorescence spectra of neodymium ions arise from the electronic transitions between the energy levels of the partially filled $4f$ shell. One key feature of the trivalent rare-earth ions (Nd^{3+}) in crystalline host media (YAG) is that the partially filled $4f$ states are well-shielded by fully occupied 5s and 5p shells. The interaction with the field of the host-crystal is therefore weak leading to a series of manifolds that are slightly perturbed from those of the free ion. However, it is important to note that the optical cross-sections

of the transitions may vary significantly. In Nd:YAG, there exist several closely spaced manifolds above the metastable $^4F_{3/2}$ manifold which are separated by energies less than the maximum phonon energy ($850\,cm^{-1}$) in YAG. These manifolds provide a broad absorption band, ideal for optical pumping. Once the ions are optically pumped to this broad band, they can rapidly cascade down via non-radiative transitions and end up being in the metastable $^4F_{3/2}$ manifold. The decay rate of $^4F_{3/2}$ is very slow as it is not coupled to the lower ^4I manifolds by phonon vibrations. It can only decay by radiative transitions to the ^4I manifolds, leading to a long fluorescent lifetime around $230\,\mu s$. On the other hand, the levels of the ^4I manifolds are separated by energies less than the maximum phonon energy leading to a very short lifetime (in the order of 100 ps) of these levels as they are coupled by non-radiative transitions. This shows that the energy level structure of Nd:YAG is ideal for laser oscillation. In Nd:YAG, lasing has been obtained for several wavelengths centered at about 0.9 μ m, 1.06 μ m, and 1.35 μ m corresponding to transitions from $^4F_{3/2}$ manifold to $^4I_{13/2}$, $^4I_{11/2}$, and $^4I_{9/2}$ manifolds, respectively. However, the most common and the strongest one, used for our experiment too, is the transition between $^4F_{3/2}$ and $^4I_{11/2}$, centered at 1064 nm wavelength. The energy level scheme of this lasing transition can be simply modeled as a four-level model like in Fig. 4.1 [Hooker and Webb, 2010]. As

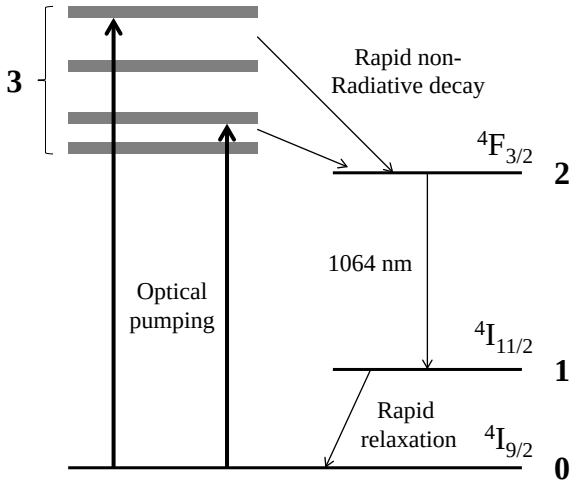

Figure 4.1: Simplified energy level diagram of Nd:YAG for $^4F_{3/2}$ to $^4I_{11/2}$ laser transition.

one can notice in Fig. 4.1 that the $^4F_{3/2}$ meta-stable manifold (**2**) can be populated by rapid non-radiative transitions from the broad pump band (**3**), while the $^4I_{11/2}$ (**1**) manifold acting as the lower laser level decays very rapidly to the $^4I_{9/2}$ manifold (**0**), which

is the ground level. The laser emission between $^4F_{3/2}$ and $^4I_{11/2}$ manifolds includes two transitions: (i) from the upper doublet of $^4F_{3/2}$ to the Y_3 level of $^4I_{11/2}$ centered at 1064.15 nm (R2 line), and (ii) from the lower doublet of $^4F_{3/2}$ to the Y_2 level of $^4I_{11/2}$ centered at 1064.4 nm (R1 line). At room temperature and for low pumping rates the R1 line contributes very little to the overall gain, and hence in our case we mostly deal with the R2 transition. At room temperature, the R2 line is homogeneously broadened by phonon collisions leading to a full-width at half-maximum bandwidth of approximately 190 GHz.

4.2.2 Cavity design for dual-frequency oscillation

Figure 4.2(a) shows the architecture of the laser cavity[1]. The cavity sustains simultaneous oscillation of **x**− and **y**-polarized modes having a frequency difference in the RF range. The laser is based on a ⟨100⟩-cut Nd:YAG crystal. The ⟨100⟩-cut crystal leads to the fact that ⟨010⟩ and ⟨001⟩ crystal axes lie in the transverse plane of the cavity, whereas the ⟨100⟩ axis corresponds to the light propagation direction inside the cavity. The reason behind this particular choice of crystal-cut will be clarified afterwords. The laser cavity is

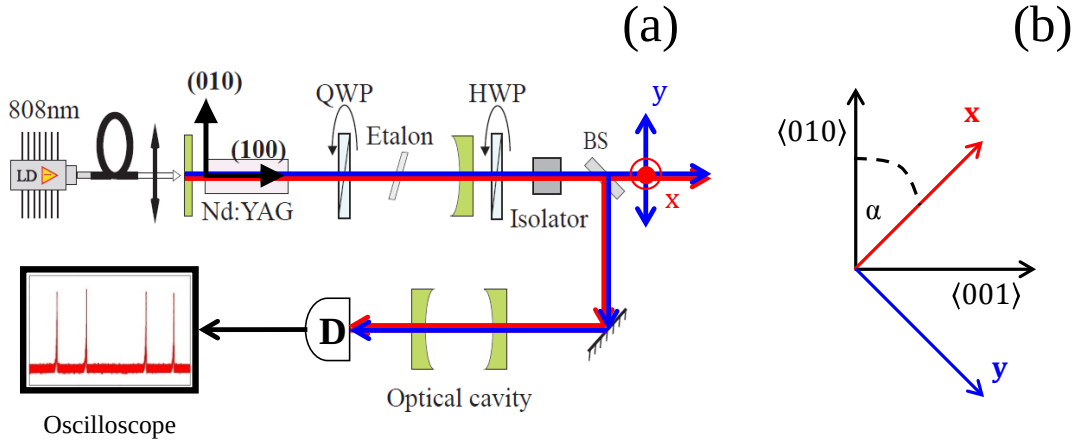

Figure 4.2: (a) Schematic representation of the cavity configuration; LD: laser diode; QWP: quarter-wave plate; HWP: half-wave plate; BS: beam splitter; PBS: polarization beam splitter. (b) Orientations of the two eigen-polarizations, **x** and **y**, with respect to the crystallographic axes ⟨010⟩ and ⟨001⟩.

[1]This experiment was performed in Institut de Physique de Rennes together with Abdelkrim El Amili, Goulc'hen Loas, and Mehdi Alouini.

a linear one of 9-cm length, and it is closed by a planar and a concave mirror. The planar mirror has a maximum reflection at 1.064 μm, and it transmits the pump wavelength. The concave mirror, acting as the output coupler, has a transmission of 2 % at 1.064 μm and a radius of curvature of 10 cm. We introduce a quarter-wave plate (QWP) inside the cavity to lift the polarization degeneracy. Because the Nd:YAG active medium is optically isotropic, the two eigenpolarizations are linear and aligned along the directions $\mathbf{x}$ and $\mathbf{y}$ of the neutral axes of the QWP. Therefore, to change the orientations of the eigenpolarizations one simply needs to rotate the QWP. To this aim, the QWP is placed on a precise rotation mount. This permits to adjust the angle α between the eigenpolarization directions and the transverse crystallographic axes (Fig. 4.2(b)), and hence enables us to assign different nonlinear coupling between the two modes [Schwartz et al., 2009]. We will subsequently elaborate this point. The Nd:YAG crystal is 2-cm long, and it is placed inside a copper mount to limit thermally induced birefringence. The crystallographic axes of the Nd:YAG are precisely determined by x-ray diffraction. The pumping is provided by a continuous wave (CW) multimode fiber-coupled laser diode, operating at 808 nm and delivering 300 mW of optical power. The dual-frequency laser is operating at 1.064 μm and its total output power is about 20 mW. We have checked that the pump beam is unpolarized, avoiding any unwanted pump-induced gain anisotropy. The free spectral range (FSR) of the laser cavity is about 1.67 GHz, which is much smaller than the gain bandwidth ($\sim$190 GHz). This leads to multi-longitudinal mode oscillation of each eigenpolarization. To force single longitudinal mode oscillation of each polarization state, we place a 1 mm-thick uncoated YAG etalon inside the cavity. The laser spectrum is continuously analyzed with a scanning Fabry-Perot interferometer to make sure that each eigenpolarization always oscillates in single-frequency regime without any mode hopping during data acquisition.

Before presenting the experimental results, we introduce a theoretical model to properly describe the noise properties of our dual-frequency Nd:YAG laser.

4.3 Theoretical model

In this section, our aim is to develop a theoretical model to assess how the intensity noise of the pump laser, which acts as the dominant source of noise in the considered frequency range (0-120 kHz), is transferred to the intensity noises of the two orthogonally polar-

ized modes of our dual-frequency Nd:YAG laser. In Chapter 2, we have shown that the noise properties of a dual-frequency VECSEL can be very well explained by a rate equation based theoretical model. We follow the same footsteps here for the dual-frequency Nd:YAG laser. To this aim, we first need to write suitable rate equations explaining the laser dynamics. In solid-state active media like Nd:YAG, the main difficulty arises from the fact that the transition dipoles typically have certain preferred orientations depending on the symmetry of the crystalline site. Therefore, the polarization direction of the light also becomes important, and hence one needs to consider the vector nature of the light-matter interaction. To clarify this further, we start by reminding the standard semiclassical description of a laser, in which the light is treated classically but the matter is described quantum mechanically. According to this semiclassical formalism, the transition electric-dipole is usually modeled by a quantum mechanical operator $\hat{\mathbf{d}}$. Since the dipoles in Nd:YAG crystal typically have a specified orientation, the dipole operator $\hat{\mathbf{d}}$ can be expressed as $\hat{\mathbf{d}} = \hat{d}\mathbf{u}$, where $\mathbf{u}$ is the unit vector along the direction of the electric-dipole. On the other hand, light is described classically with a linearly polarized electric field $\mathbf{E} = E\mathbf{v}$, where $\mathbf{v}$ is the unit vector parallel to the electric field. Then, the interaction between the dipole $\hat{\mathbf{d}}$ and the electric field $\mathbf{E}$ can be described by the electric-dipole Hamiltonian $\hat{H}_I = -\hat{\mathbf{d}}.\mathbf{E}$. As a result, in the rate equations for the intra-cavity photon number F and the population inversion number N of a single mode laser, the dipolar interaction terms can be expressed as follows [Schwartz et al., 2009; Siegman, 1986]

$$\left.\frac{dF}{dt}\right|_{\mathrm{I}} = \kappa N F \cos^2(\widehat{\mathbf{v},\mathbf{u}}) \ , \tag{4.1}$$

$$\left.\frac{dN}{dt}\right|_{\mathrm{I}} = -\kappa N F \cos^2(\widehat{\mathbf{v},\mathbf{u}}) \ , \tag{4.2}$$

where κ is the stimulated emission coefficient. It is worth mentioning that to obtain the above rate equations we have assumed that the atomic polarization lifetime is much shorter than the photon lifetime (γ_{cav}^{-1}) inside the cavity and the population inversion lifetime (Γ^{-1}). Consequently, the complete rate equations for F and N can be written as

$$\frac{dF}{dt} = -\gamma_{cav} F + \kappa N F \cos^2(\widehat{\mathbf{v},\mathbf{u}}) \ , \tag{4.3}$$

$$\frac{dN}{dt} = -\Gamma(N - N_0) - \kappa N F \cos^2(\widehat{\mathbf{v},\mathbf{u}}) \ , \tag{4.4}$$

where N_0 stands for the unsaturated population inversion number as ΓN_0 is the pumping rate. In the following, we will extend this single mode rate equation model to the two-mode situation.

As one can notice in Eqs. (4.1-4.4), the dipolar interaction strength depends on the relative orientations of the transition dipoles and the laser field. Therefore, to model the rate equations of a solid-state laser, one must have the precise knowledge about the dipole orientations in the active medium. It has been found that the crystal symmetry plays a significant role to determine the dipole orientations in saturable absorbers based on YAG-host such as Cr : YAG [Eilers et al., 1992; Brignon, 1996; Brunel et al., 1999c], Tm : YAG [Greiner et al., 1999], etc. However, the link between the dipole orientations and crystal symmetry in Nd:YAG crystal is still a point to debate. On the one hand, as described in [Schwartz et al., 2009], the light emitting dipoles in Nd:YAG behave as if they were aligned along the crystallographic axes. On the other hand, there are several studies suggesting more complex dipole orientations in Nd:YAG crystal [Lukac et al., 1992; Kravtsov et al., 2004; McKay et al., 2007]. To model our dual-frequency Nd:YAG laser, we follow the simple formalism of [Schwartz et al., 2009]. In the following, we redevelop the rate equations for our dual-frequency Nd:YAG laser as done in [Schwartz et al., 2009]. Thus, the transition dipoles are assumed to be oriented along the three crystallographic axes ($\mathbf{u_1}$,$\mathbf{u_2}$,$\mathbf{u_3}$) and associated with population inversions N_1, N_2 and N_3, respectively (Fig. 4.3(a)). Our dual-frequency laser is based on $\langle 100 \rangle$-cut Nd:YAG crystal. This leads to the fact that the wave vectors ($\mathbf{k}$) of both $\mathbf{x}$- and $\mathbf{y}$-polarized mode are aligned along one of the three crystallographic axes (say, $\mathbf{u_3}$), whereas the other two crystallographic axes ($\mathbf{u_1}$, and $\mathbf{u_2}$) are lying in the same plane as the two polarizations (Fig. 4.3(b)). This ensures that the dipoles aligned along $\mathbf{u_3}$ do not take part in the lasing transitions, and hence N_3 can be discarded from the laser rate equations. In this configuration, the two eigenpolarizations can be defined as

$$\mathbf{x} = \begin{pmatrix} \cos\alpha \\ \sin\alpha \\ 0 \end{pmatrix} \ , \ \mathbf{y} = \begin{pmatrix} -\sin\alpha \\ \cos\alpha \\ 0 \end{pmatrix} \tag{4.5}$$

where the coordinates have been written in the basis ($\mathbf{u_1}$,$\mathbf{u_2}$,$\mathbf{u_3}$) of the crystallographic axes. The two eigenpolarizations, $\mathbf{x}$ and $\mathbf{y}$, make angle α with crystal axes $\mathbf{u_1}$ and $\mathbf{u_2}$,

respectively (Fig. 4.3(b)). Therefore, Eqs. (4.3-4.4) for a single mode laser can be extended

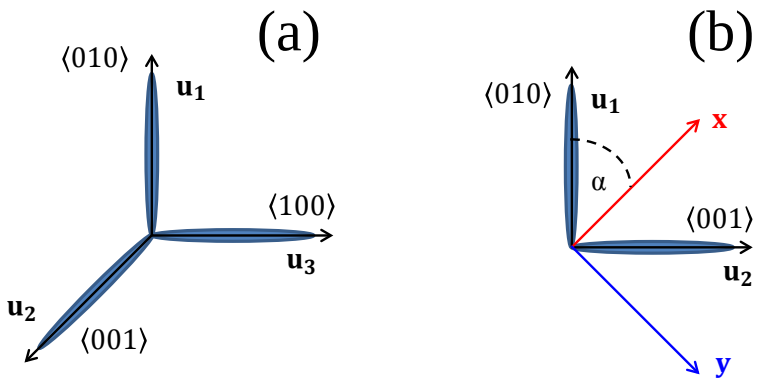

Figure 4.3: (a) Schematic representation of the crystallographic axes ($\mathbf{u_1}$, $\mathbf{u_2}$, $\mathbf{u_3}$) and the orientation of the dipoles of a ⟨100⟩-cut Nd:YAG crystal; (b) Orientation of the eigenpolarizations $\mathbf{x}$, and $\mathbf{y}$ with respect to the crystallographic axes $\mathbf{u_1}$, and $\mathbf{u_2}$.

to our dual-frequency laser as follows:

$$\frac{dF_x}{dt} = -\gamma_x F_x + \kappa F_x[N_1 \cos^2\alpha + N_2 \sin^2\alpha] \ , \tag{4.6}$$

$$\frac{dF_y}{dt} = -\gamma_y F_y + \kappa F_y[N_2 \cos^2\alpha + N_1 \sin^2\alpha] \ , \tag{4.7}$$

$$\frac{dN_1}{dt} = \Gamma(N_{01} - N_1) - \kappa N_1[F_x \cos^2\alpha + F_y \sin^2\alpha] \ , \tag{4.8}$$

$$\frac{dN_2}{dt} = \Gamma(N_{02} - N_2) - \kappa N_2[F_y \cos^2\alpha + F_x \sin^2\alpha] \ , \tag{4.9}$$

where F_x, F_y denote the intracavity photon numbers for $\mathbf{x}-$ and $\mathbf{y}-$polarized mode, respectively. We assume that the stimulated emission coefficient κ is identical for the two modes. γ_x, γ_y are the cavity decay rates (inverse of photon lifetimes, τ_x and τ_y, respectively) for the two modes, which we suppose to be different as in our experiment the two modes experience slightly different losses. Γ stands for the inverse of the population inversion lifetime τ as previously. We consider different pumping rates, N_{01}/τ and N_{02}/τ, for the two families of dipoles. As done in [Schwartz et al., 2009] to better fit the nonlinear coupling measurements, we phenomenologically introduce a small dipole ellipcity $\beta \ll 1$ in the model (Fig. 4.3). This leads to the following modified version of the rate equations

of the dual-frequency Nd:YAG laser:

$$\frac{dF_x}{dt} = -\gamma_x F_x + \kappa F_x \left[N_1(\cos^2\alpha + \beta\sin^2\alpha) + N_2(\sin^2\alpha + \beta\cos^2\alpha)\right] , \quad (4.10)$$

$$\frac{dF_y}{dt} = -\gamma_y F_y + \kappa F_y \left[N_2(\cos^2\alpha + \beta\sin^2\alpha) + N_1(\sin^2\alpha + \beta\cos^2\alpha)\right] , \quad (4.11)$$

$$\frac{dN_1}{dt} = \Gamma(N_{01} - N_1) - \kappa N_1 \left[F_x(\cos^2\alpha + \beta\sin^2\alpha) + F_y(\sin^2\alpha + \beta\cos^2\alpha)\right] , \quad (4.12)$$

$$\frac{dN_2}{dt} = \Gamma(N_{02} - N_2) - \kappa N_2 \left[F_y(\cos^2\alpha + \beta\sin^2\alpha) + F_x(\sin^2\alpha + \beta\cos^2\alpha)\right] . \quad (4.13)$$

Here, β takes into account the possible coupling between different dipole families aligned along different crystal axes. One possible reason behind the origin of β is the arbitrary orientations of the neodymium ions residing in the defect sites of the host YAG matrix that may induce energy transfer between dipoles from different intrinsic crystal sites. It is worth mentioning that in Eqs. (4.10-4.13), we have neglected the role of N_3 as it would only give terms of the order of β^2 or smaller. We rewrite Eqs. (4.10-4.13) as

$$\frac{dF_x}{dt} = -\gamma_x F_x + \kappa F_x \left[N_1 A + N_2 B\right] , \quad (4.14)$$

$$\frac{dF_y}{dt} = -\gamma_y F_y + \kappa F_y \left[N_2 A + N_1 B\right] , \quad (4.15)$$

$$\frac{dN_1}{dt} = \Gamma(N_{01} - N_1) - \kappa N_1 \left[F_x A + F_y B\right] , \quad (4.16)$$

$$\frac{dN_2}{dt} = \Gamma(N_{02} - N_2) - \kappa N_2 \left[F_y A + F_x B\right] , \quad (4.17)$$

where the coefficients A and B read

$$A = \cos^2\alpha + \beta\sin^2\alpha , \quad (4.18)$$

$$B = \sin^2\alpha + \beta\cos^2\alpha . \quad (4.19)$$

Therefore, the A and B coefficients simply determine the strengths of the interaction of the two eigenpolarizations with the two dipole families aligned along the two crystal axes of the $\langle 100\rangle$-cut Nd:YAG. This leads to the following expression for the nonlinear coupling

constant (C) (Appendix E):

$$C = \frac{4A^2B^2}{(A^2+B^2)^2} . \tag{4.20}$$

Equation (4.20) indicates that the nonlinear coupling strength between the two modes of the dual-frequency Nd:YAG laser can be changed simply by changing the angle α between the eigenpolarizations and the transverse crystallographic axes (Fig. 4.3(b)). In our laser architecture as schematized in Fig. 4.2, the choice of $\langle 100 \rangle$-cut crystal along with the intra-cavity QWP permits us to change α simply by rotating the QWP, which defines the directions of the eigenpolarizations. More importantly, this configuration may even lead to nearly complete decoupling of the two modes by aligning them along the two transverse crystallographic axes i.e. by making $\alpha = 0$, hence assigning two almost independent sets of dipoles for the two eigenpolarizations. The utility of this will be stressed in the next chapter. Among the steady-state solutions of Eqs. (4.14-4.17), the one corresponding to the simultaneous oscillation of the two orthogonally polarized modes is given as:

$$F_x \equiv F_{x0} = \frac{\Gamma[A(r_1-1)-B(r_2-1)]}{\kappa(A^2-B^2)} , \tag{4.21}$$

$$F_y \equiv F_{y0} = \frac{\Gamma[A(r_2-1)-B(r_1-1)]}{\kappa(A^2-B^2)} , \tag{4.22}$$

$$N_1 \equiv N_{1\text{th}} = \frac{(A\gamma_x - B\gamma_y)}{\kappa(A^2-B^2)} , \tag{4.23}$$

$$N_2 \equiv N_{2\text{th}} = \frac{(A\gamma_y - B\gamma_x)}{\kappa(A^2-B^2)} , \tag{4.24}$$

where $r_1 = N_{01}/N_{1\text{th}}$ and $r_2 = N_{02}/N_{2\text{th}}$ are defined as the standard excitation ratios of a usual single-mode laser, although in this case none of them can be attributed to one mode only.

Our aim is now to calculate the fluctuations of F_x and F_y around the corresponding steady-state values. In our dual-frequency Nd:YAG laser, the dominant source of noise is the intensity noise of the pump diode laser. We model the pump fluctuations for the two dipole families as following

$$N_{01}(t) = \overline{N}_{01} + \delta N_{01}(t) , \tag{4.25}$$

$$N_{02}(t) = \overline{N}_{02} + \delta N_{02}(t) \ . \tag{4.26}$$

Because of the pumping fluctuations, the population inversions corresponding to the two dipole families and the number of photons in the two laser modes fluctuate around their steady-state values [Eqs. (4.21-4.24)], which we model as

$$F_x(t) = F_{x0} + \delta F_x(t) \ , \tag{4.27}$$
$$F_y(t) = F_{y0} + \delta F_y(t) \ , \tag{4.28}$$
$$N_1(t) = N_{1\mathrm{th}} + \delta N_1(t) \ , \tag{4.29}$$
$$N_2(t) = N_{2\mathrm{th}} + \delta N_2(t) \ . \tag{4.30}$$

Now, substituting Eqs. (4.25-4.30) into Eqs. (4.14-4.17), and then performing Fourier transformation after linearization, we obtain the following expression relating the fluctuations of the photon numbers $[\widetilde{\delta F}_x(f),\ \widetilde{\delta F}_y(f)]$ of the two lasing modes to the two pump fluctuations $[\widetilde{\delta N}_{01}(f),\ \widetilde{\delta N}_{02}(f)]$ in the frequency domain:

$$\begin{bmatrix} \widetilde{\delta F}_x(f) \\ \widetilde{\delta F}_y(f) \end{bmatrix} = \begin{bmatrix} M_{11}(f) & M_{12}(f) \\ M_{21}(f) & M_{22}(f) \end{bmatrix} \begin{bmatrix} \widetilde{\delta N}_{01}(f) \\ \widetilde{\delta N}_{02}(f) \end{bmatrix} \ , \tag{4.31}$$

where the tilde $\tilde{}$ denotes Fourier transformed quantities and f corresponds to the frequency of the considered spectral component of the fluctuations. The coefficients of the linear response transfer matrix of Eq. (4.31) are given by

$$M_{11}(f) = \frac{A(A^2-B^2)\Gamma\left[(A\gamma_y - B\gamma_x) - \frac{2i\pi f}{\kappa F_{y0}}(r_2\Gamma - 2i\pi f)\right]}{\Delta} \ , \tag{4.32}$$
$$M_{12}(f) = -\frac{B(A^2-B^2)\Gamma\left[(A\gamma_x - B\gamma_y) + \frac{2i\pi f}{\kappa F_{y0}}(r_1\Gamma - 2i\pi f)\right]}{\Delta} \ , \tag{4.33}$$
$$M_{21}(f) = -\frac{B(A^2-B^2)\Gamma\left[(A\gamma_y - B\gamma_x) + \frac{2i\pi f}{\kappa F_{x0}}(r_2\Gamma - 2i\pi f)\right]}{\Delta} \ , \tag{4.34}$$
$$M_{22}(f) = \frac{A(A^2-B^2)\Gamma\left[(A\gamma_x - B\gamma_y) - \frac{2i\pi f}{\kappa F_{x0}}(r_1\Gamma - 2i\pi f)\right]}{\Delta} \ , \tag{4.35}$$

where the denominator Δ of these matrix elements reads

$$\begin{aligned}\Delta &= A^2\left[(A\gamma_x - B\gamma_y) - \frac{2i\pi f}{\kappa F_{x0}}(r_1\Gamma - 2i\pi f)\right]\left[(A\gamma_y - B\gamma_x) - \frac{2i\pi f}{\kappa F_{y0}}(r_2\Gamma - 2i\pi f)\right] \\ &\quad -B^2\left[(A\gamma_x - B\gamma_y) + \frac{2i\pi f}{\kappa F_{y0}}(r_1\Gamma - 2i\pi f)\right]\left[(A\gamma_y - B\gamma_x) + \frac{2i\pi f}{\kappa F_{x0}}(r_2\Gamma - 2i\pi f)\right] .\end{aligned} \tag{4.36}$$

In our dual-frequency Nd:YAG laser, the pumping is done by a multimode fiber-coupled diode laser, leading to an unpolarized pump beam. Therefore, we consider that the pump fluctuations for two dipole families are white noises of identical amplitude as

$$\left\langle \left|\widetilde{\delta N}_{01}(f)\right|^2 \right\rangle = \left\langle \left|\widetilde{\delta N}_{02}(f)\right|^2 \right\rangle = \left\langle \left|\widetilde{\delta N}_{0}\right|^2 \right\rangle . \tag{4.37}$$

Therefore, the pump relative intensity noise (RIN) for the two dipole families can be expressed as

$$\mathrm{RIN}_{Pump} = \frac{\left\langle \left|\widetilde{\delta N}_{0}\right|^2 \right\rangle}{\overline{N}_0^2} , \tag{4.38}$$

where we consider $\overline{N}_{0x} \equiv \overline{N}_{0y} = \overline{N}_0$. This assumption of identical pump RINs for the two dipole families as defined in Eq (4.38) are verified by experiment, which will be reported afterwards. Moreover, we assume that the pump fluctuations for the two dipole families are partially correlated with a correlation amplitude $0 < \eta < 1$ and a correlation phase $\psi = 0$. Thus, the pump noise correlation spectrum reads

$$\left\langle \widetilde{\delta N}_{01}(f)\widetilde{\delta N}^*_{02}(f) \right\rangle = \eta \left\langle \left|\widetilde{\delta N}_{0}\right|^2 \right\rangle e^{i\psi} . \tag{4.39}$$

Finally, the RINs for the two modes and the intensity noise correlation spectrum of the dual-frequency Nd:YAG laser can be obtained from the definitions respectively given in Eqs. (2.3-2.4), and Eq. (2.7) of Chapter 2.

In next section, we compare the predictions of the theoretical model developed here with the results obtained from the experiment.

4.4 Results: experiment and theory

We remind here that such noise correlation spectra have been already explored for the dual-frequency VECSEL in Chapter 2. However, the transient behaviors of the Nd:YAG laser and the VECSEL are significantly different, when the former is damped oscillatory, the latter one is exponentially damped due to their respective class-B and class-A dynamics. Therefore, it is interesting to visualize how this class-B dynamics of the dual-frequency Nd:YAG laser qualitatively modifies the intensity noise correlation spectrum compared to the class-A DF-VECSEL. To this aim, in this section, we report the experimental and theoretical results regarding the spectral behavior of the correlation between the intensity noises of the two cross-polarized modes of our dual-frequency Nd:YAG laser. We first describe the noise correlation measurement scheme.

4.4.1 Noise correlation measurement setup

The noise correlation measurement scheme for our dual-frequency Nd:YAG laser is presented in Fig. 4.4. To measure the correlation between the intensity noises of the two laser modes, they should be detected separately without mixing them. The two linear cross-polarized modes are separated using the combination of the half-wave plate ($\lambda/2$) followed by a polarization beam spliter (PBS). Then, the two modes are detected using

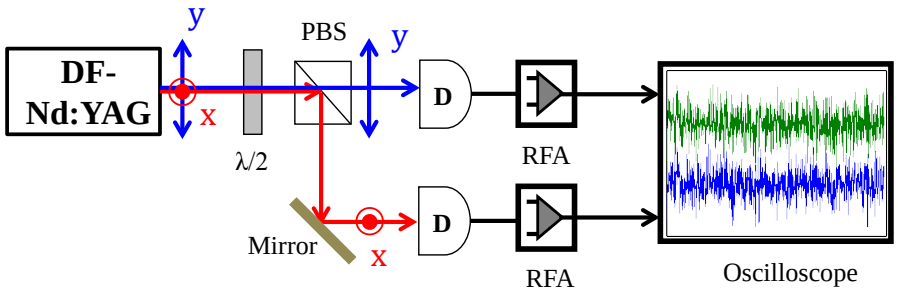

Figure 4.4: Schematic of the noise correlation measurement setup for dual-frequency Nd:YAG (DF-Nd:YAG) laser. $\lambda/2$: half-wave plate, PBS: polarization beam spliter, D: photodiode, RFA: RF amplifier.

fast photodiodes (D). We have used two identical InGaAs photodiodes (Epitaxx Inc, 3.7 MHz bandwidth) for the detection of the two modes. The detected signals are then amplified using identical low-noise homemade RF amplifiers (RFA). Thereafter, the amplified

signals are recorded in time domain by a deep memory digital oscilloscope. Finally, the oscilloscope data are numerically processed to obtain the RINs and the intensity noise correlation spectra. We repeat here that the main interest of this temporal measurement scheme is to measure the two intensity noises simultaneously, which is essential to analyze their correlation.

4.4.2 Intensity noise correlation

The nonlinear coupling between the modes, in addition to the laser dynamics class is expected to play a significant role to determine the spectral behavior of the noise correlation. In the experiment, different nonlinear coupling strengths have been achieved by changing α, the angle between the eigenpolarizations and the crystallographic axes as shown in Fig. 4.2(b). We have measured the RIN spectra and the noise correlation spectra for three different values of α, such as 20°, 30°, and 52°, which according to Eq. (4.20) correspond to $C \simeq 0.09$, $C \simeq 0.40$, and $C \simeq 0.75$, respectively.

The results for $\alpha = 20°$ corresponding to $C \simeq 0.09$ are shown in Fig. 4.5. The RIN spectra for both the laser modes, as obtained from the experiment (Fig. 4.5(a)), exhibit two relaxation oscillation peaks. The peak lying in the high frequency region of the noise spectra ($\sim$ 90 kHz) is due to the standard relaxation oscillation, whereas the low frequency peak ($\sim$ 50 kHz) is caused by the anti-phase relaxation oscillation (Fig. 4.5(a)). The presence of these relaxation oscillation peaks in the noise spectra illustrates the class-B dynamical behavior of our laser [McCumber, 1966]. The RIN spectra of $\mathbf{x}-$ and $\mathbf{y}-$polarized mode, respectively corresponding to red-squared-line and blue-circled-line in Fig. 4.5(a), are not exactly identical since in the experiment it is difficult to assign perfectly identical losses and/or gains for the two modes. The RIN spectra obtained from our theoretical model are displayed in Fig. 4.5(b). They show very good agreement with the experiment, except from the fact that the position of the anti-phase peak is at about 65 kHz in the theoretical RIN spectra (Fig. 4.5(b)), instead of at $\sim$ 50 kHz as obtained from the experiment (Fig. 4.5(a)). When one observes the experimental correlation amplitude spectrum (Fig. 4.5(c)), one can notice the presence of two dips at about 30 kHz and 55 kHz, respectively. In addition to that the correlation amplitude becomes maximum (close to 0 dB) at about 50 kHz, and it remains close to 0 dB for all frequencies higher than 70 kHz. The correlation amplitude is almost flat and equal to about -5 dB for fre-

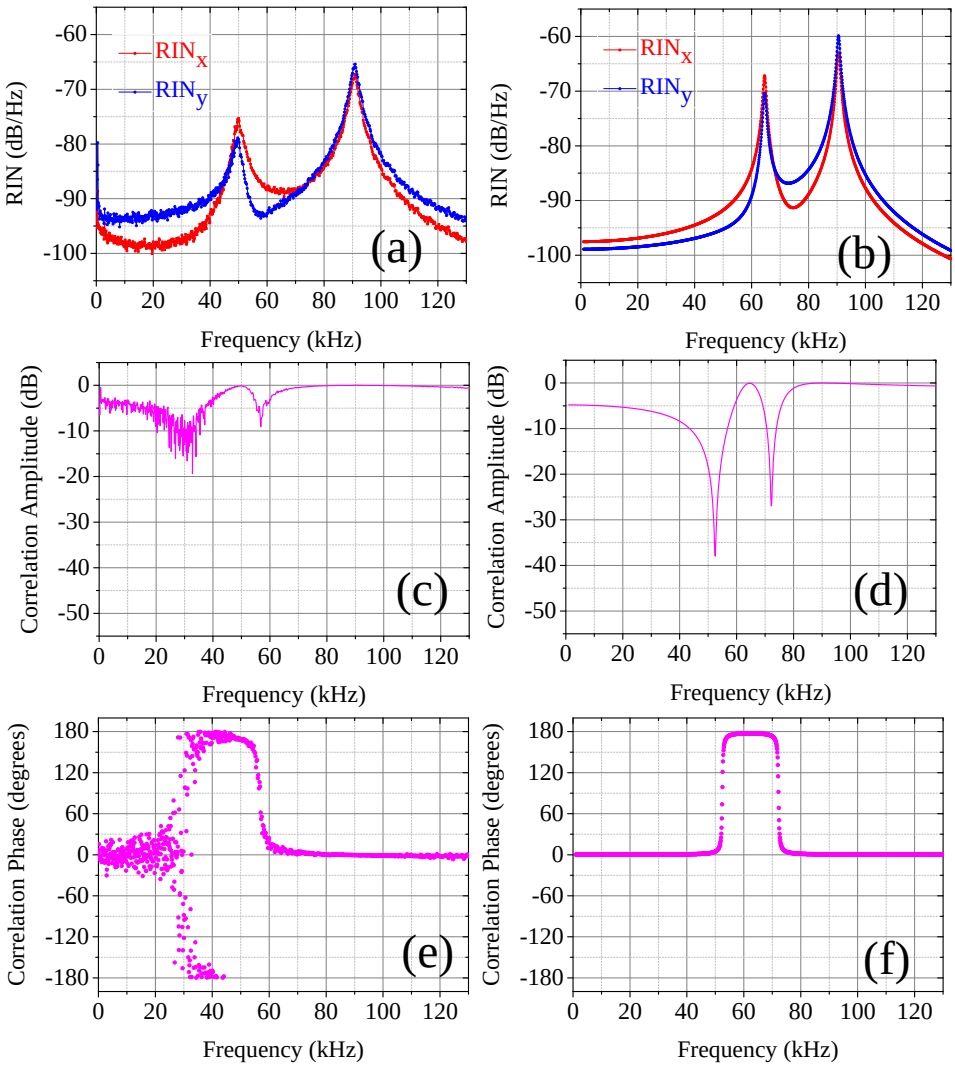

Figure 4.5: Results for $\alpha = 20°$, which corresponds to $C = 0.09$. RIN spectra: (a) experimental, and (b) theoretical; correlation amplitude spectra: (c) experimental and (d) theoretical; correlation phase spectra: (e) experimental and (f) theoretical. Parameter values used for simulations: $\beta = 0.025$, $r_1 = 1.35$, $r_2 = 1.4$, $\tau_x \simeq 5$ ns, $\tau_y \simeq 5.2$ ns, $\tau = 200$ μs, $\mathrm{RIN}_{Pump} = -110\,\mathrm{dB/Hz}$, $\eta = 0.75$, $\psi = 0$.

quencies lower than 20 kHz. The theoretical correlation amplitude spectrum is plotted in Fig. 4.5(d). It also predicts two dips, at about 50 kHz and 70 kHz, whereas the correlation amplitude reaches its maximum value (0 dB) between these dips and becomes maximum again at 80 kHz and above. It is also almost flat (at -5dB) for frequencies lower than 30 kHz. Hence, the theoretical correlation amplitude spectrum (Fig. 4.5(d)) exhibits nice

agreement with the experimental one (Fig. 4.5(c)). However, the positions of the dips in the theoretical correlation amplitude spectrum do not exactly match the experiment. Finally, the experimental correlation phase spectrum (Fig. 4.5(e)) exhibits two phase jumps: from zero to π at about 30 kHz and from π back to zero at about 55 kHz. Moreover, the correlation phase is zero for frequencies lower than 30 kHz and also for frequencies higher than 55 kHz, whereas it is π within 30 kHz to 55 kHz. The theoretical correlation phase spectrum (Fig. 4.5(f)) reproduces these two phase jumps, but again at slightly different frequencies (50 kHz, and 70 kHz, respectively) with respect to the experiment.

Figure 4.6 shows the results for $\alpha = 30°$, which leads to a coupling constant C equal to 0.4, according to Eq. (4.20). The experimental and theoretical RIN spectra for the two laser modes are presented in Figs. 4.6(a),(b), respectively. In the experimental RIN spectra (Fig. 4.6(a)), the in-phase peak occurs at ~ 90 kHz and the anti-phase peak is positioned at ~ 50 kHz. The RIN spectra for the two modes (red-squared line, blue-circled line) are again slightly different as their losses and/or gains are not identical. The theoretical RIN spectra, given in Fig. 4.6(b), is in good agreement with the experiment apart from the fact that the anti-phase peak appears at about 40 kHz (Fig. 4.6(b)), whereas experimentally we find it at about 50 kHz (Fig. 4.6(a)). The measured noise correlation amplitude and phase spectra are shown in Figs. 4.6(c),(e), respectively. There are two dips in the correlation amplitude spectrum at about 30 kHz and 60 kHz as reproduced in Fig. 4.6(c). Additionally, Fig. 4.6(c) also shows that the correlation amplitude reaches 0 dB once at about 50 kHz, and again at 70 kHz and maintains 0 dB value for all higher frequencies. Moreover, in the experimental correlation phase spectrum (Fig. 4.6(e)), one can observe two jumps, one from zero to π at about 30 kHz and the other one at about 60 kHz from π to zero. Furthermore, the correlation phase is zero for frequencies lower than 30 kHz and also for frequencies higher than 60 kHz, whereas it is π within $30 - 60$ kHz. The theoretical correlation amplitude and phase spectra, respectively reported in Figs. 4.6(d),(f), exhibit satisfactory agreement with the corresponding experimental spectrum (Figs. 4.6(c),(e), respectively). However, the positions of the phase jumps in the correlation phase spectrum (Fig. 4.6(f)), and consequently the dips in the correlation amplitude spectrum (Fig. 4.6(d)) as predicted by the theoretical model do not exactly match the phase jumps and the dips respectively in experimental correlation phase (Fig. 4.6(e)) and amplitude spectra (Fig. 4.6(c)).

Finally, the results for $\alpha = 52°$, which corresponds to $C = 0.75$ according to Eq. (4.20),

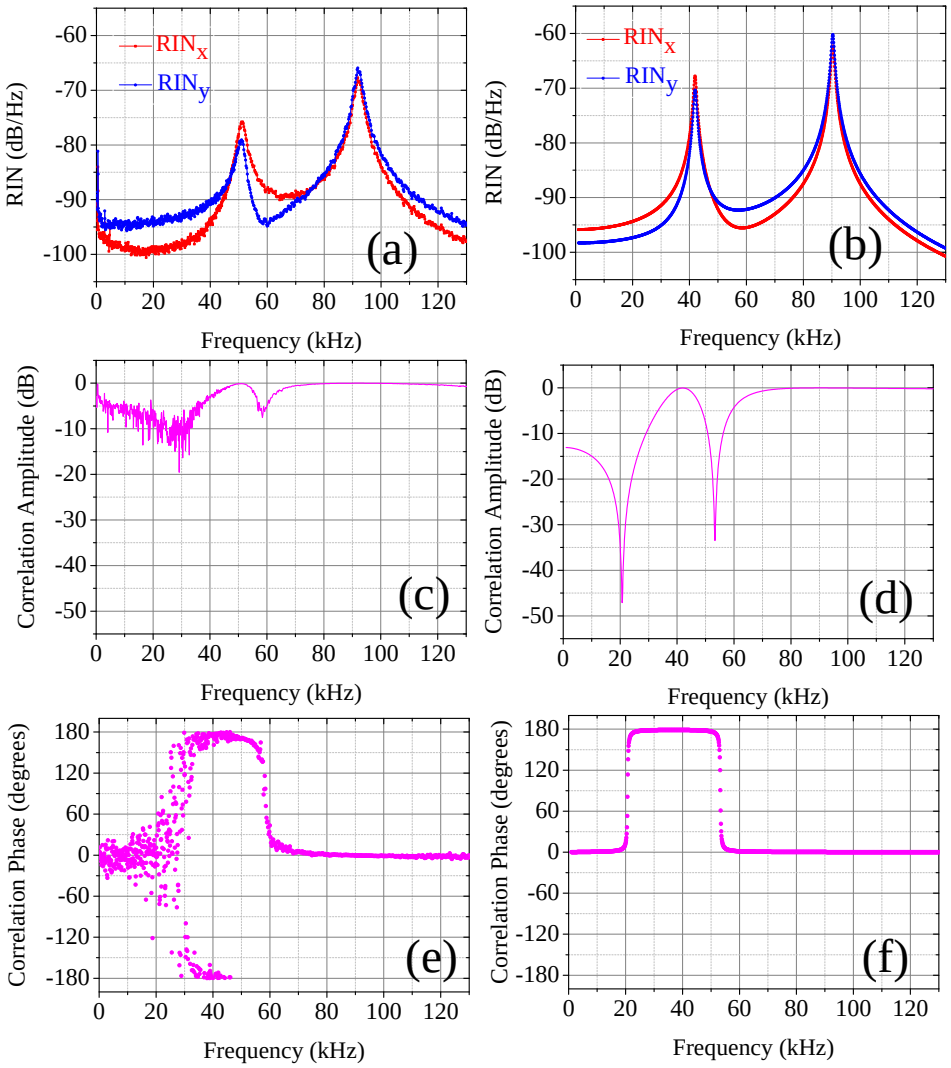

Figure 4.6: Results for $\alpha = 30°$, which corresponds to $C = 0.40$. RIN spectra: (a) experimental, and (b) theoretical; correlation amplitude spectra: (c) experimental and (d) theoretical; correlation phase spectra: (e) experimental and (f) theoretical. Parameter values used for simulations: $\beta = 0.025$, $r_1 = 1.35$, $r_2 = 1.4$, $\tau_x \simeq 5$ ns, $\tau_y \simeq 5.2$ ns, $\tau = 200$ μs, $\mathrm{RIN}_{pump} = -110\,\mathrm{dB/Hz}$, $\eta = 0.75$, $\psi = 0$.

are produced in Fig. 4.7. In this coupling situation, the in-phase relaxation oscillation peak lies at about 100 kHz as obtained from both experiment (Fig. 4.7(a)) and theory (Fig. 4.7(b)). However, the positions of the anti-phase peak are different in the experimental (at 60 kHz as in Fig. 4.7(a)) and theoretical (at 30 kHz as in Fig. 4.7(b)) RIN spectra. Nevertheless, the presence of these noise peaks resonant to the relaxation oscil-

lations reflects the class-B dynamical behavior of the dual-frequency Nd:YAG laser. The RIN spectra for the two modes, denoted by the red-squared-line and blue-circled-line in Figs. 4.7(a),(b) are not exactly identical due to the difference in losses and/or gains for the them. Figures 4.7(c),(d) respectively represent the experimental and theoretical correlation amplitude spectra. In the experimental correlation amplitude spectrum (Fig. 4.7(c)),

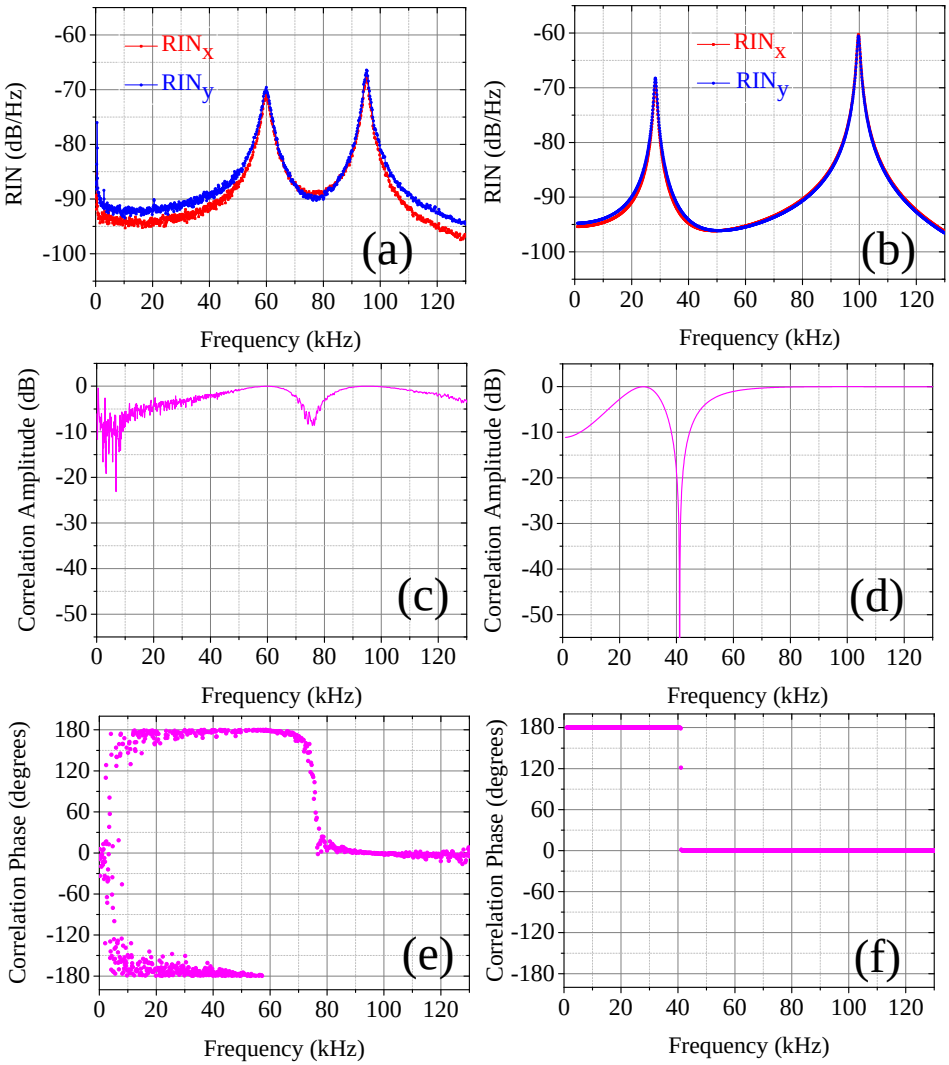

Figure 4.7: Results for $\alpha = 52°$, which corresponds to $C = 0.75$. RIN spectra: (a) experimental, and (b) theoretical; correlation amplitude spectra: (c) experimental and (d) theoretical; correlation phase spectra: (e) experimental and (f) theoretical. Parameter values used for simulations: $\beta = 0.025$, $r_1 = 1.38$, $r_2 = 1.4$, $\tau_x \simeq 5$ ns, $\tau_y \simeq 5.1$ ns, $\tau = 200$ μs,RIN$_{pump} = -110$ dB/Hz, $\eta = 0.75$, $\psi = 0$.

one can now observe only one dip located at about 70 kHz. The correlation amplitude spectrum as predicted by our theoretical model (Fig. 4.7(d)) reproduces the fact that there exists only one dip, even though its frequency is different (40 kHz) from the experiment. Moreover, experiment shows that (Fig. 4.7(c)), starting from $\sim$ - 10 dB at about 0 kHz, the correlation amplitude gradually reaches its maximum value (0 dB) at about 60 kHz, and maintains this maximum value ($\sim$ 0 dB) for all frequencies higher than 90 kHz. Theory also qualitatively reproduces the same kind of behavior of the correlation amplitude spectrum (Fig. 4.7(d)), except from the fact that theoretically the correlation amplitude attains 0 dB at frequencies 30 kHz and 60 kHz, rather than at frequencies 60 kHz and 90 kHz as shown by the experiment (Fig. 4.7(c)). The experimental and theoretical correlation phase spectra are shown in Figs. 4.7(e),(f), respectively. As obtained from the experiment (Fig. 4.7(e)), the correlation phase is π for all the frequencies lower than 70 kHz, then it jumps from π to zero at about 70 kHz and remains at zero for all the higher frequencies. The theoretical prediction as presented in Fig. 4.7(f) also exhibits only one phase jump, but the phase jump from π to zero occurs at about 40 kHz instead of 70 kHz, as shown by the experiment (Fig. 4.7(e)).

All the theoretical spectra of Figs. 4.5-4.7 are obtained considering a white pump noise for the frequency range of $0-120$ kHz with a RIN equal to -110 dB/Hz. To verify this, we measure the pump intensity noise spectrum for frequencies between 0 and 120 kHz. The simple measurement scheme is depicted in Fig. 4.8(a). The pump laser beam is detected

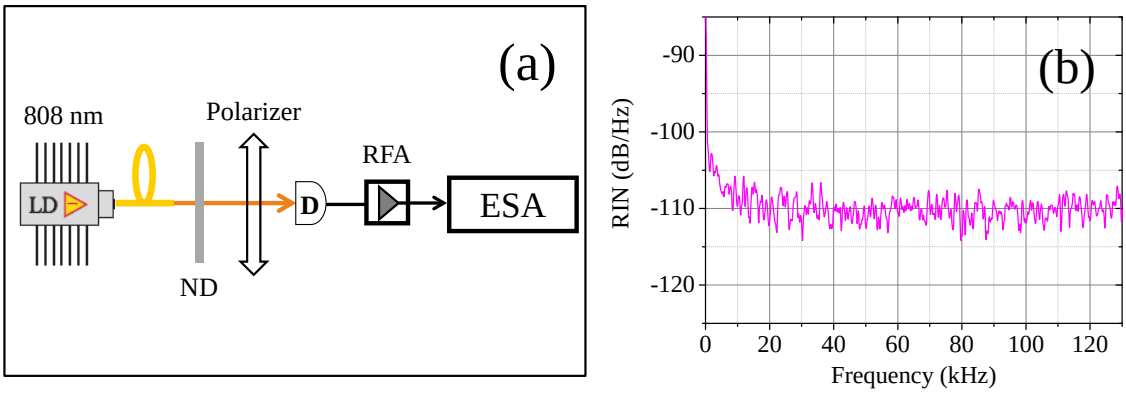

Figure 4.8: (a) Noise measrement setup for the pump laser diode (LD) operating at 808 nm. ND: neutral density filter, D: photodiode, RFA: radio frequency amplifier, ESA: electrical spectrum analyzer. (b) Relative intensity noise (RIN) spectrum of the pump laser measured by an ESA with a resolution and video bandwidth of 500 Hz.

using a photodiode (D), then the detected signal is amplified by a radio frequency amplifier (RFA), and finally it is sent to an electrical spectrum analyzer (ESA). The neutral density filter (ND) after the pump laser reduces the pump power below the maximum power rating of the photodiode. The power spectral density (PSD) of the pump noise is recorded by the ESA with a resolution bandwidth (RBW) and a video bandwidth (VBW) equal to 500 Hz. Then from this PSD, we calculate the pump RIN, which is plotted in Fig. 4.8(b). The pump noise measurement is performed after introducing a polarizer in front of the detector (D), and it is found that the pump RIN is white and independent of the orientation of the polarizer (Fig. 4.8(b)). This proves the assumption of Eq. (4.37) i.e., the pump noises for the two dipole families aligned along the two crystallographic axes of the Nd:YAG active medium are identical white noises. Moreover, we obtain a pump RIN equal to -110 dB/Hz, which is exactly the value we have taken for all the theoretical simulations of Figs. 4.5-4.7. Additionally, for all the theoretical simulations we have used a pump noise correlation factor $\eta = 0.75$, and a phase $\psi = 0$. It is important to mention that the pump noise correlation spectrum is not experimentally verified; the value of η is adjusted to fit the experimental results. However, the presence of the anti-phase peak in the RIN spectra of the two laser modes for all three coupling situations indeed confirms that the pump noises for the two dipole families are partially correlated. For all the theoretical simulations of Figs. 4.5-4.7, the values of r_1 and r_2 are estimated from the experiment by measuring the ratios of the pump power to the threshold pump power. The values of τ_x and τ_y are estimated knowing the cavity length (9 cm) and the transmission loss of the output mirror of the cavity (~ 2 %). The value of τ (200 μs) is taken from the preceding experiment performed with this active medium [El Amili et al., 2012].

4.4.3 Physical interpretation of the results

In the preceding section, we have explored the impact of the nonlinear coupling strength between the two cross-polarized modes of our dual-frequency Nd:YAG laser on the intensity noise correlation amplitude and phase spectra. In the following, we give a physical interpretation of these noise correlation spectra in the framework of the linear response of a two-coupled oscillator system as already performed in Chapter 2. To this aim, we recall the notion of the in-phase and the anti-phase relaxation mechanisms for the dual-frequency Nd:YAG laser in analogy with a two-coupled mechanical oscillator system [Ot-

suka et al., 1992]. It is important to emphasize here that the eigenrelaxation mechanisms of the dual-frequency Nd:YAG laser are significantly different from the dual-frequency VECSEL. The eigenrelaxation mechanisms are damped oscillatory for the dual-frequency Nd:YAG laser linked with its class-B dynamics, whereas theses eigenmechanisms are exponentially damped in the dual-frequency VECSEL due to its class-A dynamical behavior. In the general case, the transfer functions of the in-phase and anti-phase response can be calculated by diagonalizing the 2×2 matrix of Eq. (4.31). However, the derivation becomes fairly simple in the symmetrical-mode approximation i.e. if the two laser modes behave symmetrically (identical losses, gains, etc.) and the detailed derivation is given in Appendix C. The in-phase and anti-phase transfer functions, as obtained from Eqs. (C.25-C.26) of Appendix C, are shown in Fig. 4.9 for the three different coupling situations. It is important to remind here that the noise response of each laser mode can actually be obtained by the superposition of the in-phase and the anti-phase responses. As a results, the relative degree of dominance between the in-phase and anti-phase responses plays a pivotal role to determine the spectral properties of the intensity noises and their correlation in the dual-frequency Nd:YAG laser.

We start with the weak coupling case ($C = 0.09$), corresponding to $\alpha = 20°$. In this coupling situation, the in-phase response (pink line) and the anti-phase response (black line) are reproduced in Fig. 4.9(a). One can find that both in-phase and anti-phase responses exhibit a peak originating from the damped-oscillatory behavior of the two eigenrelaxation mechanisms linked with the class-B dynamical behavior of the Nd:YAG laser. Moreover, Fig. 4.9(a) shows that the eigenfrequency of the anti-phase relaxation oscillation is nearly equal to 70 kHz, whereas the eigenfrequency of the in-phase one is higher (100 kHz). These different eigenfrequencies of the in-phase and anti-phase relaxation oscillations lead to the two peaks in the RIN spectrum of each laser mode (Fig. 4.5(a),(b)), obtained by superposing the in-phase and anti-phase responses. One can also notice in Fig. 4.9(a) that the in-phase response dominates over the anti-phase one for frequencies lower than 50 kHz, then the anti-phase response becomes dominant within frequencies 50 kHz to 70 kHz, and finally the in-phase response prevails again for all frequencies higher than 70 kHz. This explains why the correlation phase jumps from zero at low frequencies to π at intermediate frequencies, and then back to zero again at high frequencies as shown in Figs. 4.5(e),(f). These phase jumps correspond to the crossings between the in-phase and anti-phase responses as shown in Fig. 4.9(a). The two crossings between the in-phase

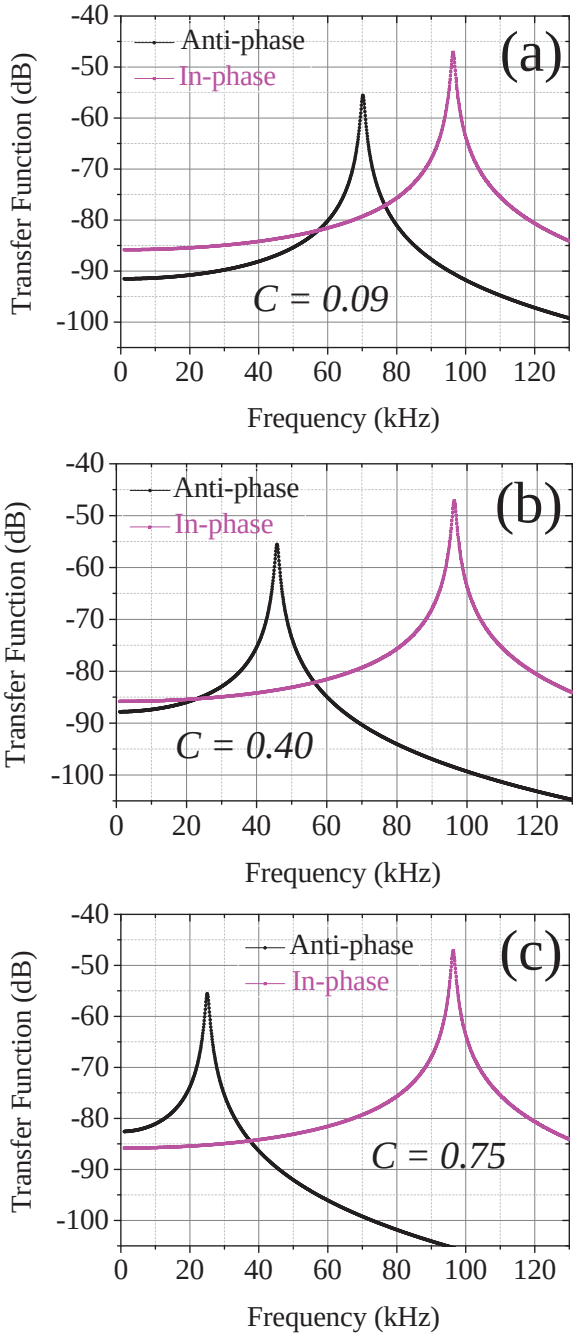

Figure 4.9: Normalized transfer functions for the in-phase (red line) and anti-phase (black line) relaxation oscillation mechanisms for three different values of α, corresponding to three different coupling situations; (a) $\alpha = 20°$, (b) $\alpha = 30°$ and (c) $\alpha = 52°$. The values of the other parameters used for the simulations are: $\beta = 0.025$ $r_1 = r_2 = r = 1.4$, $\tau_x = \tau_y = \tau_{\text{cav}} = 5$ ns, $\tau = 200\,\mu$s, $\eta = 0.75$, $\psi = 0$

and anti-phase responses also lead to the two dips in the correlation amplitude spectrum (Figs. 4.5(c),(d)). These dips in the correlation amplitude spectrum can be described as the outcome of the destructive interference between the identical noises of the two modes due to the two $\pi-$phase jumps. Moreover, the correlation strength is weak ($\leq$ - 5 dB) for frequencies lower than 20 kHz (Fig. 4.5(c),(d)) as the pump noises for the two dipole families are partially correlated ($\eta = 0.75 < 1$), and the transfer functions of the two relaxation mechanisms differ by only one order of magnitude within these frequencies (Fig. 4.9(a)). On the contrary, for frequencies higher than 80 kHz, the difference between the strengths of the in-phase and anti-phase mechanisms is of several orders of magnitude, leading to an almost perfect correlation (0 dB).

The interpretation of the results for the intermediate coupling case $C = 0.40$, corresponding to $\alpha = 30°$ (Fig. 4.6), is quite similar to the preceding coupling situation. The occurrence of the resonant peaks at different frequencies for the in-phase (pink line) and anti-phase (black line) response (Fig. 4.9(b)), linked with the class-B dynamics of the laser, give rise to the two peaks in the RIN spectrum of each laser mode (Fig. 4.6(a),(b)). In this coupling condition, the two phase jumps in the correlation phase spectrum (Figs. 4.6(e),(f)), and consequently the two dips in the correlation amplitude spectrum (Figs. 4.6(c),(d)) are again coming from the two crossings between the in-phase and anti-phase response (Fig. 4.9(b)). The dips in the correlation amplitude spectrum again originates from the destructive interference between the nearly identical fluctuations of the two modes due to the $\pi-$phase jumps. However, in the present case the main differences with respect to the weak coupling case are that i) the anti-phase relaxation oscillation frequency is smaller, leading to the fact that the two transfer functions of Fig. 4.9(b) cross at lower frequencies, which is consistent with the fact that the phase jumps for the correlation occur at lower frequencies in Figs. 4.6(e),(f) compared with Figs. 4.5(e),(f); ii) the difference between the transfer functions of the two mechanisms becomes really small in the low frequency region (lower than 20 kHz), explaining why the correlation amplitude becomes even smaller in the low frequency region (Figs. 4.6(c),(d)).

Finally, for the moderately strong coupling case $C = 0.75$ corresponding to $\alpha = 52°$, the in-phase and anti-phase response are shown in Fig. 4.9(c). In Figs. 4.7(a),(b), the two resonant peaks in the RIN spectrum of each laser mode, obtained by superposing the in-phase (pink line) and anti-phase responses (black line), are coming from the different eigenfrequencies of the in-phase and anti-phase relaxation oscillations. Moreover, one can

observe in Fig. 4.9(c) that the anti-phase relaxation oscillation frequency has decreased so much that the first crossing of the two transfer functions has disappeared unlike the previous two coupling cases. As a result, the anti-phase mechanism always dominates for low frequencies (less than 40 kHz), whereas the in-phase mechanism is dominating at high frequencies. This explains why there is only one phase jump in the correlation phase spectrum of Figs. 4.7(e),(f), and consequently only one dip in the correlation amplitude spectrum of Figs. 4.7(c),(d).

It is worth noticing that the possible existence of two phase jumps, associated with the two intersections of the transfer functions of the eigenrelaxation mechanisms, is coming from the resonant behaviors of these transfer functions due to the class-B dynamics of the Nd:YAG laser. This strongly contrasts with the case of class-A lasers that we have discussed in the case of a dual-frequency VECSEL in Chapter 2. Indeed, for a class-A laser, the transfer functions of the relaxation mechanisms look like the transfer functions of a first-order filter or of an overdamped oscillator and decrease monotonically with frequency. This implies that they can exhibit only one or no intersection, leading to the fact that a maximum of one phase jump (and sometimes no phase jump) can be observed in the correlation spectrum [De et al., 2013b].

However, one can notice by comparing the theoretical and experimental spectra in Figs. 4.5-4.7 that the shift of the anti-phase relaxation oscillation frequency with the change of α is not as large in the experiment as expected from the theoretical model. This may be due to fact that the coupling strength might not exactly vary with α as predicted by our model [Eq. (4.20)]. One possible explanation of this discrepancy may lie in the fact that our model assumes the existence of only three families of dipoles oriented along the crystallographic axes of the gain medium Schwartz et al. [2009], although several other studies suggest more complex descriptions for the spectroscopy of Nd^{3+} ions embedded in YAG matrix [Sing et al., 1974; Burdick et al., 1994; Dalgliesh et al., 1998; McKay et al., 2007]. In addition to that, the present model does not take into account the effect of the spatial hole burning [Tang et al., 1963; Kimura et al., 1971], which can lead to a reduction of C. This could partially explain why C does not evolve in such a large range. The effect of the spatial hole burning on coupling constant C is further discussed in Appendix F.

4.5 Conclusion

In this chapter, we have explored the intensity noise properties of a dual-frequency Nd:YAG laser, which sustains simultaneous oscillation of two cross-polarized modes with a tunable frequency difference lying in the RF range. Specifically, we have analyzed, both experimentally and theoretically, the spectral behaviors of the intensity noises and their correlation for different nonlinear coupling strengths between the two laser modes for frequencies between 0 and 120 kHz. There the intensity noise of the pump diode laser acts as the dominant source of noise. The measurements have shown that the pump noises for the two relevant dipole families are white noises of identical amplitudes. We remind here that such a noise correlation analysis has already been carried out in Chapter 2 for dual-frequency VECSEL, which exhibits class-A dynamics. However, since the dual-frequency Nd:YAG laser obeys class-B dynamical behavior, the noise correlation investigation of the present chapter generalizes the analysis of Chapter 2. It has been found that the class-B dynamical behavior of the dual-frequency Nd:YAG laser, in addition to the nonlinear coupling between the two modes, greatly modifies the RIN spectra as well as the noise correlation spectra compared to the class-A dual-frequency VECSEL. For example, the RIN spectra of the two laser modes in dual-frequency Nd:YAG laser exhibit resonant noise peaks at in-phase and anti-phase relaxation oscillation frequencies, whereas for dual-frequency VECSELs the RIN spectra look like a first-order filter transfer functions without any resonant peak. It is even more interesting to compare the intensity noise correlation spectra for these two types of lasers. On the one hand, for the dual-frequency Nd:YAG laser, the correlation phase spectrum exhibits either two phase jumps or at least one phase jump, consequently the correlation amplitude spectrum shows two dips or only one dip. On the other hand, there is the possibility to have a maximum of only one phase jump or sometimes no phase jump in the correlation phase spectrum, and consequently a maximum of one or even no dip in the correlation amplitude spectrum of the dual-frequency VECSEL. Moreover, the intensity noises of the two laser modes in the dual-frequency Nd:YAG laser become fully correlated (0 dB, exactly) for frequencies around the relaxation oscillation frequencies, even though the noise sources (pump noises) for the dipole families are only partially correlated. On the contrary, in the dual-frequency VECSEL, the noise correlation amplitude never attains 0 dB value as long as the noise sources for the two modes are partially correlated. Our physical interpretation in terms

of the linear response of a two-coupled oscillator system has also achieved great success in explaining this difference between the noise correlation spectra of the dual-frequency Nd:YAG laser and the dual-frequency VECSEL. The dual-frequency VECSELs exhibit similarities with the over-damped situation, whereas the dual-frequency Nd:YAG laser resembles the weak damping case of a two-coupled oscillator system. Additionally, we have introduced a theoretical model, based on the assumption that the dipoles inside the gain medium are aligned along the crystallographic axes of the medium [Schwartz et al., 2009], which has led to a fairly good agreement with the experiment. This also proves the validity of the assumption of [Schwartz et al., 2009] that the emitting dipoles indeed behave as if they were aligned along the crystallographic axes of the Nd:YAG crystal. This indicates that the noise correlation analysis can even be a good probe to find the dipole orientations in laser materials. Moreover, the remaining little discrepancy concerning the shift of the anti-phase peak with the change of α gives the opportunity for further developments of the model to take into account other effects (for example, the spatial hole burning), which could modify the coupling strength. Of course, it would be even more interesting, if this model could be extended to other laser materials, such as YAG doped with other ions, or other crystal matrices, or even doped glasses. However, this implies a careful study of the spectroscopy of these materials, which is not always available in the literature, in order to understand the orientation of the absorbing and emitting dipoles.

In the following table, we recapitulate the main results of this chapter:

- Exploration of the spectral properties of intensity noises and their correlation in a dual-frequency Nd:YAG laser.
- Investigation of the impact of nonlinear coupling strengths between the two modes in the dual-frequency Nd:YAG laser on the intensity noise correlation spectra.
- Comparison between the intensity noise correlation spectra of class-B dual-frequency Nd:YAG lasers and class-A dual-frequency VECSELs.
- Interpretation of the results in the framework of the linear response of two-coupled weakly damped oscillators.
- Successful introduction of a theoretical model, based on the assumption that the emitting dipoles in the Nd:YAG active medium were aligned along the crystal grown axes.
- Prediction for the possible existence of other mechanisms, for example, spatial-hole burning.

Chapter 5

Reduction of anti-phase noise in a dual-frequency Nd:YAG laser

Contents

5.1 Introduction

The Nd:YAG lasers suffer from resonant intensity noise at low frequencies (from few kilohertz to few megahertz) due to the relaxation oscillation inherent to their class-B dynamical behavior as the population inversion lifetime inside the active medium prevails over the photon lifetime inside the cavity. For a dual-frequency Nd:YAG laser, sustaining simultaneous oscillation of two linear-orthogonal polarizations, the noise performance is even worse. In this case, the intensity noise spectrum of each laser mode exhibits two peaks lying at the in-phase and anti-phase eigenfrequencies as we have seen in the previous chapter. These resonant intensity noises at low frequencies, typically within few kHz to few MHz, limit the use of dual-frequency Nd:YAG lasers for a large number of applications such as microwave photonics [Alouini et al., 2001; Brunel et al., 2005; Pillet et al., 2008], spectroscopy [Brunel et al., 1997], and metrology [Nerin et al., 1997; Du et al., 2005]. The in-phase noise peak, which corresponds to the standard relaxation oscillation of the laser, can be reduced electronically or optically using feedback loops [Taccheo et al., 1996; Kane, 1990; Rowan et al., 1994], and also by laser injection locking [Harb et al., 1996; Freitag and Welling, 1994]. However, the anti-phase peak, associated with a resonant exchange of energy between the two laser modes, is very difficult to circumvent [Pillet et al., 2008]. This is because the reduction of the anti-phase peak would require an additional servo-loop acting on the difference of the intensities of the two modes or two servo-loops acting independently on the intensity of each mode. The existence of the anti-phase noise being by essence due to the fact that the two laser modes share totally or partially the same population inversion, another approach is to separate spatially the two lasers modes in the active medium [Alouini et al., 1998; Yifei et al., 2001; Czarny et al., 2004]. However, such a two axis approach increases the complexity of the laser. Additionally, it reduces the correlation between the frequency jitter of the two modes as compared to a single axis, thus reducing the efficiency of the common mode noise rejection. Besides, another solution consists in using relaxation oscillation free class-A lasers such as VECSELs as has been illustrated previously. However, achieving class-A dynamical behavior in a Nd:YAG laser is not obvious as it would require a kilometer-long external cavity. Consequently, an optimal dual-frequency laser in terms of intensity noise and beat frequency stability would be a single axis laser in which the population inversions related to each mode are independent. In this chapter, we experimentally demonstrate how the proper design of

a two polarization dual-frequency Nd:YAG laser allows to get rid of the anti-phase noise in the simplest possible architecture and without using any electronic or optical feedback loop [El Amili et al., 2012]. This design is based on an appropriate choice of the active medium cut and orientation in order to assign two almost independent families of active atoms to the two laser modes.

5.2 Experimental results

The architecture of the two-frequency Nd:YAG laser is identical to the one in Fig. 4.2(a) of Chapter 4. We repeat that our aim here is to to minimize the anti-phase relaxation mechanism by completely decoupling the two eigenpolarizations of the dual-frequency Nd:YAG laser. One possible way to decouple the two laser modes is to assign two independent population reservoirs for the two modes. In order to achieve that one should properly choose the active medium cut and should also have the freedom to vary the orientations of the two eigenpolarizations. In the laser architecture that we choose (Fig. 4.2(a) of Chapter 4), the intra-cavity quarter-wave plate (QWP) defines the orientations of the two eigenpolarizations of the laser. In this case, these two eigenpolarizations are linear and aligned along the neutral axes of the QWP. The frequency difference between the two polarizations is equal to one half of the free spectral range of the cavity. It is worth mentioning that in usual two-frequency lasers [Brunel et al., 1997], one uses a variable intra-cavity retardance in order to be able to tune the frequency difference between the two modes. Here, we restrict to the simple case of an intra-cavity QWP because rotating this QWP permits to simply rotate the orientation of the eigenpolarizations. Now, the remaining question is how should we choose our active medium in order to uncouple the two polarization modes, i.e., to minimize the cross-saturation effect between the two modes? To this aim, we choose a (100)-cut Nd:YAG crystal instead of the more common (111)-cut, keeping in mind that the emitting dipoles behave as if they were aligned along the crystallographic axes of the YAG matrix [Schwartz et al., 2009]. This leads to the fact that one among the three dipole families, aligned along the $\langle 100 \rangle$ crystallographic axis, does not contribute to the lasing action i.e., the contribution from the population inversion N_3 can be discarded. Therefore, we are left with only two dipole families, associated with population inversions N_1, N_2, and aligned along the two transverse crystallographic axes ($\langle 010 \rangle$, $\langle 001 \rangle$, respectively) as shown in Fig. 4.3 of Chapter 4. In this configuration,

the nonlinear coupling (C) between the two eigenpolarizations only depends on the angle (α) between the eigenpolarization directions and the crystallographic axes as given in Eq. 4.20 of Chapter 4. In principle, it indicates that almost complete decoupling of the two cross-polarized modes could be obtained by making $\alpha = 0$, i.e., aligning the two eigenpolarizations along the $\langle 010 \rangle$ and $\langle 001 \rangle$ crystallographic axes. This explains why we have chosen such a crystal-cut. We remind that the QWP is mounted on a precise rotation mount in order to control the angle α between the Nd:YAG crystallographic axes and the polarization states. Both laser modes are continuously analyzed with a Fabry-Pérot cavity to check that the laser remains monomode without any mode hop during data acquisition. All the measurements are performed for a pump power equal to 300 mW, leading to a laser output power of about 20 mW. The noise measurement setup is schematized in Fig. 5.1. In order to measure the actual noise spectrum of each of the two laser modes, it is important to separately detect the two modes without mixing them. The combination

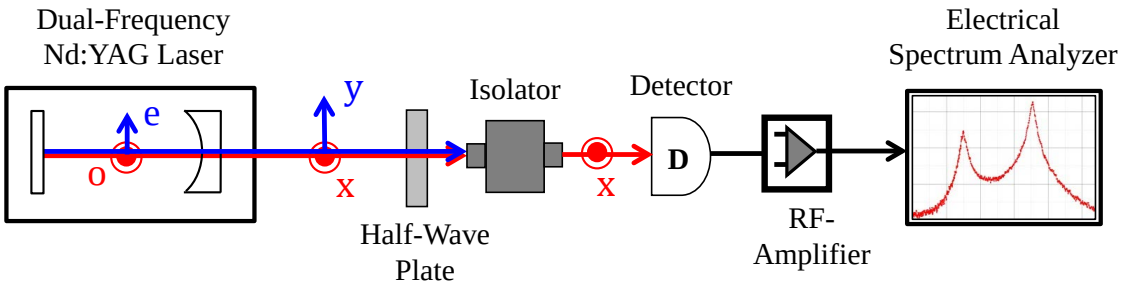

Figure 5.1: Measurement scheme for the intensity noise spectrum of each laser mode separately in a dual-frequency Nd:YAG laser.

of a half-wave plate followed by an isolator acts as a polarization analyzer, which permits to select any one of the two polarizations (say $\mathbf{x}-$polarized mode) on the detector with a bandwidth of 3.7 MHz. Then, the detected signal is amplified by an homemade RF amplifier. Finally, the amplifier output is sent to an electrical spectrum analyzer, which records the noise spectrum.

The main goal here is to illustrate the fact that the proper choice of α leads to complete reduction of the anti-phase peak in the intensity noise spectra of both laser modes of the dual-frequency Nd:YAG laser. To this aim, we vary α by rotating the intra-cavity QWP and observe the evolution of the anti-phase peak in the RIN spectrum of any one of the laser modes (say, $\mathbf{x}-$polarized mode). The measurement results are reproduced in Fig. 5.2.

This figure shows the RIN spectra of the **x**−polarized mode for only two cases: (i) when

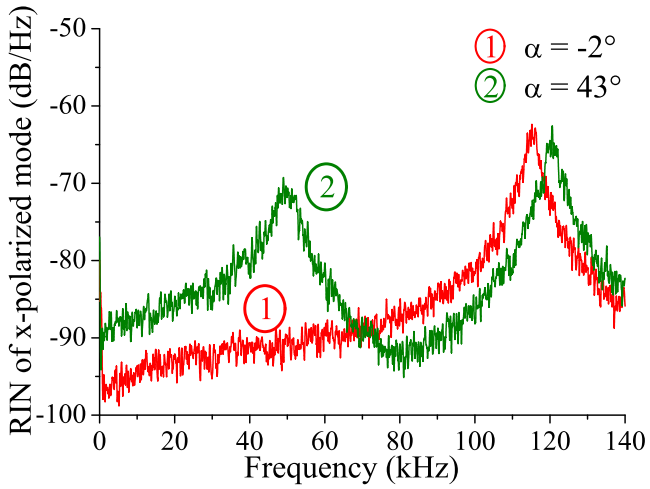

Figure 5.2: RIN spectra of only **x**−polarized mode for different values of α. We show only two spectra for $\alpha = 43°$ (green line), $\alpha = -2°$ (red line) measured with an electrical spectrum analyzer by choosing a resolution and video bandwidth of 200 Hz.

the anti-phase peak amplitude is maximum, corresponding to $\alpha = 43°$, and (ii) when the anti-phase peak amplitude is minimum, which corresponds to $\alpha = -2°$. For $\alpha = 43°$, the RIN spectrum of the **x**−polarized mode is represented by the green line in Fig. 5.2. In this RIN spectrum, one can see the presence of the standard in-phase relaxation oscillation peak at about 120 kHz, and also the anti-phase peak at about 50 kHz. Moreover, we observe that the anti-phase peak attains maximum height for $\alpha = 43°$. This indicates that $\alpha = 43°$ corresponds to the maximum nonlinear coupling between the two laser modes. This is consistent with the picture we have adopted for the dipole orientations inside the Nd:YAG crystal i.e., the dipoles are aligned along the crystallographic axes. Thus for α close to 45°, each mode equally shares the two dipole families, leading to a maximum coupling between them. On the other hand, the experiment has shown that the amplitude of the anti-phase peak in the RIN spectrum of of the **x**−polarized mode has its minimum value for $\alpha = -2°$. This is reproduced as the red line in Fig. 5.2. In this case, the anti-phase peak becomes so small that it disappears below the noise floor. This infers that $\alpha = -2°$ is not far from being the condition for minimum coupling between the two cross-polarized modes of our dual-frequency Nd:YAG laser. This is exactly what we expected as α close to zero corresponds to the situation when the two eigenpolarizations

are aligned along the two crystallographic axes, and hence they encounter two independent dipole families. Nevertheless, the RIN spectrum illustrates the presence of the in-phase relaxation oscillation peak at about 115 kHz. It must be noted that for $\alpha = -2°$ (red line) the in-phase peak is shifted in frequency by 5 kHz compared to $\alpha = 43°$ (green-line). This is linked with the unavoidable little change of the losses due to the rotation of the QWP. It corresponds to a variation of the pumping rate of 1% only. Additionally, the experiment shows that the the anti-phase (resp. in-phase) peak is minimized (resp. maximized) for α equal to $-2°$ (resp. $43°$) instead of $0°$ (resp. $45°$), as was expected from the model. This little discrepancy is within the experimental orientation uncertainty ($\pm 3°$) of the active medium in its mount when positioned inside the laser cavity. It is worth mentioning that the noise peak in the red line of Fig. 5.2, corresponding to the minimum coupling situation, should not be termed as "in-phase peak" to be technically correct. This is because for the zero coupling there is no meaning of the in-phase and the anti-phase eigenmechanisms of the global two-coupled oscillator system. However, one should remember that the standard relaxation oscillation frequency of a single mode is identical to the in-phase relaxation oscillation frequency when such two modes are coupled as in-phase eigenmechanism is independent of coupling. This is true for any two identical coupled oscillator system in which the in-phase eigenfrequency is always equal to the natural frequency of the oscillators. Of course, the term "in-phase" is applicable for all other nonzero coupling situations ($-2° < \alpha < 88°$). The RIN spectra of the $\mathbf{x}-$polarized mode for other α values are also measured, although they are not shown in Fig. 5.2. Moreover, we check that the RIN spectra of the $\mathbf{y}-$polarized mode for different α values are qualitatively identical to the ones of the $\mathbf{x}-$polarized mode.

We investigate how the anti-phase peak amplitude evolves with the change of α and the results are plotted in Fig. 5.3. One can see in Fig. 5.3 that the anti-phase peak attains maximum value for α close to $\pm\pi/4$. This indicates that for $\alpha = \pm\pi/4$ the nonlinear coupling is maximum, i.e. the two modes equally share the two dipole families. On the other hand, the anti-phase peak amplitude becomes minimum once for $\alpha = 0$ and again for $\alpha = \pi/2$ as shown in Fig. 5.3. This suggests that for α equals to 0 or $\pi/2$ the nonlinear coupling is minimum indicating that the two modes are subjected to two different dipole families. This again proves that the emitting dipoles indeed behave as if they were oriented along the crystallographic axes [Schwartz et al., 2009].

It is important to mention that if one of the two laser modes becomes much weaker

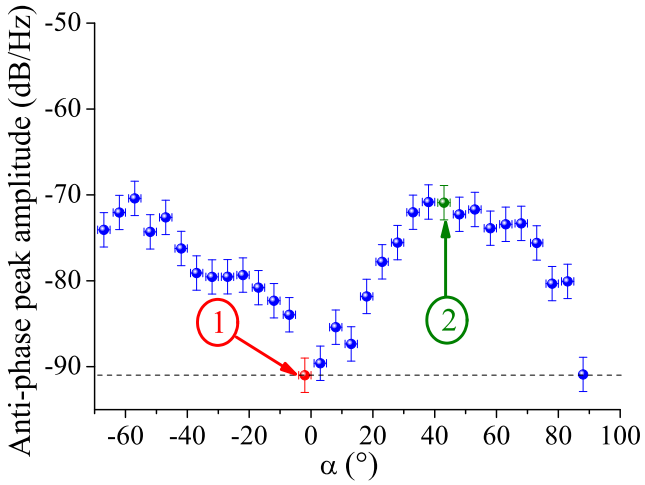

Figure 5.3: Evolution of the amplitude of the anti-phase peak versus α. Dashed line: noise floor level below which the anti-phase peak is no longer measurable.

than the other, then also the anti-phase noise vanishes. To avoid this artifact the powers of the two cross-polarized modes are carefully balanced for each orientation of the QWP by fine adjustment of the intra-cavity etalon. This is proved in Fig. 5.4, which shows that the power ratio of the two modes for all α values remains close to 1. This confirms that

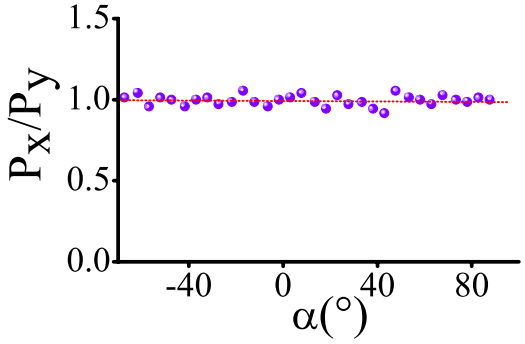

Figure 5.4: Evolution of the power ratio of the two cross-polarized modes versus α.

the evolution of the anti-phase peak versus α in Fig. 5.3 is indeed due to the variation of the nonlinear coupling between the modes.

Additionally, the anti-phase noise can be minimized irrespective of the α value when

one balances the intensities of the two modes on the detector by adjusting the polarization analyzer (Fig. 5.1), even though the noise spectrum of each mode exhibits an anti-phase peak. This is completely different from the situations for $\alpha = -2°$ or $\alpha = 88\,°$, when the anti-phase noise is minimized for each of the polarization mode. Of course, the in-phase peak always remains there. Therefore, if the anti-phase noise is indeed minimized in each

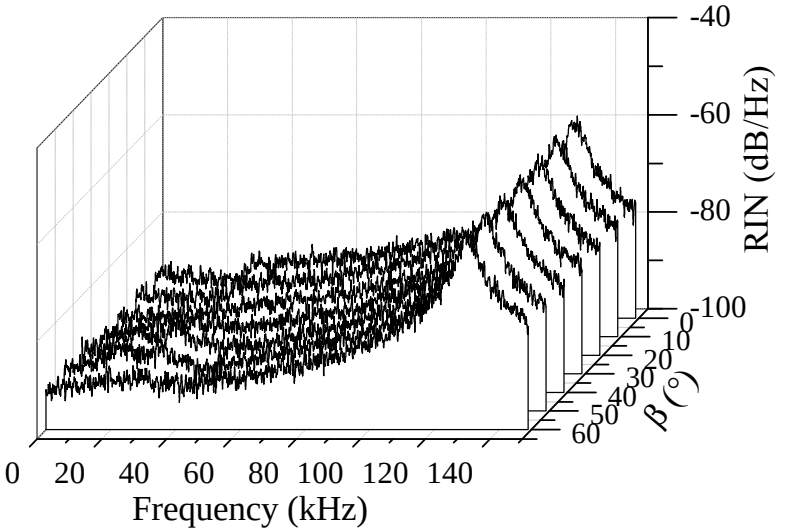

Figure 5.5: RIN spectra for different half-wave plate orientations β when the eigenpolarizations are oriented along the crystallographic axes of the Nd:YAG crystal ($\alpha = -2°$ or $\alpha = 88\,°$). electrical spectrum analyzer resolution bandwidth, 200 Hz; video bandwidth, 200 Hz.

laser mode for $\alpha = -2\,°$ and $\alpha = 88\,°$, we expect this peak to be absent for all orientations of the polarization analyzer located after the dual-frequency Nd:YAG laser (Fig. 5.1). This is what we check in Fig. 5.5, which shows the RIN spectra obtained for several orientations β between $\mathbf{x}$ and the fast axis of the half-wave plate (HWP). If the HWP is rotated by β, the analyzed polarization rotates by 2β. In the experiment, we rotate the HWP by steps of 10°. On the one hand, the experimental spectra in Fig. 5.5 reveal that the RIN behavior remains almost the same for all orientations of the polarization analyzer. More importantly, these spectra prove that the anti-phase peak is indeed drastically reduced for both polarization modes of the laser. It is worth mentioning that the principle proposed here to reduce the anti-phase noise by reducing the nonlinear coupling between the modes is conceptually analogous to that of [Oka and Kubota, 1988]. In [Oka and Kubota, 1988], the stabilization of the output power of a Nd:YAG frequency-doubled laser is obtained

when the second harmonic generation losses that couple the two polarization modes are reduced. However, in our case the coupling mechanism between the two polarization is associated with the cross-saturation in the active medium. We reduce this gain cross-saturation or effectively the coupling by fixing the orientation of the two polarization modes along two dipole families, oriented along two crystallographic axes. The intra-cavity QWP that we use is only intended to fix the orientation of the laser polarizations, the active medium being isotropic. Therefore, the amount of retardance introduced by this wave plate does not play any significant role unlike in [Oka and Kubota, 1988].

5.3 Conclusions

To conclude this chapter, we have demonstrated a new technique for the minimization of the noise induced by the anti-phase relaxation oscillation in a dual-frequency Nd:YAG laser. The technique is based on two main ingredients: (i) a proper choice of the orientation of the laser eigenpolarizations, and (ii) a proper choice of the active medium cut. We have succeeded to reduce the anti-phase peak by more than 20 dB by choosing a $\langle 100 \rangle$-cut Nd:YAG crystal and aligning the eigenpolarizations along the crystallographic axes. This is in perfect agreement with the dipole alignment model suggested in [Schwartz et al., 2009], which states that the laser behaves as if the emitting dipoles were oriented along the crystallographic axes. In this context, it is important to remind that there exist more elaborate models suggesting more complex descriptions for the spectroscopy of Nd^{3+} ions embedded in a YAG matrix [Dalgliesh et al., 1998; McKay et al., 2007]. Moreover, the anti-phase noise reduction technique proposed here opens several interesting perspectives. Firstly, it shows that a properly designed active medium with a careful control of the orientation of the emitting dipoles would permit to solve the same problem for lasers operating at other wavelengths such as 1.5 μm erbium laser, which is useful for LIDAR-RADAR applications [Morvan et al., 2002] and for optical distribution of RF local oscillators through optical fibers [Pillet et al., 2008]. Secondly, it opens new horizons of applications for dual-frequency solid-state lasers, in domains in which the noises in the intensities of the two polarization modes play a central role such as the probing of cesium clocks based on coherent population trapping phenomena [Zanon et al., 2005]. Finally, this analysis illustrates the fact that the anti-phase relaxation oscillation can be a good probe to find the orientations of the emitting dipoles in different solid-state laser media.

The following table summarizes the key takeaways of the present chapter:

- Reduction of the anti-phase noise peak in a dual-frequency Nd:YAG laser by more than 20 dB.
- The noise minimization technique is based on complete decoupling of the two cross-polarized laser modes by aligning them along the crystallographic axes of the ⟨100⟩-cut Nd:YAG active medium.
- Confirmation of the model according to which the emitting dipoles in a Nd:YAG laser medium behave as if they were aligned along the crystallographic axes as proposed in [Schwartz et al., 2009].

General Conclusion

The research work presented in this thesis aimed at understanding the different noise mechanisms occurring in some dual-frequency lasers. We have investigated the spectral properties of different noises and their correlations in two types of dual-frequency lasers based on semiconductor (VECSEL) and solid-state (Nd:YAG) active media. Apart from the obvious difference between the gain mechanisms in semiconductor and solid-state laser media, the dual-frequency VECSEL and the dual-frequency Nd:YAG laser exhibit different dynamical behaviors. The dual-frequency VECSELs exhibit relaxation oscillation free class-A dynamics as the photon lifetime inside the cavity is longer than the population inversion lifetime. On the contrary, the dual-frequency Nd:YAG lasers obey class-B dynamics linked with the fact that the photon lifetime inside the cavity is shorter than the population inversion lifetime, leading to the existence of relaxation oscillations. In this thesis, we have figured out how the laser dynamics, in addition to the nonlinear coupling between the two laser modes, governs different noise phenomena in dual-frequency lasers. This thorough inspection of different noise mechanisms in dual-frequency lasers has led to find the origin of RF beatnote noises, which degrade the beatnote spectral purity.

The ability of a dual-frequency VECSEL operating at $1\,\mu$m to generate a high-purity optically-carried microwave signal has been first demonstrated by Ghaya Baili et al. [Baili et al., 2009]. In that study, it has been shown that the relaxation oscillation free class-A dynamics of the dual-frequency VECSEL enables one to get rid of the excess electrical noise in the vicinity of the RF beatnote, generated by optically mixing the two laser modes. At the very beginning of this work, following [Baili et al., 2009], we have reinvestigated the spectral behaviors of the RF beatnote and its phase noise in a dual-frequency VECSEL at $1\,\mu$m using our own experimental setup. Later, we have exploited the operation principle of the $1\,\mu$m DF-VECSEL for the first realization of a dual-frequency VECESL operating at the desired telecom wavelength, which is most suitable for fiber-optic links. Moreover,

measurements have shown that the class-A dynamical behavior of our telecom VECSEL provides a much improved noise performance of the RF beatnote due to the absence of the excess noise induced by relaxation oscillations, commonly observed in solid-state lasers [Pillet et al., 2008]. However, it has been found that the RF beatnote is associated with a few megahertz wide pedestal coming from the remaining phase noise. Understanding the origin of this phase noise is not at all straightforward as (i) the phase fluctuations are coupled with the intensity fluctuations due to the large α-factor of the semiconductor active medium and (ii) in the RF beatnote the phase noises of the two laser modes appear with an opposite sign, thus making the correlation between the noises of the two laser modes important. Firstly, we have studied the spectral behavior of the correlation between the intensity noises of the two laser modes. It has been found that the intensity noise correlation spectra strongly depend on the amount of spatial separation (d) between the modes on the gain structure. For example, correlation phase spectra exhibit one or no phase jump, and consequently correlation amplitude spectra show one or no dip depending on d values. Additionally, the degree of correlation, excluding the dip, increases with the decrease of d. We have proved that this dependence of the intensity noise correlation spectra on d is linked with two things, nonlinear coupling strength (C) and the degree of correlation (η) between the pump noises for the two laser modes, both of which increase with the decrease of d. Secondly, we have explored the propagation mechanism of the pump noise to the RF beatnote phase noise. We have isolated two dominant mechanisms: (i) the phase-intensity coupling effect due to the large α-factor of semiconductor active medium that prevails for high offset frequencies (typically above 100 kHz), (ii) thermal fluctuations of the refractive index of the semiconductor active medium dominating for lower offset frequencies. Finally, to check the validity of the above mentioned pump noise propagation scheme, we have analyzed the correlations between the RF beatnote phase noise and the intensity noises of the two modes, which generate the RF beatnote. The correlation phase corresponding to x-polarized (or y-polarized) mode exhibits a value of $\pi/2$ (or $-\pi/2$) for low frequencies, then a phase change of $\pi/2$ around an offset frequency of about 100 kHz, and finally a zero (or $\pm\pi$) value for higher frequencies. This is indeed consistent with the considered pump noise propagation scheme. For example, the $\pi/2$-phase change around 100 kHz confirms the low-pass filter behavior of the thermal noise. Moreover, in the beatnote two optical phase noises appear with an opposite sign leading to the π-phase difference between the correlation spectra of x- and y-polarized mode. To fully

describe different noises and their correlation spectra in the dual-frequency VECSEL, we have introduced a simple model based on modified rate equations, in which the gain cross-saturation is included heuristically. The model considers pump noise as the dominant source of noise in the targeted frequency range (10 kHz to 35 MHz) and that the pump noises entering into the two spatially separated laser modes are identical in amplitude, but partially correlated with a zero correlation phase. These pump noise properties have been experimentally verified by a dedicated setup. This simple model has shown great success to reproduce all the noise correlation spectra. To further prove the consistency of the results, we have developed a more general model taking spin-dependent carrier dynamics into account. This more rigorous model has successfully reproduced different steady-state and dynamical properties of the dual-frequency VECSEL, the behavior of the nonlinear coupling between the modes, and also the spectra of the intensity noises and their correlations. The spin-dependent modeling of the dual-frequency VECSEL, on the one hand, has generalized the previous simple heuristic model and, on the other hand, has predicted few interesting phenomena for the dual-frequency VECSEL such as unequal values of the coupling coefficients, the possible existence of bistability, etc., which the simple model came short to explain. Finally, we have investigated the influence of the nonlinear coupling strengths between the two laser modes of the DF-VECSEL on the spectral behaviors of different noises and their correlation. To describe this dependence on the nonlinear coupling, we have provided a physical interpretation of the spectral behaviors of different noises and their correlations in the framework of the linear response of a two-coupled over-damped oscillator system.

In the second part of this work, we have scrutinized the spectral behaviors of the intensity noises and their correlations in a dual-frequency Nd:YAG laser for different nonlinear coupling strengths between the two cross-polarized modes. It is worth reminding that in the case of a dual-frequency Nd:YAG laser the phase-intensity coupling is negligible. Consequently, the intensity noises and their correlations hardly have any impact on the spectral purity of the RF beatnote, generated by optically mixing the two laser modes of the dual-frequency Nd:YAG laser. Nevertheless, the study of intensity noise correlations in a dual-frequency Nd:YAG laser is interesting for the following reasons: (i) applications requiring the use of the two laser modes (atomic clock, pump-probe experiments, metrology, etc.), the degree of intensity noise correlation between the two modes must be known precisely, and (ii) the dual-frequency Nd:YAG laser obeys class-B dynamics,

thus analyzing the intensity noise correlation spectra in this laser generalizes the same study performed in the class-A dual-frequency VECSEL. The presence of the relaxation oscillations in the dual-frequency Nd:YAG laser inherent to its class-B dynamics greatly modifies the spectra of the intensity noises and their correlations compared to the class-A dual-frequency VECSEL. For example, the correlation phase spectrum can exhibit a maximum of two phase jumps, and consequently there can exist up to two dips in the correlation amplitude spectrum. On the contrary, for DF-VECSEL, one can observe a maximum of one or even no phase jump in the correlation phase spectrum and as a result one or no dip in the correlation amplitude spectrum. Moreover, the presence of relaxation oscillations leads to a perfect correlation (0 dB exactly) between the intensity noises of the two modes at these oscillation frequencies, even though the noise sources (pump noises) are only partially correlated. By contrast, the intensity noise correlation amplitude never attains 0 dB value in dual-frequency VECSEL. For the physical interpretation of the noise correlation spectra we have again introduced the notion of the relaxation mechanisms of a two-coupled oscillator system. However, damped oscillatory relaxation mechanisms in dual-frequency Nd:YAG lasers are analogous to the ones in weakly damped two-coupled oscillator system. This is different from dual-frequency VECSELs, in which the exponentially damped relaxation mechanisms are rather comparable to the ones of over-damped two-coupled oscillators. To describe the experimental results a rate equation based theoretical model has been developed. In the model, it has been assumed that the emitting dipoles in active medium behave as if they were aligned along the crystallographic axes of the Nd:YAG [Schwartz et al., 2009]. Finally, this dipole orientation picture has been exploited for the minimization of the noise induced by the anti-phase relaxation oscillation in the dual-frequency Nd:YAG laser. We have succeeded to reduce the anti-phase peak in the RIN spectrum of each laser mode in excess of 20 dB by aligning the two eigenpolarizations along the crystallographic axes of a $\langle 100 \rangle$-cut Nd:YAG active medium.

The results and the concepts presented in this thesis have opened several interesting perspectives. In the following we mention only a few of them.

In the dual-frequency VECSEL, we have observed that the degree of correlation between the different noises never reaches its maximum value (0 dB). This is mainly linked with the fact that the pump noises entering into the two spatially separated modes of the dual-frequency VECSEL are only partially correlated. This partial correlation between the pump noises originates from the nonuniform intensity distribution of the pump beam

on the gain structure due to the formation of speckle at the output of the multimode fiber carrying the pump beam. This suggests that pumping the dual-frequency VECSEL with a single-mode fiber coupled diode laser may be interesting. In particular, since the intensity fluctuations of the pump coming from a single-mode fiber are expected to be uniform within the pump spot on the gain structure, one can expect a stronger correlation between the noises of the two laser modes as long as the pump noise is the dominant source of noise. In this context, electrical pumping is of course another interesting option [Kurdi et al., 2004; Keeler et al., 2005; Bousseksou et al., 2006; Frougier et al., 2013]. However, with electrical pumping it is difficult to achieve a uniform distribution of the carriers over a zone of diameter of the order of 100 μm [Tropper et al., 2004; Tropper and Hoogland, 2006], which is required for stable operation of the dual-frequency VECSEL.

It has been found that for offset frequencies higher than 10 kHz, the dominant source of noise for the RF beatnote generated by optically mixing the two laser modes of the dual-frequency VECSEL is the intensity noise of the pump diode laser. Therefore, it should be possible to improve the spectral purity of the RF beatnote by reducing the pump intensity fluctuations. This can be achieved by using an opto-electronic feedback loop. The use of opto-electronic feedback can be easily implemented for the dual-frequency VECSEL as it reacts like a low pass first order filter for low frequencies. Of course, the spectral purity of the RF beatnote can be improved by using a low noise pump source. In this context, electrical pumping or the optical pumping using a single-mode fiber coupled diode laser can again be fruitful. Moreover, the results presented in this thesis have been obtained for a DF-VECSEL under free running conditions. Therefore, the noise performance of the RF beatnote can be further improved by stabilizing it with an external RF reference using an optical phase lock loop [Pillet et al., 2008; Dumont et al., 2014].

Recently, D. Mogilevtsev et al. have proposed a microscopic model aiming at describing different noise properties of a dual-frequency VECSEL beyond classical limit [Mogilevtsev et al., 2014]. In this theoretical study, starting from quantum Langevin equations, the semiclassical rate equations for the intensities of the two cross-polarized modes of a class-A dual-frequency VECSEL have been derived. Moreover, the model includes spin-dependent carrier dynamics analogous to the model developed in Chapter 3. This model predicts several interesting non-classical features for the intensity noises of the two cross-polarized modes of a dual-frequency VECSEL such as (i) the possibility of having intensity noises below the standard quantum limit for sub-Poissonian and, even

more surprisingly for Poissonian pump fluctuations, (ii) a strong anti-correlation between the intensity fluctuations of the two laser modes for relatively strong nonlinear coupling. Notably, the model describes that the non-classical behaviors of the intensity fluctuations and their correlations originate from the correlated losses for the two laser modes. This loss correlation is established by the fact that the two modes are simultaneously coupled to a single emitter, in which the populations and the dipole polarization decay much faster than the cavity photon lifetimes for the two modes, consistent with the class-A dynamics of a DF-VECSEL. Here, the anti-correlation is linked with the coupling between the two laser modes as expected. However, the coupling between the modes originates from their common loss channel mediated by the common emitter. It is important to mention that this anti-correlation is somewhat analogous to what we have found experimentally and also verified theoretically using our two models, but remaining in purely classical picture. In our DF-VECSEL, the coupling between the two modes originates from the cross-gain saturation due to their partially common gain region. Nevertheless, it would be really interesting to experimentally verify the non-classical noise properties of a dual-frequency VECSEL as predicted by this quantum model [Mogilevtsev et al., 2014].

There is a recent study [Schmeissner et al., 2014], in which the correlations between noises (both amplitude and phase noise) corresponding to the different spectral bands of a broadband ultrafast frequency comb have been explored. It has been shown that from this spectral noise correlations one can recover the noise spectra corresponding to the global properties of the comb such as pulse energy, carrier envelope offset, temporal jitter of the pulse train. This work is based on a Ti:Sapphire mode-locked laser as the comb source. Besides, mode-locked VECSELs have shown great success for the generation of ultrafast frequency combs [Hoogland et al., 2000; Keller, 2003; Quarterman et al., 2009]. Therefore, performing such a noise correlation analysis in a mode-locked VECSEL could provide important insight about the noise dynamics of this laser. This is interesting in particular because of the fact that in a VECSEL intensity and phase noises are coupled due to the large α- factor of the semiconductor active medium [Henry, 1982].

The theoretical modeling of the dual-frequency Nd:YAG laser, based on the assumption that the dipoles are aligned along the crystallographic axes of the active medium, has shown excellent agreement with the experiments concerning the correlations between the intensity noises of the two laser modes. However, the little mismatch between the experimental results and the theoretical predictions, in particular for relative strong coupling

situations, may indicate a possible influence of spatial-hole burning. We have calculated a modified expression of the nonlinear coupling constant taking spatial-hole burning into account. Nevertheless, it would be more interesting to introduce the spatial-hole burning effect directly in the laser rate equations and then to calculate the spectra of noises and their correlation. However, the difficulty then arises from the fact that the two modes of the dual-frequency Nd:YAG laser being two polarization modes, normal mode expansion is not straightforward [Siegman, 1986].

Finally, we have shown that in a dual-frequency Nd:YAG laser the anti-phase noise can be suppressed by completely decoupling the two laser modes by aligning them along the crystallographic axes of the $\langle 100 \rangle$-cut active medium [Schwartz et al., 2009]. However, this technique cannot minimize the in-phase noise, which requires separate methods such as electronic or optical feedback loop for its minimization. It has recently been realized in a single mode Er,Yb laser that the relaxation oscillation noise can be suppressed by introducing a nonlinear saturable absorber inside the laser cavity [El Amili et al., 2014]. This technique is based on the two-photon absorption mechanism inside the saturable absorber. Therefore, once the saturable absorber is introduced inside the cavity the two-photon absorption mechanism breaks the resonant exchange of energy between the population inversion reservoir and the photon reservoir. In future, this technique can be applied in a dual-frequency Nd:YAG laser hoping to be able to reduce both the anti-phase and in-phase noises together.

Appendices

Appendix A

Characterization of amplitude and phase noises

In this appendix, we present the basic mathematical tools necessary to characterize phase and amplitude noises.

A.1 Power spectral density

Suppose $X(t)$ is a real random variable containing small fluctuations $\delta X(t)$ around the average value $\langle X \rangle$ as

$$X(t) = \langle X \rangle + \delta X(t) \ , \tag{A.1}$$

where $\langle X \rangle$ can be expressed as

$$\langle X \rangle = \lim_{T \to \infty} \frac{1}{T} \int_{t_0}^{t_0+T} X(t) dt \ . \tag{A.2}$$

For a stationary random process, which is the only one we are interested in, $\langle X \rangle$ is independent of the measuring instant t_0. Moreover, we suppose that $X(t)$ is ergodic i.e., the ensemble average is equal to the time average over a large enough interval of time. Another important quantity to characterize a random process apart from the mean is the

autocorrelation $\Gamma_{\delta X}(\tau)$, given by

$$\Gamma_{\delta X}(\tau) \;=\; \langle \delta X(t)\delta X(t+\tau)\rangle \;, \tag{A.3}$$

At $\tau = 0$, $\Gamma_{\delta X}$ is maximum and equal to the variance $\langle \delta X^2(t)\rangle$, whereas for τ tending to infinity $\Gamma_{\delta X}$ becomes zero implying that there is no more correlation between $\delta X(t)$ and $\delta X(t+\tau)$. Finally, one can calculate the power spectral density (PSD) following the Wiener-Khintchine theorem as

$$W_{\delta X}(f) \;=\; \int_{-\infty}^{+\infty} \Gamma_{\delta X}(\tau) e^{2i\pi f\tau} d\tau \;. \tag{A.4}$$

Therefore, as its name suggests, the PSD describes how the noise power is distributed over the different frequencies. In practice, $W_{\delta X}(f)$ is usually calculated as

$$W_{\delta X}(f) \;=\; \langle \widetilde{\delta X}(f)\widetilde{\delta X}(f)^*\rangle \;, \tag{A.5}$$

where tilde $\widetilde{\ }$ denotes Fourier transformed quantity, and * indicates the complex conjugate. The Fourier transformation is defined by

$$\widetilde{\delta X}(f) \;=\; \int_{-\infty}^{+\infty} \delta X(t) e^{2i\pi ft} dt \;, \tag{A.6}$$

or reciprocally,

$$\delta X(t) \;=\; \int_{-\infty}^{+\infty} \widetilde{\delta X}(f) e^{-2i\pi ft} df \;. \tag{A.7}$$

It is important to note that, in general, $\delta X(t)$ is not square-integrable, and hence its simple Fourier transform does not exist. This constraint leads to the following expression of the PSD

$$W_{\delta X}(f) \;=\; \lim_{T\to\infty} \frac{1}{T} \left| \int_{-\infty}^{+\infty} \Pi_T(t)\delta X(t) e^{2i\pi ft} dt \right|^2 \;. \tag{A.8}$$

Here, $\Pi_T(t)$ is an window function, defined as

$$\begin{aligned} \Pi_T(t) &= 1 \quad \text{if} \quad \frac{-T}{2} \leq t \leq \frac{T}{2} \ , \\ &= 0 \quad \text{if} \quad t \geq |\frac{T}{2}| \ . \end{aligned} \tag{A.9}$$

Therefore, the PSD can be expressed by

$$W_{\delta X}(f) = \lim_{T\to\infty} \frac{1}{T} \left| \int_{-\frac{T}{2}}^{\frac{T}{2}} \delta X(t) e^{2i\pi ft} dt \right|^2 \ . \tag{A.10}$$

The variance of $\delta X(t)$ can be obtained from the following expression,

$$\langle \delta X^2(t) \rangle = \int_{-\infty}^{+\infty} W_{\delta X}(f) df \ . \tag{A.11}$$

As $W_{\delta X}(f)$ is an even function, we can write

$$S_X(f) = 2W_{\delta X}(f) \ , \tag{A.12}$$

where $S_X(f)$ denotes the PSD for positive frequencies, or single sideband (SSB) PSD. In practice, the variance of noise is analyzed around an offset frequency f, and over a frequency band Δf limited by the bandwidth (BW) of the measurement system. Therefore, the noise power over the bandwidth Δf around the offset frequency f can be expressed as

$$\langle \delta X^2(t) \rangle_{\Delta f} = S_X(f) \Delta f \ . \tag{A.13}$$

Or,

$$S_X(f) = \langle \delta X^2(t) \rangle_{\Delta f} \times \frac{1}{\Delta f} \ . \tag{A.14}$$

In the following, we will use the definition of PSD as in Eq. (A.14) to quantify the different noises.

A.2 Amplitude and phase noises

Consider a signal $S(t)$ with a frequency centered at f_0, and having an amplitude $A(t)$ and a phase $\phi(t)$ as

$$S(t) \;=\; A(t)\cos(2\pi f_0 t + \phi(t)) \;. \tag{A.15}$$

We suppose that the signal contains both amplitude and phase fluctuations, which we define as follows

$$A(t) \;=\; A_0 + \delta A(t) \;, \tag{A.16}$$

$$\phi(t) \;=\; \phi_0 + \delta\phi(t) \;, \tag{A.17}$$

where A_0 and ϕ_0 are respectively the time independent part of the amplitude and phase, and $\delta A(t)$ and $\delta\phi(t)$ denote their fluctuations. Without any loss of generality, we can consider $\phi_0 = 0$. We assume that the fluctuations are small i.e., $\delta\phi(t) \ll 2\pi$ and $\delta A(t)/A_0 \ll 1$. Then, standard linearization of Eq. (A.15) leads to

$$S(t) \;\simeq\; A_0\left[\cos(2\pi f_0 t) + \frac{\delta A(t)}{A_0}\cos(2\pi f_0 t) - \delta\phi(t)\sin(2\pi f_0 t)\right] \;. \tag{A.18}$$

In practice, the amplitude and phase fluctuations are usually quantified by their respective PSDs. From Eq. (A.14), the PSD of the relative amplitude fluctuations $\delta a(t) = \frac{\delta A(t)}{A_0}$ can be written as

$$S_a(f) \;=\; \langle \delta a^2(t)\rangle \times \frac{1}{\Delta f} \;. \tag{A.19}$$

The units of $S_a(f)$ are 1/Hz. Usually, the PSDs are expressed in logarithmic scale, leading to

$$[S_a]_{\mathrm{dB}} \;=\; 10\log(S_a) \;. \tag{A.20}$$

The units of $[S_a]_{\mathrm{dB}}$ are dBc/Hz. In this thesis, the PSD of amplitude noise has always been calculated using the definition of Eq. (A.20). Similarly, the PSD of the phase fluctuations,

$S_\phi(f)$, is given by

$$S_\phi(f) \;=\; \langle \delta\phi^2(t) \rangle \times \frac{1}{\Delta f} \; . \tag{A.21}$$

The units of $S_\phi(f)$ are rad^2/Hz. The PSD of phase noise in logarithmic scale is written as

$$[S_\phi]_{\rm dB} \;=\; 10 \log(S_\phi) \; , \tag{A.22}$$

where the units are dBrad^2/Hz. It is worth mentioning here that there exists another popular representation for the phase noise PSD denoted as $\mathcal{L}(f)$, and its units are dBc/Hz or dB/Hz with respect to the power of the carrier. Originally, $\mathcal{L}(f)$ was defined as the ratio of the power in one sideband for a 1 Hz bandwidth around offset frequency f due to phase modulation by noise to the total signal power (carrier plus sidebands). However, for small sideband power compared to the carrier power, $\mathcal{L}(f)$ can be simply described as the ratio of SSB phase noise density at offset frequency f to the carrier power. In the following, we have reestablished the relation between $\mathcal{L}(f)$ and $S_\phi(f)$ using simple modulation theory [Scott et al., 2001]. Let us consider a carrier with a frequency f_0, a constant amplitude A_0, and a modulating phase $\phi(t)$ as

$$S(t) \;=\; A_0 \cos\left[2\pi f_0 t + \phi(t)\right] \; , \tag{A.23}$$

If $\phi(t)$ is modeled as a narrow-band noise process as

$$\phi(t) \;=\; m \sin(2\pi f_m t) \; , \tag{A.24}$$

we obtain

$$\begin{aligned} S(t) \;&=\; A_0 \cos\left[2\pi f_0 t + m \sin(2\pi f_m t)\right] \\ &=\; A_0 {\rm Re}\left[e^{i2\pi f_0 t} e^{im\sin(2\pi f_m t)}\right] \\ &=\; A_0 {\rm Re}\left[e^{i2\pi f_0 t} \sum_{l=-\infty}^{\infty} J_l(m) e^{il2\pi f_m t}\right] \; , \end{aligned} \tag{A.25}$$

where m and f_m respectively denote the depth and the frequency of modulation, and the J_ls are Bessel functions of the first kind. Equation (A.25) can be simplified using the approximation of small modulation depth ($m \ll 1$)

$$\begin{aligned} J_l(m) \quad &\approx 1 \quad \text{if} \quad l = 0 \\ &\approx \pm m/2 \quad \text{if} \quad l = \pm 1 \\ &\approx 0 \quad \text{if} \quad |l| > 1 \ , \end{aligned} \tag{A.26}$$

and the symmetry property of the Bessel functions $J_{-1}(m) = -J_1(m)$, leading to

$$S(t) \approx A_0 \mathrm{Re}\left[e^{i2\pi f_0 t}\left\{1 + \frac{m}{2}\left(e^{i2\pi f_m t} - e^{-i2\pi f_m t}\right)\right\}\right] \ . \tag{A.27}$$

From Eq. (A.27), the ratio of the SSB noise to the carrier power can be written as

$$\mathcal{L}(f_m) \approx \frac{m^2}{4} \ . \tag{A.28}$$

On the other hand, using the definition of Eq (A.21), we obtain

$$S_\phi(f_m) = \frac{m^2}{2} \ . \tag{A.29}$$

. Thus

$$\mathcal{L}(f) \approx \frac{S_\phi(f)}{2} \ . \tag{A.30}$$

Therefore, one simply needs to subtract 3 dB from $S_\phi(f)$ to arrive at $\mathcal{L}(f)$. However, its important to note that the above relation is valid only for small phase fluctuations so that the linear approximation to the Bessel functions holds [Eq. (A.26)]. The above definition breaks down for the mean-squared phase deviation exceeding $0.1\,\mathrm{rad}^2$, or even if there exists some correlation between the powers in the upper and lower sidebands. Nevertheless, $\mathcal{L}(f)$ is a popular choice to quantify phase noise, in particular, when amplitude noise becomes also important as then both amplitude and phase noise can be represented using the same scale, and hence can be compared. To facilitate the use of $\mathcal{L}(f)$ even when the small angle approximation is not valid or the correlation between the upper and lower

sidebands is not known, $\mathcal{L}(f)$ has been simply defined as [Allan et al., 1988]

$$\mathcal{L}(f) \;=\; \frac{S_\phi(f)}{2}\ . \tag{A.31}$$

In this thesis, to quantify phase noise we have always used the units of dBc/Hz, which simply differ by 3 dB from the units of $\mathrm{dBrad}^2/\mathrm{Hz}$.

Appendix B

Noise in a $1\,\mu$m DF-VECSEL

In this appendix, we report the results for DF-VECSEL operating at $1\,\mu$m. In particular, we analyze, both experimentally and theoretically, the spectral behaviors of intensity noises of the two laser modes and their correlation, and the RF beatnote and its phase noise spectra for different coupling situations for frequencies between 10 kHz to 50 MHz [De et al., 2013b, 2014b]. It is important to mention here that the noise analysis in the $1\,\mu$m DF-VECSEL has been performed before than in the $1.5\,\mu$m DF-VECSEL as initially we had only the $1\,\mu$m laser. For the $1\,\mu$m DF-VECSEL also, the theoretical spectra are obtained using the model, reported in Chapter 2. All the noise measurements are performed for three different coupling situations obtained by using BCs of thicknesses 1 mm, 0.5 mm and 0.2 mm, which respectively correspond to spatial separations d of 100 μm, 50 μm and 20 μm between the two modes inside the gain structure. These respectively lead to $C = 0.1$, $C = 0.35$, and $C = 0.65$ for the radii (w) of two modes on the gain structure equal to $62\,\mu$m. The coupling constant C here is calculated using Eq. (2.50) of Chapter 2 [Pal et al., 2010]. The configuration of the laser cavity is identical to the one, displayed in Fig. 1.3 of Chapter 1.

B.1 Intensity noise correlation

In this section, we deal with the spectral behaviors of the intensity noises of the two cross-polarized modes and the correlation between these two intensity noises both experimentally and theoretically [De et al., 2013b]. We start by showing in Fig. B.1, the

measured pump RIN in the targeted frequency range from 10 kHz to 50 MHz. The pump

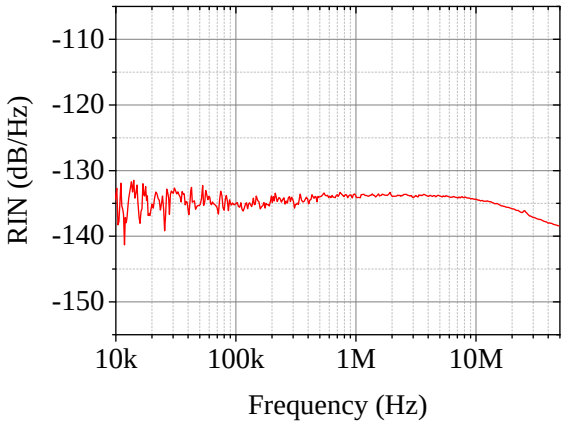

Figure B.1: RIN spectrum of the pump laser.

noise is white within the considered frequency range. Moreover, we find that the level of pump noises entering into the two laser modes are almost identical. In the following, we will utilize this pump RIN spectrum to calculate the intensity noise properties of the DF-VECSEL. However, in this case we have not carried out the pump noise correlation measurement. We consider that the pump noises entering into the two laser modes are partially correlated ($\eta < 1$), and the correlated part of the noises are in phase ($\psi = 0$) as obtained in the case of 1.55 μm$-$DF-VECSEL. Then, we adjust the value of η to match the experimental results for different coupling situations.

Figure B.2 shows the experimental and theoretical results for $C = 0.1$. The first order filter like behavior of the measured RIN spectra of the two modes as depicted in Fig. B.2(a) confirms the class-A dynamical behavior of the laser. The RIN spectra of the two modes (blue-circled, and red-squared lines of Fig. B.2(a)) are not exactly identical because of the slight difference between the losses and/or gains for them. The experimental noise correlation amplitude and phase spectra are shown in Figs. B.2(c),(e), respectively. Figure B.2(c) shows that the intensity noises of the two modes are partially correlated (-7 dB, 0 dB corresponds to full correlation), whereas Fig. B.2(e) shows that the correlation phase is zero in the considered frequency range (10 kHz to 50 MHz). The theoretical RIN, correlation amplitude, and correlation phase spectra are respectively reproduced in Figs. B.2(b),(d),(f). A good agreement is observed with the corresponding experimental spectra (Figs. B.2(a),(c),(e), respectively). The staircase like black curve in Fig. B.2(c) is

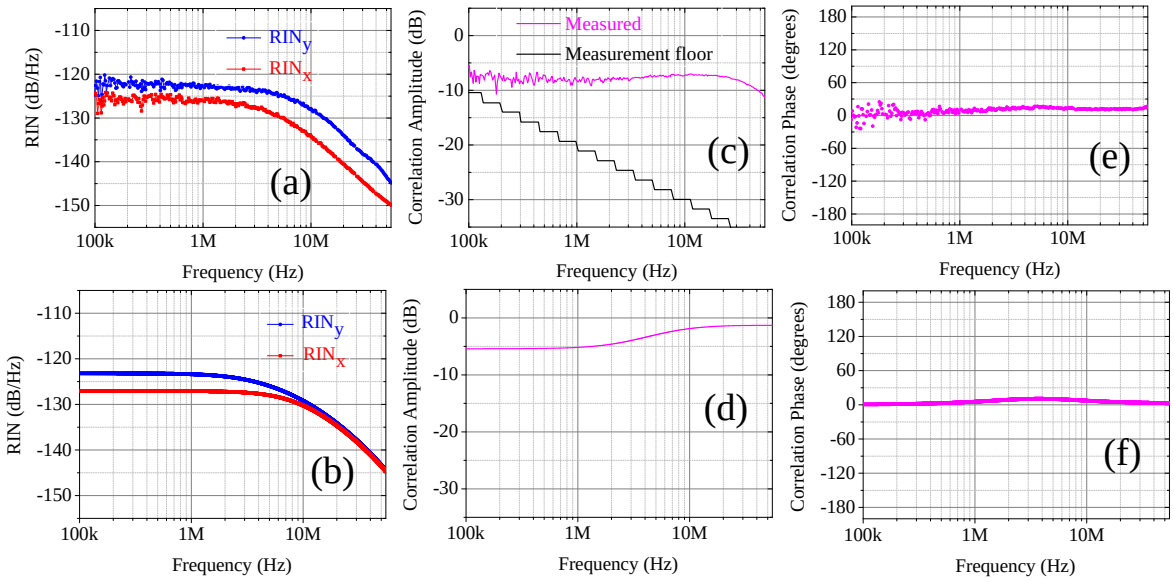

Figure B.2: Results for $C = 0.34$. RIN spectra (a) experimental and (b) theoretical; correlation amplitude spectra (c) experimental and (d) theoretical; correlation phase spectra (e) experimental and (f) theoretical. Parameter values: $r_x = 1.42$, $r_y = 1.3$, $1/\gamma_x \approx 5$ ns, $1/\gamma_y \approx 5.4$ ns, $1/\Gamma = 3$ ns, $\eta = 0.4$, $\psi = 0$, $\mathrm{RIN}_{\mathrm{Pump}} = -138$ dB/Hz.

showing the level of the minimum measurable correlation.

The experimental and theoretical results for $C = 0.35$ are reproduced in Fig. B.3. As one can see in Fig. B.3(c), the degree of correlation is close to the level of minimum correlation for frequencies lower than 2 MHz, and for higher frequencies the correlation gradually increases and reaches -3 dB at about 20 MHz. Moreover, the correlation phase spectrum of Fig. B.3(e) reveals that the correlation phase is zero for frequencies higher than 2 MHz, whereas for low frequencies it can not be measured as the correlation amplitude equals the minimum level. The theoretical spectra of RIN, correlation amplitude and phase as shown in Figs. B.3(b),(d),(f), respectively, are nicely matching the corresponding experimental one (Figs. B.3(a),(c),(e), respectively).

Finally, the experimental as well as the theoretical results for $C = 0.65$ are reproduced in Fig. B.4. In this coupling case, one can observe a change of slope around 2 MHz in the experimental RIN spectra of both the laser modes (Fig. B.4(a)). Additionally, there is a dip at about 2 MHz in the experimental correlation amplitude spectrum (Fig. B.4(c)), and apart from this dip the level of correlation is high (-2 dB) for both low and high frequencies. Furthermore, the experimental correlation phase spectrum (Fig. B.4(e)) shows

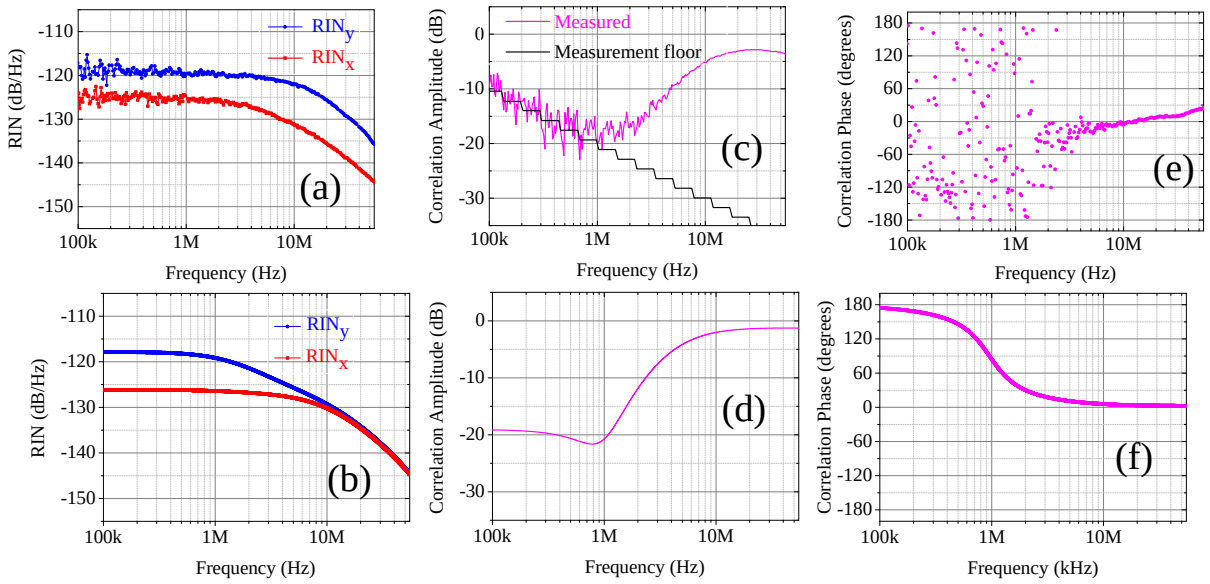

Figure B.3: Results for $C = 0.34$. RIN spectra (a) experimental and (b) theoretical; correlation amplitude spectra (c) experimental and (d) theoretical; correlation phase spectra (e) experimental and (f) theoretical. Parameter values: $r_x = 1.4$, $r_y = 1.32$, $1/\gamma_x \approx 5$ ns, $1/\gamma_y \approx 5.5$ ns, $1/\Gamma = 3$ ns, $\eta = 0.65$, $\psi = 0$, $\mathrm{RIN}_{\mathrm{Pump}} = -138$ dB/Hz.

that the phase of correlation is π for frequencies lower than 2 MHz, whereas it is zero for frequencies higher than this cut-off frequency. In this coupling situation also the theoretical model exhibits very good agreement with the experimental results regarding the RIN (Figs. B.4(a,b)), the correlation amplitude (Figs. B.4(c,d)) and correlation phase spectra (Figs. B.4(e,f)).

B.2 Phase noise of the RF beatnote

After having discussed the intensity noises and their correlation in the previous section, we present here the spectral behavior of the RF beatnote and its phase noise for frequencies between 10 kHz and 50 MHz. Figure B.5 shows the experimental and theoretical phase noise PSDs along with the spectra of the corresponding RF beatnotes for the same three different coupling strengths ($C = 0.1$, 0.35, 0.65, respectively) as previously. In Figs. B.5(a),(c),(e) the pink-filled circles and the violet line respectively represent the experimental and theoretical PSDs of the RF phase noise. The theoretical

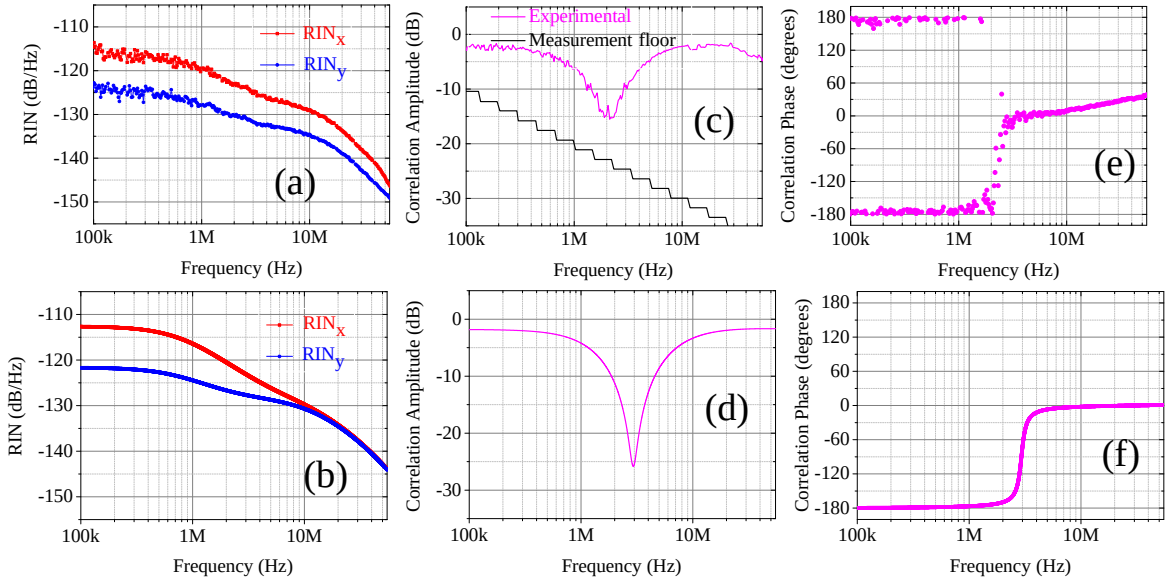

Figure B.4: Results for $C = 0.65$. RIN spectra (a) experimental and (b) theoretical; correlation amplitude spectra (c) experimental and (d) theoretical; correlation phase spectra (e) experimental and (f) theoretical. Parameter values: $r_x = 1.45$, $r_y = 1.5$, $1/\gamma_x \approx 5.2$ ns, $1/\gamma_y \approx 5$ ns, $1/\Gamma = 3$ ns, $\eta = 0.8$, $\psi = 0$, $\mathrm{RIN_{Pump}} = -138$ dB/Hz.

RF phase noise PSDs are obtained by considering two different physical mechanisms induced by pump noise as described in Chapter 2: (i) phase-intensity coupling due to the large $\alpha-$factor of the semiconductor gain medium, and (ii) fluctuations of the refractive index of the semiconductor gain structure due to its temperature fluctuations. The contributions from the phase-intensity coupling and the thermal effect to the RF phase noise are respectively represented by the dash-dotted blue and dashed-green lines in Figs. B.5(a),(c),(e). For $C = 0.1$, the phase noise and the corresponding RF beatnote spectra are shown in Figs. B.5(a),(b), respectively. In this case, the dominant contribution to the RF phase noise for offset frequencies higher than 700 kHz originates from phase-intensity coupling, whereas thermal noise is dominant for lower frequencies (10 kHz − 700 kHz). Figure B.5(c),(d) respectively displays the phase noise PSD and corresponding RF beatnote for $C = 0.35$. In this coupling situation, thermal effect is dominant for lower offset frequencies (10 kHz - 500 kHz), whereas the contribution from phase-intensity coupling mechanism prevails for frequencies higher than 500 kHz (Fig. B.5(c)). The phase noise PSD and the corresponding beatnote spectra for $C = 0.65$ are depicted in Figs. B.5(e),(f), respectively. Here, the thermal effect dominates for frequencies between

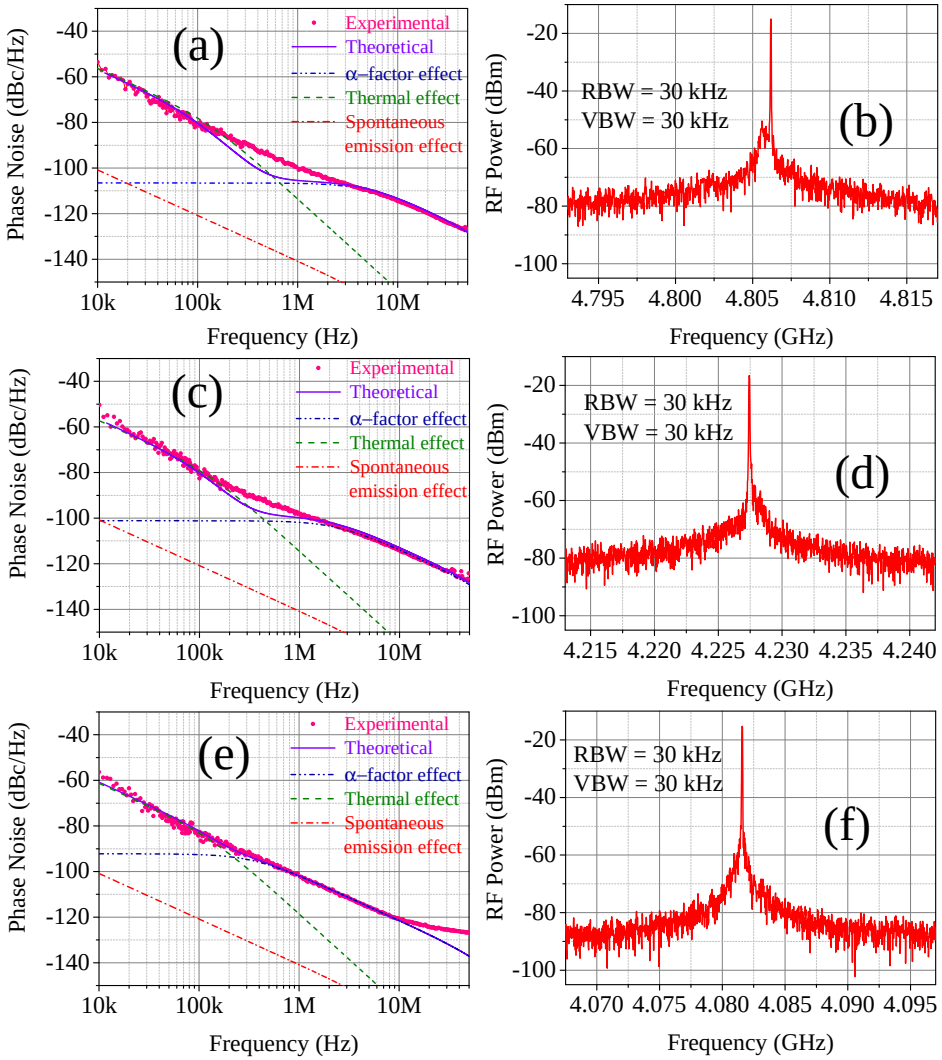

Figure B.5: Results for RF beatnote phase noise. $C = 0.1$: (a) phase noise, (b)beatnote; $C = 0.35$: (c) phase noise, (d)beatnote; $C = 0.65$: (e) phase noise, (f) beatnote. Beatnote spectrum is measured by ESA with resolution bandwidth (RBW) = 30 kHz and video bandwidth (VBW) = 30 kHz. Parameter values: $\alpha = 12$, $\tau = 3$ ns, $\mathrm{RIN_{Pump}} = -138$ dB/Hz, $\eta = 0.85$, $D_T = 0.22$ cm^2.s^{-1}, $d\overline{n}/dt = 2.7 \times 10^{-4}$ K^{-1}, $L_{\mathrm{SC}} = 2.3$ μm, $L_{\mathrm{cav}} = 1.5$ cm, $w_{\mathrm{Pump}} = 50$ μm, $R_T = 6$ K.W^{-1}, $P_{\mathrm{Pump}} = 1.5$ W. The other parameter values used for the simulation in (a), (c), and (e) are identical as in Figs. B.2, B.3, B.4.

10 kHz and 200 kHz, while the high frequency contribution predominantly comes from phase-intensity coupling effect. The RF beatnotes for all three coupling situations as shown in Figs. B.5(b),(d),(f) are around 4-5 GHz and sitting on a noise pedestal mainly

due to the phase noises as given in Figs. B.5(a),(c),(e), respectively. The little discrepancy between theory (violet line) and experiment (pink squares) around 500 kHz in the phase noise PSD for low and moderate couplings (Figs B.5(a),(c), respectively) probably comes from the crude approximation of the thermal response of the structure by a simple first order filter, and also from the approximate expression we choose for the thermal response time of the structure as discussed in Chapter 2 [Davis et al., 1998]. For strong coupling, the little discrepancy for frequencies higher than 20 MHz comes from the fact that the phase noise approaches the measurement floor (~ -130 dBc/Hz), and it should not be taken into account. Apart from this, theory shows excellent agreement with the experiment for all coupling situations.

B.3 Physical explanation

To explain the spectral behaviors of the intensity noises and their correlations as well as the phase noise of the RF beatnote we can again draw the analogy between our two-mode laser and a two-coupled meachanical oscillator system as discussed in Chapter 2. Analogous to any symmetric two-coupled oscillator system, the DF-VECSEL exhibits two eigenrelaxation mechanisms: (i) in-phase relaxation mechanism and (ii) anti-phase relaxation mechanism [Otsuka et al., 1992]. These two relaxation mechanisms are associated with two different eigenfrequencies and/or damping rates. Moreover, since the 1 μm DF-VECSEL exhibit class-A dynamics, the relaxation mechanisms are exponentially damped (without any relaxation oscillation). The transfer functions of the in-phase and the anti-phase response, as obtained from Eqs. (C.14-C.15) in Appendix C, are shown in Fig. B.6 for three different coupling situations in the frequency range from 10 kHz to 50 MHz. As one can see in Fig. B.6, the cut-off frequency of the anti-phase response (black line) is lower than the cut-off frequency of the in-phase response (pink line). Moreover, the anti-phase response strongly depends on the coupling strength, whereas the in-phase one does not. Therefore, the noise response of each laser mode, obtained by superposing the anti-phase and the in-phase responses, must depend on the relative dominance between these two eigenrelaxation mechanisms. In the case of $C = 0.1$, the intensity noise spectra of the two modes are governed mainly by the in-phase relaxation mechanism for all frequencies as shown in Fig. B.6(a). This leads to the zero correlation phase for all frequencies as depicted in Figs. B.2(e),(f). Moreover, the two modes are pumped by the same pump and

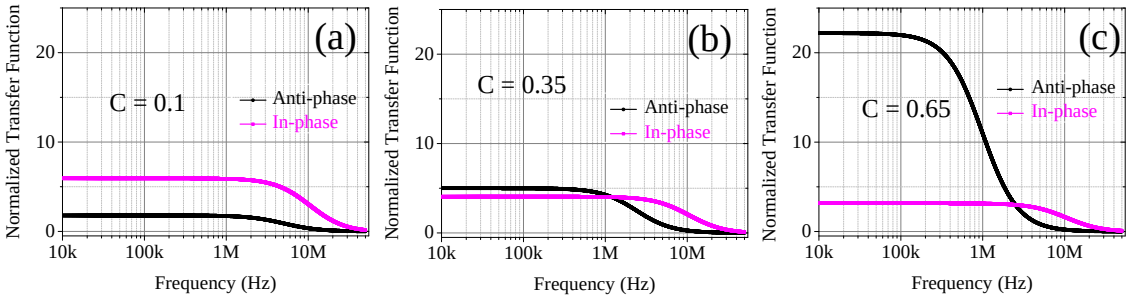

Figure B.6: The theoretical normalized transfer function for both in-phase and anti-phase relaxation mechanism for three different values of coupling (a) $C = 0.1$, (b) $C = 0.65$ and (c) $C = 0.35$. Parameter values used for simulation: (a) $r = 1.4$, $1/\gamma_{\text{cav}} = 5.2$ ns, $\eta = 0.4$; (b) $r = 1.35$, $1/\gamma_{\text{cav}} = 5.2$ ns, $\eta = 0.65$; (c) $r = 1.42$, $1/\gamma_{\text{cav}} = 5.1$ ns, $\eta = 0.8$. The other parameter values: $1/\Gamma = 3$ ns, $\psi = 0$.

the pump intensity fluctuations entering into the two laser modes are identical white noises with partial positive correlation ($\eta = 0.4$, $\psi = 0$). Therefore, the intensity fluctuations of the two-modes are also partially correlated (Figs. B.2(c),(d)). For $C = 0.35$, the in-phase and the anti-phase responses are comparable for frequencies lower than 2 MHz, whereas above this cut-off frequency the in-phase mechanism strongly dominates over the anti-phase one (Fig. B.6(b)). This explains why the correlation amplitude is very low for frequencies lower than 2 MHz, but increases to a high value above this cut-frequency as shown in Figs. B.3(c),(d). In addition to that, for frequencies lower than 2 MHz, the correlation phase has no significant meaning as the correlation amplitude is very low, whereas for higher frequencies the correlation phase is zero due to dominating in-phase mechanism. This is what we have seen in Figs. B.3(e),(f). In the case of $C = 0.65$, the low frequency behavior (below 2 MHz) of the noise spectrum of each mode is mainly governed by the anti-phase relaxation mechanism, whereas above this cut-frequency the dominant contribution comes from the in-phase response (Fig. B.6(c)). This transition from dominant anti-phase to dominant in-phase behavior of the noise response at about 2 MHz frequency leads to a change of slope in the RIN spectra around this cut-off frequency as shown in Fig. B.4(a),(b). This crossing between the in-phase and anti-phase responses is also responsible for the π-phase jump at about 2 MHz. Additionally, the correlation phase is zero or π for frequencies higher or lower than 2 MHz as the in-phase or the anti-phase response dominates over the other, respectively. This has been reproduced in Figs. B.4(e),(f). Moreover, destructive interference between the two nearly identical

intensity noises of the two modes due to the π-phase jump around 2 MHz accounts for the dip in the correlation amplitude. Apart from the dip the degree of correlation is higher (~ -2 dB) than the weaker coupling situations because of the stronger coupling between the modes and the higher pump noise correlation factor. Figures B.4(c),(d) reproduce this spectral behavior of the correlation amplitude.

The beatnote phase noise spectra for different coupling cases as shown in Fig. B.5 can also be explained from the view point of the in-phase and anti-phase eigenrelaxation mechanisms. Figure B.5 illustrates that the thermally induced phase noise (dashed-green line) is almost independent of C, whereas the phase noise coming from the phase-intensity coupling (dash-dotted blue line) via the large $\alpha-$factor of the semiconductor active medium strongly depends on C. Specifically, one can notice that the RF phase noise induced by the phase-intensity coupling mechanism increases with the increase of the nonlinear coupling strength, in particular, for low frequencies. This can be explained as follows: in case of $C = 0.65$, for the low frequencies (below 2 MHz), the correlation between the intensity noises is high (- 2 dB) but with opposite phases as for these frequencies anti-phase mechanism dominates. Therefore, the optical phase noises coming from the intensity noises of the two laser modes due to the phase-intensity coupling mechanism add up, leading to a high RF phase noise for low frequencies. However, for $C = 0.1$ or $C = 0.35$, the anti-phase response is lower than or comparable to the in-phase response for frequencies lower than 2 MHz (Figs. B.6(a),(c) respectively). As a result for these frequencies, the phase noise of the RF beatnote coming from the intensity noises, which are either positively correlated ($C = 0.1$) or almost uncorrelated ($C = 0.35$), is relatively low for these weaker coupling situations. This also explains why the matching between the experiment (pink circles) and theory (violet line) is so perfect for strongest coupling (Fig. B.5(e)) compared to the relatively weaker couplings (Fig. B.6(a),(c)).

B.4 Conclusion

In this appendix, we have presented the experimental results regarding the intensity noises and their correlations, the RF beatnote and its phase noise for different coupling strengths between the two cross-polarized modes of a DF-VECSEL operating at 1 μm. We have compared the experimental results with the predictions of the theoretical model introduced in Chapter 2 to explain the different noise properties of a 1.55 μm-DF-VECSEL.

We evidenced that the very same model could well explain different noise properties of the 1 μm-DF-VECSEL. This proves the generality of our simple rate equation based model to explain the different noise properties of DF-VECSELs operating at different wavelengths.

Appendix C

In-Phase and anti-phase relaxation mechanism

Let us consider a laser driven out of its steady-state intensity by a small distance. Then the laser will relax back to its steady-state solution, following either an exponential or a damped oscillation, depending on whether the laser belongs the class-A or class-B dynamical regime [Arecchi et al., 1986; Otsuka et al., 1992]. This is somewhat analogous to a single mechanical or electrical oscillator, in which the relaxation mechanism can also be either exponential or damped oscillatory depending on the damping factor. Similarly, for a dual-frequency laser we can draw an analogy with a two-coupled mechanical oscillator system. Henceforth, the relaxation mechanism of the dual-frequency laser can be analyzed like any two-coupled mechanical oscillator system by introducing the eigenrelaxation mechanism of the global system [Otsuka et al., 1992]. In this appendix, we aim at deriving the transfer functions associated with the in-phase and anti-phase relaxation mechanisms in the case of a class-A dual-frequency VECSEL and a class-B dual-frequency Nd:YAG laser.

C.1 Class-A dual-frequency VECSEL

The class-A dynamics of the dual-frequency VECSEL due to a photon lifetime inside the cavity longer than the carriers' lifetime leads to the exponentially damped relaxation mechanisms. In general, deriving the analytical expressions of the relaxation modes is

quite cumbersome. However, this becomes fairly simple if someone considers that the two modes of the dual-frequency laser play symmetrical role, i.e., they have identical losses, gains, etc,. In that case, the relaxation mechanisms become the symmetric (in-phase) and asymmetric (anti-phase) mechanisms. In the case of a dual-frequency VECSEL as described in Chapter 2, this leads to

$$\gamma_x = \gamma_y \equiv \gamma_{\rm cav} \ , \tag{C.1}$$

$$N_{0x} = N_{0y} \equiv N_0 \ , \tag{C.2}$$

$$\xi_{xy} = \xi_{yx} \equiv \xi \ . \tag{C.3}$$

Then, the steady solution corresponding to the simultaneous oscillation of the two modes for the DF-VECSEL, as given in Eqs. (2.25-2.28) of Chapter 2, simplifies as

$$r_x = r_y \equiv r \ , \tag{C.4}$$

$$N_{x\rm th} = N_{y\rm th} = \frac{\gamma_{cav}}{\kappa} \equiv N_{\rm th} \ , \tag{C.5}$$

$$F_{x0} = F_{y0} = \frac{\Gamma/\kappa(r-1)}{(1+\xi)} \equiv F_0 \ . \tag{C.6}$$

This leads to the following expressions for the coefficients of the linear response transfer matrix relating the photon number fluctuations $[\widetilde{\delta F}_x(f), \widetilde{\delta F}_y(f)]$ to the pump fluctuations $[\widetilde{\delta N}_{0x}(f), \widetilde{\delta N}_{0y}(f)]$ as mentioned in Eqs. (2.41-2.44) of Chapter 2:

$$M_{xx}(f) = M_{yy}(f) = \frac{\Gamma\left[\gamma_{\rm cav} - \frac{2i\pi f}{\kappa F_0}(r\Gamma - 2i\pi f)\right]}{\Delta(f)} \ , \tag{C.7}$$

$$M_{xy}(f) = M_{yx}(f) = -\frac{\Gamma\gamma_{\rm cav}\xi}{\Delta(f)} \ , \tag{C.8}$$

where

$$\Delta(f) = \left[\gamma_{\rm cav} - \frac{2i\pi f}{\kappa F_0}(r\Gamma - 2i\pi f)\right]^2 - C\gamma_{\rm cav}^2 \ . \tag{C.9}$$

We define the in-phase and anti-phase fluctuations as follows,

$$\widetilde{\delta F}_{\rm In}(f) = \widetilde{\delta F}_x(f) + \widetilde{\delta F}_y(f) \ , \tag{C.10}$$

$$\widetilde{\delta F}_{\rm Anti}(f) = \widetilde{\delta F}_x(f) - \widetilde{\delta F}_y(f) \ . \tag{C.11}$$

Then, using Eqs. (C.7-C.11), we obtain

$$\widetilde{\delta F}_{\rm In}(f) = \frac{\Gamma^2(r-1)(\widetilde{\delta N}_{0x} + \widetilde{\delta N}_{0y})}{(1+\xi)\left[\{\Gamma\gamma_{\rm cav}(r-1) - 4\pi^2 f^2\} - 2i\pi f r\Gamma\right]} \ , \tag{C.12}$$

$$\widetilde{\delta F}_{\rm Anti}(f) = \frac{\Gamma^2(r-1)(\widetilde{\delta N}_{0y} - \widetilde{\delta N}_{0y})}{(1+\xi)\left[\{\Gamma\gamma_{\rm cav}(r-1)\frac{(1-\xi)}{(1+\xi)} - 4\pi^2 f^2\} - 2i\pi f r\Gamma\right]} \ . \tag{C.13}$$

Now, we recall the properties of the pump noise fluctuations as described in Chapter 2. The pump noises for the two modes are taken as identical white noises [Eq. (2.31)], and these pump fluctuations are partially correlated ($\eta < 1$) with the phase (ψ) of the correlation equal to zero [Eq. (2.32)]. Using these pump noise properties in Eqs. (C.12-C.13), we obtain the following transfer functions for the in-phase and anti-phase responses

$$\begin{aligned} T_{\rm In}(f) &= \frac{|\widetilde{\delta F}_{\rm In}(f)|^2}{|\widetilde{\delta N}_0|^2} \\ &= \frac{2\Gamma^4(r-1)^2(1+\eta\cos\psi)}{(1+\xi)^2\left[\{\Gamma\gamma_{\rm cav}(r-1) - 4\pi^2 f^2\}^2 + (2\pi f r\Gamma)^2\right]} \ , \end{aligned} \tag{C.14}$$

$$\begin{aligned} T_{\rm Anti}(f) &= \frac{|\widetilde{\delta F}_{\rm Anti}(f)|^2}{|\widetilde{\delta N}_0|^2} \\ &= \frac{2\Gamma^4(r-1)^2(1-\eta\cos\psi)}{(1+\xi)^2\left[\{\Gamma\gamma_{\rm cav}(r-1)\frac{(1-\xi)}{(1+\xi)} - 4\pi^2 f^2\}^2 + (2\pi f r\Gamma)^2\right]} \ . \end{aligned} \tag{C.15}$$

Then, we introduce the following normalized spectra for the in-phase and anti-phase noises

$$\begin{aligned} S_{\rm In}(f) &= \frac{|\widetilde{\delta F}_{\rm In}(f)|^2}{F_0^2} \\ &= \frac{2\Gamma^2\gamma_{\rm cav}^2 r^2(1+\eta\cos\psi)\times {\rm RIN}_{\rm pump}}{\left[\Gamma\gamma_{\rm cav}(r-1) - 4\pi^2 f^2\right]^2 + (2\pi f r\Gamma)^2} \ , \end{aligned} \tag{C.16}$$

$$
\begin{aligned}
S_{\mathrm{Anti}}(f) &= \frac{|\widetilde{\delta F}_{\mathrm{Anti}}(f)|^2}{F_0^2} \\
&= \frac{2\Gamma^2\gamma_{\mathrm{cav}}^2 r^2(1-\eta\cos\psi)\times \mathrm{RIN}_{\mathrm{pump}}}{\left[\Gamma\gamma_{\mathrm{cav}}(r-1)\frac{(1-\xi)}{(1+\xi)} - 4\pi^2 f^2\right]^2 + (2\pi f r\Gamma)^2} \ . \qquad \text{(C.17)}
\end{aligned}
$$

The in-phase and anti-phase noise spectra as given by Eqs. (C.16-C.17) exhibit first-order transfer functions, provided the photon lifetimes ($\gamma_{\mathrm{cav}}^{-1}$) inside the cavity of the two modes are longer than the carriers' lifetime (Γ^{-1}). This is exactly what happens for dual-frequency VECSELs as the photon lifetimes (γ_x^{-1}, γ_y^{-1} $\sim$ 10 ns) inside the cavity are longer than the carriers' lifetime (Γ^{-1} $\sim$ 1 ns). Moreover, the in-phase and anti-phase responses exhibit different cut-off frequencies. This leads to different types of spectral behaviors for the noise spectrum of the laser modes obtained by superposing the in-phase and anti-phase responses. Additionally, Eqs. (C.16-C.17) show that the anti-phase response depends on the nonlinear coupling, whereas the in-phase one does not. This is translated to the coupling dependent spectral properties of the intensity noises for the two modes of the DF-VECSEL (Chapter 2).

C.2 Class-B dual-frequency Nd:YAG laser

In this section, we derive the transfer functions of the in-phase and the anti-phase relaxation mechanisms for a dual-frequency Nd:YAG lasers. These lasers exhibit class-B dynamics as the photon lifetimes (γ_x^{-1}, γ_y^{-1} $\sim$ 10 ns) for the two cross-polarized modes inside the cavity are shorter than the population inversion lifetime (Γ^{-1} $\sim$ 200 μs). This leads to the damped oscillatory behaviors of the in-phase and anti-phase eigenrelaxation mechanisms. Here also, we choose the simple case of symmetrical modes i.e., the two laser modes have identical losses, gains, etc. This gives the following steady-state solution for the simultaneous oscillation of the two cross-polarized modes in the dual-frequency Nd:YAG laser as obtained from Eqs. (4.21-4.24) of Chapter 4

$$
N_{1\mathrm{th}} = N_{2\mathrm{th}} = \frac{\gamma_{cav}}{\kappa(A+B)} \equiv N_{\mathrm{th}} \ , \qquad \text{(C.18)}
$$

$$
F_{x0} = F_{y0} = \frac{\Gamma/\kappa(r-1)}{(A+B)} \equiv F_0 \ . \qquad \text{(C.19)}
$$

We can then simplify the linear response transfer matrix coefficients in Eqs. (4.32-4.35) of Chapter 4 as follows

$$M_{xx}(f) = M_{yy}(f) = \frac{\Gamma A(A^2-B^2)\left[\gamma_{\rm cav}(A-B) - \frac{2i\pi f}{\kappa F_0}(r\Gamma - 2i\pi f)\right]}{\Delta(f)} , \quad \text{(C.20)}$$

$$M_{xy}(f) = M_{yx}(f) = \frac{\Gamma B(A^2-B^2)\left[\gamma_{\rm cav}(A-B) + \frac{2i\pi f}{\kappa F_0}(r\Gamma - 2i\pi f)\right]}{\Delta(f)} , \quad \text{(C.21)}$$

where

$$\begin{aligned}\Delta(f) = \quad & A^2\left[\gamma_{\rm cav}(A-B) - \tfrac{2i\pi f}{\kappa F_0}(r\Gamma - 2i\pi f)\right]^2 \\ & -B^2\left[\gamma_{\rm cav}(A-B) + \tfrac{2i\pi f}{\kappa F_0}(r\Gamma - 2i\pi f)\right]^2 .\end{aligned} \quad \text{(C.22)}$$

As previously, we use the definitions of Eqs. (C.10-C.11) for the in-phase and anti-phase fluctuations to obtain

$$\widetilde{\delta F}_{\rm In}(f) = \frac{\Gamma^2(r-1)(\widetilde{\delta N}_{01} + \widetilde{\delta N}_{02})}{[\{\Gamma\gamma_{\rm cav}(r-1) - 4\pi^2 f^2\} - 2i\pi f r\Gamma]} , \quad \text{(C.23)}$$

$$\widetilde{\delta F}_{\rm Anti}(f) = \frac{\Gamma^2(r-1)\frac{(A-B)}{(A+B)}(\widetilde{\delta N}_{01} - \widetilde{\delta N}_{02})}{\left[\{\Gamma\gamma_{\rm cav}(r-1)\frac{(A-B)^2}{(A+B)^2} - 4\pi^2 f^2\} - 2i\pi f r\Gamma\right]} . \quad \text{(C.24)}$$

Then, using the properties of the pump fluctuations ($\widetilde{\delta N}_{01}$, $\widetilde{\delta N}_{02}$) as shown in Chapter 4, i.e., the pump noises for the two dipole families in the Nd:YAG active medium are identical white noises [Eq. (4.37)], and they are partially positively correlated [Eq. (4.39)], we obtain

$$\begin{aligned} T_{\rm In}(f) &= \frac{|\widetilde{\delta F}_{\rm In}(f)|^2}{|\widetilde{\delta N}_0|^2} \\ &= \frac{2\Gamma^4(r-1)^2(1+\eta\cos\psi)}{[\Gamma\gamma_{\rm cav}(r-1) - 4\pi^2 f^2]^2 + (2\pi f r\Gamma)^2} , \end{aligned} \quad \text{(C.25)}$$

$$\begin{aligned} T_{\rm Anti}(f) &= \frac{|\widetilde{\delta F}_{\rm Anti}(f)|^2}{|\widetilde{\delta N}_0|^2} \\ &= \frac{2\Gamma^4(r-1)^2\frac{(A-B)^2}{(A+B)^2}(1-\eta\cos\psi)}{\left[\Gamma\gamma_{\rm cav}(r-1)\frac{(A-B)^2}{(A+B)^2} - 4\pi^2 f^2\right]^2 + (2\pi f r\Gamma)^2} . \end{aligned} \quad \text{(C.26)}$$

The transfer functions of the in-phase and anti-phase relaxation mechanisms as given in Eqs. (C.25-C.26) exhibit resonant peak like a second-order filter illustrating class-B dynamical behavior of the dual-frequency Nd:YAG laser. In addition to that, the eigen-frequencies of the in-phase and anti-phase relaxation oscillations are different, and they can be easily obtained from Eqs. (C.25-C.26) as

$$f_{\mathrm{In}} = \frac{1}{2\pi}\sqrt{\Gamma\gamma_{\mathrm{cav}}(r-1)}\ , \tag{C.27}$$

$$f_{\mathrm{Anti}} = \frac{1}{2\pi}\sqrt{\Gamma\gamma_{\mathrm{cav}}(r-1)\frac{(A-B)^2}{(A+B)^2}}\ . \tag{C.28}$$

These different eigenfrequencies lead to the two peaks in the RIN spectrum of each laser mode of the dual-frequency Nd-YAG laser as shown in Chapter 4. Moreover, Eqs. (C.25-C.26) infer that the in-phase response is independent of the nonlinear coupling between the modes, whereas the anti-phase response strongly depends on the nonlinear coupling. This explains why the intensity noises and their correlation spectra exhibit strong dependence on the nonlinear coupling between the two modes in the dual-frequency Nd:YAG laser as reported in Chapter 4. Moreover, one can notice from Eq. (C.26) that the anti-phase peak should disappear for $\eta = 1$, i.e., for perfect correlation of the pump noises seen by the two dipole families. The presence of the anti-phase peak in the experimental RIN spectra for all three coupling situations (Figs. 4.5-4.7) proves that the pump fluctuations intercepted by the two dipole families are indeed not perfectly correlated, i.e., $\eta < 1$. This validates our assumption in Eq. (4.39) for the theoretical modeling of Chapter 4.

Appendix D

Spontaneous emission noise

In this appendix, our goal is to analyze the effect of spontaneous emission on the phase noise of the RF beatnote generated by optical mixing of the two cross-polarized modes in a DF-VECSEL. We start from the rate equations of the single mode laser as given in Eqs. (2.15-2.17) of Chapter 2. In these equations, we then introduce spontaneous emission terms heuristically as Langevin noise sources. This leads to the following Langevin rate equations [Agrawal and Dutta, 1993; Baili et al., 2008]

$$\frac{dF}{dt} = -\gamma_{\rm cav}F + \kappa FN + \zeta_F(t) \ , \tag{D.1}$$

$$\frac{dN}{dt} = -\Gamma(N - N_0) - \kappa FN + \zeta_N(t) \ , \tag{D.2}$$

$$\frac{d\phi}{dt} = \frac{\alpha}{2}\kappa N + \zeta_\phi(t) \ . \tag{D.3}$$

The Langevin forces $\zeta_F(t)$, $\zeta_\phi(t)$ come from the spontaneous emission falling in the lasing mode, whereas the Langevin force $\zeta_N(t)$, driving the carrier number fluctuations, arises from both spontaneous emission and the probabilistic nature of the carrier recombination process. In the absence of Langevin noise forces, the steady-state above-threshold solution can be expressed as

$$F \equiv F_0 = \frac{\Gamma}{\kappa}(r-1) \ , \tag{D.4}$$

$$N \equiv N_{\rm th} = \frac{\gamma_{\rm cav}}{\kappa} \ , \tag{D.5}$$

where $r = N_0/N_{\rm th}$. The Langevin noise sources drive the laser out of its steady-state. The laser then exhibits random fluctuations governed by the stochastic rate equations (D.1-D.3). We consider Markovian assumptions for the random Langevin processes i.e., the correlation time of the noise sources is much shorter than all characteristic time scales of the system. This leads to the following relations for the Langevin forces

$$\langle \zeta_i(t) \rangle = 0 \ , \tag{D.6}$$

$$\langle \zeta_i(t)\zeta_j(t+\tau) \rangle = 2D_{ij}\delta(\tau) \ , \tag{D.7}$$

where $\langle . \rangle$ means ensemble average and D_{ij} is the diffusion coefficient related with the corresponding noise source. The explicit expressions of the diffusion coefficients D_{ij} read [Agrawal and Dutta, 1993; Baili et al., 2008]

$$\begin{aligned} D_{FF} = \gamma_{\rm cav}F_0, \ D_{NN} = \gamma_{\rm cav}F_0 + \Gamma N_{\rm th}, \ D_{\phi\phi} = \frac{\gamma_{\rm cav}}{F_0}, \\ D_{FN} = -\gamma_{\rm cav}F_0, \ D_{N\phi} = 0, \ D_{F\phi} = 0 \ . \end{aligned} \tag{D.8}$$

The power spectral density (PSD) of the Langevin forces can be obtained by Fourier transforming the corresponding correlation functions (Wiener-Khintchine theorem). This provides the following expressions of the PSDs associated with the different Langevin forces

$$S_{\zeta_F}(\omega) = \frac{1}{2\pi}\int_{-\infty}^{\infty}\langle \zeta_F(t)\zeta_F(t+\tau)\rangle e^{i\omega\tau}d\tau = \frac{\gamma_{\rm cav}F_0}{\pi} \ , \tag{D.9}$$

$$S_{\zeta_N}(\omega) = \frac{1}{2\pi}\int_{-\infty}^{\infty}\langle \zeta_N(t)\zeta_N(t+\tau)\rangle e^{i\omega\tau}d\tau = \frac{\gamma_{\rm cav}F_0 + \Gamma N_{\rm th}}{\pi} \ , \tag{D.10}$$

$$S_{\zeta_{FN}}(\omega) = \frac{1}{2\pi}\int_{-\infty}^{\infty}\langle \zeta_F(t)\zeta_N(t+\tau)\rangle e^{i\omega\tau}d\tau = -\frac{\gamma_{\rm cav}F_0}{\pi} \ , \tag{D.11}$$

$$S_{\zeta_\phi}(\omega) = \frac{1}{2\pi}\int_{-\infty}^{\infty}\langle \zeta_\phi(t)\zeta_\phi(t+\tau)\rangle e^{i\omega\tau}d\tau = \frac{\gamma_{\rm cav}}{4\pi F_0} \ . \tag{D.12}$$

Now considering that the Langevin noise sources perturb the laser from its steady-state by a small margin, we linearize the equations around the steady-state solutions. To this

aim, we introduce the fluctuations as follows

$$F(t) = F_0 + \delta F(t) \ , \tag{D.13}$$

$$N(t) = N_{\rm th} + \delta N(t) \ , \tag{D.14}$$

$$\phi(t) = \phi_0 + \delta\phi(t) \ . \tag{D.15}$$

Inserting Eqs. (D.13-D.15) into the rate equations (D.1-D.3), we obtain the Langevin equations for the fluctuations in time domain as

$$\frac{d}{dt}\delta F(t) - \Gamma(r-1)\delta N(t) = \zeta_F(t) \ , \tag{D.16}$$

$$\gamma_{\rm cav}\delta F(t) + r\Gamma\delta N(t) + \frac{d}{dt}\delta N(t) = \zeta_N(t) \ , \tag{D.17}$$

$$\frac{d}{dt}\delta\phi(t) - \frac{\alpha}{2}\kappa\delta N(t) = \zeta_\phi(t) \ . \tag{D.18}$$

Performing Fourier transformation on Eqs. (D.16-D.18) leads to the following Langevin equations of the fluctuations in the frequency domain

$$i\omega\widetilde{\delta F} + \Gamma(r-1)\widetilde{\delta N} = -\widetilde{\zeta}_F \ , \tag{D.19}$$

$$\gamma_{\rm cav}\widetilde{\delta F} + (r\Gamma - i\omega)\widetilde{\delta N} = \widetilde{\zeta}_N \ , \tag{D.20}$$

$$i\omega\widetilde{\delta\phi} + \frac{\alpha}{2}\kappa\widetilde{\delta N} = \widetilde{\zeta}_\phi \ , \tag{D.21}$$

where tilde ~ denotes Fourier transformed quantities. Solving Eqs. (D.19-D.20), we obtain the following expressions for the fluctuations of the photon number and the population inversion number

$$\widetilde{\delta F}(\omega) = \frac{(r\Gamma - i\omega)\widetilde{\zeta}_F + \Gamma(r-1)\widetilde{\zeta}_N}{\Gamma\gamma_{\rm cav}(r-1) - \omega^2 - i\omega r\Gamma} \ , \tag{D.22}$$

$$\widetilde{\delta N}(\omega) = -\frac{i\omega\widetilde{\zeta}_N + \gamma_{\rm cav}\widetilde{\zeta}_F}{\Gamma\gamma_{\rm cav}(r-1) - \omega^2 - i\omega r\Gamma} \ . \tag{D.23}$$

From Eq. (D.22), the PSD of the photon number fluctuation can be obtained as

$$\begin{aligned} S_F(\omega) &= |\widetilde{\delta F}(\omega)|^2 \\ &= \frac{(r^2\Gamma^2+\omega^2)|\widetilde{\zeta}_F|^2+\Gamma^2(r-1)^2|\widetilde{\zeta}_N|^2+2Re\left[(r\Gamma-i\omega)\Gamma(r-1)\widetilde{\zeta}_N^*\widetilde{\zeta}_F\right]}{\left[\Gamma\gamma_{\rm cav}(r-1)-\omega^2\right]^2+\omega^2r^2\Gamma^2} \\ &= \frac{(r^2\Gamma^2+\omega^2)S_{\zeta_F}+\Gamma^2(r-1)^2S_{\zeta_N}+2\Gamma^2r(r-1)S_{\zeta_F\zeta_N}}{\left[\Gamma\gamma_{\rm cav}(r-1)-\omega^2\right]^2+\omega^2r^2\Gamma^2} \ . \end{aligned} \tag{D.24}$$

Using Eqs. (D.9-D.11) in Eq. (D.24), and simplifying, we find

$$S_F(\omega) = \frac{\gamma_{\rm cav}F_0}{\pi}\times\frac{\omega^2+r\Gamma^2}{\left[\Gamma\gamma_{\rm cav}(r-1)-\omega^2\right]^2+\omega^2r^2\Gamma^2} \ . \tag{D.25}$$

Therefore, the relative intensity noise (RIN) due to the spontaneous emission can be expressed as

$$\begin{aligned} \text{RIN(f)} &= \frac{2S_F(f)}{F_0^2} \\ &= \frac{\gamma_{\rm cav}}{\pi F_0}\times\frac{4\pi^2f^2+r\Gamma^2}{\left[\Gamma\gamma_{\rm cav}(r-1)-4\pi^2f^2\right]^2+4\pi^2r^2\Gamma^2f^2} \ . \end{aligned} \tag{D.26}$$

The RIN spectrum given in Eq. D.26 is plotted in Fig. D.1. The parameter values used for

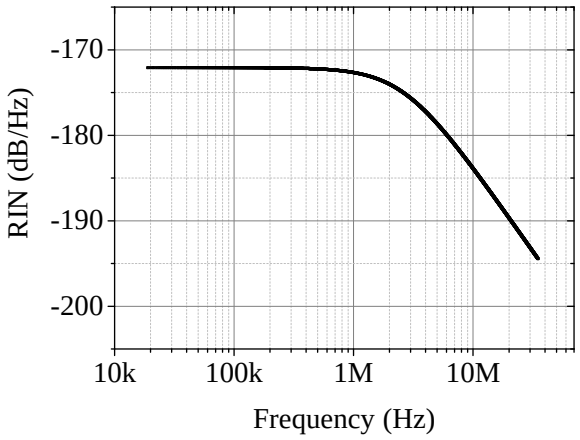

Figure D.1: RIN spectrum associated with spontaneous emission noise. Parameter values used for simulation: $1/\gamma_{cav} = 15\,\text{ns}$, $1/\Gamma = 1\,\text{ns}$, $r = 1.35$, $F_0 \simeq 9.45\times10^9$.

simulation are close to our experimental conditions as discussed in Chapter 2. The RIN

spectrum of Fig. D.1 confirms the fact that the spontaneous emission is indeed negligible compared to the pump noise (-145 dB/Hz) in the frequency range of interest (10 kHz to 50 MHz) for the DF-VECSEL (Chapter 2).

After discussing the effect of spontaneous emission on the intensity noise, we will describe the effect of spontaneous emission on the phase noise. In particular, our aim is to calculate the power spectral density of the phase noise of the RF beatnote coming from spontaneous emission in our DF-VECSEL. Now, substituting Eq. D.23 in Eq. D.21, we obtain

$$\widetilde{\delta\phi}(\omega) \;=\; \frac{\alpha\kappa}{2i\omega} \times \frac{i\omega\widetilde{\zeta}_N + \gamma_{\rm cav}\widetilde{\zeta}_F}{\Gamma\gamma_{\rm cav}(r-1) - \omega^2 - i\omega r\Gamma} + \widetilde{\zeta}_\phi \;. \tag{D.27}$$

Therefore, the PSD of the optical phase noise can be written as

$$\begin{aligned} S_\phi(\omega) &= |\widetilde{\delta\phi}(\omega)|^2 \\ &= \frac{\alpha^2\kappa^2}{4\omega^2} \times \frac{\omega^2|\widetilde{\zeta}_N|^2 + \gamma_{\rm cav}^2|\widetilde{\zeta}_F|^2}{\left[\Gamma\gamma_{\rm cav}(r-1) - \omega^2\right]^2 + \omega^2 r^2\Gamma^2} + |\widetilde{\zeta}_\phi|^2 \\ &= \frac{\alpha^2\kappa^2}{4\omega^2} \times \frac{\omega^2 S_{\zeta_N} + \gamma_{\rm cav}^2 S_{\zeta_F}}{\left[\Gamma\gamma_{\rm cav}(r-1) - \omega^2\right]^2 + \omega^2 r^2\Gamma^2} + S_{\zeta_\phi} \;. \end{aligned} \tag{D.28}$$

Using Eqs. (D.9-D.12) in Eq. (D.28) and doing some simplifications, we find the following expression

$$S_\phi(f) \;=\; \frac{\gamma_{\rm cav}}{4\pi F_0}\left[1 + \frac{\alpha^2\Gamma^2(r-1)\left[r(4\pi^2 f^2 + \gamma_{\rm cav}^2) - \gamma_{\rm cav}^2\right]}{\left[\Gamma\gamma_{\rm cav}(r-1) - 4\pi^2 f^2\right]^2 + 4\pi^2 r^2\Gamma^2 f^2}\right] \;. \tag{D.29}$$

The optical phase noise PSD of a single-mode laser given by Eq (D.29) can be easily extended to calculate the optical phase noises of the two modes of our DF-VECSEL. Finally, the contribution of the spontaneous emission to the phase noise of the RF beatnote in the dual-frequency VECSEL can simply be written as

$$\begin{aligned} S_{\rm Beat}(f) &= |\widetilde{\delta\phi_x}(f) - \widetilde{\delta\phi_x}(f)|^2 \;=\; S_{\phi_x}(f) + S_{\phi_y}(f) \\ &= \frac{\gamma_x}{2\pi F_{0x}}\left[1 + \frac{\alpha^2\Gamma^2(r_x-1)\left[r_x(4\pi^2 f^2 + \gamma_x^2) - \gamma_x^2\right]}{\left[\Gamma\gamma_x(r_x-1) - 4\pi^2 f^2\right]^2 + 4\pi^2 r_x^2\Gamma^2 f^2}\right] \\ &\quad + \frac{\gamma_y}{2\pi F_{0y}}\left[1 + \frac{\alpha^2\Gamma^2(r_y-1)\left[r_y(4\pi^2 f^2 + \gamma_y^2) - \gamma_y^2\right]}{\left[\Gamma\gamma_y(r_y-1) - 4\pi^2 f^2\right]^2 + 4\pi^2 r_y^2\Gamma^2 f^2}\right] \;. \end{aligned} \tag{D.30}$$

In Eq. (D.30) the symbols have identical meanings as in Chapter 2. Now, the spontaneous emission falling in the two modes are expected to be uncorrelated, and hence the optical phase fluctuations of the two cross-polarized modes due to spontaneous emission should be uncorrelated. Therefore, the RF beatnote phase noise coming from the spontaneous emission can be obtained by adding the PSDs of the two optical phase noises associated with spontaneous emission as shown in Eq. (D.30). We simulate Eq. (D.30) and the result is shown in Fig. D.2. The values of the parameters used for simulation are taken from the

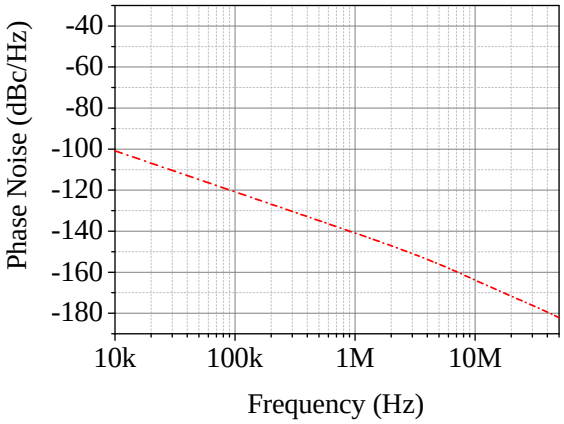

Figure D.2: Phase noise PSD of the RF beatnote due to spontaneous emission. Parameter values used for simulation: $r_x = 1.32$, $r_y = 1.35$, $1/\gamma_x = 13.9\,\text{ns}$, $1/\gamma_y = 16.7\,\text{ns}$, $1/\Gamma = 1\,\text{ns}$, $F_{0x} \simeq 2.42 \times 10^9$, $F_{0y} \simeq 4.12 \times 10^9$.

experiment described in Chapter 2. Comparing the theoretically expected noise spectrum (Fig. D.2) with the measured spectrum (Fig. 2.11 of Chapter 2) for the RF beatnote phase noise, we find that spontaneous emission hardly contributes to the phase noise of the RF beatnote in our DF-VECSEL.

Appendix E

Description of the coupling constant in a dual-frequency Nd:YAG laser

In this appendix, we rederive, following [Schwartz et al., 2009], the analytic expression of the nonlinear coupling constant in a dual-frequency laser based on a $\langle 100 \rangle-$cut Nd:YAG crystal, as mentioned in Eq. 4.20 of chapter 4. To this aim, Lamb's model is extended to fit the case of our dual-frequency Nd:YAG laser. As described by Lamb's model for a two-mode laser [Sargent III et al., 1974], the equations of evolution governing the photon numbers (intensities) in the eigenstates of a laser read

$$\frac{dF_x}{dt} = 2F_x \left[\alpha_x - \beta_x F_x - \theta_{xy} F_y\right] \ , \tag{E.1}$$

$$\frac{dF_y}{dt} = 2F_y \left[\alpha_y - \beta_y F_y - \theta_{yx} F_x\right] \ , \tag{E.2}$$

where F_x, F_y denote the number of photons in the two modes. α_x, α_y stand for the net gain of the two modes. β_x, β_y are the self-saturation coefficients, whereas the coefficients θ_{xy} and θ_{yx} take into account cross-gain saturation. Then according to Lamb, the nonlinear coupling constant C is defined as

$$C = \frac{\theta_{xy}\theta_{yx}}{\beta_x \beta_y} \ . \tag{E.3}$$

The steady-state solution corresponding to simultaneous oscillation of the two modes is

$$[\alpha_x - \beta_x F_{x0} - \theta_{xy} F_{y0}] = 0 \,, \tag{E.4}$$

$$[\alpha_y - \beta_y F_{y0} - \theta_{yx} F_{x0}] = 0 \,. \tag{E.5}$$

Stable simultaneous oscillation of the two modes requires that C be less than unity. In this case, the solutions of Eqs. (E.4-E.5) can be written as

$$F_{x0} = \frac{\alpha_x \beta_y - \alpha_y \theta_{xy}}{\beta_x \beta_y (1 - C)} \,, \tag{E.6}$$

$$F_{y0} = \frac{\alpha_y \beta_x - \alpha_x \theta_{yx}}{\beta_x \beta_y (1 - C)} \,. \tag{E.7}$$

Therefore, to define the coupling constant C of a dual-frequency Nd:YAG laser in the framework of the Lamb's model, one needs to find steady-state solutions analogous to Eqs. (E.4-E.5). To this aim, we start from the rate equations (4.14-4.17) governing the dynamics of the dual-frequency Nd:YAG laser as shown in Chapter 4. The steady-state solutions for the population inversions can be written as

$$N_1 \equiv N_{1\text{th}} = \frac{N_0}{1 + \frac{1}{F_{\text{sat}}}(F_{x0} A + F_{y0} B)} \,, \tag{E.8}$$

$$N_2 \equiv N_{2\text{th}} = \frac{N_0}{1 + \frac{1}{F_{\text{sat}}}(F_{y0} A + F_{x0} B)} \,, \tag{E.9}$$

where F_{sat} is equal to Γ/κ. In the weak-saturation limit (F_x, $F_y \ll F_{\text{sat}}$), Eqs. (E.8-E.9) can be simplified as

$$N_{1\text{th}} = N_0 \left[1 - \frac{F_{x0} A}{F_{\text{sat}}} - \frac{F_{y0} B}{F_{\text{sat}}}\right] \,, \tag{E.10}$$

$$N_{2\text{th}} = N_0 \left[1 - \frac{F_{x0} B}{F_{\text{sat}}} - \frac{F_{y0} A}{F_{\text{sat}}}\right] \,. \tag{E.11}$$

Now, to obtain the steady-state solutions for the photon numbers we set $dF_x/dt = 0$, $dF_y/dt = 0$ in Eqs. (4.14-4.15) of Chapter 4, leading to

$$0 = -\gamma_x F_{x0} + \kappa F_{x0}(N_{1\text{th}} A + N_{2\text{th}} B) \,, \tag{E.12}$$

$$0 = -\gamma_y F_{y0} + \kappa F_{y0}(N_{2\text{th}} A + N_{1\text{th}} B) \,. \tag{E.13}$$

Using Eqs. (E.8-E.9) in Eqs. (E.12-E.13) and doing some simplification, we find

$$-\gamma_x + \kappa N_0(A+B) - \frac{\kappa N_0}{F_{\text{sat}}}(A^2+B^2)F_{x0} - \frac{\kappa N_0}{F_{\text{sat}}}(2AB)F_{y0} = 0 \ , \tag{E.14}$$

$$-\gamma_y + \kappa N_0(A+B) - \frac{\kappa N_0}{F_{\text{sat}}}(A^2+B^2)F_{y0} - \frac{\kappa N_0}{F_{\text{sat}}}(2AB)F_{x0} = 0 \ . \tag{E.15}$$

Comparing Eqs. (E.4-E.5) with Eqs. (E.14-E.15), one can obtain the following expressions for the net gains:

$$\alpha_x = -\gamma_x + \kappa N_0(A+B) \ , \tag{E.16}$$

$$\alpha_y = -\gamma_y + \kappa N_0(A+B) \ . \tag{E.17}$$

The self-saturation coefficients are:

$$\beta_x = \beta_y = \frac{\kappa N_0}{F_{\text{sat}}}(A^2+B^2) \ , \tag{E.18}$$

and the cross-saturation coefficients read:

$$\theta_x = \theta_y = \frac{\kappa N_0}{F_{\text{sat}}}(2AB) \ . \tag{E.19}$$

Therefore, using the definition in Eq. E.3, we find the expression of the coupling constant C as mentioned in in Eq. 4.20 of chapter 4.

It is important to mention here that the Lamb's model only considers class-A laser. However, our dual-frequency Nd:YAG laser exhibits class-B dynamical behavior. To overcome this limitation, Lamb's model can be reformulated in the following manner [Brunel et al., 1997]. Let's suppose now that a small change of α_x, denoted as $\Delta\alpha_x$ ($\ll \alpha_x$), induces variations ΔF_x and ΔF_y for the two modes. Then, from Eqs. (E.6-E.7) we obtain

$$\frac{\Delta F_x}{\Delta \alpha_x} = \frac{\beta_y}{\beta_x\beta_y(1-C)} \ , \tag{E.20}$$

$$\frac{\Delta F_y}{\Delta \alpha_x} = -\frac{\theta_{yx}}{\beta_x\beta_y(1-C)} \ . \tag{E.21}$$

Similarly, for a small change $\Delta\alpha_y$ of α_y ($\Delta\alpha_y \ll \alpha_y$), we get

$$\frac{\Delta F_x}{\Delta \alpha_y} = -\frac{\theta_{xy}}{\beta_x \beta_y (1-C)} , \tag{E.22}$$

$$\frac{\Delta F_y}{\Delta \alpha_y} = \frac{\beta_x}{\beta_x \beta_y (1-C)} . \tag{E.23}$$

Using Eqs. (E.20-E.23), one can find the following useful expression of C:

$$C = \frac{\frac{\Delta F_x}{\Delta \alpha_y} \times \frac{\Delta F_y}{\Delta \alpha_x}}{\frac{\Delta F_x}{\Delta \alpha_x} \times \frac{\Delta F_y}{\Delta \alpha_y}} . \tag{E.24}$$

The advantage of using the definition in Eq. E.24 is that, the coupling constant can be obtained for both class-A and class-B lasers.

Appendix F

Effect of spatial-hole burning

Spatial-hole burning plays an important role in the strength of the coupling between the modes of a multimode Nd:YAG laser [Tang et al., 1963; Kimura et al., 1971]. In this appendix, we aim at exploring the effect of spatial-hole burning on the nonlinear coupling constant for our dual-frequency Nd:YAG laser, sustaining simultaneous oscillation of two linear cross-polarized modes. We start by the case of a laser with two longitudinal oscillating modes, and then extend this to our dual-frequency Nd:YAG laser.

F.1 Coupling between two longitudinal modes

In this section, we investigate the effect of spatial hole burning on the coupling between the two longitudinal modes of a laser, in which the gain medium does not fill the whole cavity. The schematic of the laser cavity is shown in Fig. F.1. The linear cavity of length l is closed by two mirrors: one is at $z = 0$, and the output coupler is at $z = l$. The active medium of thickness e and refractive index n is placed at $z = d$. The longitudinal modes of the cavity must satisfy the following relation

$$d + ne + l - (d + e) \;=\; p\frac{\lambda_p}{2}\ , \tag{F.1}$$

where p is an integer defining the mode of wavelength λ_p. Equation F.1 can be simplified as

$$\lambda_p \;=\; \frac{2[l + (n-1)e]}{p}\ . \tag{F.2}$$

Therefore, the corresponding propagation constant in vacuum reads

$$k_p^{(0)} \equiv \frac{2\pi}{\lambda_p} = p\frac{\pi}{l+(n-1)e} . \tag{F.3}$$

Now we suppose that the cavity is sustaining stable simultaneous oscillation of only two

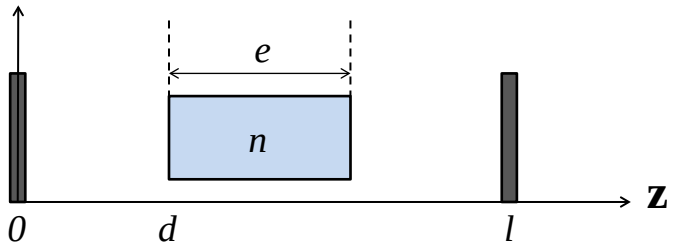

Figure F.1: Schematic of the laser cavity aligned along $z-$direction with the end mirrors at $z = 0$, and $z = l$. Cavity length: l; thickness and refractive index of active medium: e, n, respectively; position of the active medium: $z = d$.

longitudinal modes, labeled p and q. Each mode field forms a standing wave pattern due to the interference of the forward and backward waves in the linear cavity. Therefore, the amount of overlap between the pth and qth longitudinal mode inside the gain medium can be expressed by the following integral

$$F(p,q) = \int_d^{d+e} dz F_p(z)F_q(z) , \tag{F.4}$$

where

$$F_p(z) = F_{p0}\sin^2(k_p^{(0)}z), \qquad 0 \le z \le d, \tag{F.5}$$

$$F_p(z) = F_{p0}\sin^2(k_p z + \psi_p), \qquad d \le z \le (d+e), \tag{F.6}$$

and

$$k_p = \frac{2n\pi}{\lambda_p} = p\frac{n\pi}{l+(n-1)e} . \tag{F.7}$$

Here, $F_p(z)$ denotes the photon number distribution inside the cavity along the $z-$axis for the pth mode. The qth mode also satisfies equations (F.4-F.7) (the subscript p must be

replaced by q). The continuity of the mode field at $z = d$ leads to the following relation

$$\sin(k_p^{(0)} d) \;=\; \sin(k_p d + \psi_p) \; . \tag{F.8}$$

Using Eqs. (F.3),(F.7) in Eq. (F.8), we obtain

$$\psi_p \;=\; (1-n) k_p^{(0)} d \; . \tag{F.9}$$

Similarly, for qth mode, we can write

$$\psi_q \;=\; (1-n) k_q^{(0)} d \; . \tag{F.10}$$

When both pth and qth modes are oscillating, the saturated population inversion density at position z can be expressed as

$$n(z) \;=\; \frac{n_0}{1 + \dfrac{F_p(z) + F_q(z)}{F_{\rm sat}}} \; , \tag{F.11}$$

where n_0 defines the unsaturated population inversion density and $F_{\rm sat}$ stands for the saturation photon number. Therefore, the gain terms in the rate equations of the photon numbers for pth and qth mode read as follows:

$$\left[\frac{dF_p}{dt}\right]_{\rm gain} \;=\; \kappa S \int_d^{d+e} dz \frac{n_0}{1 + \frac{F_p(z)+F_q(z)}{F_{\rm sat}}} F_p(z) \; , \tag{F.12}$$

$$\left[\frac{dF_q}{dt}\right]_{\rm gain} \;=\; \kappa S \int_d^{d+e} dz \frac{n_0}{1 + \frac{F_p(z)+F_q(z)}{F_{\rm sat}}} F_q(z) \; , \tag{F.13}$$

and $\kappa S = \frac{\sigma c}{L_{cav}}$ with $L_{cav} = 2[l + (n-1)d]$ where S is mode section area, σ is stimulated emission cross-section, and c is the speed of light. In the weak-saturation limit (F_p, $F_q \ll F_{\rm sat}$), Eqs. (F.12-F.13) reduce to

$$\left[\frac{dF_p}{dt}\right]_{\rm gain} \;=\; \kappa S n_0 \int_d^{d+e} dz F_p(z) \left[1 - \frac{F_p(z)}{F_{\rm sat}} - \frac{F_q(z)}{F_{\rm sat}}\right] \; , \tag{F.14}$$

$$\left[\frac{dF_q}{dt}\right]_{\rm gain} \;=\; \kappa S n_0 \int_d^{d+e} dz F_q(z) \left[1 - \frac{F_q(z)}{F_{\rm sat}} - \frac{F_p(z)}{F_{\rm sat}}\right] \; . \tag{F.15}$$

Therefore, considering Lamb's formalism as described in the Appendix E and using Eqs. (F.14-F.15), we can express the coupling constant (C) as follows:

$$C \equiv \frac{\theta_{pq}\theta_{qp}}{\beta_p\beta_q} = \frac{\left[\int_d^{d+e} dz F_p(z)F_q(z)\right]^2}{\left[\int_d^{d+e} dz F_p^2(z)\right]\left[\int_d^{d+e} dz F_q^2(z)\right]} . \tag{F.16}$$

where θ_{pq}, θ_{qp} denote the cross-saturation coefficients, and β_p, β_q stand for the self-saturation coefficients. Taking into account the intra-cavity photon number distribution of Eq. F.6, and substituting it in Eq. F.16, we find the following expressions for the cross- and self-saturation coefficients

$$\theta_{pq} = \theta_{qp} = \theta = \int_d^{d+e} dz \sin^2(k_p z + \psi_p)\sin^2(k_q z + \psi_q) , \tag{F.17}$$

$$\beta_p = \int_d^{d+e} dz \sin^4(k_p z + \psi_p) , \tag{F.18}$$

$$\beta_q = \int_d^{d+e} dz \sin^4(k_q z + \psi_q) . \tag{F.19}$$

where k_p, k_q, ψ_p, and ψ_q are given by Eqs. (F.7-F.10). Equation (F.17) can be simplified as follows

$$\begin{aligned}\theta = {} & \frac{1}{4}[e + \frac{1}{4(k_p - k_q)}(\sin 2[(k_p - k_q)(d+e) - (\psi_p - \psi_q)] - \sin 2[(k_p - k_q)d - (\psi_p - \psi_q)]) \\ & + \frac{1}{4(k_p + k_q)}(\sin 2[(k_p + k_q)(d+e) - (\psi_p + \psi_q)] - \sin 2[(k_p + k_q)d - (\psi_p + \psi_q)]) \\ & - \frac{1}{2k_p}(\sin 2[k_p(d+e) + \psi_p] - \sin 2[k_p d + \psi_p]) \\ & - \frac{1}{2k_q}(\sin 2[k_q(d+e) + \psi_q] - \sin 2[k_q d + \psi_q])] .\end{aligned} \tag{F.20}$$

The self-saturation coefficients of Eqs. (F.18-F.19) can be simply expressed as

$$\begin{aligned}\beta_p = \theta_{pp} = {} & \frac{1}{4}[\frac{3e}{2} + \frac{1}{8k_p}(\sin 4[k_p(d+e) + \psi_p] - \sin 4[k_p d + \psi_p]) \\ & - \frac{1}{k_p}(\sin 2[k_p(d+e) + \psi_p] - \sin 2[k_p d + \psi_p])] ,\end{aligned} \tag{F.21}$$

$$\beta_q = \theta_{qq} = \frac{1}{4}[\frac{3e}{2} + \frac{1}{8k_q}(\sin 4[k_q(d+e)+\psi_q] - \sin 4[k_q d+\psi_q]) - \frac{1}{k_p}(\sin 2[k_q(d+e)+\psi_q] - \sin 2[k_q d+\psi_q])] \ . \quad \text{(F.22)}$$

Therefore, considering the expressions of θ_{pq}, θ_{qp}, β_p, β_q as mentioned in Eqs. (F.20-F.22), we can calculate coupling constant C from Eqs. F.16.

F.2 Coupling constant in dual-frequency Nd:YAG

In this section, we extend the derivation of the coupling constant (C) between the two longitudinal modes of the previous section to the dual-frequency Nd:YAG laser, which sustains oscillation of two linear cross-polarized modes. The schematic of the dual-frequency Nd:YAG laser cavity of length l is shown in Fig. F.2. The cavity is closed by two mirrors placed at $z = 0$, and $z = l$. The mirror at $z = l$ serves as the output coupler. The gain is provided by $\langle 100\rangle-$cut Nd:YAG crystal, which is placed at $z = d$ and has a thickness e. The Nd:YAG crystal is assumed to be isotropic and having refractive index n. The quarter-wave plate ($\lambda/4$-plate) of thickness t determines the directions of the two linear orthogonal polarization modes (o(x): ordinary, e(y): extraordinary). n_o and n_e respectively denote the refractive indices along the ordinary and extraordinary directions inside the quarter-wave plate. Following Eqs. (E.8-E.9) in Appendix E, the saturated pop-

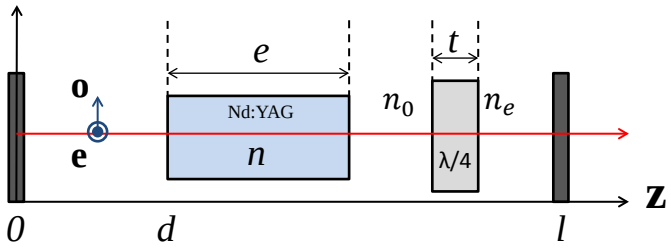

Figure F.2: Schematic of the dual-frequency Nd:YAG laser cavity with the end mirrors at $z = 0$, and $z = l$. Cavity length: l; thickness and refractive index of active medium: e, n, respectively; position of the active medium: d; thickness of $\lambda/4$-plate: t, o(x): ordinary polarization; e(y): extraordinary polarization; n_o, n_e: ordinary and extraordinary refractive indices of $\lambda/4$-plate.

ulation inversions in the weak-saturation limit and considering the z-dependence of the

intra-cavity photon numbers of the two modes can be written as

$$N_1(z) = N_0[1 - \frac{F_x(z)A}{F_{\rm sat}} - \frac{F_y(z)B}{F_{\rm sat}}] \ , \tag{F.23}$$

$$N_2(z) = N_0[1 - \frac{F_y(z)A}{F_{\rm sat}} - \frac{F_x(z)B}{F_{\rm sat}}] \ . \tag{F.24}$$

where

$$F_x(z) = F_{x0}\sin^2(k_x^{(0)}z), \qquad 0 \le z \le d \ , \tag{F.25}$$

$$F_x(z) = F_{x0}\sin^2(k_x z + \psi_x), \qquad d \le z \le d+e \ , \tag{F.26}$$

and

$$F_y(z) = F_{y0}\sin^2(k_y^{(0)}z), \qquad 0 \le z \le d \ , \tag{F.27}$$

$$F_y(z) = F_{y0}\sin^2(k_y z + \psi_y), \qquad d \le z \le d+e \ . \tag{F.28}$$

Now, the continuity of the field at $z = d$ leads to

$$k_x = p\frac{n\pi}{l + (n-1)e + (n_o - 1)t} \ , \tag{F.29}$$

$$k_x^{(0)} = p\frac{\pi}{l + (n-1)e + (n_o - 1)t} \ , \tag{F.30}$$

$$k_y = p\frac{n\pi}{l + (n-1)e + (n_e - 1)t} \ , \tag{F.31}$$

$$k_y^{(0)} = p\frac{\pi}{l + (n-1)e + (n_e - 1)t} \ , \tag{F.32}$$

$$\psi_x = (1-n)k_x^{(0)}d \ , \tag{F.33}$$

$$\psi_y = (1-n)k_y^{(0)}d \ . \tag{F.34}$$

Here, we assume that the two cross-polarized modes belong to same longitudinal mode (p). Now, following the derivation of Appendix E and taking into account the z-dependence of the photon numbers as shown in the previous section, we obtain the following expression

for the nonlinear coupling constant (C):

$$C = \frac{4A^2B^2}{(A^2+B^2)^2}\frac{\left[\int_d^{d+e} dz F_x(z)F_y(z)\right]^2}{\left[\int_d^{d+e} dz F_x^2(z)\right]\left[\int_d^{d+e} dz F_y^2(z)\right]} . \tag{F.35}$$

Thereafter, substituting Eqs. (F.25-F.28) into Eq. F.35, we find

$$C = \frac{4A^2B^2}{(A^2+B^2)^2}\frac{\left[\int_d^{d+e} dz \sin^2(k_x z+\psi_x)\sin^2(k_y z+\psi_y)\right]^2}{\left[\int_d^{d+e} dz \sin^4(k_x z+\psi_x)\right]\left[\int_d^{d+e} dz \sin^4(k_y z+\psi_y)\right]} . \tag{F.36}$$

Equation F.36 can be expressed as

$$C = \frac{4A^2B^2}{(A^2+B^2)^2}\frac{\theta_{xy}\theta_{yx}}{\beta_{xx}\beta_{yy}} , \tag{F.37}$$

where

$$\begin{aligned}\theta_{xy} = \theta_{yx} = {} & \frac{1}{4}e + \frac{1}{16(k_x-k_y)}\sin 2\left[(k_x-k_y)(d+e)-(\psi_x-\psi_y)\right] \\ & -\frac{1}{16(k_x-k_y)}\sin 2\left[(k_x-k_y)d-(\psi_x-\psi_y)\right] \\ & +\frac{1}{16(k_x+k_y)}\sin 2\left[(k_x+k_y)(d+e)-(\psi_x+\psi_y)\right] \\ & -\frac{1}{16(k_x+k_y)}\sin 2\left[(k_x+k_y)d-(\psi_p+\psi_q)\right] \\ & -\frac{1}{8k_x}\left(\sin 2[k_x(d+e)+\psi_x]-\sin 2[k_x d+\psi_x]\right) \\ & -\frac{1}{8k_y}\left(\sin 2[k_y(d+e)+\psi_y]-\sin 2[k_y d+\psi_y]\right) ,\end{aligned} \tag{F.38}$$

$$\begin{aligned}\beta_x = {} & \frac{3e}{8} + \frac{1}{32k_x}\left(\sin 4[k_x(d+e)+\psi_x]-\sin 4[k_x d+\psi_x]\right) \\ & -\frac{1}{4k_x}\left(\sin 2[k_x(d+e)+\psi_x]-\sin 2[k_x d+\psi_x]\right) ,\end{aligned} \tag{F.39}$$

$$\beta_y = \frac{3e}{8} + \frac{1}{32k_y}\left(\sin 4[k_y(d+e)+\psi_y] - \sin 4[k_y d+\psi_y]\right) - \frac{1}{4k_y}\left(\sin 2[k_y(d+e)+\psi_x] - \sin 2[k_y d+\psi_y]\right) \ . \quad \text{(F.40)}$$

Equation F.37 illustrates how the spatial-hole burning modifies the expression of the

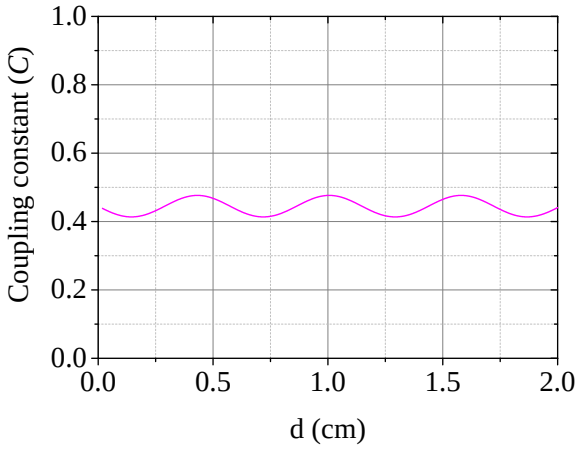

Figure F.3: Variation of the coupling constant (C) with the position (d) of the active medium inside the laser cavity. Parameter values used for simulation: $l = 9\,\text{cm}$, $e = 2\,\text{cm}$, $t = 7.8 \times 10^{-2}\,\text{cm}$, $n = 1.8197$, $n_o = 1.534$, $n_e = 1.543$, $\lambda = 1\,\mu\text{m}$, $\beta = 0.025$, $\alpha = \pi/4$.

coupling constant of Eq. 4.20. For better understanding, the coupling constant C is plotted as a function of the active medium position d inside the cavity, and the result is shown in Fig. F.3. The important point to note here is that the coupling constant is always much less than unity, even though α is equal to $\pi/4$. The other parameter values are taken from our experimental condition as described in Chapter 4. This explains why the anti-phase peak in the experimental RIN spectra of the two modes of the dual-frequency Nd:YAG laser does not shift as much with the change of α as expected from the theoretical model of Chapter 4, which did not include spatial-hole burning effect.

List of Publications

Publications in peer reviewed journals

- De, S., Baili, G., Bouchoule, S., Alouini, M., and Bretenaker, F., *Intensity- and phase- noise correlations in a dual-frequency vertical-external-cavity surface-emitting laser operating at telecom wavelength*, Phys. Rev. A **91**, 053828 (2015).

- De, S., Baili, G., Alouini, M., Harmand, J.-C., Bouchoule, S., and Bretenaker, F., *Class-A dual-frequency VECSEL at telecom wavelength*, Opt. Lett. **39**, 5586 (2014).

- De, S., Potapchuk, V., and Bretenaker, F., *Influence of spin-dependent carrier dynamics on the properties of a dual-frequency vertical-external-cavity surface-emitting laser*, Phys. Rev. A **90**, 013841 (2014).

- De, S., El Amili A., Fsaifes I., Pillet G., Baili G., Goldfarb F., Alouini M., Sagnes I., and Bretenaker F., *Phase Noise of the radio frequency (RF) beatnote generated by a dual-frequency VECSEL*, J. Lightwave Technol. **32** 1307 (2014).

- De, S., Loas, G., El Amili, A., Alouini, M., and Bretenaker, F., *Theoretical and experimental analysis of intensity noise correlations in an optically pumped, dual-frequency Nd:YAG laser*, J. Opt. Soc. Am. B **30** 2830 (2013).

- De, S., Pal, V., El Amili, A., Pillet, G., Baili, G., Alouini, M., Sagnes, I., Ghosh, R., and Bretenaker, F., *Theoretical and experimental analysis of intensity noise correlations in an optically pumped, dual-frequency Nd:YAG laser*, Opt. Exp. **21** 2538 (2013).

- El Amili, A., Loas, G., De, S., Schwartz, S., Feugnet, G., Pocholle, J.-P., Bretenaker, F., and Alouini, M., *Experimental demonstration of a dual-frequency laser free from*

antiphase noise, Opt. Lett. **37** 4901 (2012).

International conferences and workshops

- De, S., Baili, G., Alouini, M., Harmand, J.-C., Bouchoule, S., and Bretenaker, F., *Relaxation oscillation free tunable dual-frequency VECSEL at telecom wavelength*, 12th International Conference on Fiber Optics and Photonics, Oral presentation (Karaghpur, India, 2014).

- Labidi, T., Fsaifes, I., De, S., Goldfarb, F., and Bretenaker, F., *Optical phase sensitive amplification for microwave photonics applications: intermodulation distortion analysis*, 12th International Conference on Fiber Optics and Photonics, Oral presentation (Karaghpur, India, 2014).

- De, S., Loas, G., El Amili, A., Alouini, M., and Bretenaker, F., *Study of intensity noise correlations in dual-frequency Nd:YAG laser*, 12th International Conference on Fiber Optics and Photonics, Poster presentation (Karaghpur, India, 2014).

- Bretenaker, F., De, S., El Amili, A., Pillet, G., Baili, G., Morvan, L., Bouchoule, S., Sagnes, I., Alouini, M., *Dual-frequency VECSELs for microwave photonics applications*, 12th International Conference on Fiber Optics and Photonics, Invited talk (Karaghpur, India, 2014).

- De, S., El Amili, A., Pillet, G., Baili, G., Sagnes, I., Alouini, M., and Bretenaker, F., *Noise properties of dual-frequency VECSELs*, School and discussion meeting frontiers in light-matter interactions, Poster presentation (Kolkata, India, 2014).

- De, S., El Amili, A., Pillet, G., Baili, G., Sagnes, I., Alouini, M., and Bretenaker, F., *Noise properties of a Class-A dual-frequency VECSEL*, European Semiconductor Laser Workshop, Oral presentation (Paris, France, 2014).

- De, S., El Amili, A., Pillet, G., Baili, G., Goldfarb, F., Sagnes, I., Alouini, M., and Bretenaker, F., *Experimental and theoretical study of noise in a dual-frequency VECSEL*, SPIE Photonics West, Oral presentation (San Francisco, USA, 2014).

- De, S., Pal, V., El Amili, A., Pillet, G., Baili, G., Alouini, M., Sagnes, I., Ghosh, R., Bretenaker, F., *Phase noise of the radio frequency beatnote generated by a dual-frequency VECSEL*, IEEE International Topical Meeting on Microwave Photonics, Oral presentation (Virginia, USA, 2013)

- Bretenaker, F., De, S., Pal, V., El Amili, A., Pillet, G., Baili, G., Alouini, M., Sagnes, I., and Ghosh, R., *Noise correlations in dual frequency VECSEL*, French-Israeli Symposium on Non-linear and Quantum Optics, Invited talk (Ein Gedi, Israel, 2013).

- De, S., El Amili, A., Loas, G., Schwartz, S., Feugnet, G., Pocholle, J.-P., Bretenaker, F., and Alouini, M., *Intensity noise reduction of dual-frequency Nd:YAG lasers*, 11th International Conference on Fiber Optics and Photonics, Oral presentation (Chennai, India, 2012).

- De, S., Pal, V., El Amili, A., Pillet, G., Baili, G., Alouini, M., Sagnes, I., Ghosh, R., and Bretenaker, F., *Noise correlations in dual frequency VECSEL*, 11th International Conference on Fiber Optics and Photonics, Poster presentation (Chennai, India, 2012).

Bibliography

Agarwal, G. P. (2002). *Fiber-Optic Communication Systems*. Wiley-Interscience, 3rd edition.

Agrawal, G. P. (1989). Intensity dependence of the linewidth enhancement factor and its implications for semiconductor lasers. *IEEE Photon. Technol. Lett.*, 1:212–214.

Agrawal, G. P. and Dutta, N. K. (1993). *Semiconductor Lasers*. Van Nostrand Reinhold.

Allan, D., Hellwig, H., Kartaschoff, P., Vanier, J., Vig, J., Winkler, G. M. R., and Yannoni, N. F. (1988). Standard terminology for fundamental frequency and time metrology. *Proc. 42nd Ann. Frequency Control Symp.*, pages 419–425.

Alouini, M., Benazet, B., Vallet, M., Brunel, M., Di Bin, P., Bretenaker, F., Le Floch, A., and Thony, P. (2001). Offset phase locking of Er, Yb : glass laser eigenstates for RF photonics applications. *IEEE Photon. Technol. Lett.*, 13:367–369.

Alouini, M., Bretenaker, F., Brunel, M., Le Floch, A., and Vallet, M. (2000). Existence of two coupling constants in microchip lasers. *Opt. Lett.*, 25:896–898.

Alouini, M., Brunel, M., Bretenaker, F., Vallet, M., and Le Floch, A. (1998). Dual tunable wavelength Er:Yb:Glass laser for terahertz beat frequency generation. *IEEE Photon. Tech. Lett.*, 10:1554–1556.

Arecchi, F. T., Gadomski, W., and Meucci, R. (1986). Generation of chaotic dynamics by feedback on a laser. *Phys. Rev. A*, 34:1617(R).

Arecchi, F. T., Lippi, G. L., Puccioni, G. P., and Tredicce, J. R. (1984). Deterministic chaos in laser with injected signal. *Opt. Commun.*, 51:308–314.

Baili, G. (2008). *Contribution à la réduction du bruit d'intensité relatif des lasers à semiconducteurs pour des applications aux radars*. PhD thesis, Université Paris Sud - 11.

Baili, G., Alouini, M., Dolfi, D., Bretenaker, F., Sagnes, I., and Garnache, A. (2007). Shot-noise-limited operation of a monomode high-cavity-finesse semiconductor laser for microwave photonics applications. *Opt. Lett.*, 32:650–652.

Baili, G., Bretenaker, F., Alouini, M., Morvan, L., Dolfi, D., and Sagnes, I. (2008). Experimental investigation and analytical modeling of excess intensity noise in semiconductor class-A lasers. *J. Lightwave Technol.*, 26:952–961.

Baili, G., Morvan, L., Alouini, M., Dolfi, D., Bretenaker, F., Sagnes, I., and Garnache, A. (2009). Experimental demonstration of a tunable dual-frequency semiconductor laser free of relaxation oscillations. *Opt. Lett.*, 34:3421–3423.

Baili, G., Morvan, L., Pillet, G., Bouchoule, S., Zhao, Z., Oudar, J.-L., Ménager, L., Formont, S., Van Dijk, F., Faugeron, M., Alouini, M., Bretenaker, F., and Dolfi, D. (2014). Ultralow noise and high-power VECSEL for high dynamic range and broadband RF/optical links. *J. Lightwave Technol.*, 32:3489–3494.

Bar-Ad, S. and Bar-Joseph, I. (1992). Exciton spin dynamics in GaAs heterostructures. *Phys. Rev. Lett.*, 68:349–352.

Bergé, P., Pomeau, Y., and Vidal, C. (1987). *Within Chaos: Towards a Deterministic Approach to Turbulence*. Wiley.

Bousseksou, A., Bouchoule, S., El Kurdi, M., Strassner, M., Sagnes, I., Crozat, P., and Jacquet, J. (2006). Fabrication and characterization of 1.55 μm single transverse mode large diameter electrically pumped VECSEL. *Opt. Quantum Electron.*, 38:1269–1278.

Brignon, A. (1996). Anisotropic properties of pulsed four-wave mixing in Cr^{4+} : YAG saturable absorbers. *J. Opt. Soc. Am. B*, 13:2154–2163.

Brunel, M., Amon, A., and Vallet, M. (2005). Dual-polarization microchip laser at 1.53 μm. *Opt. Lett.*, 30:2418–2420.

Brunel, M., Bretenaker, F., and Le Floch, A. (1997). Tunable optical microwave source using spatially resolved laser eigenstates. *Opt. Lett.*, 22:384–386.

Brunel, M., Emile, O., Alouini, M., Le Floch, A., and Bretenaker, F. (1999a). Experimental and theoretical study of longitudinally monomode vectorial solid-state lasers. *Phys. Rev. A*, 59:831–840.

Brunel, M., Emile, O., Alouini, M., Le Floch, A., and Bretenaker, F. (1999b). Self-mode-locked pulsed monomode laser. *Opt. Lett.*, 24:229–231.

Brunel, M., Emile, O., Vallet, M., Bretenaker, F., and Le Floch, A. (1999c). Experimental and theoretical study of monomode vectorial lasers passively Q switched by a Cr^{4+} : yttrium aluminum garnet absorber. *Phys. Rev. A*, 60:4052–4058.

Burdick, G. W., Jayasankar, C. K., and Richardson, F. S. (1994). Energy level and line-strength analysis of optical transitions between Stark levels in $Nd^{3+} : Y_3Al_5O_{12}$. *Phys. Rev. B*, 50:16309–16325.

Chang-Hasnain, C. J., Harbison, J. P., Hasnain, G., and Von Lehmen, A. (1991a). Dynamic, polarization, and transverse mode characteristics of vertical cavity surface emitting lasers. *IEEE J. Quantum Electron.*, 27:1402–1409.

Chang-Hasnain, C. J., Harbison, J. P., and Stoffel, N. (1991b). Polarisation characteristics of quantum well vertical cavity surface emitting lasers. *Electron. Lett*, 27:163–165.

Chow, W. W. and Koch, S. W. (1999). *Semiconductor Laser Fundamentals*. Springer.

Chui, T. C. P., Swanson, D. R., Adriaans, M. J., Nissen, J. A., and Lipa, J. A. (1992). Temperature fluctuations in the canonical ensemble. *Phys. Rv. Lett.*, 69:3005–3008.

Corzine, S., Geels, R., Scott, J., Yan, R.-H., and Coldren, L. (1989). Design of Fabry-Perot surface-emitting lasers with a periodic gain structure. *IEEE J. Quantum Electron.*, 25:1513–1524.

Czarny, R., Alouini, M., Larat, C., Krakowski, M., and Dolfi, D. (2004). THz-dual-frequency $Yb^{3+} : KGd\,(WO_4)_2$ laser for continuous wave THz generation through photomixing. *Electron. Lett.*, 40:942–943.

Dalgliesh, R., May, A. D., and Stphan, G. (1998). Polarization states of a single-mode Nd^{3+} : YAG laser-part I: theory. *IEEE J. Quantum Electron.*, 34:1485–1492.

Damen, T. C., Vina, L., Cunningham, J. E., Shah, J., and Sham, L. J. (1991). Subpicosecond spin relaxation dynamics of excitons and free carriers in gaas quantum wells. *Phys. Rev. Lett.*, 67:3432–3435.

Dargys, A. and Kundrotas, J. (1994). *Handbook on Physical Properties of Ge, Si, GaAs and InP*. Science and Encyclopedia Publishers.

Davis, M. K., Digonnet, M. J. F., and Pantel, R. H. (1998). Thermal effects in doped fibers. *J. Lightwave Technol.*, 16:1013–1023.

De, S., Baili, G., Alouini, M., Harmand, J.-C., Bouchoule, S., and Bretenaker, F. (2014a). Class-A dual-frequency VECSEL at telecom wavelength. *Opt. Lett.*, 39:5586–5589.

De, S., Baili, G., Bouchoule, S., Alouini, M., and Bretenaker, F. (2015). Intensity- and phase-noise correlations in a dual-frequency vertical-external-cavity surface-emitting laser operating at telecom wavelength. *Phys. Rev. A*, accepted.

De, S., El Amili, A., Fsaifes, I., Pillet, G., Baili, G., Goldfarb, F., Alouini, M., Sagnes, I., and Bretenaker, F. (2014b). Phase noise of the radio frequency (RF) beatnote generated by a dual-frequency VECSEL. *J. Lightwave Technol.*, 32:1307–1316.

De, S., Loas, G., El Amili, A., Alouini, M., and Bretenaker, F. (2013a). Theoretical and experimental analysis of intensity noise correlations in an optically pumped, dual-frequency Nd:YAG laser. *J. Opt. Soc. Am. B*, 30:2830–2839.

De, S., Pal, V., El Amili, A., Pillet, G., Baili, G., Alouini, M., Sagnes, I., Ghosh, R., and Bretenaker, F. (2013b). Intensity noise correlations in a two-frequency VECSEL. *Opt. Exp.*, 21:2538–2550.

De, S., Potapchuk, V., and Bretenaker, F. (2014c). Influence of spin-dependent carrier dynamics on the properties of a dual-frequency vertical-external-cavity surface-emitting laser. *Phys. Rev. A*, 90:013841(1)–013841(11).

Du, W., Zhang, S., and Li, Y. (2005). Principles and realization of a novel instrument for high performance displacement measurement nanometer laser ruler. *Opt. Laser Eng.*, 43:1214–1225.

Dumont, P., Camargo, F., Danet, J.-M., Holleville, D., Guerandel, S., Pillet, G., Baili, G., Morvan, L., Dolfi, D., Gozhyk, I., Beaudoin, G., Sagnes, I., Georges, P., and Lucas-Leclin, G. (2014). Low-noise dual-frequency laser for compact Cs atomic clocks. *J. Lightwave Technol.*, 32:3817–3823.

Eilers, H., Hoffman, K. R., Dennis, W. M., Jacobsen, S. M., and Yen, W. M. (1992). Saturation of $1.064\,\mu$m absorption in $\mathrm{Cr, Ca : Y_3Al_5O_{12}}$ crystals. *App. Phys. Lett.*, 61:2958–2960.

El Amili, A., Loas, G., De, S., Schwartz, S., Feugnet, G., Pocholle, J.-P., Bretenaker, F., and Alouini, M. (2012). Experimental demonstration of a dual-frequency laser free from antiphase noise. *Opt. Lett.*, 37:4901–4903.

El Amili, A., Loas, G., Pouget, L., and Alouini, M. (2014). Buffer reservoir approach for cancellation of laser resonant noises. *Opt. Lett.*, 39:5014–5017.

Freitag, I. and Welling, H. (1994). Investigation on amplitude and frequency noise of injection-locked diode-pumped Nd:YAG lasers. *Appl. Phys. B*, 58:537–543.

Frougier, J., Baili, G., Alouini, M., Sagnes, Jaffrés, I. H., Garnache, A., Deranlot, C., Dolfi, D., and George, J.-M. (2013). Control of light polarization using optically spin-injected vertical external cavity surface emitting lasers. *Appl. Phys. Lett.*, 103:252402.

George Pan, Z., Jiang, S., Dagenais, M., Morgan, R. A., Kojima, K., Asom, M. T., Leibenguth, R. E., Guth, G. D., and Focht, M. W. (1993). Optical injection induced polarization bistability in vertical-cavity surface-emitting lasers. *Appl. Phys. Lett.*, 63:2999–3001.

Gliese, U., Christensen, E. L., and Stubkjaer, K. E. (1991). Laser linewidth requirements and improvements for coherent optical beam forming networks in satellites. *J. Lightwave Technol.*, 9:779–790.

Gorodetsky, M. L. and Grudinin, I. S. (2004). Fundamental thermal fluctuations in microspheres. *J. Opt. Soc. Am. B*, 21:697–705.

Greiner, C., Boggs, B., Loftus, T., Wang, T., and Mossberg, T. W. (1999). Polarization-dependent Rabi frequency beats in the coherent response of Tm^{3+} in YAG. *Phys. Rev. A*, 60:R2657–R2660.

Hadley, M. A., Wilson, G. C., Lau, K. Y., and Smith, J. S. (1993). High single-transverse-mode output from external-cavity surface-emitting laser-diodes. *Appl. Phys. Lett.*, 63:1607–1609.

Harb, C. C., Ralph, T. C., Huntington, E. H., Freitag, I., McClelland, D. E., and Bachor, H.-A. (1996). Intensity noise properties of injection locked lasers. *Phys. Rev. A*, 54:4370–4382.

Henry, C. H. (1982). Theory of the linewidth of semiconductor lasers. *IEEE J. Quantum Electron.*, 18:259–264.

Henry, C. J. (1986). Phase noise in semiconductor lasers. *J. Lightwave Technol.*, 4:298–311.

Hoogland, S., Dhanjal, S., Tropper, A. C., Roberts, J. S., Häring, R., Paschotta, R., Morier-Genoud, F., and Keller, U. (2000). Passively mode-locked diode-pumped surface-emitting semiconductor laser. *IEEE Photon. Technol. Lett.*, 12:1135–1137.

Hooker, S. and Webb, C. (2010). *Laser Physics*. Oxford University Press.

Horak, P., Voo, N. Y., Ibsen, M., and Loh, W. H. (2006). Pump-noise-induced linewidth contributions in distributed feedback fiber lasers. *IEEE Photon. Technol. Lett.*, 18:998–1000.

Jewell, J. L., McCall, S. L., Lee, Y. H., Scherer, A., Gossard, A. C., and English, J. H. (1989). Lasing characteristics of GaAs microresonators. *Appl. Phys. Lett*, 54:1400–1402.

Kaiser, J., Degen, C., and Els asser (2002). Polarization-switching influence on the intensity noise of vertical-cavity surface-emitting lasers. *J. Opt. Soc. Am. B*, 19:672–677.

Kane, T. J. (1990). Intensity noise in a diode-pumped single frequency Nd : YAG laser and its control by electronic feedback. *IEEE Photon. Technol. Lett.*, 2:244–245.

Kapon, E. e. (1999a). *Semiconductor Lasers I: Fundamentals*. Academic Press.

Kapon, E. e. (1999b). *Semiconductor Lasers II: Materials and Structures*. Academic Press.

Keeler, G. A., Serkland, D. K., Geib, K. M., Peake, G. M., and Mar, A. (2005). Single transverse mode operation of electrically pumped vertical-external-cavity surface-emitting lasers with micromirrors. *IEEE Photon. Technol. Lett.*, 17:522–523.

Keller, U. (2003). Recent developments in compact ultrafast lasers. *Nature*, 424:831–838.

Keller, U. and Tropper, A. C. (2006). Passively modelocked surface-emitting semiconductor lasers. *Phys. Rep.*, 429:67–120.

Kimura, T., Otsuka, K., and Saruwatari, M. (1971). Spatial hole-burning effects in a Nd^{3+} : YAG laser. *IEEE J. Quantum Electron.*, 7:225–230.

Knappe, S., Shah, V., Schwindt, P. D. D., Hollberg, L., Kitching, J., Liew, L.-A., and Moreland, J. (2007). A microfabricated atomic clock. *App. Phys. Lett.*, 85:1460–1462.

Koechner, W. (2006). *Solid-State Laser Engineering*. Springer, 6th edition.

Koechner, W. and Bass, M. (2003). *Solid-State Lasers: A Graduate Text*. Springer.

Kravtsov, N. V., Lariontsev, E. G., and Naumkin, N. (2004). Dependence of polarisation of radiation of a linear Nd:YAG laser on the pump radiation polarisation. *Quantum Electron.*, 34:839–842.

Kurdi, M. E., Bouchoule, S., Bousseksou, A., Sagnes, I., Plais, A., Strassner, M., Symonds, C., Garnache, A., and Jacquet, J. (2004). Room-temperature continuouswave laser operation of electrically pumped 1.55 μm VECSEL. *Electron. Lett.*, 40:671–672.

Kuznetsov, M., Hakimi, F., Sprague, R., and Mooradian, A. (1997). High-power (>0.5-W CW) diode-pumped vertical external-cavity surface-emitting semiconductor lasers with circular TEM_{00} beams. *IEEE Photon. Technol. Lett.*, 9:1063–1065.

Kuznetsov, M., Hakimi, F., Sprague, R., and Mooradian, A. (1999). Design and characteristics of high-power (>0.5-W CW) diode-pumped vertical-external-cavity surface-emitting semiconductor lasers with circular TEM_{00} beams. *IEEE J. Sel. Top. Quantum Electron.*, 5:561–573.

Lau, K. Y. (1988). Efficient narrow-band direct modulation of semiconductor injection lasers at millimeter wave frequencies of 100 GHz and beyond. *Appl. Phys. Lett.*, 52:2214–2216.

Lauer, C. and Amann, M.-C. (2005). Calculation of the linewidth broadening in vertical-cavity surface-emitting lasers due to temperature fluctuations. *App. Phys. Lett.*, 86:191108(1)–191108(3).

Laurain, A. (2010). *Sources laser à semiconducteur à émission verticale de haute cohérence et de forte puissance dans le proche et le moyen infrarouge*. PhD thesis, Université Montpellier II.

Laurain, A., Myara, M., Beaudoin, G., Sagnes, I., and Garnache, A. (2009). High power single-frequency continuously-tunable compact extended-cavity semiconductor laser. *Opt. Exp.*, 17:9503–9508.

Laurain, A., Myara, M., Beaudoin, G., Sagnes, I., and Garnache, A. (2010). Multiwatt-power highly-coherent compact single-frequency tunable vertical-external-cavity-surface-emitting-semiconductor-laser. *Opt. Exp.*, 18:14627–14636.

Levinshtein, M., Rumyantsev, S., and Shur, M. (1996). *Handbook Series on Semiconductor Parameters*. World Scientific.

Lima, C., Wake, D., and Davies, P. (1995). Compact optical millimetre-wave source using a dual-mode semiconductor laser. *Electron. Lett.*, 31:364–366.

Lindberg, H., Strassner, M., and Larsson, A. (2005). Improved spectral properties of an optically pumped semiconductor disk laser using a thin diamond heat spreader as an intracavity filter. *IEEE Photon. Technol. Lett.*, 17:1363–1365.

Lukac, M., Trost, S., and Kazic, M. (1992). Flip-flop polarization effect in cube-corner-flat cavity Nd:YAG laser. *IEEE J. Quantum Electron.*, 28:2560–2562.

Maiman, T. H. (1960). Optical and microwave-optical experiments in ruby. *Phys. Rev. Lett.*, 4:564–566.

Martín-Regalado, J., Prati, F., San Miguel, M., and Abraham, N. B. (1997). Polarization properties of vertical-cavity surface-emitting lasers. *IEEE J. Quantum Electron.*, 33:765–783.

Martín-Regalado, J., Prati, F., San Miguel, M., and Abraham, N. B. (1999). Polarization dynamics of optically pumped VCSEL's. *IEEE J. Quantum Electron.*, 35:342–351.

Martín-Regalado, J., San Miguel, M., and Abraham, N. B. (1996). Polarization switching in quantum-well vertical-cavity surface-emitting lasers. *Opt. Lett.*, 21:351–353.

McCumber, D. E. (1966). Intensity fluctuations in the output of cw laser oscillators. I. *Phys. Rev.*, 141:306–322.

McKay, A., Dawes, J. M., and Park, J.-D. (2007). Polarization-mode coupling in (100)-cut Nd:YAG. *Opt. Exp.*, 15:16342–16347.

Mogilevtsev, D., Horoshko, D. B., Golubev, Y. M., and Kolobov, M. I. (2014). Quantum correlations and nonclassicality in a system of two coupled vertical external cavity surface emitting lasers. *Phys. Rev. A*, 90:063819.

Morvan, L., Dolfi, D., Lai, N. D., Huignard, J. P., Brunel, M., Bretenaker, F., and Floch, A. L. (2002). The building blocks for a two-frequency laser lidar-radar: concept and preliminary experimental results. *Appl. Opt.*, 41:5702–5712.

Mulet, J., Mirasso, C. R., and San Miguel, M. (2001). Polarization resolved intensity noise in vertical-cavity surface-emitting lasers. *Phys. Rev. A*, 64:023817(1)–023817(8).

Narbonneau, F., Lours, M., Bize, S., Clairon, A., Santarelli, G., Lopez, O., Daussy, C., Amy-Klein, A., and Chardonnet, C. (2007). High resolution frequency standard dissemination via optical fiber metropolitan network. *Rev. Sci. Instrum.*, 77:064701.

Nerin, P., Puget, P., Besesty, P., and Chartier, G. (1997). Selfmixing using a dual-polarisation Nd:YAG microchip laser. *Electron. Lett.*, 33:491–492.

Ni, D. C., Fetterman, H. R., and Chew, W. (1990). Millimeter-wave generation and characterization of a GaAs FET by optical mixing. *IEEE Trans. Microwave Theory Tech.*, 38:608–614.

Oka, M. and Kubota, S. (1988). Stable intracavity doubling of orthogonal linearly polarized modes in diode-pumped Nd:YAG lasers. *Opt. Lett.*, 13:805–807.

Okhotnikov, O. G. e. (2010). *Semiconductor Disc Lasers: Physics and Technology*. Wiley-VCH.

O'Reilly, J. and Lane, P. (1994). Remote delivery of video services using mm-waves and optics. *J. Lightwave Technol.*, 12:369–375.

Otsuka, K., Mandel, P., Bielawski, S., Derozier, D., and Glorieux, P. (1992). Alternate time scale in multimode lasers. *Phys. Rev. A*, 46:1692–1695.

Pal, V., Trofimoff, P., Miranda, B.-X., Baili, G., Alouini, M., Morvan, L., Dolfi, D., Goldfarb, F., Sagnes, I., Ghosh, R., and Bretenaker, F. (2010). Measurement of the coupling constant in a two-frequency VECSEL. *Opt. Exp.*, 18:5008–5014.

Pieroux, D., Erneux, T., and Otsuka, K. (1994). Minimal model of a class-B laser with delayed feedback: Cascading branching of periodic solutions and period-doubling bifurcation. *Phys. Rev. A*, 50:1822.

Pillet, G., Morvan, L., Brunel, M., Bretenaker, F., Dolfi, D., Vallet, M., Huignard, J.-P., and Le Floch, A. (2008). Dual-frequency laser at 1.5 μm for optical distribution and generation of high-purity microwave signals. *J. Lightwave Technol.*, 26:2764–2773.

Prati, F., Caccia, P., and Castelli, F. (2002). Effects of gain saturation on polarization switching in vertical-cavity surface-emitting lasers. *Phys. Rev. A*, 66:063811(1)–063811(7).

Quarterman, A. H., Wilcox, K. G., Apostolopoulos, V., Mihoubi, Z. Elsmere, S. P., Farrer, I., Ritchie, D. A., and Tropper, A. (2009). A passively mode-locked external-cavity semiconductor laser emitting 60-fs pulses. *Nat. Photon.*, 2:729–731.

Raja, M. Y. A., Brueck, S. R. J., Osinsky, M., Schaus, C. F., and Mclnerney, J. G. (1989). Resonant periodic gain surface-emitting semiconductor laser. *IEEE J. Quantum Electron.*, 25:1500–1512.

Rautiainen, J., Lyytikäinen, J., Sirbu, A., Mereuta, A., Caliman, A., Kapon, E., , and Okhotnikov, O. (2008). 2.6 W optically-pumped semiconductor disk laser operating at 1.57-μm using wafer fusion. *Opt. Exp.*, 16:21881–21886.

Rideout, H., Seregelyi, J., and Yao, J. (2007). A true time delay beamforming system incorporating a wavelength tunable optical phase-lock loop. *J. Lightw. Technol.*, 25:1761–1770.

Rowan, S., Campbell, A. M., Skeldon, K., and Hough, J. (1994). Broadband intensity stabilization of a diode-pumped monolithic miniature Nd:YAG ring laser. *J. Mod. Opt.*, 41:1263–1269.

San Miguel, M., Feng, Q., and Moloney, J. V. (1995). Light-polarization dynamics in surface-emitting semiconductor lasers. *Phys. Rev. A*, 81:1728–1739.

Sargent III, M., Scully, M. O., and Lamb, W. E. (1974). *Laser Physics*. Addison-Wesley Publishing Company.

Scheller, M., Yarborough, J. M., Moloney, J. V., Fallahi, M., Koch, M., and Koch, S. W. (2010). Room temperature continuous wave milliwatt terahertz source. *Opt. Exp.*, 18:27112–27117.

Schmeissner, R., Roslund, J., Fabre, C., and Treps, N. (2014). Spectral noise correlations of an ultrafast frequency comb. *Phys. Rev. Lett.*, 113:263906.

Schwartz, S., Feugnet, G., Rebut, M., Bretenaker, F., and Pocholle, J.-P. (2009). Orientation of Nd^{3+} dipoles in yttrium aluminum garnet: experiment and model. *Phys. Rev. A*, 79:063814(1)–063814(6).

Scott, D. C., Plant, D. V., and Fetterman, H. R. (1992). 60 GHz sources using optically driven heterojunction bipolar transistors. *Appl. Phys. Lett.*, 61:1–3.

Scott, J. W., Thibeault, B. J., Mahon, C. J., Coldren, L. A., and Peters, F. H. (1994). High modulation efficiency of intracavity contacted vertical cavity lasers. *Appl. Phys. Lett.*, 65:1483–1485.

Scott, R. P., Langrock, C., and Kolner, B. H. (2001). High-dynamic-range laser amplitude and phase noise measurement techniques. *IEEE J. Sel. Top. Quantum Electron.*, 7:641–655.

Seeds, A. J. and Williams, K. J. (2006). Microwave photonics. *J. Lightw. Technol.*, 24:4628–4641.

Siegman, A. (1986). *Lasers*. University Science Books.

Sing, S., Smith, R. G., and Van Uitert, L. G. (1974). Stimulated-emission cross section and fluorescent quantum efficiency of Nd^{3+} : in yttrium aluminum garnet at room temperature. *Phys. Rev. B*, 10:2566–2572.

Steele, R. C. (1983). Optical phase-locked loop using semiconductor laser diodes. *Electron. Lett.*, 19:69–71.

Taccheo, S., Laporta, P., and Svelto, O. (1996). Intensity noise reduction in a single-frequency ytterbium-codoped erbium laser. *Opt. Lett.*, 21:1747–1749.

Tang, C. H., Statz, H., and deMars, G. (1963). Spectral output and spiking behavior of solid-state lasers. *App. Phys. Lett.*, 34:2289–2295.

Tauber, D., Wang, G., Geels, R. S., Bowers, J. E., and Coldren, L. A. (1993). Large and small signal dynamics of vertical cavity surface emitting lasers. *Appl. Phys. Lett.*, 62:325–327.

Tonda-Goldstein, S., Dolfi, D., Monsterleet, A., Formont, S., Chazelas, J., and Huignard, J.-P. (2006). Optical signal processing in radar systems. *IEEE Trans. Microwave Theory Tech.*, 54:847–853.

Tourrenc, J.-P., Bouchoule, S., Khadour, A., Harmand, J.-C., Decobert, J. Lagay, N., Lafosse, X., Sagnes, I., Leroy, L., and Oudar, J.-L. (2008). Thermal optimization of 1.55 μm OP-VECSEL with hybrid metal-metamorphic mirror for single-mode high power operation. *Opt. Quantum Electron.*, 40:155–165.

Travagnin, M., van Exter, M. P., Jansen van Doorn, A. K., and Woerdman, J. P. (1996). Role of optical anisotropies in the polarization properties of surface-emitting semiconductor lasers. *Phys. Rev. A*, 54:1647–1660.

Travagnin, M., van Exter, M. P., and Woerdman, J. P. (1997). Influence of carrier dynamics on the polarization stability and noise-induced polarization hopping in surface-emitting semiconductor lasers. *Phys. Rev. A*, 56:1497–1507.

Tropper, A. C., Foreman, H. D., Garnache, A., Wilcox, K. G., and Hoogland, S. H. (2004). Vertical-external-cavity semiconductor lasers. *J. Phys. D: Appl. Phys.*, 37:R75–R85.

Tropper, A. C. and Hoogland, S. (2006). Extended cavity surface-emitting semiconductor lasers. *Prog. Quantum Electron.*, 30:1–43.

Vahala, K., Chiu, L. C., Margalit, S., and Yariv, A. (1983). On the linewidth enhancement factor α in semiconductor injection lasers. *Appl. Phys. Lett.*, 42:631–633.

van Exter, Willemsen, M. B., and Woerdman, J. P. (1998a). Polarization fluctuations in vertical-cavity semiconductor lasers. *Phys. Rev. A*, 58:4191–4205.

van Exter, M. P., Al-Remawi, A., and Woerdman, J. P. (1998b). Polarization fluctuations demonstrate nonlinear anisotropy of a vertical-cavity semiconductor laser. *Phys. Rev. Lett.*, 80:4875–4878.

van Exter, M. P., Hendriks, R. F. M., and Woerdman, J. P. (1998c). Physical insight into the polarization dynamics of semiconductor vertical-cavity lasers. *Phys. Rev. A*, 57:2080–2090.

Vanier, J. (2005). Atomic clocks based on coherent population trapping: A review. *App. Phys. B*, 81:421–442.

Virte, M., Panajotov, K., and Sciamanna, M. (2013a). Bifurcation to nonlinear polarization dynamics and chaos in vertical-cavity surface-emitting lasers. *Phys. Rev. A*, 87:013834(1)–013834(10).

Virte, M., Panajotov, K., Thienpont, H., and Sciamanna, M. (2013b). Deterministic polarization chaos from a laser diode. *Nat. Photon.*, 7:60–65.

Wieczorek, S. and Chow, W. W. (2004). Bifurcations and interacting modes in coupled lasers: A strong-coupling theory. *Phys. Rev. A*, 69:033811(1)–033811(17).

Wieczorek, S. and Chow, W. W. (2005). Global view of nonlinear dynamics in coupled-cavity lasers − a bifurcation study. *Opt. Comm.*, 246:471–493.

Williams, K., Goldberg, L., Esman, R., Dagenais, M., and Weller, J. (1989). 6-34 GHz offset phase-locking of Nd:YAG 1319 nm nonplanar ring lasers. *Electron. Lett.*, 25:1242–1243.

Yao, J. (2009). Microwave photonics. *J. Lightwave Technol.*, 27:314–335.

Yao, X. S. and Maleki, L. (1996). Converting light into spectrally pure microwave oscillation. *Opt. Lett.*, 21:483–485.

Yao, X. S. and Maleki, L. (1997). Dual microwave and optical oscillator. *Opt. Lett.*, 22:1867–1869.

Yariv, A. (1975). *Quantum Electronics*. Wiley.

Yifei, L., Amarildo, J. C., Goldwasser, S. M., and Herczfeld, P. R. (2001). Rapidly tunable millimeter-wave optical transmitter for lidar-radar. *IEEE Trans. Microw. Theory Tech.*, 49:2048–2054.

Zanon, T., Guérandel, S., de Clercq, E., Holleville, D., Dimarcq, N., and Clairon, A. (2005). High contrast Ramsey fringes with coherent population trapping pulses in a double lambda atomic system. *Phys. Rev. Lett.*, 94:193002.

Zhao, Z., S., Bouchoule, Song, J., Galopin, E., Harmand, J.-C., Décobert, J., Aubin, G., and Oudar, J.-L. (2011). Subpicosecond pulse generation from a 1.56 μm mode-locked VECSEL. *Opt. Lett.*, 36:4377–4379.

Noise in dual-frequency semiconductor and solid-state lasers

Coherent sources emitting two optical frequencies with a widely tunable frequency difference lying in the radio-frequency range and having a high degree of correlation between their fluctuations can be useful for numerous applications such as microwave photonics, ultra-stable atomic clocks, atom manipulation and probing, metrology, etc. Dual-frequency lasers, which emit two orthogonal linearly polarized modes with a frequency difference lying in the radio-frequency range, have huge potentials for the above mentioned applications. We compare the characteristics of such dual-frequency oscillation in lasers based on either semiconductor (VECSEL: vertical-external-cavity surface-emitting laser) or solid-state active media (mainly Nd3+, or Er3+ doped crystalline host). Apart from the obvious difference between the gain mechanisms in semiconductor and solid-state laser media, the dual-frequency VECSEL and the dual-frequency Nd:YAG laser exhibit different dynamical behaviors. The dual-frequency VECSELs exhibit relaxation oscillation free class-A dynamics as the photon lifetime inside the cavity is longer than the population inversion lifetime. On the contrary, the dual-frequency Nd:YAG lasers obey class-B dynamics linked with the fact that the photon lifetime inside the cavity is shorter than the population inversion lifetime, leading to the existence of relaxation oscillations. In this thesis, we figure out how the laser dynamics, in addition to the nonlinear coupling between the two laser modes, governs different noise phenomena in dual-frequency lasers. In particular, we demonstrate, both experimentally and theoretically, the influence of the laser dynamics and the nonlinear coupling between the two modes on the laser noise, by analyzing the spectral properties of the different noises (intensity, phase) and their correlation in a class-A dual-frequency VECSEL (vertical-external-cavity surface emitting laser) and a class-B dual-frequency Nd:YAG laser. Moreover, the noise correlation results are interpreted in terms of the linear response of two coupled damped oscillators.

Keywords

dual-frequency laser	VECSEL	Nd:YAG laser
laser dynamics	nonlinear coupling	noise

Bruit dans les lasers à semiconducteurs et les lasers à solide en régime d?émission bifréquence

Les sources cohérentes de lumière émettant deux fréquences optiques avec une différence largement accordable dans le domaine radiofréquence et un fort degré de corrélation entre leurs fluctuations respectives peuvent être d?un grand intérêt pour de nombreuses applications telles que la photonique micro-onde, les horloges atomiques ultra stables, la physique atomique, la métrologie, etc. C?est le cas des lasers bifréquences émettant deux modes de polarisations linéaires croisées avec une différence de fréquence dans le domaine radiofréquence. Nous comparons les caractéristiques de telles sources bifréquences basées sur des lasers à semiconducteurs (VECSEL: vertical-external-cavity surface-emitting laser) ou des lasers à solide (notamment les solides dopés Nd3+ ou Er3+). Au-delà de la différence évidente entre les mécanismes de gain dans les lasers à semiconducteurs et dans les lasers à solide, le VECSEL bifréquence et le laser Nd:YAG bifréquence ne présentent pas la même dynamique. Le VECSEL bifréquence, comme pour un laser de classe A, a une dynamique dénuée d?oscillations de relaxation puisque la durée de vie des photons dans la cavité est beaucoup plus longue que celle de l?inversion de population. A l?opposé, le laser Nd:YAG bifréquence possède une dynamique présentant des oscillations de relaxation comme pour un laser de classe B, en vertu du fait que la durée de vie des photons dans la cavité est plus courte que celle de l?inversion de population. Dans cette thèse, nous explorons les mécanismes par lesquels cette dynamique, en plus du couplage non linéaire entre les deux modes, gouverne le bruit dans les lasers bifréquences. En particulier, nous analysons à la fois expérimentalement et théoriquement les propriétés spectrales des différents bruits (intensité, phase) ainsi que leurs corrélations dans le cas d?un VECSEL bifréquence de classe A et d?un laser Nd:YAG bifréquence de classe B. Enfin, un modèle de réponse linéaire de deux oscillateurs amortis couplés permet d?interpréter les résultats obtenus sur la corrélation entre ces différents bruits.

Mots-Clefs

laser bifréquences	VECSEL	Nd:YAG laser
dynamique de laser	couplage non linéaire	bruit